Control and Collisions of 87Rb and 133Cs Atoms in Optical Tweezers

RALPH VINCENT BROOKS

Control and Collisions of ^{87}Rb and ^{133}Cs Atoms in Optical Tweezers

Ralph Vincent Brooks

A thesis submitted in partial fulfilment
of the requirements for the degree of
Doctor of Philosophy

Department of Physics
Durham University

2022

Control and Collisions of ^{87}Rb and ^{133}Cs Atoms in Optical Tweezers

Ralph Vincent Brooks

This thesis reports the first steps towards the production of an optical tweezer array of ultracold ^{87}Rb^{133}Cs molecules. Such a system represents a long-standing goal: the full quantum control of individual polar molecules. Harnessing the long-range dipolar interactions and the rich rovibrational structure of ultracold molecules will unlock new applications in quantum computation, quantum simulation and quantum chemistry.

We demonstrate loading of single Rb and Cs atoms into species-selective optical tweezers of wavelengths 814 nm and 938 nm from magneto-optical traps of each species. We characterise the tweezers, detailing measurements of the trap frequency, light shift, trap waist and mean atom temperature. These measurements are performed using a newly-built apparatus, the design and construction of which are described in depth.

Next, we demonstrate control of the internal state of the atoms through optical pumping and microwave transfer. Using an acousto-optic deflector, we demonstrate control of the tweezer position, which is used to produce and rearrange a 1D array of five Cs atoms. Furthermore, we use this positional control to merge species-selective tweezers, which is used to prepare exactly one Rb atom and one Cs atom in the same optical tweezer.

We then use our control of individual atoms to study interatomic collisions. We demonstrate transfer of two or three Cs atoms into the same optical tweezer without heating, and discuss a method of separating tweezers to image multiple homonuclear atoms. We perform Feshbach resonance spectroscopy using pairs of Cs atoms prepared in the same optical tweezer. We observe nine loss features corresponding to Cs Feshbach resonances, and one loss feature corresponding to a zero in the scattering length. Finally, we study interspecies collisions of one Rb atom and one Cs atom.

The next steps towards an array of ground-state polar molecules, namely magnetoassociation and stimulated Raman adiabatic passage, will build on the work presented here.

Declaration

I confirm that no part of the material offered has previously been submitted by myself for a degree in this or any other university. Where material has been generated through joint work, the work of others has been indicated.

Ralph Vincent Brooks
Durham, May 22, 2022

Acknowledgements

A PhD is an arduous undertaking at the best of times, never mind during a global pandemic. I wish to thank the host of people who have supported me and contributed to the project since I joined.

Firstly I must thank my fantastic supervisor Simon Cornish. I am deeply grateful for all of the encouragement, advice and constructive criticism he has given me over the last 5 years. I am thankful for his belief in me, and hope that some of his diligence and eye for detail has rubbed off. I also thank my co-supervisor Ifan Hughes for his considered advice and the many fascinating anecdotes he has shared over the years.

An experiment such as this is very much a team endeavour, and I have had the fortune of working with a very talented group of labmates. I thank Ana Rakonjac, who led the tweezer project in the first half of my PhD, for teaching me the basics and helping me orient myself. Similarly I thank Alex Guttridge, who led the project in the second half of my PhD, for sharing his deep insight and encyclopedic knowledge of atomic physics. I have been lucky to share the lab with fellow PhD students Stefan Spence and Daniel Ruttley, who I thank for their boundless enthusiasm and hard work. I am sure the experiment will flourish in their capable hands. I express my gratitude to everyone mentioned thus far for their generous feedback on this thesis.

Thank you also to the others who have contributed to the project and shared their expertise with me. I am especially grateful to Lewis McArd, who has always been quick to share his deep understanding of all things electronic and mechanical. Thank you to Alex Alampounti for his help and enthusiasm. Thank you also to Rahul Sawant and Phil Gregory for their contributions to the project. Thanks to Sarah Bromley and Kali Wilson for their advice and suggestions over the years. I also thank Jeremy Hutson and Matthew Frye for lending theory support to our experimental results. Thank you to Jonas Rodewald and Mike Tarbutt at Imperial College London for useful discussions and sharing equipment for characterising our high-NA objective.

The expertise of the technical support staff in the Durham physics department has been an invaluable resource during my PhD. Thank you to the staff

of the mechanical workshop, whose craftsmanship never ceases to amaze me. In particular, I thank Stephen Lishman for his patience and professionalism in the face of my unreasonable requests. Thank you similarly to the staff of the electronics workshop, in particular John Scott and Bob Platt.

It has been a pleasure to be part of the wider QLM group here in Durham. I have enjoyed the many excursions to the Vic with Callum, Liam, Jack, Tom, Nick, Jake and Lucy. A massive thank you to the FitMol group, who include Claire, Dani and Jemma, for inspiring me to build my fitness through running, tennis and swimming.

Thank you to Durham University for funding my PhD studentship.

I have been fortunate to have so many friends and family who I have supported me during my PhD. Here, I need to express my sincere gratitude to Mum and Dad, without whose commitment to my education I would not have made it this far.

Moving in with two strangers was a risky move, but it turned out well. Thank you to Danny and Parisa, who have been such fantastic housemates over the entirety of our PhDs. I am grateful to the other friends I made, Ugne, Beth, Jack and Dean for the many welcome board game nights and hands of poker lost.

My undergraduate friends have been a great support and distraction from the lab. Cheers to the Skyebois TJ, Tom, Jack and Patrick for keeping me sane during the interminable lockdowns through many a game of Civ 5. Thanks also to my friends Hannah, Catherine, Toni, Luke, Ella, Gill, Jess and Galina for being such a lovely lot.

My final and deepest thanks go to Tia, who has had to put up with a lot from me these last few years. I could not have done this without your patience, wisdom, thoughtfulness or love. And fine, I acknowledge Brandy.

Contents

List of Figures

List of Tables

Chapter 1

Introduction

Ultracold polar molecules are an increasingly popular experimental platform, because their physical properties give rise to a number of diverse applications [1, 2]. In particular, polar molecules possess a permanent electric dipole moment which gives rise to long-ranged dipole-dipole interactions (DDIs). Furthermore, in comparison to atoms, molecules have a rich internal structure: they possess additional rotational and vibrational degrees of freedom, which can be exquisitely manipulated via experimental means.

Polar molecules can be used for quantum simulation [3], precise tests of fundamental physics [4], studies of quantum-controlled chemistry [5] and quantum logic [6]. Several applications require single-molecule resolution and control, and so the tools which have been successfully developed to control single atoms are now being turned towards molecules: namely the quantum gas microscope [7] and the optical tweezer [8, 9].

1.1 Quantum Science with Ultracold Molecules

Polar molecules are well suited to the quantum simulation [10] of many-body Hamiltonians [3]. Pseudo-spins can be encoded onto the rotational states of a molecule using microwave fields [11], which are experimentally convenient. The dipole moment of polar molecules, which is typically a few Debye in magnitude [12], means they can interact via the long-ranged anisotropic DDI. Molecules pinned in an optical lattice and interacting via the DDI exhibit

spin-exchange interactions [13], and can be used to study models of quantum magnetism [14] and to explore exotic phases [15, 16]. Investigation of these spin-lattice models is motivated by their wide applicability to condensed matter physics [17, 18].

Other systems exhibit long-ranged DDIs, for example magnetic atoms and Rydberg atoms. The magnetic dipole moment of magnetic atoms such as Cr [19], Er [20, 21], and Dy [22] is only $\sim 10\ \mu_{\mathrm{B}}$, so that their DDIs are several orders of magnitude weaker than for molecules. Rydberg atoms offer electric dipole moments several orders of magnitude higher than polar molecules, resulting in much faster interaction times. However, Rydberg atoms in low angular momentum states have much shorter lifetimes than molecules, and the optical traps which are red-detuned to the alkali-atom ground state repulse the Rydberg state[1] [24], resulting in limited interaction times [25].

Molecules can be used to probe fundamental physics with fantastic precision [26]. In contrast to high-energy collider experiments, tabletop atomic and molecular physics experiments typically occupy a single room and are orders of magnitudes less expensive to build. New theories which extend the standard model of particle physics (e.g. to explain the observed matter-antimatter asymmetry of the universe) typically imply new values for the electric dipole moment of the electron (eEDM). Ultracold molecules may be used to directly probe the eEDM and thus set constraints on models in fundamental physics [4]. The relativistic motion of the electron means that even modest applied electric fields can result in huge internal electric fields of order GV cm^{-1} inside the molecule. The high interaction energies which result allow the eEDM to be measured with extreme precision. eEDM experiments with YbF [27] and ThO [28, 29] molecules have set increasingly stringent bounds on the EDM of the electron. Furthermore, measurement of the fine structure constant has been proposed [30], as well as measurement of time variation in the electron-proton mass ratio, to which molecular vibrational energy levels are highly sensitive [31–33].

The production of molecules at ultracold temperatures has enabled the study

[1] A solution to this problem was recently demonstrated for alkaline earth Rydberg atoms, where the polarisability of the Rydberg atom ion core enabled confinement in red-detuned tweezers lasting $> 100\ \mu$s [23].

of molecular collisions and quantum-controlled chemistry. Molecules such as $^{40}K^{87}Rb$ are chemically unstable [34], exhibiting exoergic reactions of the form $KRb + KRb \rightarrow K_2 + Rb_2$, resulting in loss from the confining trap [35]. It was shown that these chemical reactions could be suppressed via control of the molecular stereodynamics[2] via confinement in a pancake dipole trap [36].

Surprisingly, other experiments with energetically stable molecules still exhibit larger than expected loss rates, largely independent of the reaction energetics [37]. The mechanism proposed to explain this loss was the formation of long-lived 2-molecule collisional complexes, which arise because of the dense Feshbach spectrum of two molecules [38, 39]. The complexes formed in so-called 'sticky collisions' were suggested to be long-lived, so that collisions with a third molecule result in loss of all three molecules from the trap. It was later shown that the complex lifetime had been overestimated and that enhanced three-body loss could not be responsible. Instead, fast photo-induced loss of the complexes by the trapping light was suggested [40], and later verified [41, 42]. Techniques which could suppress the photo-induced loss of complexes are modulation of the trapping light [41], confinement blue-detuned box potentials [40], microwave shielding [43] and isolation of molecules, for example using optical tweezers.

Quantum computation is a key area of interest in modern science. When applied to certain problems, it has been shown that quantum computers can outperform their classical counterparts [44]. Quantum computation with ultracold molecules was first proposed in 2002 [6] since their long qubit coherence times and strong dipole-dipole interactions make them promising qubits. Typically, computational basis states are encoded onto the hyperfine levels of a molecule, because of their long radiative lifetime. In this scheme, a DDI-mediated CNOT (controlled-NOT) gate can be realised between two molecules using microwave excitation; selective excitation of specific sites is provided by an electric field gradient [6, 45]. Other quantum gate schemes for polar molecules have since been proposed [46–49], however as will be discussed in section 1.3.2, more recent proposals make use of optical tweezers.

[2] That is, control of the molecules' motion and relative angles.

1.2 Production of Ultracold Molecules

The methods for producing cold molecules can be broadly divided into two categories: 'direct', where hot molecules are cooled by some mechanism to low temperatures, and 'indirect', where atoms are first cooled to low temperatures and then combined to make molecules. We compare these approaches, which have both been used to prepare single molecules in optical tweezers [50, 51].

1.2.1 The Direct Approach

Perhaps the most intuitive way to produce cold molecules would be to cool them directly using lasers, in analogy to the now-routine method of atomic laser cooling. Unfortunately, the same molecular structure which makes molecules experimentally interesting also makes them experimentally challenging to cool.

Atoms in a magneto-optical trap (MOT) typically require $\sim 10^4$ photon scattering events to be slowed from room-temperature velocity, requiring a closed transition to cycle on [52]. The challenge for molecules is in identifying such a transition. Molecules excited from the ground state suffer from rotational and vibrational branching, whereby they decay to a different rovibrational level from where they started, and are decoupled from the cooling light [53]. For most molecules, an impractical number of repump lasers would be required to plug leaks from the cycling transition. However for certain molecules, the Frank-Condon matrix which governs vibrational decay is highly diagonal [54], so that only a few repump lasers are required. Rotational branching can then be suppressed by the choice of a rotationally closed transition, where selection rules prohibit decay from the cooling cycle. This choice of rotationally closed transition results in dark states in the ground-state Zeeman substructure which must be destabilised for an efficient MOT. This can be done using a radio-frequency (RF) MOT [55], or a dual-frequency MOT [56].

Laser cooling of molecules is inefficient compared to atoms, because of their numerous internal states and low scattering rate. The capture velocity of a molecular MOT is therefore very low, typically ~ 5 m s^{-1} [57], so typically a high-density sample of molecules must first be pre-cooled before loading into a

MOT. Cold molecular beams have been prepared via buffer gas cooling, where molecules are first produced via laser ablation of a target, and then thermalise with a cryogenic buffer gas such as helium or neon [58]. The molecular beam must then be decelerated, which can be achieved using methods such as laser slowing [59], mechanical deceleration [60], Stark deceleration [61], Zeeman deceleration [62] and Zeeman-Sisyphus slowing [63]. To date, direct laser cooling of molecules has been demonstrated for SrF [64], YO [65, 66], CaF molecules [57, 67], SrOH [68] and YbF [69] molecules.

1.2.2 The Indirect Approach

An attractive alternative to direct cooling methods is to first cool atoms to ultracold temperatures and then associate them to make molecules. The resulting molecules retain the high density and low temperature of the original atoms. Molecules can be formed optically via photoassociation [70], or magnetically via magnetoassociation [71].

During one-photon photoassociation, colliding atoms absorb a photon and form a weakly-bound molecule [70]. Photoassociation (PA) is a powerful experimental tool for probing ultracold collisions. It can be used to measure the atomic scattering lengths [72], knowledge of which was essential in realising Bose-Einstein condensation of ^{85}Rb [73], ^{133}Cs [74], and ^{39}K [75]. Photoassociation can be used to precisely measure the absolute binding energy of a molecule, and to manipulate the collisional properties of a gas via an optical Feshbach resonance [76].

Excited molecules formed via photoassociation can decay to the ground vibrational state of the molecular potential, however this happens with low probability due to a low Frank-Condon overlap between the two states. Typically only a small molecular fraction is produced in the rovibrational ground state [77, 78], with the rest distributed over many rotational and vibrational states.

In contrast to photoassociation, several thousand ground state polar molecules can be created via magnetoassociation [71]. In this technique, a magnetic field is ramped across a magnetic Feshbach resonance, which occurs when the free state of two atoms energetically approaches that of a bound state [79]

(see section 5.1.2). Coupling between the two channels results in an avoided crossing which can be adiabatically followed by ramping the magnetic field at less than a critical speed [80]. The molecules produced are loosely-bound, short-lived 'Feshbach molecules'. The excited molecules have a vanishingly small dipole moment, and so to access useful dipolar physics, they must be transferred to the ground state of the molecular potential. This is done using STImulated Raman Adiabatic Passage (STIRAP), a coherent two-photon process [81]. Molecules which have been formed via magnetoassociation and transferred to the ground state are the fermionic species ^{40}K^{87}Rb [82, 83], ^{23}Na^{40}K [84, 85] and ^{23}Na^{6}Li [86], and the bosonic species ^{133}Cs$_2$ [87], ^{87}Rb$_2$ [88], ^{87}Rb^{133}Cs [89, 90] and ^{23}Na^{87}Rb [91].

1.3 Control of Single Molecules

Coherent control of the internal states of bulk-gas polar molecules is now well established. Microwave control of the internal hyperfine and rotational states [92, 93] has been used to demonstrate the long coherence times of rotational states via Ramsey interferometry [3]. The permanent dipole moment of the ground state can be accessed using electric fields, and measured using Stark spectroscopy [82, 90]. Despite these impressive milestones, several applications of molecules require full motional state control over single molecules as well.

1.3.1 Top-Down or Bottom-Up?

For atomic systems, two complimentary tools have emerged for exerting control over single atoms in ordered arrays. The 'top down' quantum gas microscope deals with large arrays of atoms, and is well suited for studying many-body systems and spin-lattice models. Optical tweezers in contrast, enable the study of small arrays and few-body interactions, in a 'bottom-up' approach. The QSUM collaboration, of which the experiment detailed in this thesis is a part, is pursuing both of these approaches, with the goal of achieving full quantum control over ultracold molecules. We first review the application of these techniques to atomic systems.

A quantum gas microscope consists of an optical lattice into which cold atoms are loaded, and a high-numerical aperture microscope objective which directly images a single plane of the lattice, with single-site resolution [7]. The optical lattice is formed from interfering laser beams, and the lattice plane typically contains hundreds of sites. Near-unity filling of the array can be achieved by exploiting the superfluid to Mott insulator phase transition. Deep in the Mott insulator regime, where atom interactions dominate lattice site tunnelling [94], the number of atoms per site can be fixed to one [95]. Single-atom manipulation can be realised by applying a tightly-focussed off-resonant beam to a single site [96].

In contrast, optical tweezers enable the study of scalable few-body systems. An optical tweezer is a far red-detuned optical dipole trap with a micron-scale waist. Atoms are trapped at a minimum in the potential, which occurs at the focus of the tweezer [97]. Light-assisted collisions result in stochastic loading of the tweezer, with one atom loaded with $\sim 50\%$ probability [8, 98]. Optical tweezers are a versatile tool, with diverse applications in atomic physics as well as bioscience [99, 100]. Arrays of optical tweezers can be produced using acousto-optic or spatial-light modulator technology. Sophisticated rearrangement algorithms can be employed to reduce the entropy of the stochastically loaded arrays to yield near-unitary filling [101–104]. These methods have contributed greatly to the scalability of tweezer arrays for applications in quantum science.

Restricted initially to alkali metals, more recently tweezer arrays of alkaline-earth atoms have recently been realised [105, 106]. The technology has also been extended to arrays of Rydberg atoms, which have been used to demonstrate quantum simulation of Ising-like spin models in 1D [107] and 2D arrays [108]. Furthermore, systems of interacting Rydberg atoms are a promising and scalable architecture for digital quantum computation [109].

1.3.2 Ultracold Molecules in Tweezers

Optical tweezers can provide versatile single-site control for single atoms. In recent years, the platform has been extended to polar molecules. Highly-excited ^{21}Na^{133}Cs molecules were first assembled via photoassociation [50]

and later magnetoassociation [110, 111]. Production of an array of ground-state NaCs molecules has since been achieved [112, 113]. At a similar time, laser-cooled CaF molecules were directly loaded into an optical tweezer array [51], and intermolecular collisions were observed [114]. There are distinct advantages to each approach: for indirectly formed molecules, cooling of the constituent atoms is more straightforward than directly cooling a molecule. On the other hand, directly-cooled molecules, possessing a cycling transition, may be fluorescence imaged whereas indirectly cooled species must first be separated. A current drawback of indirectly cooled molecules is that it is more challenging to cool them to the motional ground-state of an optical tweezer [115], whereas indirectly formed species inherit the low motional state of the pre-cooled atoms.

The tweezer platform is well suited for realising several proposals which rely on precise control of only a few polar molecules. One such scheme is a dipolar exchange gate between two molecules in tweezer, proposed by Ni *et al.* [116]. Two hyperfine states of the $N = 0$ rotational manifold are chosen as the computational basis states $|0\rangle$ and $|1\rangle$, since they have long coherence times and do not interact. A microwave pulse transfers a $|0\rangle$ molecule to a rotationally excited $N = 1$ state, labelled $|e\rangle$ which can interact with a second molecule left in $|1\rangle$. The excitation hops via the dipolar exchange interaction [13], and a second pulse de-excites the molecule, realising an iSWAP gate. The method can be scaled to many qubits, which are held in storage until required for a gate.

Sawant *et al.* have proposed the creation of a molecular *qudit* [117]. A qudit is a higher dimensional quantum bit consisting of d levels, rather than just two, which allows a similarly sized Hilbert space to be realized as for n qubits, utilising only $n/\log_2(d)$ qudits. This relaxes the scalability criterion for quantum computation somewhat [118], so that quantum advantage[3] can be achieved with as few as 15 qudits. The proposal suggests that the rich rovibrational structure of polar molecules can be used to implement a four-level qudit on an ^{87}RbCs molecule. This scheme is attractive, because only one molecule is required, and the qudit states can be conveniently accessed

[3]Quantum advantage is the outperformance of a classical computer by a quantum computer on a class of problems which are unfeasible to solve using the classical computer [119].

via microwave transitions.

Other applications of molecules in tweezers include an entanglement gate realised using the DDI [120], and quantum simulation of lattice gauge theories in a 1D array of molecules [121]. Furthermore, it has been proposed that non-destructive imaging of a molecule in a tweezer, and readout of its rotational state, could be achieved by interfacing it with a Rydberg atom [122–124].

1.3.3 Plan to Build Single Molecules

There are six steps we must implement to realise a single RbCs molecule in an optical tweezer, summarised in Fig. 1.1. Firstly a reservoir of cold ^{87}Rb and ^{133}Cs atoms is prepared in dual magneto-optical traps. Secondly, species-selective optical tweezers are loaded with single atoms. Next, the atoms are transferred to the motional ground state of each tweezer via Raman sideband cooling (RSC), which has been demonstrated elsewhere with high fidelity for both Rb [125–127] and Cs [128]. The fourth step is to adiabatically merge the tweezers, and then magnetoassociate the atoms using an interspecies Feshbach resonance to make a weakly-bound Feshbach molecule. The final step is transfer to the molecular ground state via STIRAP. This scheme will be extended to an array of tweezers to form several molecules, which will be used to study few-body interactions and perform proof-of-principle quantum gate operations.

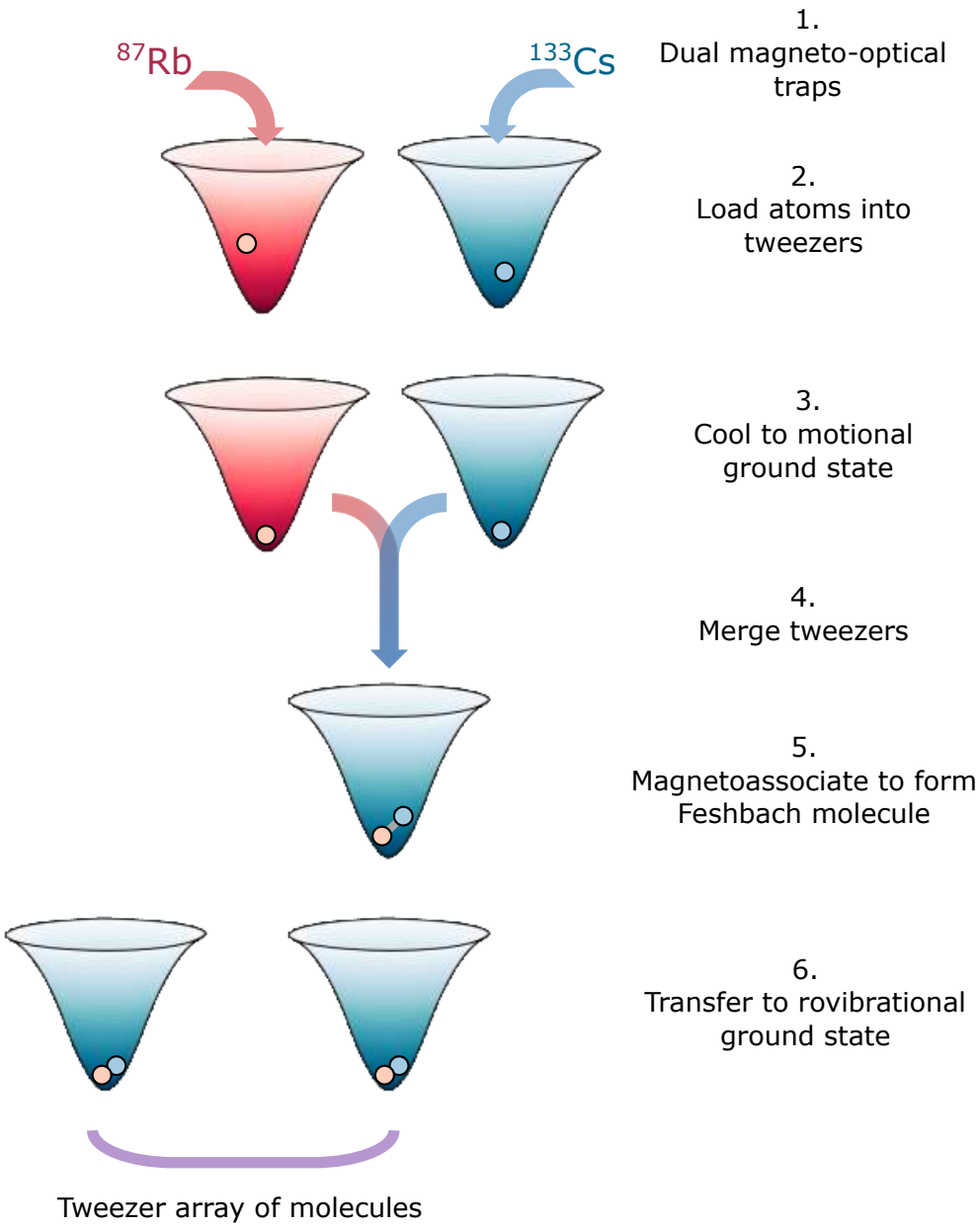

Figure 1.1: The roadmap for building single RbCs molecules in optical tweezers. 1: A dual-species MOT of Rb and Cs atoms is prepared. 2: Single atoms are loaded from the MOT into species-selective tweezers. 3: Both atoms are transferred to the motional ground state of their respective tweezers via Raman sideband cooling. 4: The tweezers are merged, preparing two atoms in a single tweezer. 5: The atoms are magnetoassociated to form a weakly-bound molecule. 6: The molecule is transferred to rovibrational ground state via STIRAP. These steps can be performed on several tweezers simultaneously to create an array of ground-state molecules.

1.4 Outline of this Thesis

This thesis details the construction of an experimental apparatus designed to build arrays of single RbCs molecules in optical tweezers. We characterise the apparatus and use it to study interatomic collisions. The thesis is structured as follows:

- **Chapter 2:** The experimental apparatus and laser systems used for the work of following chapters are detailed.
- **Chapter 3:** We demonstrate loading and imaging of atoms in optical tweezers, and characterise tweezers of several wavelengths.
- **Chapter 4:** We detail how the internal states of the atoms are controlled. We present positional control of the tweezers and rearrangement of arrays of tweezers.
- **Chapter 5:** Results of collision studies of Rb+Cs atom pairs and Cs+Cs Feshbach spectroscopy are presented.
- **Chapter 6:** We conclude the thesis and give an outlook towards molecule formation.

1.5 Contributions of the Author

I arrived in the lab before the optical tables, so everything described in this thesis has been built from scratch over the course of my PhD. Such a project is a team effort, with significant contributions from a team of PhD students including myself, Stefan Spence and Dan Ruttley. Several postdoctoral researchers have been involved, including Ana Rakonjac, Alex Guttridge, Lewis McArd, Alex Alampounti, Rahul Sawant and Phil Gregory. We have also had the assistance of summer and master's students Wendy Tomboza and Jie (Ben) Zhang. Simon Cornish has overseen the project throughout.

The vacuum chamber and coil layouts presented in Chapter 2 were designed by Phil. They were assembled and tested by Lewis and myself. The laser systems for the magneto-optical trap (MOT) and optical pumping were constructed by Ana and myself. The Rb and Cs MOTs were characterised by Ana and myself. I characterised the high-NA lens, and Ana and I designed and assembled the tweezer optical setup. The experimental control was upgraded and expanded by Stefan. The tweezer loading, imaging and characterisation experiments presented in Chapter 3 were performed by myself, Alex G and Stefan. Rahul performed early Monte Carlo simulations of the experiment, and the atomic polarisability code was written by Stefan. In Chapter 4, the state control was established by myself, Alex G and Stefan. The AWG code was written by Alex A. The experiments with the AOD for merging and tweezer arrays were undertaken by me, and I implemented the array rearrangement. Dan wrote the code for, and characterised the SLM. I performed the collision experiments of Chapter 5, with help from Alex G and Dan. The bias coils used for these experiments were characterised by Alex G, Dan and Stefan. The Raman sideband cooling discussed in Chapter 6 was implemented in parallel to this work by Stefan and Alex G, with assistance from me on the optical setup.

Theory support for the Rb+Cs collisions and Cs+Cs Feshbach spectroscopy was provided by Jeremy Hutson and Matthew Frye, who calculated k_2 loss rate coefficients and shared many insights.

1.6 Publications

The following publications have arisen from the work presented in this thesis:

- **Preparation of one ^{87}Rb and one ^{133}Cs atom in a single optical tweezer**
  R. V. Brooks, S. Spence, A. Guttridge, A. Alampounti, A. Rakonjac, L. A. McArd, Jeremy M. Hutson and Simon L. Cornish
  *New Journal of Physics **23** 065002 (2021)*

- **Feshbach Spectroscopy of Cs Atom Pairs in Optical Tweezers**
  R. V. Brooks, A. Guttridge, Matthew D. Frye, D. K. Ruttley, S. Spence, Jeremy M. Hutson and Simon L. Cornish
  Submitted 2022, preprint available at: arXiv:2204.08877

- **Preparation of ^{87}Rb and ^{133}Cs in the motional ground-state of a single optical tweezer**
  S. Spence, R. V. Brooks, D. K. Ruttley, A. Guttridge, and Simon L. Cornish
  Submitted 2022, preprint available at: arXiv:2205.09457

Chapter 2

Experimental Apparatus

2.1 Overview

This chapter describes the experimental apparatus constructed over the course of my PhD. The apparatus is designed for producing arrays of RbCs molecules in optical tweezers using the protocol presented in Fig. 1.1.

The main features of the apparatus discussed in this chapter are summarised in Fig. 2.1, which shows a side-on view of the experiment. We first discuss the vacuum apparatus and science cell, which are necessary to produce an ultra-high vacuum (UHV) environment. We then detail the internally-mounted electrode array necessary for aligning molecule dipole moments. Next, we give an overview of the magnetic field coils, which are necessary for producing magneto-optical traps (MOTs), eliminating stray fields and applying bias fields. We present the lasers and optics for preparing beams at the correct frequency for laser cooling and optical trapping. We then discuss characterisation of the high-numerical aperture objective lens used both to produce the optical tweezers and to image confined atoms. Finally, we discuss the experimental control software which is used to program, trigger and synchronise the above.

The experiment is distributed over two optical tables, referred to as the 'laser table' and the 'main table'. The lasers and frequency preparation optics responsible for producing all the beams used in the experiment are situated on the laser table. Light is transported from the laser table to the main table

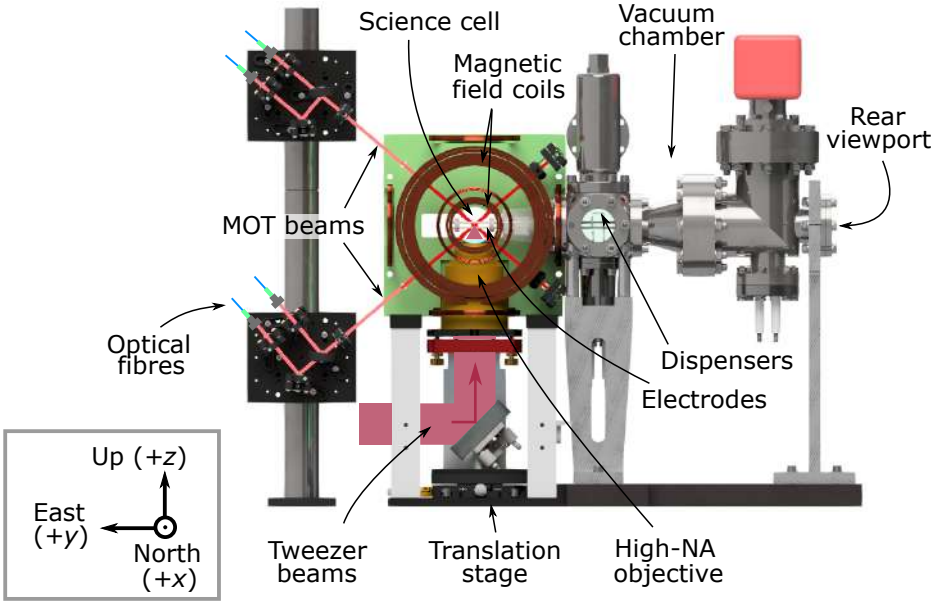

Figure 2.1: Overview of the experiment, seen from the north side. The lab coordinates are defined as shown. The labels in brackets define the positive x, y and z axes, which are more convenient coordinates when discussing tweezers in the science cell.

via long polarisation-maintaining optical fibres. Experiments with optical tweezers and cold atoms occur on the main table, which is the site of the apparatus shown in Fig. 2.1. It is convenient to use two coordinate systems: when discussing the optical layouts in the lab, we use compass coordinates North-South (N/S), East-West (E/W) and Up/Down (U/D) as defined in the figure. In later chapters when working with optical tweezers in the science cell, it is more appropriate to define a new coordinate system x, y and z, with the positive directions as labelled.

A laminar airflow unit installed on the main table canopy mitigates dust build up on the table. The main table may be floated using pressurised air to reduce vibrational instability. Both the main and laser tables are enclosed with Palight laser safety guards, with black-anodised aluminium guards rising 300 mm about the table edges. An air conditioning unit maintains a constant lab temperature of 21 °C, with variations of ±0.5 °C.

2.2 Vacuum System

Cold-atom experiments must take place under UHV conditions to suppress the rate of collisions of the trapped atomic species with room-temperature background gases. In such a collision, the enormous kinetic energy gained by the trapped atoms would be sufficient to eject them from the trapping potential.

The experiment is designed to balance two primary requirements: numerical aperture (NA) and optical access. To produce tweezers with a tight waist and to optimise fluorescence collection, a high-NA objective subtending a large solid angle is required, favouring a large-diameter lens located close to the atoms which is able to capture a maximal number of photons. This requirement must be weighed against the exactingly high demand for optical access in a dual-species experiment, where beams for two MOTs, two RSC setups, STIRAP and more are required. Additionally, we must also find room to accommodate the alkali-metal dispensers (AMDs) *and* the electrode array.

To satisfy these many competing requirements, the vacuum chamber is designed around a glass science cell, which allows optical access from the six directions defined in Fig. 2.1 (with access from the west facilitated by the rear viewport), as well as several more in the U/D-E/W plane. The high-NA lens is located out of vacuum and mounted underneath the science cell. Its large size owes to the multiple internal optics which suppress chromatic focal length shifts between the tweezer and imaging wavelengths.

2.2.1 Vacuum Chamber

Fig. 2.2(a) shows an image of the single-chamber vacuum system. The key feature is the science cell, which is mounted at the front of the chamber. The science cell connects to a 'spherical cube[1]', which was chosen for its compatibility with 'groove-grabbers[2]'. The electrode array is internally mounted using four groove-grabbers at contact points at the east and west entrances of the spherical cube (section 2.3).

[1]Kimball Physics MCF275-SphCube-C6
[2]Kimball Physics MCF275-GrvGrb-CB03

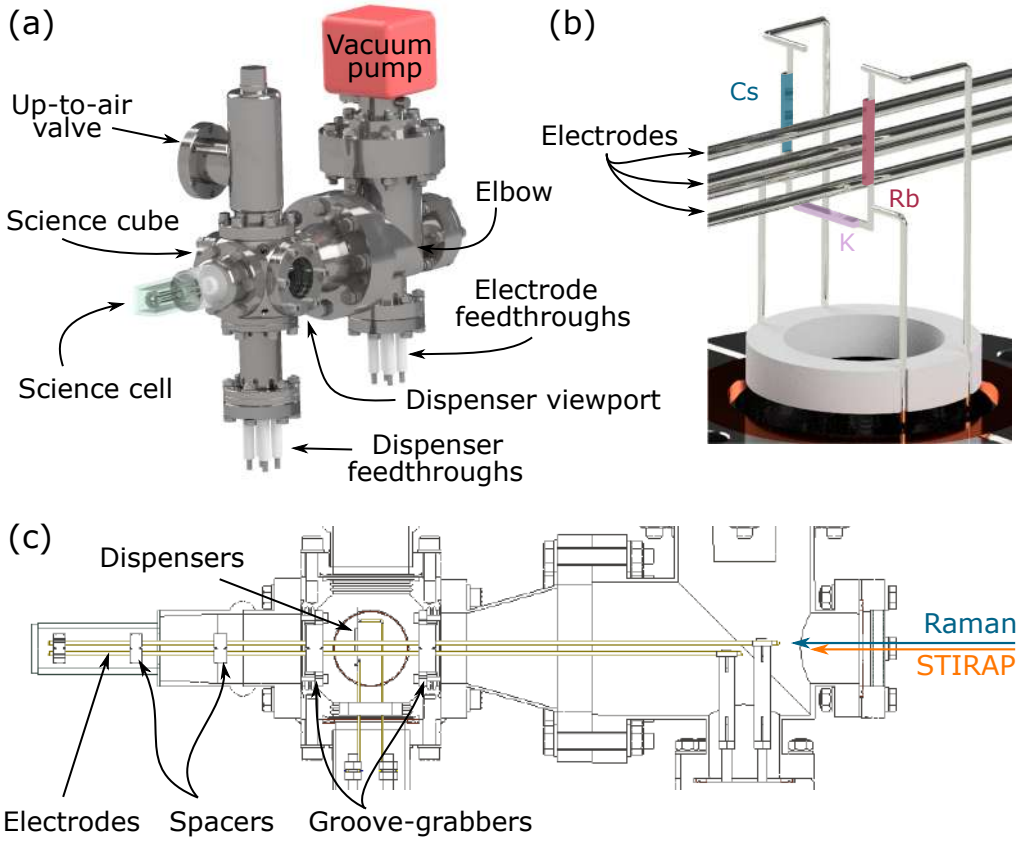

Figure 2.2: Schematic views of the vacuum apparatus. (a) Rendering of the vacuum chamber highlighting the main features. (b) U-shape configuration of the Cs (blue), Rb (red) and K (lilac) dispensers inside the vacuum cube. The electrodes pass through the centre of the arrangement. The feedthrough connections are splayed out by a macor ring (white). (c) Cross-section view of the vacuum chamber viewed from the north. The electrodes run the length of the chamber from a feedthrough at the rear all the way to the science cell. The rear viewport allows access for Raman and STIRAP beams.

The spherical cube houses AMDs[3] for Rb, Cs and potassium (K) as shown in Fig. 2.2(b). The dispensers are mounted in a U-configuration, to make clearance for the electrode array, and face towards the science cell. The dispensers are spot-welded to four pins running via a straight tube[4] to feedthroughs[5] at the base of the chamber. A dispenser may be activated using the feedthroughs to run current through across it. Typically a current of ~ 2 A is applied through the Rb and Cs dispensers, however, we have found it possible to

[3]SAES 5G0010, 5G0050, 5G0125 (Rb, Cs, K respectively)
[4]Scanwel CFSCR070-080
[5]VacGen ZEFT34A (for both dispensers and electrode feedthroughs)

operate the experiment with the dispensers switched off for several weeks at a time. The dispenser activation threshold of 6 A should not be exceeded, to avoid depleting the dispensers and flooding the chamber.

The top port of the spherical cube is attached to an up-to-air valve[6], which was used in the initial pumping-down and baking of the chamber. Viewports[7] are mounted on the side ports of the cube which are useful for checking that the dispensers are firing correctly (using an infrared viewer to observe fluorescence from the hot dispensers). A conical reducer[8] connects the cube to an elbow piece[9]. The elbow allows optical access via a rear viewport for Raman and STIRAP beams Fig. 2.2(c), while also allowing connection of a vacuum pump and an electrical feedthrough for the electrodes, without obstructing optical access. The ion pump[10] maintains an ultra-high vacuum of $< 1 \times 10^{-10}$ torr, and connects to the elbow via a zero-length reducer[11].

2.2.2 Science Cell

At the front of the chamber is the science cell[12], where atoms released from the dispensers are cooled, trapped and manipulated. The cell comprises five glass plates of thickness 3 mm bonded together to give interior dimensions of $20 \times 20 \times 60$ mm. The glass used is Schott Borofloat-33, a borosilicate glass with refractive index $n \approx 1.47$ at near-IR wavelengths. The glass cell was bonded to a DN40 rotatable flange by the manufacturer using a *Houskeeper seal*, whereby the metal section is heated to cause expansion, and then allowed to shrink over the glass for a snug fit. The flange is fabricated from 316LN stainless steel which we chose for its low magnetic susceptibility.

The cell is anti-reflection (AR) coated to suppress detrimental back-reflections. In an earlier RbCs experiment, such reflections were observed to form standing waves which interfered with the experiment [129]. Furthermore, back-reflections could give rise to 'ghosting', an imaging artefact where the same

[6] MDC MAV-150_V
[7] Scanwel CFVPZ070
[8] Scanwel CFRCR114-070
[9] Scanwel CFE114SP
[10] NexTorr D100
[11] Scanwel CFRZ114-070
[12] ColdQuanta CQDU0010

object is imaged multiple times onto the camera. The inner and outer surfaces of the cell used in our experiment are coated with a CRK coating, designed to be highly transmissive for wavelengths $750 < \lambda < 1100$ nm at 0° angle of incidence. Transmission is also high at 55°, which is exploited by the vertically-mounted MOT beams shown in (Fig. 2.1) As a result of the coating, the science cell displays beautiful shifts from green to deep pink as it is rotated.

The rotatable flange allows for fine-tuning of the cell's angle about its long axis. This is necessary for matching the angle of the objective to the angle of the cell to avoid optical aberration, as discussed in section 2.7. The cell was made parallel to the optical table using a beam retro-reflected from the lower face of the cell over a long path length. We estimate the lower cell face is parallel to the table to within 6.00(6) minutes of arc. In a similar fashion, we have measured the parallelism of the top and bottom cell walls and find there is a relative angle of 14.4(6) arcminutes. We have not measured the parallelism of two faces of the same cell wall, but the specified tolerance is 30 seconds of arc.

Glass vacuum cells will naturally bow under vacuum, due to atmospheric pressure. The flatness of the cell walls was measured by the manufacturer using Fizeau interferometry. Under vacuum, the cell surface deviates by $\sim 0.7\lambda$, bowing inwards at the centre, and agreeing with the manufacturer's finite-element analysis of the cell.

2.3 In-Vacuum Electrodes

An electrode array is built into the vacuum chamber so that large direct-current (DC) electric fields can be applied to molecules at the centre of the science cell. We now motivate why electric fields are required and discuss the design and assembly of the array.

2.3.1 Molecule Dipole Moment in a DC Electric Field

Heteronuclear diatomic molecules have an electric dipole moment (EDM) of $d_0 \sim 1$ D in the molecule frame, arising from the charge difference of the nuclei. A dipolar molecule has a rotational degree of freedom about an axis perpendicular to the internuclear axis. The corresponding rotational quantum number is $N = 0, 1, 2, ...$, with a projection M_N along a quantisation axis in the laboratory frame defined by some field. The electric dipole operator is an odd function, so it only has a non-zero expectation value between states of opposite parity. To take advantage of the long-ranged dipolar interaction between ultracold molecules, a controllable electric dipole must be induced in the laboratory frame. An oscillating dipole moment may be induced in the laboratory frame by creating a superposition of rotational states [130]. Alternatively, the molecule EDMs may be aligned in the laboratory frame by applying a static DC electric field E_{DC}, which mixes rotational states of opposite parity [131, 132].

The matrix element between rotational states $|N, M_N\rangle$ and $|N', M'_N\rangle$ is the sum of the rotational energy of the field-free molecule and the Stark shift due to E_{DC} [14, 133]:

$$\begin{aligned}\langle N, M_N|\,\hat{H}\,|N', M'_N\rangle &= B_0 \cdot N(N+1) \cdot \delta_{N,\,N',\,M_N,\,M'_N} \\ - d_0 E_{\mathrm{DC}} &\sqrt{(2N+1)(2N'+1)} \cdot (-1)^{M_N} \cdot \begin{pmatrix} N & 1 & N' \\ -M_N & 0 & M'_N \end{pmatrix} \begin{pmatrix} N & 1 & N' \\ 0 & 0 & 0 \end{pmatrix},\end{aligned} \tag{2.1}$$

where B_0 is the rotational constant, which is 0.51 GHz for the RbCs molecule [134]. The final terms in large parentheses are Wigner-3j symbols which encapsulate angular momentum addition rules and ensure mixing only of states with the same M_N.

The energy shift of the rotational levels with applied E_{DC} may be obtained by diagonalising the matrix constructed from the elements given in Eq. (2.1). Differentiating the energy shift yields the dipole moment induced in the laboratory frame by the external electric field. Contributions to the Stark effect are dominated by lower lying rotational states, so it is sufficient to consider

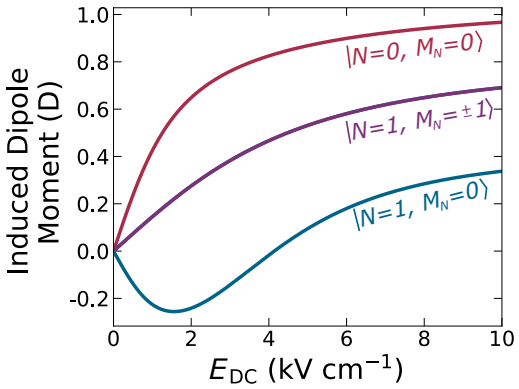

Figure 2.3: Laboratory-frame dipole moment with applied electric field for the $N = 0$ and $N = 1$ rotational states of a RbCs molecule.

mixing of rotational levels up to $N = 6$ [129, 133]. For d_0, we take the value measured for RbCs of 1.225 D [90]. The results are plotted in Fig. 2.3 for the lowest rotational levels $|N = 0, M_N = 0\rangle$ and $|N = 1, M_N = 0, \pm 1\rangle$. The induced dipole moment of the $N = 0$ state increases monotonically, saturating to the molecule-frame EDM at high field. Experimentally we expect to produce fields of ≈ 2 kV cm^{-1}, inducing a dipole moment of ≈ 0.7 D in the laboratory frame. The induced dipole moment of the state $|N = 1, M_N = 0\rangle$ crosses zero at 4.1 kV cm^{-1}, a fact which could be exploited to suppress dipolar interactions for molecules in $N = 1$ and engineer quantum gates based on ground-state interactions [46].

2.3.2 Design of the Electrode Array

The four-rod design of the array shown in Fig. 2.4(a) is motivated by the work of Gempel *et al.* [135]. While simple, the quadrupole configuration we have chosen allows for the electric field direction to be tuned to any angle in the plane orthogonal to the electrodes. Fig. 2.4(b) shows two possible field configurations: in (i), the molecules are aligned head-to-tail using a horizontal field; in (ii) they are aligned side-by-side using a vertical field. A drawback of using only four electrodes is that the field curvature along both axes cannot be eliminated simultaneously[13], which results in a reduced field uniformity near the trapping region along one axis. Nevertheless, the aspect

[13]This issue may be addressed with a more complex eight-rod array [135]. We compromised on a four-rod design due to the space concerns discussed in 2.2.1.

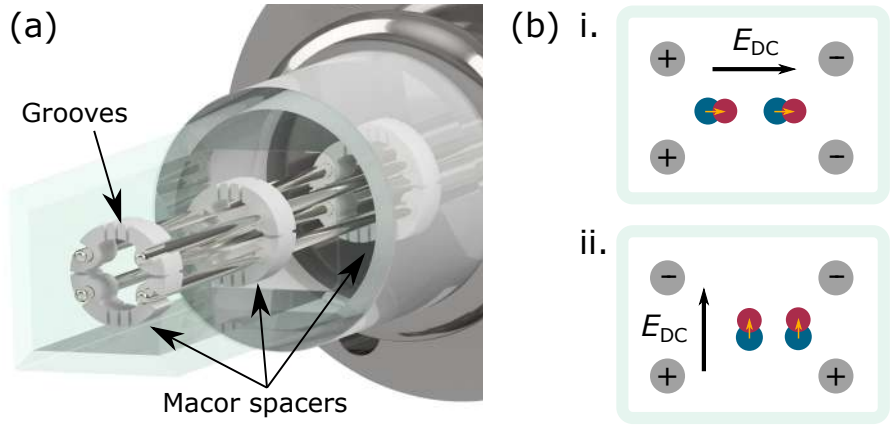

Figure 2.4: The in-vacuum electrode array. (a) Cut-away of the electrodes and macor spacers inside the science cell. Grooves machined into the spaces increase the surface path length to mitigate dielectric breakdown. (b) Arbitrary field directions can be set by choosing the charge pattern of each rod. (i) Molecules are aligned head-to-tail by a horizontal electric field. (ii) Molecules are aligned side-by-side using a vertical electric field.

ratio of the array may be chosen to eliminate the curvature along one axis. This occurs for an aspect ratio of $1:\sqrt{3}$, so correspondingly we suppress the horizontal field curvature by spacing the electrodes horizontally by 9.6 mm and vertically by 5.6 mm.

The electrode array is mounted inside the vacuum chamber. This is because in an earlier RbCs experiment, the electric field applied by externally mounted electrodes measurably polarises the science cell for $E_{\mathrm{DC}} > 1$ kV cm^{-1}. The cell is polarised against E_{DC} and therefore limits the fields achievable inside the science cell [90, 136]. We expect to mitigate this issue in our experiment by installing the electrodes in-vacuum.

Temporal Stability

The electric fields produced must be stable shot-to-shot over many thousands of experimental cycles lasting many hours. The level of stability required can be estimated by considering a rotational transition of the ^{87}RbCs molecule that will be addressed using microwaves in future experiments. The rotational transition $N = 0 \rightarrow N' = 1$ has a linewidth of $\sim$ 10 kHz and a frequency of 980 MHz [92] which are in the ratio $\sim 1/10^5$. The energy splitting of the rotational states must therefore be stable to one part in 10^5 for

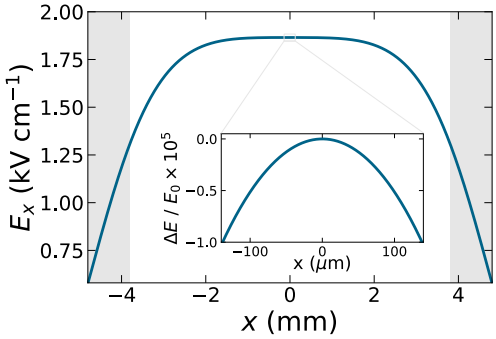

Figure 2.5: The spatial uniformity of the electric field. The main figure shows the horizontal component of electric field between the electrodes for the charge configuration shown in Fig. 2.4(b)(i). The vertical E_y components cancel. The shaded regions indicate the electrode material. The inset figure shows the fractional change in electric field for a small region about the array centre, where the fractional change is less than one part in 10^5.

the driving microwaves to remain resonant with the transition. Since the shift of the rotational transition frequency is proportional to E_{DC} (Eq.(2.1)), the requisite stability of the electric field is also one part in 10^5.

Spatial Uniformity

Similarly, the electric field must be sufficiently uniform in space so that two molecules in separate optical tweezers are resonant with the same microwave pulse. By the same argument, the required spatial uniformity is one part in 10^5. The uniformity at the centre of the array is limited intrinsically by the quadrupole configuration (section 2.3.3), and mechanically by the straightness and parallelism of the electrodes.

Each electrode can be modelled analytically as an infinite rod, for which the radial field is $E(\mathbf{r}) = E_0\,\hat{\mathbf{r}}/r$. In Fig. 2.5, we model the electric field distribution for rods charged to ± 3 kV for the charge pattern shown in Fig. 2.4(b)(i). The vertical field components cancel, so that only E_x is plotted. The grey-shaded regions indicate the positions of the electrodes. Due to the specific aspect ratio chosen for the array, the central field is very uniform. The inset shows a zoom of a 300 μm region about the array centre, where the vertical axis shows the fractional deviation with respect to the central field ($\Delta E/E_0$).

The electric field is uniform to better than one part in 10^5 over the plotted region. For the typical 30 μm extent of a tweezer array produced along this axis in our system at present, this field uniformity is sufficient. For two tweezers spaced by 5 μm, the electric field is expected to be uniform to better than one part in 10^8.

2.3.3 Assembly of the Electrode Array

The electrode array consists of four parallel rods in a rectangular quadrupole configuration, running from electric feedthroughs at the rear of the vacuum chamber through to the science cell, as shown in Fig. 2.2(c). The electrodes are 300 mm-long cylindrical tungsten rods with diameter 2 mm, manufactured via a centreless grinding process[14] which ensures a tight tolerance on the diameter and surface roughness. Tungsten was chosen because of its exceptionally low magnetisation and high work function. The quadrupole arrangement is fixed using custom-made macor pieces. Macor is a non-conductive glass-ceramic with a low coefficient of thermal expansion, and is often used in ultra-high vacuum environments because it is non-porous with low outgassing. Two of the macor spacers are anchored at the east and west ports of the spherical cube using groove-grabbers, as discussed above. The electrodes are fixed at a third point at the electrode feedthrough near the rear of the chamber.

Three additional macor spacers, which only contact the electrodes, are used to maintain the correct array aspect ratio inside the science cell, and are shown in Fig. 2.4(a). The spacers must be able to support a voltage difference of several kV between oppositely-charged electrodes without dielectric breakdown. Dielectric breakdown occurs if the applied electric field exceeds the dielectric strength of the material, causing the insulator to become conductive. The maximum field that can be applied in the experiment is then limited by the breakdown voltage. The dielectric strength of macor is > 1000 kV cm^{-1}, far larger than any electric field we expect to apply, so dielectric breakdown of the bulk macor is not anticipated.

Although bulk breakdown is not expected to be limiting, surface breakdown

[14] Manufactured by PLANSEE, PSE-610-PS-105

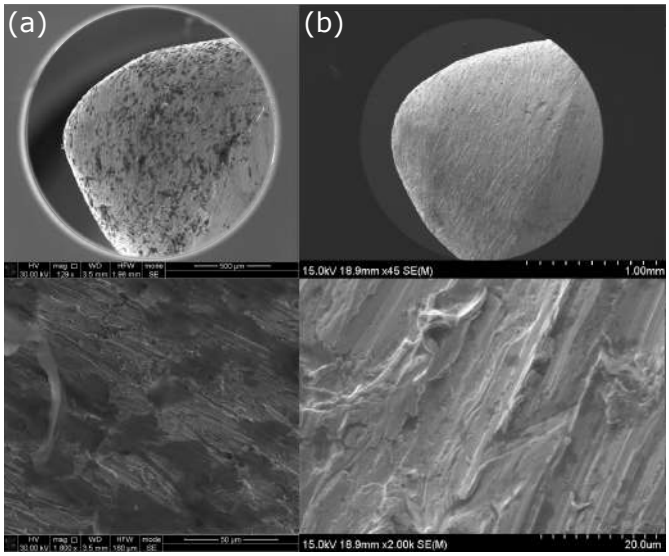

Figure 2.6: Scanning electron microscopy of the electrodes. The top row shows the electrode tips. The lower row shows higher-resolution images at lower length-scales. (a) Black deposits of grime can be seen on the tip of the electrode before cleaning. (b) Electrode after ultrasonic cleaning protocol.

can occur at lower fields. This effect is caused by electrons which flow along paths across the surface of the macor, resulting in a short circuit [137]. As can be seen in Fig. 2.4(a), grooves have been machined into the macor in order to increase the surface pathlength, which helps to protect against flashover. The electron flow originates from triple points, which are the junction of a metal, a dielectric and a vacuum [138], i.e. where the tungsten rods pass through the macor spacers. The electron cascade which occurs at a triple point and initiates flashover can be suppressed for certain angles θ between the macor and tungsten surfaces. $\theta = 90°$ mitigates the flashover effect [139], which can be easily achieved by having the electrode tips extend beyond the macor pieces to terminate in free space.

To reduce the likelihood of surface breakdown and to limit outgassing, all in-vacuum components were thoroughly cleaned to remove grime from the machining process. The macor was prepared for the UHV environment through sequential cleaning in an series of 30 minute ultrasonic baths of soapy water, deionised water, methanol and finally acetone. The electrode rods were similarly cleaned: the effect of cleaning can be seen in the scanning electron microscope (SEM) images of the electrode tips presented in Fig. 2.6. In image

(a), microscopic deposits (black) can be seen on the surface of the electrode. In image (b), taken after cleaning, it can be seen that the deposits have been removed. We used similar images to determine that the softer macor did not scratch the surface of the harder tungsten rods during assembly of the array.

In addition to cleaning, it was important to condition the electrodes to remove microscopic bumps and surface irregularities, since they can nucleate electron discharge much like triple points. In the conditioning process, incrementally higher voltages up to ± 5 kV were applied to the array over the course of an hour to induce electron discharge. This induced localised heating of the electron surface which ablated bumps and smoothed the electrode surface [140]. The electrodes were conditioned under vacuum in a sealed tube rather than inside the science cell to avoid damage.

2.4 Magnetic Field Coils

Most stages of the experiment require control of the magnetic field at the position of the atoms. For example, we must cancel stray external fields, define quantisation axes and vary the scattering length in the vicinity of Feshbach resonances. Experimentally this is achieved using pairs of wound copper coils located near the science cell. The six pairs of magnetic field coils used in the experiment are highlighted in Fig. 2.7(a). The quadrupole field coils (blue) are used to produce a linear field gradient for generating dual magneto-optical traps (section 3.2). The bias coils (red) and jump coils (yellow) are used to apply bias fields of up to ~ 200 G along the N/S axis, which is necessary for accessing magnetic Feshbach resonances (see section 5.1.2). The three pairs of shim coils (green) are used for cancellation of external fields, and for applying relatively small bias fields up to ~ 5 G.

All the coils are firmly fixed to a mount constructed from G10, an epoxy glass resin (green in Fig. 2.1). G10 was chosen for its high-strength, electric neutrality and very low thermal expansion. The quadrupole, bias and jump coil pairs are sealed in place with epoxy. The shim coil pairs are wound around plastic 3D-printed formers which are screwed into the G10 mount.

All coils are made from copper wire. The quadrupole, bias and jump coils are

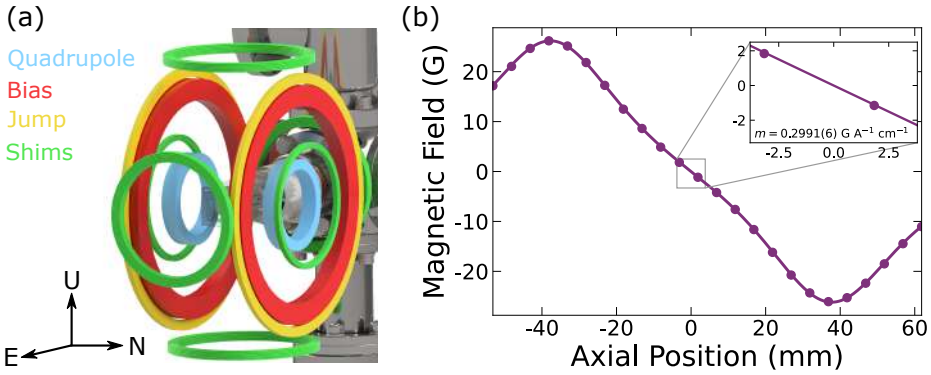

Figure 2.7: Magnetic field coils used in the experiment. (a) A colourised schematic of the magnetic field coils around the science cell. The G10 mounting blocks are not shown. (b) Magnetic field profile measured through the central axis of the quadrupole field coils. The inset shows a magnified view around the midpoint of the coils.

made from square wire of gauge 3.5×3.5 mm with a hollow core of diameter 2 mm to allow water cooling of the coils. The wire is coated in insulating Kapton tape, to avoid short-circuiting of adjacent coil turns. The shim coils are all made from wound circular wire with a 1 mm diameter.

In the following sections we give an overview of each coil pair. Further details can be found in Appendix A.

2.4.1 Quadrupole Field Coils

The quadrupole coil pair is arranged in an anti-Helmholtz configuration, where the coil separation S is $\sqrt{3}\times$ the coil radius (Appendix A), and the coil currents run in the opposite sense to each other. Each coil is composed of $3 \times 2 = 6$ turns of the square square hollow-core wire.

Fig. 2.7(b) shows a measurement of the field along the coil axis, where the solid line is a fit to the measured data. The anti-Helmholtz configuration results in a uniform magnetic field gradient near the midpoint of the coils, shown in the inset. From the fit, a magnetic field gradient of 0.2991(6) G A^{-1} cm^{-1} is extracted. Under typical operation, the coils run at a current of 28.3 A for $\sim$ 100 ms during the MOT phase of the experimental sequence, with a duty cycle of $\sim$ 20%. This applied current results in a field gradient of 8.47 G cm^{-1} at the midpoint of the coil pair, chosen for reasons

discussed in section 3.2. The current through the coils is stabilised using an electronic servo circuit built by the electronics workshop.

2.4.2 Bias Coils

The bias coils are used to apply bias fields at the centre of the science cell of order ~ 200 G. This field is sufficient to perform magnetoassociation of Rb and Cs across the routinely used interspecies Feshbach resonance at 197 G (section 6.2.3).

The bias coils are arranged in the Helmholtz configuration, where the coil separation is equal to the coil radius to produce a uniform bias field at the coil pair centre (see Appendix A). Each coil is formed of $3 \times 4 = 12$ turns of the same hollow-core wire as the quadrupole field coils, allowing water-cooling. The field produced per ampere of current has been measured using Raman spectroscopy on the Cs spin-stretched $(3, 3) \rightarrow (4', 4')$ transition to be 1.3926(7) G A^{-1}.

2.4.3 Jump Coils

The jump coils are formed of $1 \times 2 = 2$ turns of hollow core wire, and are also water-cooled. The jump coils are used in conjunction with the bias coils. Having fewer turns than the bias coils, their lower inductance allows for faster field ramps about the mean value set by the bias coils. The field produced per ampere of current has been measured using microwave spectroscopy (section 4.1.4), yielding 0.2184(1) G A^{-1}.

2.4.4 Shim Coils

There are three pairs of shim coils, shown in green in Fig. 2.7(a), mounted orthogonally to each other along the axes of the science cell. The E/W shim pair is aligned to the long axis of the cell, labelled the y-axis in the tweezer coordinate system. The N/S shim pair produces fields along the horizontal short axis of the cell, also labelled the x-axis in the tweezer coordinate system, and is aligned to the same axis as the quadrupole, bias and jump coils. The

U/D shim coil pair, labelled the z axis in the tweezer coordinate system, produces fields in the vertical direction.

The shim coils are used to overlap the MOT with the optical tweezers by displacing the position of the quadrupole field-zero (see section 3.4.2). They are also used to define a quantisation axis during optical pumping and for collision studies (see section 4.1.3).

The current through both shim coils in a pair is same-sense (though not in a Helmholtz configuration) to produce a bias field at the science cell centre. The shim coils are driven using a bipolar current supply designed in the electronics workshop which allows the field direction to be flipped by inverting the current flow through the coils. The shim coils can produce fields of up to ~ 5 G.

The E/W and U/D shim coils are each made of $7 \times 6 = 42$ turns of the 1 mm circular wire. They produce bias fields of 0.927(4) G A^{-1} and 0.939 G A^{-1} respectively. The N/S shim pair is made of $4 \times 4 = 16$ turns of the 1 mm circular wire. Using microwave spectroscopy, the bias field produced per setpoint voltage applied to the bipolar current driver has been measured to be 0.6068(2) G V^{-1}, as discussed in section 4.1.4.

2.5 Optical Frequency Preparation

Production of $^{87}Rb^{133}Cs$ molecules via magnetoassociation first requires independent control of the atomic species. In this section, we discuss the lasers and optics for producing the correct optical frequencies for laser cooling and optical pumping (OP)of both species. To understand how rubidium and caesium vapours may be manipulated using lasers, we first discuss their atomic structure.

2.5.1 Atomic Structure

^{87}Rb and ^{133}Cs are alkali metals belonging to Group 1 of the periodic table of elements, and both have a rich history of usage in experimental physics. The first Bose-Einstein condensate was realised over a quarter of a century

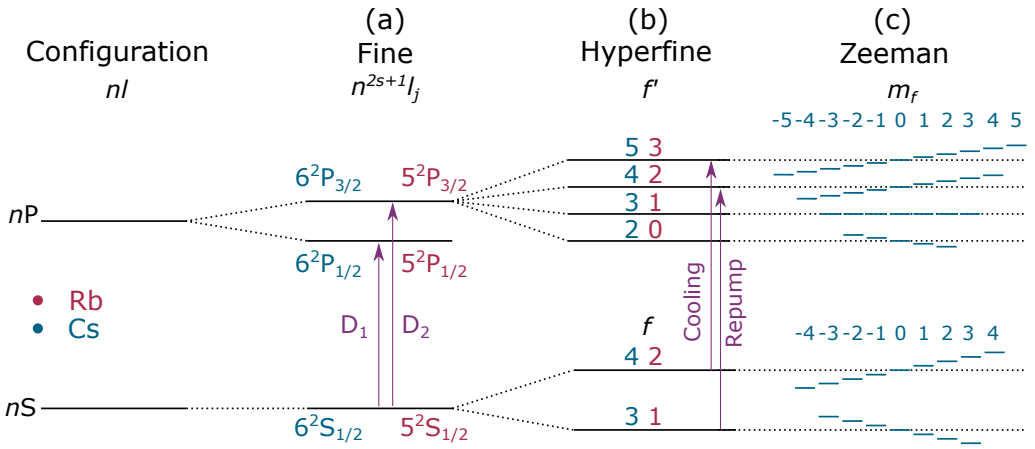

Figure 2.8: Energy level splitting hierarchy of the Rb and Cs ground state and first excited state. (a) Coupling of the electronic angular momentum and spin give rise to fine structure. The D_1 and D_2 lines correspond to transitions from the ground state to the fine structure sublevels of the first excited state. (b) Coupling of the nuclear angular momentum to the total angular momentum j gives rise to hyperfine structure. The f quantum numbers for Cs (Rb) are shown in blue (red). By convention, the excited states are labelled with a dash: f'. (c) Qualitative Zeeman shift of Cs m_f sublevels in an external field.

ago using ^{87}Rb [141], and the ground-state splitting of ^{133}Cs is currently used to define the second [142].

They each possess one valence electron; their lower orbitals are fully occupied by inner-shell electrons. The valence electron may occupy an orbital labelled by the quantum numbers nl, where n is the principle quantum number and l is the orbital angular momentum quantum number. n takes integer values of 1 or greater, and l takes values $\{0, 1, 2, 3, 4, ...\}$ which are usually written in spectroscopic notation as {S, P, D, F, G,...}. The electronic ground state is the lowest available orbital that the valence electron may occupy, which for Rb and Cs are the 5S and 6S levels respectively. The next available states are 5P and 6P respectively, which is termed in this work the (first) excited state.

Coupling between the electron spin angular momentum and orbital angular momentum splits the ground and excited states, giving rise to atomic fine structure. The valence electron has a spin $s = \frac{1}{2}$. The total electronic angular momentum j is given by $|l - s| < j < l + s$. For the ground states of Rb and Cs, $j = \frac{1}{2}$, and for their first excited states, $j = \frac{1}{2}$ or $j = \frac{3}{2}$. The resulting fine

structure level is denoted by adding a subscript j and a superscript $2s+1$ to the quantum number label: $n^{2s+1}l_{\mathrm{j}}$. The Rb ground state for example, is written $5^2\mathrm{S}_{1/2}$.

Coupling between the total electronic angular momentum j and the nuclear spin i gives rise to further splitting of the fine structure levels, producing hyperfine structure. The resulting levels are labelled by the quantum number f, given by $|i-j| < f < i+j$. For ^{87}Rb, $i = \frac{3}{2}$, and for ^{133}Cs, $i = \frac{7}{2}$. The Rb $5^2\mathrm{S}_{1/2}$ state is split into the hyperfine levels $f = 1$ and $f = 2$, with an energy splitting at zero magnetic field of $\approx h \times 6.8$ GHz. The excited state $5^2\mathrm{P}_{3/2}$ is split into four hyperfine levels with $f = \{0, 1, 2, 3\}$. The transition $5^2\mathrm{S}_{1/2} \rightarrow 5^2\mathrm{P}_{3/2}$ is known as the Rb D_2 line[15] and has an energy splitting of $\approx h \times 384.2$ THz, corresponding to a wavelength of 780.2 nm. Similarly, the Cs $6^2\mathrm{S}_{1/2}$ state is split into the hyperfine levels $f = 3$ and $f = 4$, with an energy splitting at zero magnetic field of $\approx h \times 9.2$ GHz. The excited state $6^2\mathrm{P}_{3/2}$ is split into four hyperfine levels with $f = \{2, 3, 4, 5\}$. The transition $6^2\mathrm{S}_{1/2} \rightarrow 6^2\mathrm{P}_{3/2}$ is known as the Cs D_2 line and has an energy splitting of $\approx h \times 351.7$ THz, corresponding to a wavelength of 852.3 nm. The hyperfine levels of the excited states are separated by $\approx h \times 100$ MHz.

Each f state is split into $(2f+1)$ Zeeman sublevels labelled the quantum number m_f, which have values from $-f$ to f in steps of 1. The m_f sublevels are degenerate unless an external magnetic field is applied, in which case there is a field-dependent splitting between sublevels. At low magnetic fields the energy shift is approximately linear, given for a magnetic field B defining a quantisation axis by [52, 143]:

$$E_{f,m_f}(B) = \mu_{\mathrm{B}} g_f m_f B, \tag{2.2}$$

where μ_{B} is the Bohr magneton and g_f is the hyperfine Landé g-factor. The exact field dependence of the ground state manifolds is described analytically by the Breit-Rabi equation, discussed in section 4.1.1.

[15] The electronic transitions of alkali metals from the ground state are referred to as the D_1 and D_2 lines, stemming from historic spectroscopic labels given to the 'doublet' Fraunhofer lines observed for sodium.

2.5.2 Lasers for Cooling Rb and Cs

Two lasers are required per species: one cooling laser and one repump laser, which address the hyperfine transitions shown in Fig. 2.8(b). The cooling laser is responsible for cycling on a nearly-closed transition during laser cooling. Since some of the atomic population may leak to other states during cycling, a repump laser is required to pump the leaked population back to the cycling transition. Transitions on the rubidium and caesium D_2 lines may be addressed using commercially available laser diodes operating at infrared wavelengths. The cooling and repump for each species are all external cavity diode lasers (ECDLs) operating in the Littrow configuration. The Rb and Cs cooling lasers are commercial Toptica DL100 ECDLs, and the repump lasers are homebuilt ECDLs.

In the Littrow configuration, the diode emission is immediately collimated using an aspheric lens and shone onto a diffraction grating. Light diffracted into the first order is back-coupled into the laser diode, forming an external cavity. Slight adjustments to the cavity length allow the emission frequency to be fine-tuned. Tuning of the cavity length is enabled by a piezo-electric transducer (PZT) epoxied to the grating. Typically optical feedback of around $15-30$ % is required for good operation. The laser linewidths are $\lesssim 1$ MHz. The ECDLs are temperature-stabilised using PID-controlled thermoelectric coolers. The laser optical frequency may be coarsely tuned using the temperature, which is kept above the condensation point (roughly ~ 16°C) to avoid condensation and short-circuiting of the diode. The laser table optical setup and positions of the ECDLs are shown in Fig. 2.12.

The beam profile emerging from a laser diode is typically low-quality, with an aspect ratio of $\sim 1:3$, and therefore requires correction to produce a workable Gaussian beam. We use beam-shaping optics such as anamorphic prism pairs and cylindrical lenses immediately after each laser to tune the divergence and beam waist for coupling into an optical fibre. The optical fibres decouple the lasers from the main table optics to facilitate laser maintenance, and improve the beam profile since only propagation of the lowest-order Gaussian spatial mode is supported. The decoupling fibres have efficiencies of ~ 60 % due to the poor profile from the diodes.

2.5.3 Spectroscopy and Laser Frequency Stabilisation

The lasers must be frequency-stabilised ('locked') to eliminate drifts associated with e.g. thermal expansion of the external cavity, changes in pressure and mechanical disturbance. A laser can be locked by referencing it to the spectroscopic signal of an atomic transition.

We use sub-Doppler spectroscopy to resolve hyperfine spectral features of narrower linewidth than the thermally-broadened width. The diagram in Fig. 2.9(a) illustrates an optical setup for performing saturated absorption spectroscopy[16] (SAS) [144]. A beam is split into a probe and a pump, which counter-propagate through a vapour cell. The more intense pump beam depletes the ground-state population, with a reduction in the absorption of the probe beam which can be detected on a photodiode. All signals shown in this section are acquired from spectroscopy performed in the weak probe regime [145]. The optical power in the pump and probe beams are ~ 100 μW and ~ 10 μW respectively.

SAS signals for the Cs D_2 line are shown for transitions from the $f = 4$ ground state using the cooling laser Fig. 2.9(b), and from the $f = 3$ ground state using the repump laser Fig. 2.9(c). The several hundred MHz linewidth of the background absorption features are due to thermal broadening in the room-temperature vapour cell. The amplitudes are given in arbitrary voltage units measured on the photodiode.

Superimposed on the broad absorption feature of Fig. 2.9(b) are six sub-Doppler features arising from the hyperfine structure of the atom (c.f. Fig. 2.11). Three of the features correspond to the electronic transitions $f = 4 \rightarrow 3'$, $f = 4 \rightarrow 4'$ and $f = 4 \rightarrow 5'$. These features are the direct result of ground state depletion caused by the pump beam [144]. The remaining three peaks, labelled $X_{f'_1,f'_2}$, are crossover resonances which occur when the laser frequency is exactly midway between two atomic transitions [52]. The repump spectrum in Fig. 2.9(c) similarly exhibits three features corresponding to electronic transitions and three crossover resonances.

[16] Due to the presence of hyperfine pumping, a more accurate label is 'pump-probe' spectroscopy [144]. However, since several pump-probe schemes are discussed in this section, we will continue to use the SAS misnomer for ease of distinction.

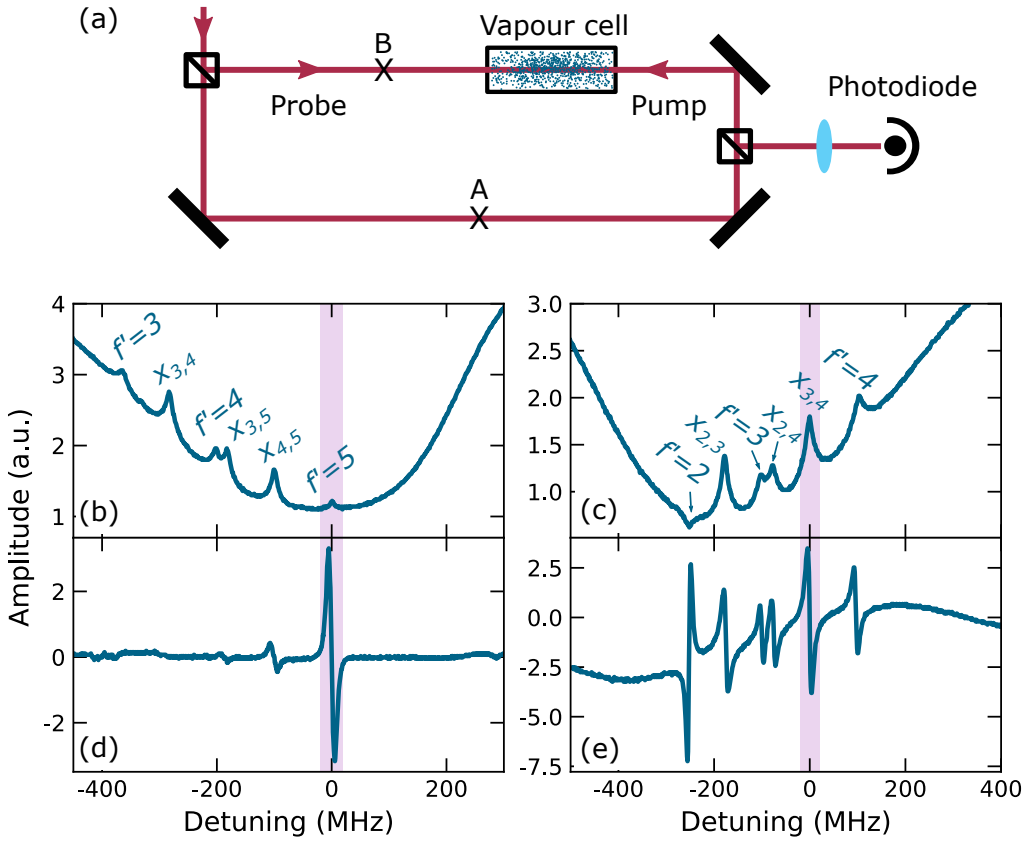

Figure 2.9: Cs spectroscopy and error signals. The sub-Doppler spectral features used for frequency stabilisation are highlighted in lilac. (a) Pump-probe SAS optical setup. Insertion of an EOM at A forms an MTS setup, or at B forms an FMS setup. (b) SAS on the Cs cooling transition (c)SAS on the Cs repump transition (d) MTS signal used to lock the Cs cooling laser. (e) FMS signal used to lock the Cs repump laser.

The Rb and Cs cooling lasers are both locked using modulation transfer spectroscopy (MTS) [146], which is performed by inserting an electro-optic modulator (EOM) at point A in Fig. 2.9(a). The EOM applies frequency sidebands to the pump beam at $\sim \pm 5$ MHz. The pump and probe beams interact in the vapour cell via a four-wave mixing process which adds sidebands to the probe beam [146]. The probe carrier and probe sidebands beat on the photodiode producing a signal which is electronically demodulated to produce the signal shown in Fig. 2.9(d). MTS is most effective for a closed transition and provides a zero-crossing on resonance which makes it ideal for locking the cooling transition highlighted.

The Rb and Cs repump lasers are both locked using frequency modulation

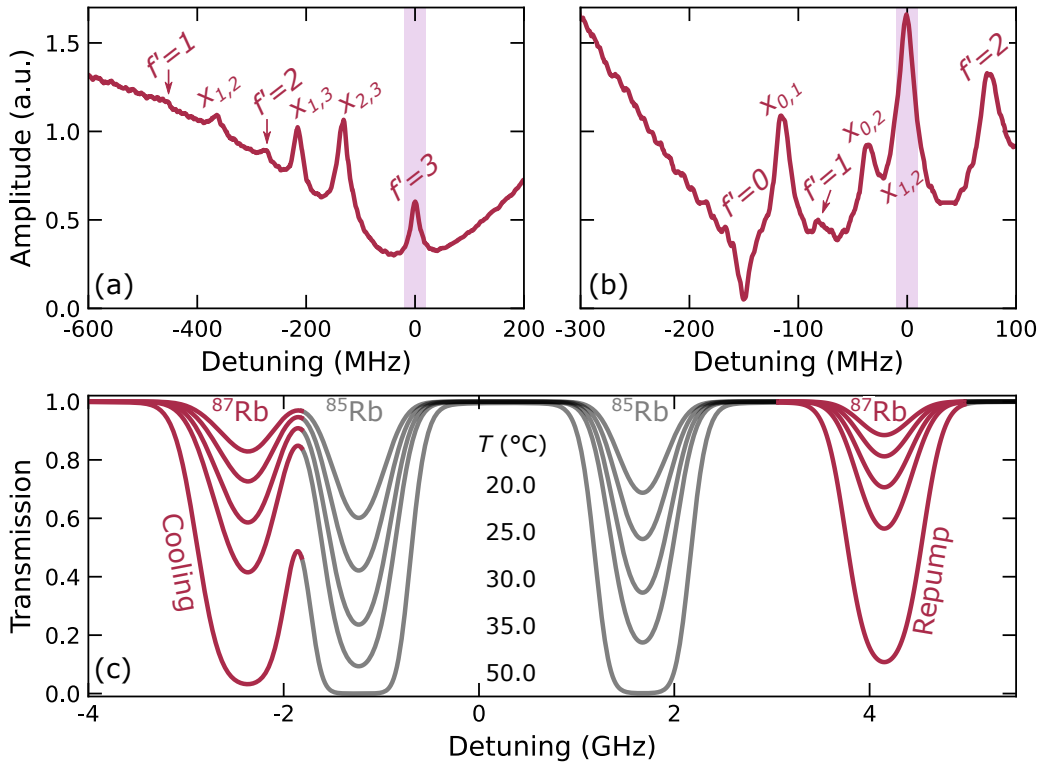

Figure 2.10: ^{87}Rb saturated absorption spectroscopy on (a) the cooling transition and (b) the repump transition for vapour cells heated to 50 °C. The lasers are frequency stabilised to the highlighted features. (c) Simulated temperature-dependent absorption for a 50 mm long vapour cell. The absorption features corresponding to the ^{85}Rb D_2 line are shown in grey for reference.

spectroscopy[17] (FMS) [147]. This time, the EOM is inserted at position B Fig. 2.9(a) to apply frequency sidebands to the probe instead. The modulated sidebands on the probe beam beat with the carrier and demodulated to produce the signal shown in Fig. 2.9(e). The laser is locked to the highlighted $X_{3,4}$ crossover, which is a convenient lockpoint for addressing the $f' = \{2, 3, 4\}$ hyperfine levels shown in Fig. 2.11.

Frequency stabilisation of the cool and repump lasers is achieved by feeding the error signals highlighted in Fig. 2.9(d) and Fig. 2.9(e) respectively into electronic stabilisation servos. The ECDL piezo-electric transducers controlling the cavity length are dynamically tuned to compensate for drifts in the error signal.

[17]FMS is less effective for the repump transition, which is not closed. This can be seen from the small amplitude of the peaks corresponding to open transitions in Fig. 2.9(d).

The spectra used to lock the Rb cooling and repump lasers are very similar. We present SAS spectroscopic signals for the ^{87}Rb cooling and repump transitions in Fig. 2.10(a) and Fig. 2.10(b) respectively. The highlighted features show the transitions we lock to.

The signals presented are for Rb vapour cells heated to 50 °C. The cells must be heated due to relatively low absorption at room temperature. This can be attributed to the lower natural abundance of ^{87}Rb ($\sim$ 28 %) compared to ^{85}Rb in the cell. Raising the temperature increases the mean atomic velocity, which increases the number of atoms traversing the probe beam per unit time and thus causes greater absorption. Fig. 2.10(c) shows the evolution of the Doppler-broadened features in a 50 mm vapour cell with temperature, simulated using the ElecSus software [148]. ElecSus calculates electric susceptibilities of alkali gases which are used to model the frequency-dependent absorption of a thermal vapour to an accuracy of < 0.5 % [149, 150]. At 50 °C, it can be seen that the absorption on the repump transition increases by $\sim \times 8$ compared to room temperature.

2.5.4 Laser Table Optical Setup

The lasers described in the preceding sections are used, among other things, for laser cooling, optical pumping and fluorescence imaging. For these applications, the emission from each laser must be split into separate beam paths whose frequency is independently tuned to address the hyperfine transitions shown in Fig. 2.11. This figure should be read in conjunction with Fig. 2.12, which shows the optical setup we have constructed to achieve this effect. The setup is split in two, with dedicated optical paths for Rb (red) and Cs (blue), which are roughly mirror images of each other.

After they are launched from the decoupling fibres shown in Fig. 2.12, the beams from the cool and repump lasers are divided into multiple paths using polarising beam splitter cubes (PBSs). The ratio of transmitted to reflected light through a PBS is controlled by setting the ratio of S to P polarisation in a beam by using a half-wave ($\lambda/2$) plate.

The frequencies of individual beam paths are set using acousto-optic modulators (AOMs), driven with a tunable radio-frequency (RF) tone of frequency

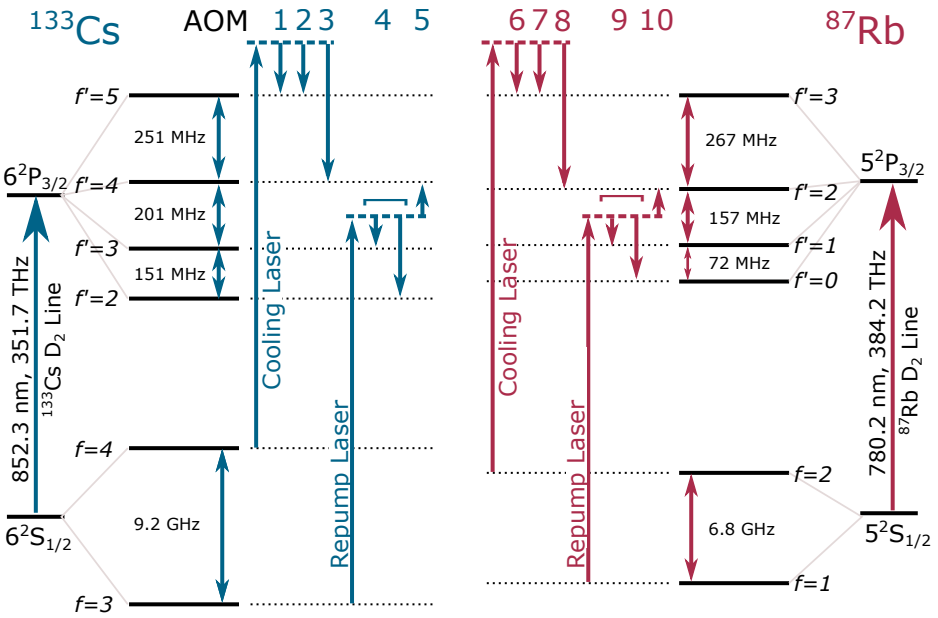

Figure 2.11: Hyperfine energy level structure relevant for laser cooling of Cs (blue) and ^{87}Rb (red). The lasers are stabilised to the frequencies marked by the dashed lines as discussed in the text. The arrows indicate the frequency shifts applied to the lasers by each AOM. 1: Cs spectroscopy, 2: Cs cool, 3: Cs optical pumping (OP) $4 \rightarrow 4'$, 4: Cs OP $3 \rightarrow 2'$ or $3 \rightarrow 3'$, 5: Cs repump, 6: Rb spectroscopy, 7: Rb cool, 8: Rb OP $2 \rightarrow 2'$, 9: Rb OP $1 \rightarrow 1'$ or $1 \rightarrow 0'$, 10: Rb repump.

$f_{\mathrm{RF}} \approx 100$ MHz. The frequency of a beam diffracted by an AOM is shifted by $\pm f_{\mathrm{RF}}$, depending on the diffraction order chosen, which is set by the alignment of the AOM. Electronic control of f_{RF} allows precise tuning of the optical frequencies during an experimental cycle. As shown for e.g. AOM 1 in Fig. 2.12, an AOM may be arranged in a double-pass configuration, which allows the optical frequency to be shifted by $\pm 2 f_{\mathrm{RF}}$. The optical power of each beam can be tuned by adjusting the power of the driving RF tone to adjust the AOM diffraction efficiency. A more complete discussion of acousto-optic theory is given in section 4.2.1, in the context of acousto-optic deflection of tweezer beams.

The AOMs are used for fast switching on and off of the beams, since the rise times of the AOMs are typically ~ 100 ns. However, even when nominally switched off, a small amount ($\lesssim 10$ μW) of light is leaked into the diffracted order, which can be sufficient to impact the experiment. Each beam path

therefore also includes a mechanical shutter to enable full optical extinction. We use homebuilt 3D-printed mechanical shutters based off a design detailed in ref. [151]. The shutters have a switching time of ~ 10 ms, which means they cannot be used for rapid switching, so appropriate sequence delays must be programmed.

852 nm Beam Paths

About 30 mW of laser power emerges from the Cs cool decoupling fibre, of which 2 mW is used for the MTS spectroscopy path. As shown in Fig. 2.11, the laser emission frequency is in fact shifted above resonance, since the spectroscopy is performed using light downshifted by a double-passed 95 MHz AOM (AOM 1). The cooling AOM (AOM 2) is also double-passed to downshift the beam frequency by 190 MHz into resonance with the cooling transition. OP light on the $4 \rightarrow 4'$ transition is produced using a double-passed 220 MHz AOM (AOM 3) to downshift the laser frequency.

Approximately 20 mW of Cs repump light emerges from the decoupling fibre, of which ~ 2 mW are sent to the FMS spectroscopy setup for locking to the $X_{3,4}$ crossover. Repump light on the $3 \rightarrow 4'$ transition is produced using a single-passed 100 MHz AOM (AOM 5). A 100 MHz AOM (AOM 4) can be single- or double-passed to produce $3 \rightarrow 3'$ or $3 \rightarrow 2'$ OP light, corresponding to the dashed beam path in Fig. 2.12.

780 nm Beam Paths

The Rb optical setup is shown in red in Fig. 2.12, with the corresponding transitions addressed by the AOMs shown in Fig. 2.11. The Rb scheme is very similar to the Cs scheme detailed in the previous section.

Around 30 mW of Rb cooling light emerges from the Rb cool decoupling fibre. Similarly to Cs, since the spectroscopy is performed using light shifted down by a double-passed 95 MHz AOM (AOM 6), the laser is frequency is shifted above the $2 \rightarrow 3'$ transition. Around 30 mW of Rb repump light is launched form the repump fibre. Since the Rb optical setup is a mirror of the Cs setup, the AOMs perform the same respective functions as their 852 nm

counterparts, with a shift of frequencies and hyperfine f numbers.

The frequency-tuned cooling and repump light for the Rb MOT is overlapped on a PBS and coupled into a $1 \rightarrow 3$ fibre splitter[18] which transports light to the main table. The fibre splitter divides the light into three fibre paths approximately equally, allowing three beams to be launched immediately on the main table. This eliminates the need for beam-splitting optics on the main table, allowing for a compact setup. The Cs cooling and repump light is similarly overlapped and coupled into a fibre splitter of the same model. Optical pumping (OP) light for both Rb and Cs originating from four beam paths is combined using PBSs and a dichroic mirror, and coupled into a single optical fibre leading to the main table. A fraction of Rb and Cs cooling light is coupled into a separate "pushout" optical fibre to be transported to the main table, where it is used for state-sensitive detection (see section 4.1.2).

2.6 Optical Tweezer Preparation

The lasers which generate the light for the optical tweezers are located on the laser table. There are three tweezer lasers which produce light at a wavelength of 814 nm, 938 nm and 1064 nm respectively. The reasons for this choice of wavelengths are detailed in section 3.3.2. The three optical setups are shown in Fig. 2.13, and share many similarities.

The 814 nm and 938 nm lasers are simple bare diodes[19] mounted in monolithic aluminium blocks. They are temperature-stabilised by PID-controlled thermoelectric coolers mounted beneath the blocks, and the laser diodes are powered by commercial current sources[20]. The emission linewidth of the diodes is several nanometres. The diverging beam profile from each diode is collimated using an aspheric lens housed inside the aluminium block. The emission wavelength of the lasers can be tuned several nm by changing the diode current and temperature. Although the laser diodes only produce a few hundred mW of optical power, the extremely tight waist at the focus of an optical tweezer means there is enough power to produce several tweezers

[18] Evanescent Optics Nufern PM780-HP
[19] Thorlabs L820P200 and M9-940-0200 respectively
[20] e.g. Thorlabs LDC205C

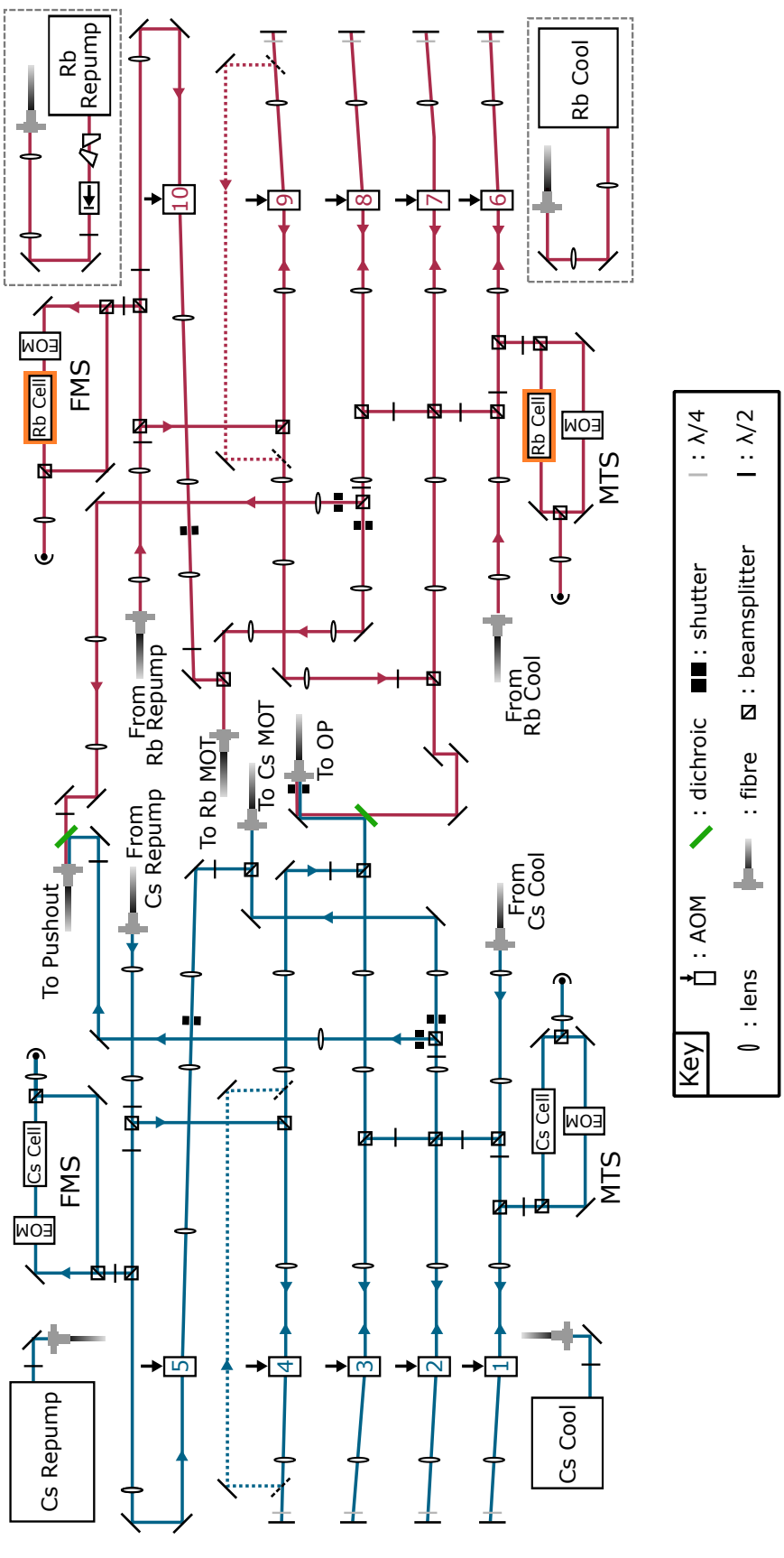

Figure 2.12: The lasers and optics used to prepare light at 780 nm and 852 nm for cooling, trapping, OP and imaging of Rb (red) and Cs (blue) respectively. Short optical fibres decouple the lasers from the optical setup. The Rb cells are heated (orange squares) to $\sim 50°$. 780 nm and 852 nm light are combined on dichroic mirrors (green) and coupled into the pushout and OP fibres. The red and blue dashed lines indicate optional OP paths which can be selected using flipper mirrors (black dashed lines). The black squares indicate the positions of shutters.

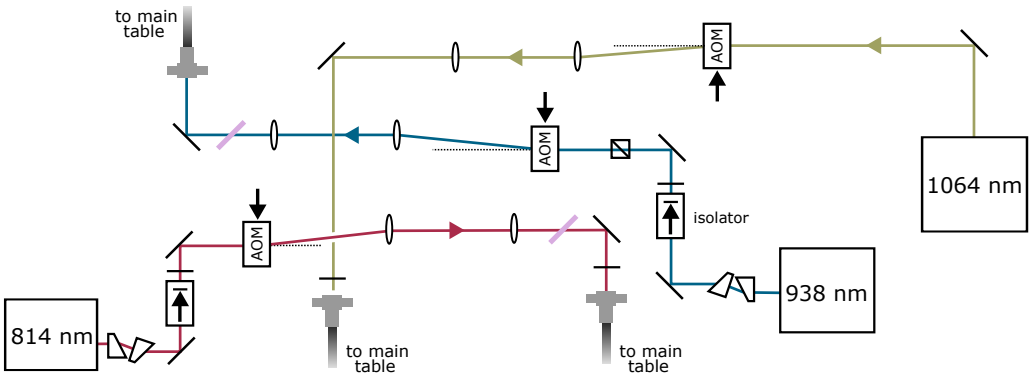

Figure 2.13: The three lasers and beam-shaping optics used to generate the 814 nm, 938 nm and 1064 nm optical tweezers. The tweezers are switched rapidly using AOMs. The 814 nm and 938 nm beams pass through laser-line filters to suppress emission at undesirable optical frequencies.

with a trap depth of $U/k_{\mathrm{B}} \sim 1$ mK.

Approximately 150 mW linearly-polarised 938 nm light is emitted from the 938 nm diode. The elliptical spatial profile is corrected with an anamorphic prism pair. An optical isolator is required to prevent back-reflection into the laser diode, however it rotates the beam polarisation by 45°. This is corrected by a $\lambda/2$ waveplate, and the polarisation is purified by a PBS. An AOM is used for fast switching of the tweezer beam, and then beam-shaping optics couple $\sim 75\%$ of the light into a long polarisation-maintaining optical fibre which delivers ~ 50 mW of optical power to the main table. The frequency shift induced by the AOM is negligible compared to the far detuning of the laser frequency with respect to the atomic D_1 and D_2 lines. The setups for the 814 nm and 1064 nm optics are very similar.

The emission profile of a bare laser diode includes a broad spontaneous emission feature with a spectral width of tens of nanometres. As a consequence, there can be emission at undesirable wavelengths. Specifically, we detected spontaneous emission at 920 nm, resonant with a transition from $6^2P_{3/2}$ to a higher-lying state. Initially, we were unable to load Cs atoms into the 938 nm tweezer, which we attribute to fast atom loss during fluorescence imaging due to excitation to the anti-trapping higher. We suppress the undesirable emission by inserting a laser line filter[21] with a pass-band of a few nm (pink in

[21] Semrock Maxline LL01-976-12.5

Fig. 2.13). As a precaution, the 814 nm path also includes a filter[22]. Around 90 % of the laser light is transmitted through the filters, which is slightly worse than expected.

We use a commercial high-power laser[23] to produce up to 6 W optical power at 1064 nm. In this thesis, we transfer atoms to a 1064 nm tweezer to leverage the lower spontaneous Raman scattering rate (section 4.1.5). Furthermore, the improved frequency mode stability of this laser produced a 50-fold improvement in the $1/e$ lifetime compared to a previous bare diode laser (section 3.5.1). In future, the high optical power available will be utilised with a spatial light modulator to produce large 2D arrays of optical tweezers (section 6.2.1).

2.7 Characterising the Objective Lens

Site-resolved imaging of single atoms in an optical tweezer or quantum gas microscope requires a high-numerical aperture (NA) objective lens. In optical tweezer experiments, it is common practice to produce the tweezer traps using the same objective. The objective should operate close to the diffraction limit, which gives the best imaging resolution and tightest-waist traps. The added complexity of dual-species trapping in a molecule experiment introduces a second requirement: the chromatic focal length shift (CFLS) of the two wavelengths used for imaging must be minimised so that coplanar rubidium and caesium atoms can be simultaneously imaged with sufficient resolution. Fluorescing Rb spontaneously emits at a wavelength of 780 nm, and Cs at a wavelength of 852 nm. The FLS between the tweezer wavelengths can be compensated by adjusting the collimation of each beam before the objective.

The objective lens was designed and manufactured by SpecialOptics to a custom specification. It is comprised of seven anti-reflection coated elements, with a nominal CFLS of less than 1 μm between the imaging wavelengths of 780 nm and 852 nm. The effective focal length of the objective is 35.34 mm and has NA = 0.55. The objective compensates for the thickness of the

[22] Semrock Maxline LL01-830-12.5
[23] Azurlight systems ALS-IR-1064-10-I-CC-SF

glass wall of the cell, with a front working distance is 15.5 mm. The front face of the objective sits $\sim$ 2 mm below the lower face of the science cell. The objective housing is machined from Ultem, a high strength plastic which should be robust against magnetic eddy currents, which could be problematic due to the proximity of the field coils.

Before incorporating the lens into the main experiment, we tested it, characterising some parameters that would otherwise be difficult to measure *in-situ*. We compare our measurements to simulations using Zemax, which is a software package for simulating optical systems via ray tracing and other methods.

2.7.1 Point-Spread Function

A fluorescing atom emits light approximately isotropically. Not all of the emitted photons are collected, due to finite numerical aperture of the lens used to image it. The NA is a measure of the solid angle subtended by the objective lens, and for an object in vacuum is defined as:

$$\mathrm{NA} = n \sin \alpha, \tag{2.3}$$

where α is the collection half-angle and n is the refractive index submerging the object. An estimate of the smallest resolvable distance of the microscope objective is given by the Abbe diffraction limit: $x = \lambda/(2\ \mathrm{NA})$ [152]. Better spatial resolution can therefore be achieved for larger NA and at shorter wavelengths.

To characterise the objective imaging quality, an appropriate approximation to a fluorescing atom must be used. An atom is a point-like emitter, since its spatial extent is smaller than the emission wavelength. The image of a point source formed in the imaging plane is known as the point-spread function, and has the functional form of an Airy disc [153]. Optical aberrations in the imaging system modify this functional form, broadening the disc and reducing the optical power in the central maximum [154].

The objective was characterised *ex-situ* using a scanning near-field optical

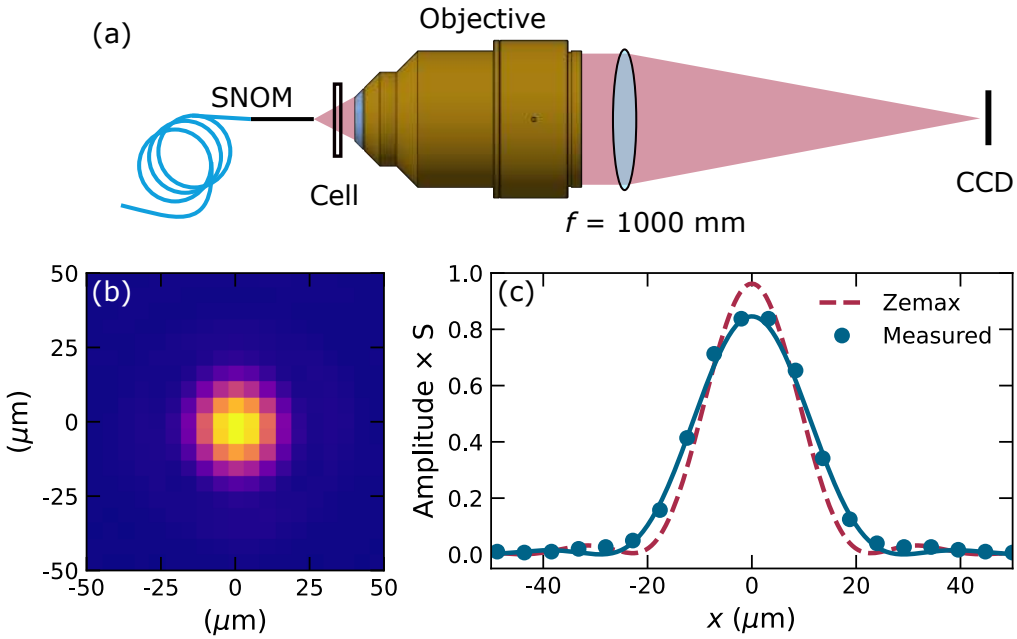

Figure 2.14: Characterisation of the lens. (a) Setup for objective imaging characterisation. Light from the SNOM fibre is collected by the objective and focussed onto a CCD. (b) Point-spread function measured in using the test setup with 780 nm light outcoupled from the SNOM fibre tip. (c) Cross-section of the PSF image. The blue points are data extracted from a CCD image, and the solid line is an Airy function fit. The dashed red line is a PSF simulated using the Zemax ray-tracing software. Both curves are normalised to the Strehl ratio.

microscopy (SNOM) fibre[24] as an approximation to a point source [155]. The SNOM fibre is an optical fibre with an exposed glass core tapering to a of diameter $\sim$ 200 nm. Light coupled into the fibre is emitted from the tapered tip in a radiation pattern approximating a point source, since the core diameter is less than the out-coupled wavelength. The optical setup used to characterise the objective lens is shown in Fig. 2.14(a). Linearly polarised light from the SNOM fibre is transmitted through a coated glass window and is collected by the objective lens. An $f = 1000$ mm achromatic doublet focusses the light onto a CCD of pixel size 5.2 μm. The glass window is a test piece provided by SpecialOptic and is identical to the science cell, with the same thickness, material and coating. The magnification of the test setup is $M = 28.3$.

[24]Nova Lab E50-MONO780-AL-200

A PSF image acquired using this setup is shown in Fig. 2.14(b). The PSF is produced by out-coupling 780 nm light from the SNOM fibre tip. In Fig. 2.14(c) we plot a cross-section of the PSF (blue). The solid line is an Airy function fit to the data. The first Airy fringe occurs at ± 37 μm. The red dashed line is a PSF calculated using Zemax analysis. Both PSFs are normalised to their respective Strehl ratio S. The Strehl ratio[25] is a measure of the PSF quality, and is the ratio of the peak PSF intensity compared to the peak intensity of an ideal Airy disc of the same width[26]. A Strehl ratio $S > 0.80$ is considered to indicate diffraction-limited performance [153]. By normalising to the PSF power [155], we estimate a Strehl ratio for the measured PSF of 0.83(3). While this value of S is still considered diffraction limited, it is lower than predicted Zemax value of $S = 0.91$. Furthermore, the fitted width of the Airy function is 27.0(8) μm and broader than the predicted value. This may be due the finite tolerance in manufacture, but is more likely due to misalignments in the test setup, or due to under-filling of the objective.

2.7.2 Chromatic Focal Length Shift

The chromatic focal length shift (CFLS) can be measured by translating the SNOM fibre tip through the focal plane of the objective. The depth of field is the maximal axial displacement of an object in object space from the focus that can be tolerated; that is, where the object remains acceptably sharply resolved.

The CFLS arises due to the wavelength-dependant refractive index of optical elements, which causes the axial position of the focus to depend on wavelength. Such a shift is disastrous if it exceeds the depth of focus of the objective, because it would not be possible simultaneously resolve both atomic species. The depth of field is given by[27] $d = \lambda/(2\ \mathrm{NA})^2$ [156], so that for NA = 0.55, the depth of field at 780 nm is 1.3 μm and at 852 nm, it is

[25] At lower Strehl ratios, more optical power is located in the Airy fringes, which is a symptom of optical aberration.

[26] The width of an Airy function is defined as the distance from the central peak to the first radial minimum

[27] The entire range over which the object is acceptably resolved is twice the depth of field $\pm d$, corresponding to a displacement either side of the focus.

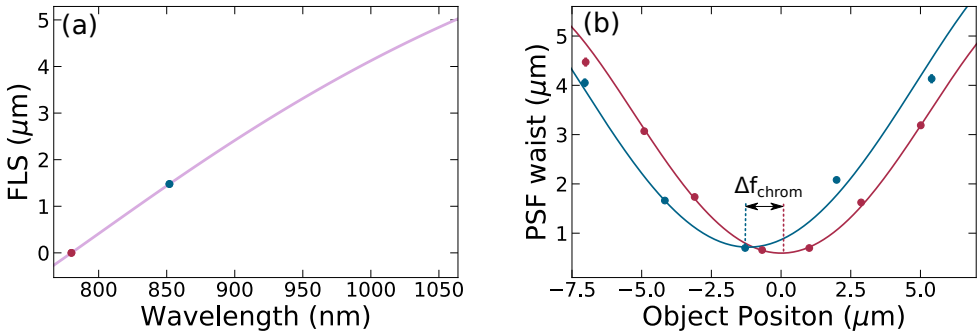

Figure 2.15: Chromatic focal length shift (CFLS) of the high-NA objective lens. (a) Focal length shift with wavelength, calculated using Zemax. The imaging wavelengths at 780 nm and 852 nm are shown in red and blue respectively. The expected CFLS is 1.5 μm. (b) The measured CFLS between 780 nm (red) and 852 nm (blue). Each point is a width extracted from a Gaussian fit to the PSF. The solid lines are even-power fits to the data.

1.4 μm. As long as $\Delta f_{\text{chrom}} < 2.7$ μm, it should be possible to resolve both atoms simultaneously. Fig 2.15(a) shows the predicted FLS as a function of wavelength, calculated using the Zemax ray tracing software. The imaging wavelengths are highlighted in red (780 nm) and blue (852 nm). The predicted chromatic shift is 1.5 μm, which is within experimental tolerance. The FLS is plotted up to 1064 nm, which is the longest wavelength handled by the objective.

We measure the CFLS by measuring the PSF as a function of the SNOM fibre position through the focus of the objective at both 780 nm and 852 nm. Fitting the PSFs fitted with Gaussian functions, we extract the $1/e^2$ widths plotted in Fig. 2.15(b). The y-axis is normalised to the effective pixel size (pixel size / magnification). The widths were fitted with an even-powers expansion to extract a minimum waist and focus position for each wavelength (solid lines). Δf_{chrom} is then the difference between the fitted minima: we extract a focal length shift of 1.2(2) μm. This is somewhat less than the Zemax simulation, which is surprising since the simulation of CFLS does not include the wavelength dependence of the achromatic tube lens. Regardless, this CFLS is certainly small enough to resolve co-planar Rb and Cs atoms as required.

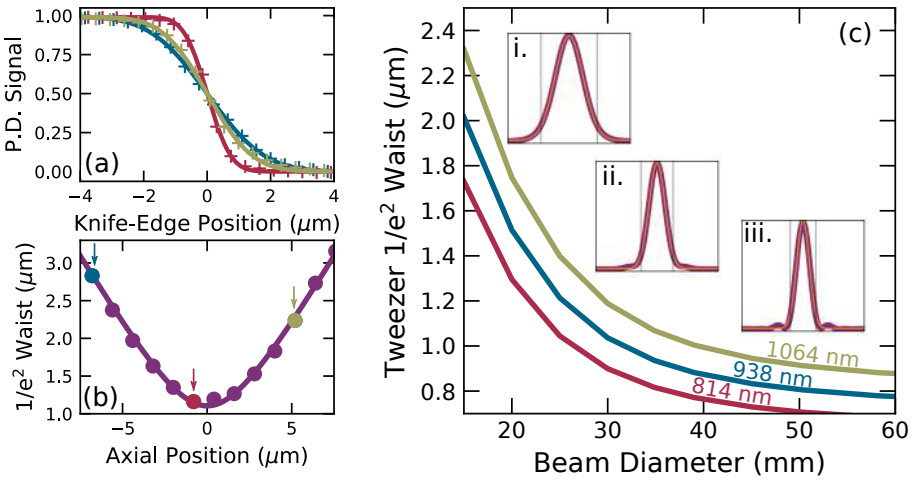

Figure 2.16: Ex-situ characterisation of a 1064 nm optical tweezer. (a) Knife-edge measurements near the focus of the tweezer for some sample positions indicated by arrows in (b) Axial profile through the focus of the optical tweezer. The knife-edge was finely controlled with a closed-loop piezo-motor translation stage. The points are extracted widths from knife-edge measurements. The highlighted points are the measurements in (a). The solid line is a hyperbolic fit to the data. (c) The simulated tweezer profile with diameter of beam input into the objective lens for the three tweezer wavelengths. The inset figures show profiles for an objective which is (i) underfilled, (ii) filled and (iii) overfilled.

2.7.3 Depth of Field and Rayleigh Range

The depth of field of the imaging system can be estimated from the even power fits of Fig. 2.15(b). The depth of field is the axial distance from the focus at which the intensity of the central PSF peak drops to half the value of the in-focus PSF [157]. This will occur when the PSF extent increases by a factor of $\sqrt{2}$. From the fits to Fig. 2.15(b), we can estimate depths of field of $d_{780} = \pm 1.4(1)$ μm and $d_{852} = \pm 1.7(1)$ μm. These are both close to the expected depths of field in the previous section. The fits in Fig. 2.15(b) can be further used to determine the $1/e^2$ extent of the PSF extent when the SNOM tip is at the focus of the objective. At 780 nm the $1/e^2$ radius is 0.60(2) μm, and at 852 nm it is 0.72(7) μm. These are similar to the expectation from the Abbe criterion, indicating satisfactory diffraction-limited performance.

The compliment to the depth of field is the Rayleigh range of the tweezers formed by the objective. The Rayleigh range of the tweezer cannot be easily

probed in-situ. Knowledge of the Rayleigh range is useful when considering the overlap of two merged tweezers of different wavelengths (section 4.3.1). A test optical tweezer is formed ex-situ by launching a large 1064 nm Gaussian beam into the objective ($1/e^2$ waist $\sim$ 30 mm), which was focussed down through the cell window to $1/e^2$ radius of ~ 1 μm. We profile the tweezer via a knife-edge measurement. In such a measurement, the beam power incident on a photodiode is measured as a hard edge is translated across the beam. The resulting intensity profile is an error function, which is the cumulative integral of the Gaussian beam profile.

Typically knife-edge measurements are straightforward, however the microscopic extent of an optical tweezer makes control of the knife-edge position challenging. We are grateful to Jonas Rodewald at Imperial College London who designed and tested the following method and shared the necessary equipment with us. For knife-edging, we use a microtome blade glued to a photodiode which is mounted on a closed-loop piezo-actuated translation stage, with 10 nm resolution[28]. The microtome blade edge is straight, even at sub-micron length scales, which is important for accurate characterisation of the tweezer.

Knife-edge measurements of the test tweezer are shown in Fig. 2.16(a). The solid lines are standard error function fits to the measured data points. The colours correspond to the highlighted points in Fig. 2.16(b), which shows the tweezer $1/e^2$ radius as a function of axial position. The solid line is a hyperbolic fit to the data, from which we extract a beam waist of the optical tweezer of 1.10(2) μm and a Rayleigh range of 2.87(7) μm.

Fig. 2.16(c) shows a Zemax simulation of the tweezer waists for 814, 938 and 1064 nm as a function of the beam diameter input to the objective lens. This simulation is useful for estimating the beam size that should be used for producing optical tweezers in the main experiment. For small beam diameters (c)(i), the objective is underfilled, and the tweezer formed has a Gaussian profile but a large waist. For beam diameters larger than the objective back-aperture of 30.6 mm, there is overfilling (iii). The aperture of the objective clips the input beam, which approaches uniform filling, resulting in a tweezer with an Airy profile and small side lobes. When the input beam diameter

[28]Thorlabs NanoMax 300.

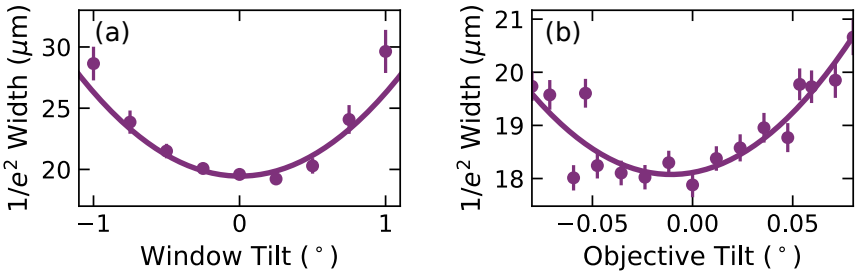

Figure 2.17: The effect of misalignment of the imaging system on the PSF waist. (a) PSF width with tilt of the window test piece. (b) The PSF width with the tilt of the objective. Each point is the Gaussian width of a fitted PSF. The solid line is a parabolic fit to the data.

is set to the aperture of the tweezer, an intermediate case occurs with some Airy character (ii). For a beam diameter of ~ 32 mm, the expected 1064 nm tweezer waist is 1.1 μm, in agreement with the measurement presented in Fig. 2.16(b).

2.7.4 Sources of Aberration

In the absence of optical aberration, the tweezer waists and PSF widths are diffraction limited. In a real system, optical aberration is introduced from several sources such as misalignment of the optics and defocus. Aberrations can result in larger tweezer waists and PSFs, and astigmatism.

Zemax simulations indicated that misalignment of the lens with respect to the cell is a likely source of optical aberration. We measured the sensitivity of the imaging system to this misalignment by independently adjusting the tilt of the window test piece and tilt of the objective. The measured PSF waists as a function of angle are shown in Fig 2.17. The waist of the PSF is relatively robust against the tilt of the window in Fig. 2.17(a), with a tolerance of $\sim \pm 0.5$ °. A more accurate comparison to the real experiment is given in Fig. 2.17(b) since in situ, only the tilt of the objective can be adjusted. The waist of the PSF is much more sensitive to this misalignment because tilting the objective changes several aspects of the imaging system simultaneously: the angle of the cell with respect to the lens, the displacement of the object from the optical axis, and misalignment of the objective with respect to the

rest of the imaging optics.

2.8 Cooling and Trapping Optical Setup

We now discuss how the beams described thus far are launched into the science cell to cool and trap Rb and Cs atoms. The experiments are performed on the main table, inside the science cell. Views of the beam geometry in the science cell are shown in Fig. 2.18 and Fig. 2.19.

2.8.1 Beams in the Science Cell

The 780 nm beams used to generate a ^{87}Rb MOT are shown in red. Light is launched directly from the output ports of the $3 \rightarrow 1$ fibre splitter. Beam pairs are generated by retro-reflection of each beam off a mirror and back through the science cell. The fibres to producing the 'upper' and 'lower' MOT beam pairs lie in the plane perpendicular to the optical bench and are mounted on vertical breadboards, which are clamped to a sturdy 2-inch thick steel post (shown in Fig. 2.1). There is 150 mm clearance beneath the lower breadboard, which allows sufficient optical access for launching tweezer beams into the objective lens. The blue paths in each figure show the 852 nm beam pairs for generating the Cs MOT, which are similarly produced by retro-reflection.

The vertical 780 nm and 852 nm beams are overlapped on short-pass dichroics and share the same path. Since both beam pairs share the same retro-reflection mirror, there is limited independent adjustment of each. In practice, the 780 nm beams are overlapped to match the 852 nm beams. Some degree of independent adjustment is allowed by the horizontally-mounted MOT beams, which are not overlapped, as shown in Fig. 2.19. The polarisation of each MOT beam pair is set to circular using a quarter-wave ($\lambda/4$) plate. The 780 nm and 852 nm vertical beam pairs share a $\lambda/4$ waveplate, and share the same handedness. The shared waveplate[29] is a compromise to maintain a compact setup. The handedness of the horizontal beams is circu-

[29] Thorlabs WPQSM05-808

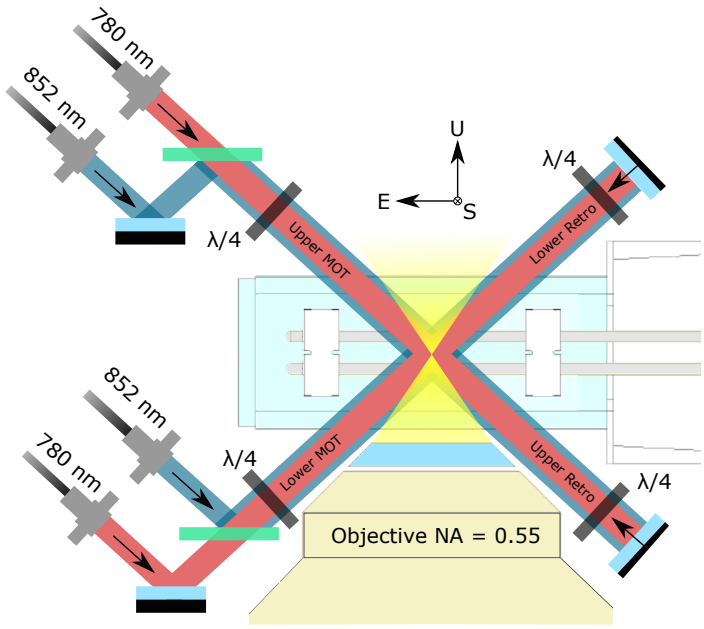

Figure 2.18: South-facing view of the science cell. The optical tweezers enter the cell from below and are focussed at its centre. The MOT beams are overlapped with the tweezer. The 780 nm and 852 nm beams are delivered via $1 \rightarrow 3$ fibre splitters from the laser table. They are overlapped on dichroic mirrors (green) and enter the cell at an angle of 50° from vertical. All beam pairs are formed by retroreflection

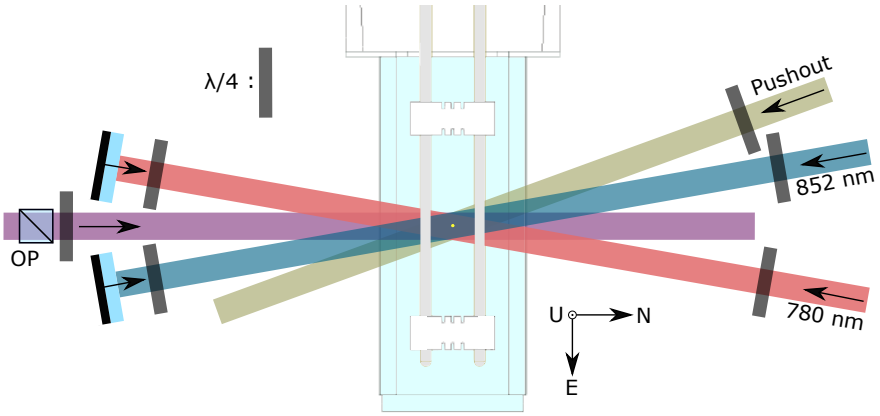

Figure 2.19: Bird's eye view of the science cell. The horizontal 780 nm and 852 nm beams are not overlapped, allowing independent adjustment. Both enter the cell at an angle of 10° to normal and are retro-reflected. An optical pumping beam lies parallel to the N/S axis. The off-axis pushout beam enters the cell at an angle of 18° and is normally used for state detection in the tweezer.

lar, with opposite handedness to the vertical pairs. The beam waists of the 780 nm and 852 nm MOT beams are ≈ 1.5 mm and ≈ 1.6 mm respectively, which is sufficiently tight to avoid the in-vacuum electrodes.

The objective is situated 2 mm below the science cell, as in Fig 2.18. The lens is seated on a kinematic mount which allows for 2-axis angular control and adjustment of the U/D vertical displacement. The kinematic mount is supported by thick aluminium columns mounted on a 2-axis translation stage[30] (Fig. 2.20(c)) bolted to the optical table, allowing for displacement of the lens along the N/S and E/W directions. The 1" hole in the translation stage allows for a static 3" mirror to be placed under the high-NA lens which is used to deflect beams from the plane of the optical table into the objective. The optical tweezers are formed at the focus of the objective, which is at the centre of the science cell, and intersects all six MOT beams for both species.

The pushout and optical pumping beam are shown in Fig. 2.19. Both of these deliver 780 nm and 852 nm light from the main table. The pushout light is resonant with the cooling transitions of each atomic species and is used for state-selective imaging. The OP beam delivers light from the four laser table OP paths. State-sensitive detection and optical pumping are discussed in section 4.1.

2.8.2 Main Table Tweezer Optics

The beam-shaping optics on the main table are responsible for producing optical tweezers and for fluorescence imaging atoms trapped in the tweezers. A diagram of the tweezer optics is given in Fig. 2.20(a). There are three tweezer beam paths, corresponding to each of trapping wavelength: 814 nm (red), 938 nm (blue) and 1064 nm (yellow). Each beam is launched from tunable fibre coupler[31] to ensure a high-quality Gaussian beam shape and good collimation. The polarisation of all beams is set parallel to the table (horizontal polarisation) and is purified using PBS cubes mounted immediately after the fibres. The beam intensities are stabilised using picked-off light imaged onto the photodiodes, which are connected to servo circuits.

[30] Thorlabs XYT1/M
[31] Schäfter + Kirchoff 60FC-F-0-A7.5-02

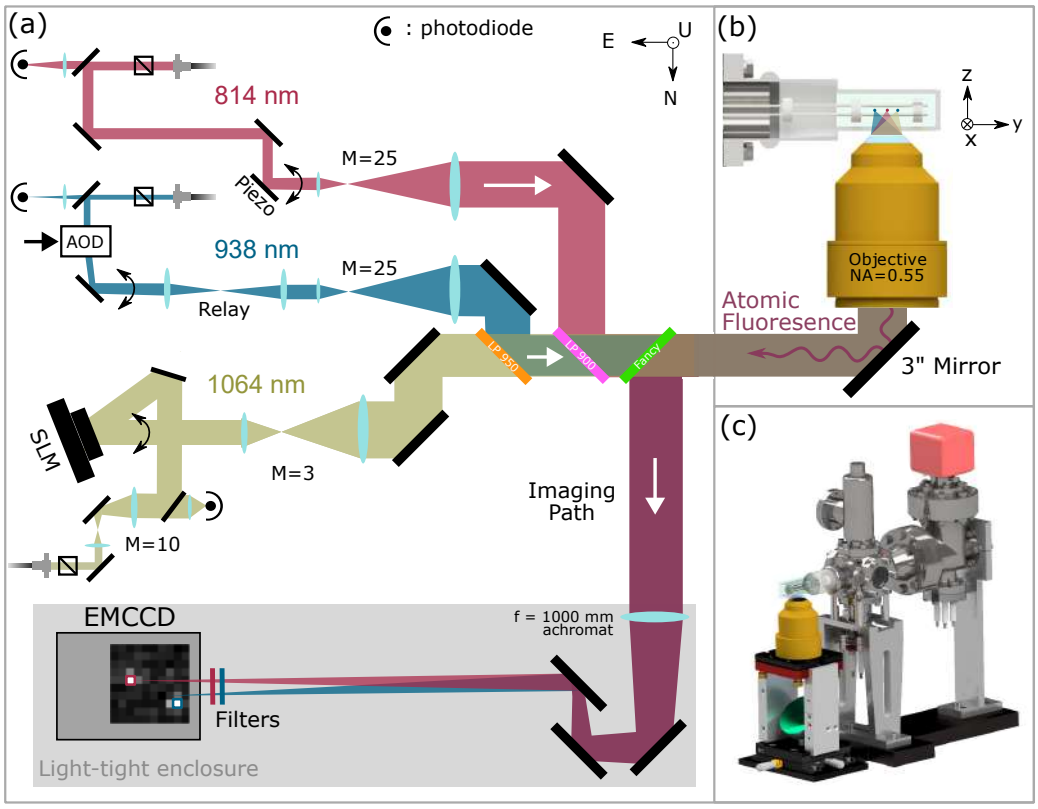

Figure 2.20: Main table optics for preparing optical tweezers with wavelengths 814 nm, 938 nm and 1064 nm. (a) All beams are magnified by $\approx 25-30$ mm in order to achieve a tight tweezer focus. The beams are combined on dichroics. A custom dichroic separates the imaging fluorescence from the tweezer light, and images it onto a camera. (b) A 3" mirror deflects the tweezer beams from the plane of the main table into the vertically mounted objective. (c) Render showing the mounting of the lens with respect to the cell.

Beam steering for the 814 nm, 938 nm and 1064 nm beam is achieved using a piezo-electric mirror, an acousto-optic deflector (AOD) and a spatial light modulator respectively. These are discussed in depth in section 4.2.

The $1/e^2$ beam waists output from the fibre couplers are ≈ 0.6 mm. The beams are magnified by a factor of $M = 25-30$ in order to achieve the large diameter of ≈ 25 mm required to form tight tweezers of waist ≈ 1 μm in the cell. The $1:1$ relay telescope in the 938 nm beam path images the deflected beam from the AOD onto the expansion telescope, which reduces optical aberration from off-axis pointing.

The three beams are combined using a series of dichroic mirrors. A long-

Table 2.1: Tweezer efficiency: the fractional optical power measured before the expansion telescope that is transmitted to the focus of the objective to form optical tweezers. The each value is the product of the independently measured transmissions of each optic in the tweezer beam path.

Tweezer	814 nm	938 nm	1064 nm
Efficiency	0.66(2)	0.73(2)	0.69(3)

pass dichroic mirror with a cutoff wavelength of 950 nm is used to overlap the 938 nm and 1064 nm beams. A long-pass dichroic mirror with a cutoff wavelength of 900 nm is used to combine these beams with the 814 nm beam path. All of the beams are overlapped before entering the objective. Practically the beams are aligned to each other using a series of irises and the fluorescence image of the trapped atoms. The beams shown in Fig. 2.20(a) propagate parallel to the main table. The combined beam is deflected 90 ° upwards into the science cell, forming optical tweezers as shown in Fig. 2.20(b). Note the change of coordinate system used in the cell. The x axis is parallel to the axis of symmetry of the bias and of the quadrupole and bias field coil axes of symmetry. Fig. 2.20(c) shows a render of the vacuum system and objective lens, where the kinematic mount, 3" mirror and translation stage may be seen.

It is important to make note of the tweezer efficiency, i.e. the fractional optical power which reaches the focus of the tweezer, after losses. Optical power is lost primarily due to clipping and imperfect transmission through optical elements. The measured transmission for each tweezer beam path is tabulated in table 2.1, where the efficiency is relative to the optical power measured before the respective expansion telescope.

As well as forming the optical tweezers, the objective lens is used to capture atomic fluorescence. The fluorescence is separated from the 3 tweezer beam paths into the imaging path using a custom "fancy" dichroic[32]. The dichroic coating is designed to reflect > 95 % of unpolarised photons at 780 nm and 852 nm, while transmitting ≈ 100 % of photons at the trapping wavelengths, for horizontally polarised light. Light is imaged onto an

[32]LaserOptik, custom coating.

electron-multiplying charge-coupled device (EMCCD[33]), using an achromatic lens with $f = 1000$ mm to minimise the CFLS between the imaging wavelengths. A light-tight enclosure is necessary to eliminate stray photons of scattered laser and ambient light which otherwise contribute significantly to the image background. Notch filters before the EMCCD are necessary to suppress a high background arising from the ≈ 0.01 % of tweezer beam photons which are back-reflected off the objective into the imaging path (see section 3.4.1).

Alignment of the Objective

It is clear from section 2.7.4 that the imaging quality will be sensitive to the alignment of the objective with respect to the science cell. When installing the objective in the experiment, we took great care to ensure the front face of the objective was parallel to the science cell. The science cell was already set parallel with respect to the optical table, as described in section 2.2.2.

A series of visible guiding beams were used to measure the angle of the objective and science cell via retro-reflection. The beams retro-reflected from the cell and lens were overlapped over a ~ 5 m path length. From this, we estimated that the science cell and objective were parallel to $< 0.01°$, which is near the optima of Fig. 2.17.

In section 3.6.2, we explain how the alignment is fine-tuned to a final optimal angle, using the tweezer trap frequency as a diagnostic.

2.9 Experimental Control

The precise timing required when triggering the many independent hardware components during an experimental sequences necessitates a sophisticated control system. Typically analogue voltages need to be triggered with a timing resolution resolution of < 1 ms. In addition to the reliable execution of experimental sequences, a robust and streamlined analysis software is required to handle the amount of data produced by the thousands of exper-

[33] Andor iXon 897 Ultra.

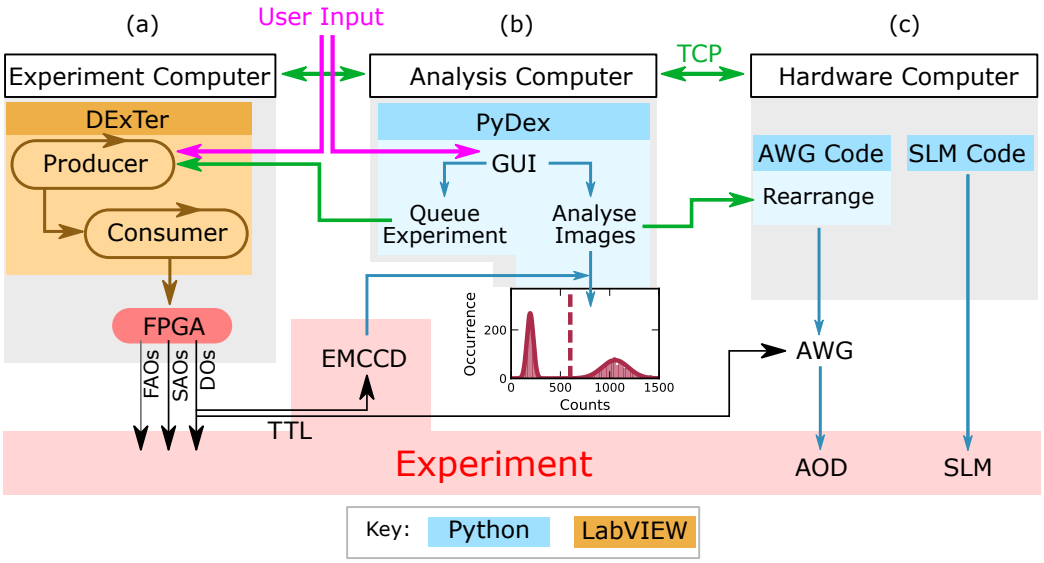

Figure 2.21: High-level schematic showing the experimental control system. The control is distributed over three computers which interface via TCP messenger protocol (green) and TTL triggers (black). The Experiment (a) computer hosts DExTer which is responsible for programming and triggering an FPGA. The Analysis computer (b) hosts PyDex, which is responsible for real-time data analysis and storage. The Hardware computer (c) is used to control complex hardware such as the AWG and SLM which require digital programming. The red region represents all of the hardware which comprises the experiment.

imental shots taken daily, each of which generates several images and other metadata.

The control software is distributed over three computers which each manage distinct but interconnected aspects of the experiment. A high-level schematic of the experimental control is shown in Fig. 2.21, illustrating how the computers are interfaced with each other and with the experimental hardware. The experiment control software, written in-house, is coded principally in a combination of the LabVIEW and Python 3 programming languages. The drivers for some hardware are written in other languages such as C, which we interface with Python using e.g. the `ctypes` library.

Experiment Computer

The Durham Experimental Terminal (DExTer) is used by several cold-atom experiments at Durham. It is described in detail elsewhere [158], so we

give only a brief description. DExTer is hosted on a dedicated Experiment computer Fig. 2.21(a). Written in Labview, DExTer provides a graphical user interface (GUI) for programming experimental sequences onto a field-programmable gate array[34] (FPGA). A sequence is divided into discrete timesteps during which the voltage output of any channel may be independently set. Furthermore, the voltage of analogue channels may be linearly ramped.

The FPGA may be programmed to simultaneously output time-varying voltages across many channels. There are 8 'fast' analogue output (FAO) channels which may output up to ± 10 V with a minimal time step length of 1 μs. There are 16 'slow' analogue output (SAO) channels which output with a minimal time step length of 40 μs. The 72 digital output (DO) channels can be set to a binary voltage of 0 V or 3.3 V, and are used to trigger transistor-to-transistor logic (TTL) inputs of experimental hardware.

While sophisticated, DExTer was originally designed for cold-atom experiments with cycle times of $\sim$ 1 minute. Tweezer experiments must be run several hundred times to acquire a single data point, so the experiment typically cycles at $>$ 1 Hz. Furthermore, the data from each shot must be stored and compiled into a histogram. Analysis of the large volumes of data produced is better handled in Python 3 than the graphical language of LabVIEW. For that purpose, a Python-based image analysis software is hosted on a separate Analysis computer so that it may run in parallel with DExTer.

Analysis Computer

The Analysis computer (Fig. 2.21(b)) hosts PyDex (Python-Dexter), which is the master control software for the experiment. We give a high-level overview of PyDex, however a more technical discussion of its functions is left to the future thesis of PyDex author S. Spence.

PyDex serves three main roles. Firstly, since the object-oriented Python programming language is better-suited than LabVIEW to processing the large volumes of data generated by the experiment, PyDex is used to analyse atom

[34] National Instruments 7833R.

fluorescence images. The camera is controlled via a Python wrapper[35] to a software development kit (SDK) written in the C language. Images acquired by the EMCCD during an experiment are read directly into PyDex, where they are processed. Information such as the fluorescence counts registered on a pixel is extracted from a single shot. The data from hundreds of shots is compiled into a histogram, from which observables such as atom survival probabilities are determined in real time. The measurement data is saved in comma-separated variable (.csv) format which may be later accessed and reanalysed.

The second important function of PyDex is to maintain synchronicity between software running independently on the three control computers. The EMCCD acquires an image on receipt of a TTL trigger from DExTer. PyDex continuously monitors for a signal emitted after an EMCCD image acquisition, whereafter it grabs the image from the EMCCD buffer. Since multiple TTLs are sent to the EMCCD per experimental cycle, lag on the analysis computer could result in loss of synchronisation between the Experiment and Analysis computers. PyDex ensures synchronicity by communication with the Experiment and Hardware computers between experimental shots via Transmission Control Protocol (TCP) message (green arrows in figure). Commands encoded in human-readable strings may be sent via TCP messages that can be issued *or* received by PyDex *or* LabVIEW.

The third function of PyDex is the queuing of multiple experiments in which any experimental variable in any timestep may be modified. Normally, a user inputs commands via the DExTer GUI, which are processed by the LabVIEW producer-consumer architecture (orange in Fig. 2.21). Making use of the TCP network established for synchronisation, commands from the PyDex GUI may be passed directly to the producer loop in place of user commands input via the LabVIEW GUI. The experimental variables (such as timings and channel voltages) of a sequence constructed in the DExTer GUI may be efficiently varied by queued commands in PyDex. Used in this way, PyDex is essentially a Python wrapper for DExTer which is designed to streamline data collection.

[35] A *wrapper* is code written in one language which can be used to run blocks of code written in a second language.

Hardware Computer

The Hardware computer (Fig. 2.21(c)) hosts software for programming an arbitrary waveform generator (AWG) and for setting the phase mask of a spatial light modulator (SLM). The operation of these components is discussed in more detail in Chapter 4.

Fixed sequences of waveforms are programmed onto the AWG before initialisation of an experiment (see section 4.2.2). Playback of the sequence of waveforms is triggered on receipt of a TTL signal from DExTer. Since playback of individual segments of an AWG sequence are not directly controlled by DExTer, care must be taken to maintain synchronicity. Optionally, the AWG sequence may be modified on-the-fly during an experiment to achieve dynamic array rearrangement as described in section 4.2.6. In this mode, the occupancy of an array, determined from a fluorescence image, is transmitted via TCP message to the AWG code. The time-varying waveform necessary to achieve rearrangement is computed on the Hardware computer, and is played back on receipt of a TTL trigger.

Chapter 3

Optical Tweezers

An optical tweezer [9] is an extreme case of an optical dipole trap [159], where the diffraction-limited beam waist approaches a size comparable to the wavelength. Atoms may be loaded directly from a magneto-optical trap or optical molasses into the deep (≈ 1 mK) tweezers which result from the tight waist. The tight confinement due to the narrow waist also gives rise to the collisional blockade regime, whereby only one atom can be loaded into the tweezer at a time due to the occurrence of rapid[1] light-assisted collisions [8, 160]. Optical tweezers are therefore a means to prepare and study single atoms and molecules.

In this chapter, we describe the loading of Rb and Cs magneto-optical traps and subsequent loading of atoms into the optical tweezers, using the apparatus established in Chapter 2. We review the physics of optical dipole trapping, and show how the optical tweezers can be made species-selective through a careful choice of laser wavelength. We then take a pedagogical approach in presenting the routine characterisation measurements of the tweezers, for the benefit of future experimenters. These measurements include characterisation of the atom temperature in the tweezer and characterisation of the tweezer waists. First however, to contextualise the theory and measurements of this chapter, we present an overview of a typical experimental sequence.

[1] Rapid with respect to the atom loading rate into the optical tweezers.

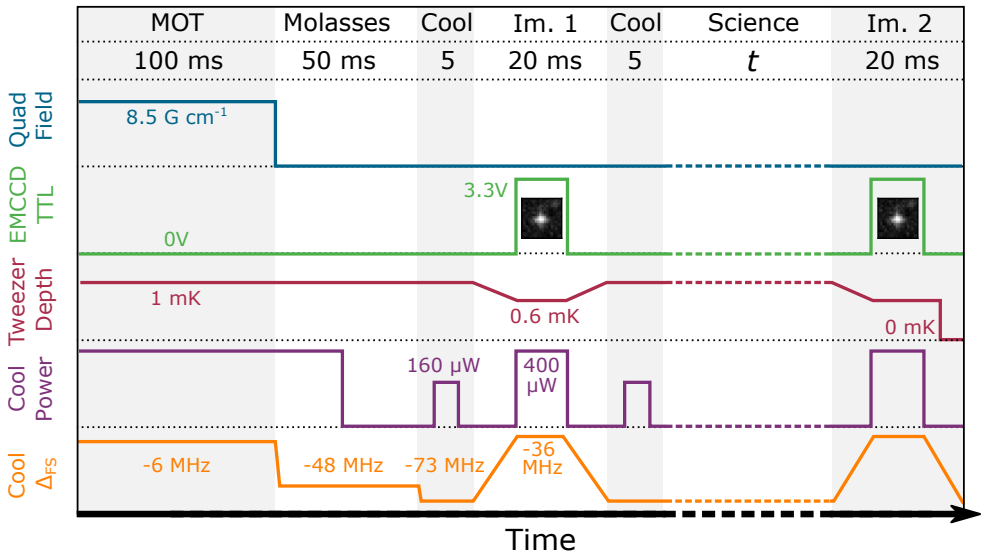

Figure 3.1: Simplified timing diagram outlining the main stages of a typical experimental sequence. Atoms are loaded into the optical tweezers in the MOT and molasses stages. The atom occupancy is verified in stage Im. 1, and a survival probability is calculated by probing the remaining occupancy in Im. 2. During the science step of variable duration t, various experimental parameters can be varied.Typical values for a Cs routine are shown: the orange line shows the free-space detuning of the Cs MOT cool beams with time, and the purple their power. Note that additional timing delays are omitted from the figure.

3.1 A Typical Experimental Sequence

The main stages of a typical experimental sequence are shown for Cs in Fig. 3.1. In the first stage a MOT is loaded for $\sim$ 100 ms, which is sufficient[2] to saturate the loading probability of a tweezer of depth 1 mK. The quadrupole field gradient is extinguished for a $\sim$ 50 ms optical molasses stage which further reduces the temperature of atoms loaded into the tweezers. Atoms are loaded into the tweezers with a probability of $\sim$ 50 %, so a first fluorescence image (Im. 1) probes the occupancy with a 20 ms pulse. Experimental shots are post-selected on instances where an atom was loaded, and other shots are discarded. The cooling stages are used to counteract any heating before the science stage. During the science stage, experimental parameters are varied (dashed lines) to induce an atom response. The atom

[2]When loading into an array of 5 shallower traps, a longer MOT time of up to 250 ms can be required (section 4.2.3).

response is mapped onto a a binary survival or loss event of the atom, which is probed in the second fluorescence pulse (Im. 2). At the end of the sequence, the tweezer is extinguished to clear any atoms from the tweezer before the next run.

Since the result of a single shot is binary, the experiment must be run many (~ 200) times. The *survival probability* is the ratio of atom survival events detected in the second fluorescence image. Experiments typically involve measuring the loading probability as a function of the MOT and molasses parameters, or the survival probability as a function of parameters varied during the science stage. Since the experiment must be repeated many times, a fast cycle time is desirable to increase the data collection rate. For short the science stage times, the experiment can run at > 2 Hz (note that additional delays such as shutter opening times and ramping times are not shown in the simplified sequence presented in Fig. 3.1).

3.2 Magneto-Optical Traps of Rb and Cs

The thermal Rb and Cs atoms emitted by the dispensers discussed in section 2.2.1 possess a high mean kinetic energy of around $E/k_{\mathrm{B}} \approx 300$ K. To load the atoms into optical tweezers of depth $U/k_{\mathrm{B}} \approx 1$ mK, they must be prepared in sufficient density and their mean kinetic energy must be reduced by a factor of $\approx 10^6$. The atoms are first cooled and confined in separate magneto-optical traps (MOTs) before loading into the optical tweezers. Since MOTs are routinely produced in many laboratories and their principle of operation is well understood [161–164], we give a brief overview of the underlying physics and some characterisation of the Cs MOT used in the experiment. For simplicity, we restrict our discussion to Cs, however the principle is identical for the Rb MOT. The lasers, coils and optics for producing the MOTs were discussed in the previous chapter.

Figure 3.2(a) shows the beam and coil geometry for producing a Cs MOT. The black arrows show the counter-propagating beams which form each beam pair. The MOT beams, red-detuned of the D_2 line, laser cool the atoms through repeated momentum kicks. An atom moving towards a MOT beam

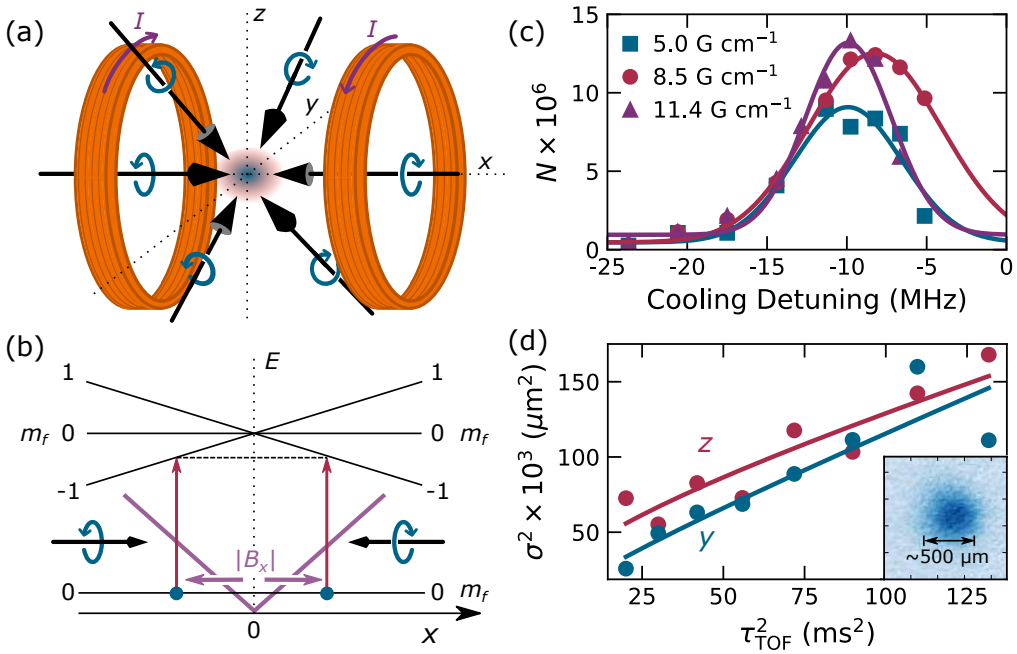

Figure 3.2: Production and optimisation of a Cs MOT. (a) MOT coil and beam geometry. (b) Diagram illustrating the principle of a MOT for a simple atom with $f = 0$ in the ground state and $f = 1$ in the excited state. The m_f state-dependent Zeeman shift depends on the atom position in the MOT. (c) Selection of a suitable magnetic field gradient. The detunings are with respect to the Cs D_2 line. (d) Time-of-flight imaging after a 50 ms pulse of polarisation gradient cooling. Inset: absorption image of the MOT after a 4 ms TOF, imaged along the x axis.

experiences a Doppler shift and becomes resonant in its moving frame with the beam, absorbing a laser photon and spontaneously re-emitting it in a random direction. This reduces the atom's momentum along the beam axis. By applying cooling beams in three orthogonal axes, the atoms can be cooled in 3D. Each MOT beam is arranged in a balanced pair to cancel the directional momentum gain during each photon absorption.

The three beam pairs alone are not sufficient induce confinement, and in the absence of a magnetic field, the atoms diffuse from the beam centre. The coil pair shown are connected in series with current I running in the opposite sense to produce a quadrupole magnetic field gradient dB_x/dx at the geometric centre of the coils. The magnetic field gradient induces a position-dependent Zeeman shift as shown in Fig. 3.2(b). Around the coil centre where $|B_x| = 0$ G, the direction of the magnetic field flips. The beams

in a pair are circularly polarised with the same handedness. The beams along the x-axis propagate antiparallel to the quadrupole field and are left-hand circularly polarised[3] (LHCP), so drive σ^- transitions ($\Delta m_f = -1$). The beam pairs in the $y-z$ plane propagate parallel to the magnetic field and are right-hand circularly polarised (RHCP), so also drive σ^- transitions. The position-dependent Zeeman shift means that an atom which diffuses from the trap centre is shifted into resonance with the one of red-detuned MOT beams, so that photon scattering returns it to the trap centre.

The atom number, density and spatial extent of an atom cloud may be measured using absorption imaging, as described in Appendix B. These quantities may be probed as a function of experimental parameters in order to optimise the MOTs. An absorption image of the Cs MOT is shown in the inset of Fig. 3.2(d). The $1/e$ extent of the MOT was ~ 250 μm for these measurements, however it later reduced to ~ 100 μm after the dispenser current was reduced. Absorption imaging was used to set the magnetic field gradient of the MOT and to probe the MOT temperature.

A suitable magnetic field gradient for the quadrupole coils during the MOT stage chosen following the measurement presented in Fig. 3.2(c). Here, the number N of atoms in the MOT was measured as a function of the detuning of the cooling beams from the Cs D_2 line, after a loading time of 20 s for several field gradients. We chose a field gradient of 8.5 G cm^{-1} since this yielded a high number of atoms and the feature was broad, and therefore less sensitive to field noise. At this field, the optimal frequency of the MOT cooling beams is 8 MHz red-detuned of the D_2 resonance. The same field gradient is used for the Rb MOT, where the optimal detuning of the Rb cool beams was found to be -13 MHz.

We measure the MOT temperature by absorption imaging the expansion of the atom cloud a variable time τ_{TOF} after the MOT field and beams have been extinguished. When the trap is extinguished, the atoms travel ballistically, and the expansion rate of the cloud can be mapped onto the mean kinetic energy and temperature of the atomic distribution. The spatial extent σ of

[3]Note that the polarisation handedness is defined with respect to an observer, following the convention for optics used in ref. [152]. An observer facing into an approaching RHCP (LHCP) beam witnesses the polarisation rotate (anti-)clockwise in time, with an angular momentum projection along the propagation direction $-\hbar$ ($+\hbar$).

the absorption images is extracted from a Gaussian fit. The temperature can be extracted from the measured rate of expansion over successive images of variable τ_{TOF} using [165, 166]:

$$\sigma^2 = \sigma_0^2 + \left(\frac{k_{\mathrm{B}}T}{m}\right)\tau_{\mathrm{TOF}}^2, \tag{3.1}$$

where m is the atomic mass and σ_0 is an offset corresponding to the initial extent of the cloud. The mean temperature of the MOT in the y and z axes is 85 μK. This value is likely lower than the Doppler temperature for Cs $T_{\mathrm{D}} = \hbar\Gamma/(2k_{\mathrm{B}}) = 125$ μK [163] due to the presence of sub-Doppler processes.

We reduce the mean temperature of the atoms even further below the Doppler limit by applying 50 ms of polarisation gradient cooling [167] during which the quadrupole field is extinguished and the cooling beams are further detuned to -48 MHz to produce an optical molasses. Fig. 3.2(d) shows the results of time of flight imaging after the optical molasses stage. The mean temperature extracted in the y and z directions is 15 μK, which is likely greater than the photon recoil-limited temperature of $T_{\mathrm{rec}} = \hbar^2k^2/(mk_{\mathrm{B}}) = 200$ nK due to imbalances in the beam pairs.

Nevertheless, this temperature is sufficient to load atoms into tweezers of depth $U/k_{\mathrm{B}} \sim 1$ mK. The mean temperature measured after optical molasses is comparable to the mean energy of the atom ensemble measured in the tweezers (see section 3.5.2). We did not characterise the Rb MOT as extensively as for these early Cs measurements, since it became apparent that a more accurate and relevant diagnostic is the loading probability and temperature of atoms measured directly in the tweezers.

3.3 Species-Selective Optical Tweezers

We now turn to the optical tweezers used in our experiment. We first review the optical dipole force, which is the mechanism which enables confinement of atoms in a conservative optical potential. We then discuss how the choice of tweezer wavelength tunes the species-selectivity of the tweezer.

3.3.1 Optical Dipole Trapping

A far-detuned light field $\mathbf{E}$ induces a dipole moment $\mathbf{d} = \tilde{\alpha}(\lambda)\mathbf{E}$ on an atom, where $\tilde{\alpha}(\lambda)$ is the wavelength-dependent complex atomic polarisability. The interaction potential of the induced dipole moment at the focus of a laser beam is [97]

$$U_0 = -\frac{1}{2\epsilon_0 c}\Re(\tilde{\alpha})I_0, \tag{3.2}$$

where the intensity at the focus is given by $I_0 = 2P/\pi w_0^2$, with P the beam power and w_0 the beam waist. For simplicity we will write the real part of the atomic polarisability for a species i as $\alpha_i(\lambda)$ from now on.

The optical tweezer beams propagate in the lowest transverse electromagnetic (TEM00) spatial mode, so that the radial profile (in directions x and y) follows a Gaussian function, shown in Fig. 3.3(a). The beam waist w_0 is the $1/e^2$ radius at the focus of the tweezer. The beam propagates along the axial direction z, where the beam radius $w(z)$ varies as

$$w(z) = w_0\sqrt{1 + \left(\frac{z}{z_R}\right)^2} \doteq w_0\tilde{z}, \tag{3.3}$$

where $z_R = \pi w_0^2/\lambda$ is the Rayleigh range and $\tilde{z}$ has been defined as an effective scaled distance along z. Eq. (3.3) is plotted in Fig. 3.3(b). z_R marks the position where the beam radius reaches $\sqrt{2}w_0$, or equivalently, the beam intensity drops to half the value at the focus. z_R is approximately $3w_0$ for the tweezer wavelengths and waists used in this experiment, resulting in a much weaker axial confinement and therefore a lower trap frequency than in the radial directions. In our system, the z axis lies along the direction of gravity. The effect of gravity, which reduces the axial tweezer depth by $\lesssim 1$ μK by tilting the trap, is negligible compared to the tweezer depths, which are typically $U/k_\mathrm{B} \sim 1$ mK.

Combining the axial propagation with the radial intensity distribution yields the 3D optical potential for species i of:

$$U_i(r, z) = U_{0,i} \times \frac{e^{-2r^2/(w_0^2\tilde{z}^2)}}{\tilde{z}^2}, \tag{3.4}$$

where $U_{i,0}(\lambda) = \frac{1}{2\epsilon_0 c}\alpha_i(\lambda)I_0$ is the species-dependent trap depth at the tweezer

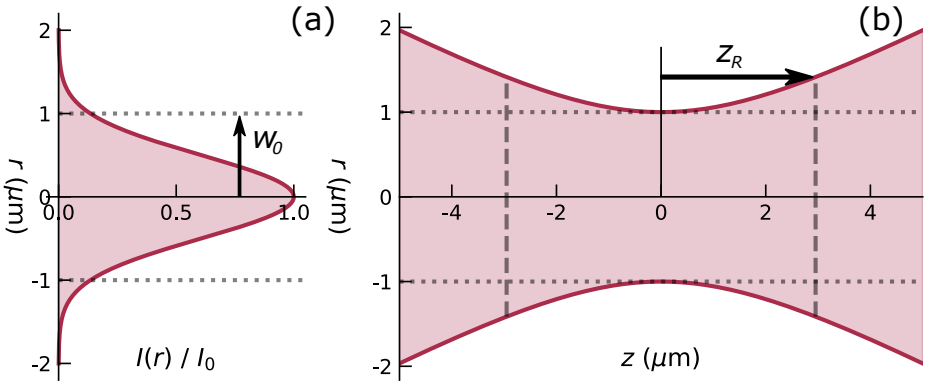

Figure 3.3: Profile of a TEM00 Gaussian beam with waist $w_0 = 1$ μm. (a) The intensity decreases exponentially in the radial directions. The $1/e^2$ waist is indicated by the dotted lines. (b) The $1/e^2$ radius with axial (z) position. Atoms are confined at the focus, $z = 0$ μm, where $w(z) = w_0$. The dashed lines indicate the Rayleigh range, where the beam radius is $\sqrt{2}w_0$.

focus and r is the radial coordinate. In the following discussion we use subscript notation to denote the wavelength of the tweezer used to trap each species $\{\lambda_{\mathrm{Rb}}, \lambda_{\mathrm{Cs}}\}$ and the shorthand notation $\tilde{U}_i(\lambda) = U_i(\lambda)/k_{\mathrm{B}}$ to denote the potential depths experienced by each species in units of temperature.

The magnitude of the potential U_0 is determined by the $\alpha_i(\lambda)$. Although the polarisability is the sum of scalar, vector and tensor components, for an atom in the $^2\mathrm{S}_{1/2}$ manifold it is sufficient to consider just the scalar contribution. There is no vector component for a linearly polarised tweezer beam[4]. The tensor contribution is negligible (< 1 ppm) for monovalent atoms with a spherically symmetric wave function such as Rb or Cs in the ground state [168]. This contribution becomes important for precision measurements such as the determination of tune-out wavelengths [169].

The frequency-dependent scalar polarisability for an atom in state v can be calculated by summing over states k using the formula [170]:

$$\alpha_0^v(\omega) = \frac{2}{3(2J_v+1)} \sum_{k \neq v} \frac{\langle k \| d \| v \rangle^2 \, (E_k - E_v)}{(E_k - E_v)^2 - \omega^2}, \tag{3.5}$$

[4]In reality there is a small vector component arising from the tight focussing of the optical tweezer [126] which we neglect for calculation of the polarisability, but which can become limiting for state preparation fidelity.

where $\omega = 2\pi c/\lambda$ is the laser frequency, J_v is the total angular momentum of state v, $\langle k\|d\|v\rangle$ is the reduced dipole matrix element, and $(E_k - E_v)$ is the energy difference between states k and v. To calculate the polarisabilities, we use dipole moments and transition frequencies determined in Refs. [171, 172].

3.3.2 Engineering Species-Selective Traps

The preparation of heteronuclear atom pairs in a single optical tweezer, and the subsequent separation of the atoms back into their original tweezers for detection, are best achieved using species-selective optical tweezers, i.e. tweezers which preferentially only trap one atomic species. The polarisability is wavelength- and species-dependant, so it is possible through a judicious choice of wavelength to engineer species-selective optical potentials which can achieve just this. We now explore, following Ref. [173], the conditions which decide the wavelengths of the Rb and Cs tweezers.

The polarisabilities for Cs in the $6^2S_{1/2}$ ground state (blue) and Rb in the $5^2S_{1/2}$ ground state (red) are shown in Fig. 3.4(a). The poles in the polarisability curves correspond to the D_1 and D_2 transitions of each species. From Eq. (3.2), it can be seen that α_i must be positive to produce an attractive potential (negative U_0) for either species. This is guaranteed for wavelengths red-detuned from the atomic D_1 transition, which corresponds to tweezer wavelengths $\lambda_{\mathrm{Rb}} > 795.0$ nm and $\lambda_{\mathrm{Cs}} > 894.6$ nm.

Due to the micron-scale waist of an optical tweezer, high intensities at the focus ($\sim$ 1 GW cm^{-2}) can result in a high scattering rate, Γ_{sc}, of tweezer photons despite the far detuning, further restricting the choice of tweezer wavelength. Scattering is detrimental, because it causes recoil heating of the confined atoms. The heating rate is proportional to the scattering rate [97]:

$$\dot{T} = \frac{1}{3} T_{\mathrm{rec}} \Gamma_{\mathrm{sc}}, \tag{3.6}$$

where T_{rec} is the recoil temperature. The recoil temperature depends on the mass of the atomic species, and quantifies the heating associated with a spontaneous absorption and emission event of a tweezer photon: $T_{\mathrm{rec}} = \frac{\hbar k}{m k_{\mathrm{B}}}$, with k the wavevector of the laser. The relevant recoil temperatures are

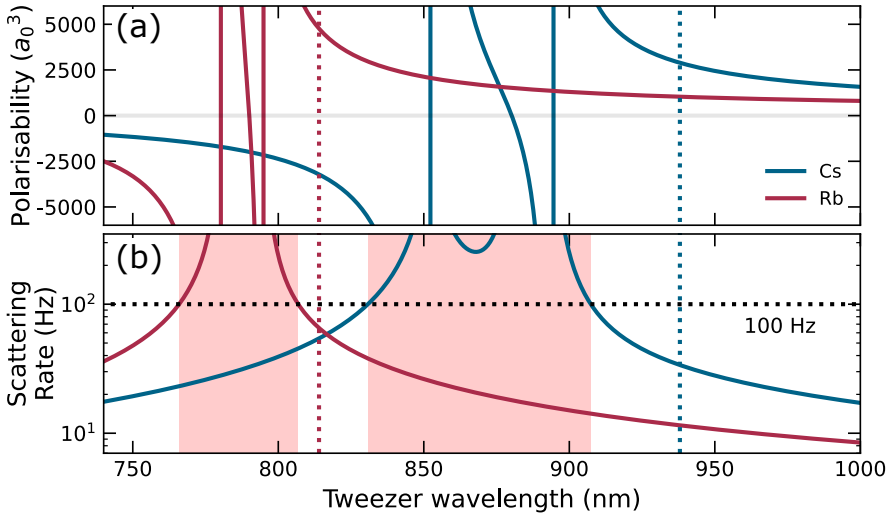

Figure 3.4: Polarisability and scattering rate for Cs and ^{87}Rb (a) The wavelength-dependent polarisabilities for Cs in the $6^2S_{1/2}$ ground state and Rb in the $5^2S_{1/2}$ ground state (b) Photon scattering rates for Rb and Cs in a 1 mK deep tweezer. High scattering rates > 100 Hz (dotted line) preclude tweezer wavelengths in the red-shaded regions. The dotted red line at 814 nm indicates the wavelength chosen for trapping Rb, and the dotted blue line at 938 nm indicates the wavelength chosen for trapping Cs.

$T_{\mathrm{rec}}^{\mathrm{Cs}} = 198$ nK and $T_{\mathrm{rec}}^{^{87}\mathrm{Rb}} = 362$ nK respectively [174]. Furthermore, a fraction of scattering events result in off-resonant spontaneous Raman scattering, which changes the hyperfine and/or Zeeman state of the confined atom [175]. We discuss this problem in more detail in the context of state preparation in section 4.1.5.

The tweezer wavelengths must therefore be chosen with care to suppress the scattering rate to within a tolerable limit. The photon scattering rate is given by [176, 177]:

$$\Gamma_{\mathrm{tot}} = \sum_{i=\mathrm{D}_1,\mathrm{D}_2} \frac{\Gamma_i}{2} \frac{I/I_{\mathrm{sat}}}{1 + 4(\Delta_i/\Gamma_i)^2 + I/I_{\mathrm{sat}}}, \tag{3.7}$$

where Γ_i is the natural linewidth of the transition, Δ_i is the laser detuning and I_{sat} the saturation intensity. Only contributions from the D_1 and D_2 lines are included in the sum, because at the near-IR tweezer wavelengths used in the experiment, the contribution from higher transitions is $\lesssim 1$ ppm. The scattering rates for each species in a tweezer of depth $|U_{i,0}(\lambda)|/k_{\mathrm{B}} = 1\,\mathrm{mK}$

(which is a typical depth) are shown in Fig 3.4(b). There is a sharp increase in the photon scattering rate for wavelengths near resonance with the D_1 and D_2 lines. The red-shaded regions highlight where the scattering rate for each species exceeds 100 Hz (dashed black line). We restrict our choice of tweezer wavelengths to outside of these regions so as to constrain the heating rate due to photon scattering to $\lesssim 20$ μK s^{-1}, and to reduce the effect of off-resonant spontaneous Raman scattering.

Together, the conditions on the polarisability and scattering rate indicate that a viable choice of wavelength for the Rb tweezer is 806.7 nm $< \lambda_{\mathrm{Rb}} <$ 830.9 nm. In this region, the tweezer is attractive for Rb, but repels Cs, since $\alpha_{\mathrm{Cs}} < 0$. Suitable wavelengths for the Cs tweezer lie in the region $\lambda_{\mathrm{Cs}} > 907.3$ nm, where $\alpha_{\mathrm{Cs}} > \alpha_{\mathrm{Rb}}$ so that the tweezer is more attractive to Cs.

Further restrictions on the possible tweezer wavelengths become apparent when considering the potentials once the tweezers for Rb and Cs are overlapped. This occurs when the tweezers are merged together to transfer both atoms into the same tweezer. We denote the potential experienced by Cs in its own tweezer $\tilde{U}_{\mathrm{Cs}}(\lambda_{\mathrm{Cs}})$ and in the Rb tweezer by $\tilde{U}_{\mathrm{Cs}}(\lambda_{\mathrm{Rb}})$, with similar notation for Rb.

Firstly, we require the Rb atom to experience a more confining potential in the Rb tweezer than in the Cs tweezer, i.e. that $|\tilde{U}_{\mathrm{Rb}}(\lambda_{\mathrm{Rb}})| > |\tilde{U}_{\mathrm{Rb}}(\lambda_{\mathrm{Cs}})|$. This is to avoid spilling of the Rb atom into the Cs tweezer in an uncontrolled manner, as shown in Fig 3.5(a), which results in heating. If the Rb tweezer is deeper for Rb, then the Rb atom experiences an adiabatic trap stiffening during the merge and does not change motional level, shown in Fig 3.5(b). Heating during merging is discussed and quantified in more detail in sections 4.2.4 and 5.2.3.

Secondly, since Cs experiences a repulsive potential from the Rb tweezer, if $|\tilde{U}_{\mathrm{Cs}}(\lambda_{\mathrm{Rb}})| > |\tilde{U}_{\mathrm{Cs}}(\lambda_{\mathrm{Cs}})|$, the confinement of the Cs atom will be destroyed by the Rb tweezer potential, as shown in Fig 3.5(c). The condition $|\tilde{U}_{\mathrm{Cs}}(\lambda_{\mathrm{Cs}})| > |\tilde{U}_{\mathrm{Cs}}(\lambda_{\mathrm{Rb}})|$ must be fulfilled in order to retain the Cs atom when the tweezers are overlapped, as shown in Fig 3.5(d).

For each atomic species we must consider the ratio of potentials it experiences

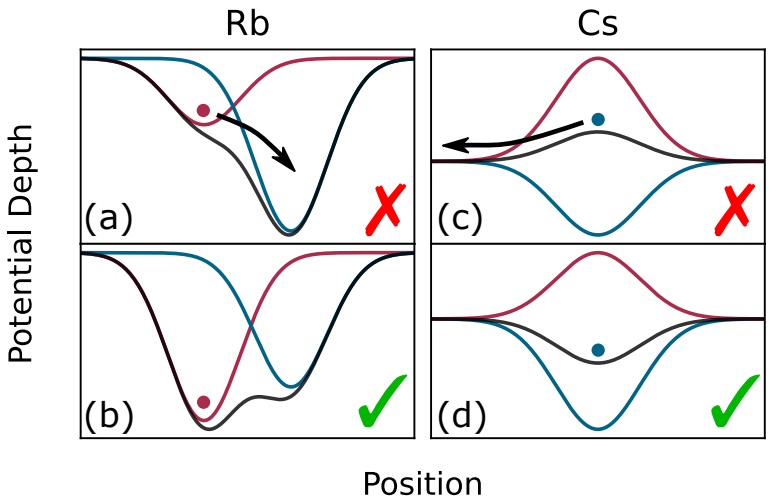

Figure 3.5: Cartoons showing the restrictions on the relative tweezer depths when the Cs (blue) and Rb (Red)tweezers are overlapped during merging. (a) The Rb atom spills into the deeper Cs tweezer, causing it to be heated. (b) The condition $|\tilde{U}_{\mathrm{Rb}}(\lambda_{\mathrm{Rb}})| > |\tilde{U}_{\mathrm{Rb}}(\lambda_{\mathrm{Cs}})|$ is fulfilled and the Rb atom is not heated. (c) The Cs atom is expelled by the repulsive Rb tweezer. (d) The potential of the Cs tweezer is deeper than the repulsion of the Rb tweezer, so the Cs atom is not expelled from the tweezer.

from each tweezer when they are overlapped. Since U_0 can depends on several experimental parameters such as the beam waist and power, for clarity we restrict our discussion to the case where the tweezer waists and powers are the same. The ratio of potentials then reduces to the ratio of atomic polarisabilities the atom experiences from each tweezer: $\xi_{\mathrm{Cs}} = \alpha_{\mathrm{Cs}}(\lambda_{\mathrm{Rb}})/\alpha_{\mathrm{Cs}}(\lambda_{\mathrm{Cs}})$ for Cs and $\xi_{\mathrm{Rb}} = \alpha_{\mathrm{Rb}}(\lambda_{\mathrm{Cs}})/\alpha_{\mathrm{Rb}}(\lambda_{\mathrm{Rb}})$ for Rb. In Fig. 3.6(a), the heatmap shows ξ_{Cs} as a function of each tweezer wavelength in the range 740 nm $< \lambda_i <$ 950 nm. The colour bar is shared with (b) in the figure. Overlaid on the heatmap are several hatched regions where the combination of λ_{Cs} and λ_{Rb} violates one of the conditions established. First are the unsuitable regions that have been described above: The regions covered by the black circles are where $\alpha_{\mathrm{Cs}}(\lambda_{\mathrm{Cs}})$ or $\alpha_{\mathrm{Rb}}(\lambda_{\mathrm{Rb}})$ are negative, so that an atom in its own tweezer is not confined, and the white-hatched regions indicate where $\Gamma_i > 100$ Hz and heating occurs. The blue hatched regions indicate regions we dismiss because $\xi_{\mathrm{Cs}} > 1$, so that a Cs atom is ejected by the Rb tweezer when the tweezers are overlapped (as in Fig. 3.5(c)). There is a similar plot (not shown) for $\xi_{\mathrm{Rb}}(\lambda_{\mathrm{Cs}}, \lambda_{\mathrm{Rb}})$, from which we obtain the pink hatched region, where $\xi_{\mathrm{Rb}} > 1$,

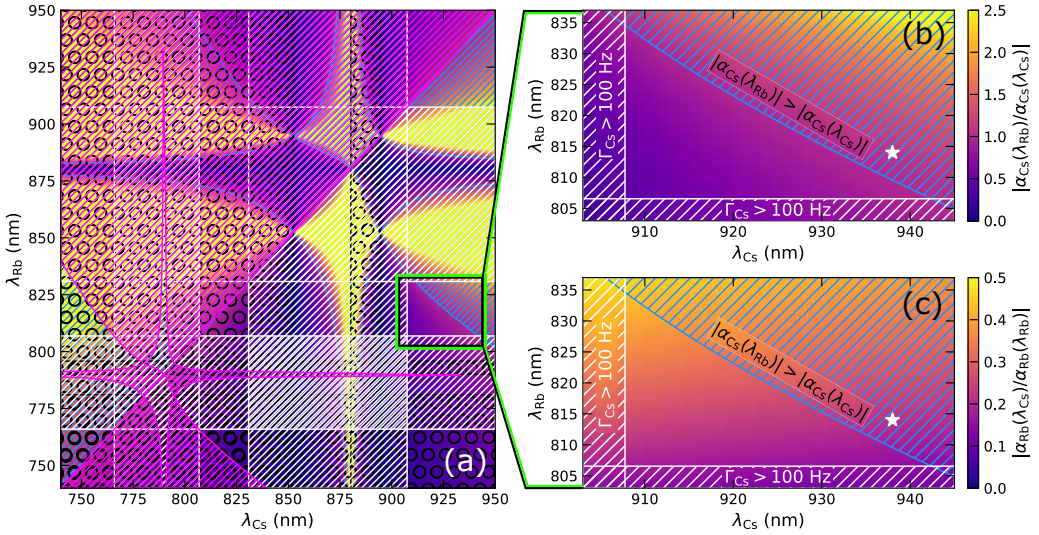

Figure 3.6: Conditions restricting the choice of tweezer wavelength. (a) Polarisability ratio $\xi_{Cs} = \alpha_{Cs}(\lambda_{Rb})/\alpha_{Cs}(\lambda_{Cs})$ for Cs as a function of tweezer wavelengths λ_{Cs} and λ_{Rb} in the range 740 nm to 950 nm. The colour bar is shared with (b). The regions indicated by the hatching are unsuitable choices of tweezer wavelengths as explained in the text. The only suitable choice of λ_{Cs} and λ_{Rb} lies in the unhatched region within the black box where $\xi_{Cs} < 1$. (b) Magnified view of the triangle marked in (a). The white hatching indicates where the scattering rate exceeds 100 Hz. The blue hatching marks where the repulsion of the Cs from the Rb tweezer is sufficient to cause the Cs atom to be ejected. Inside the triangle, the Cs atom is not ejected.(c) Polarisability ratio for Rb, $\xi_{Rb} = \alpha_{Rb}(\lambda_{Cs})/\alpha_{Rb}(\lambda_{Rb})$. Within the triangle, $\xi_{Rb} < 1$ so that the Rb atom does not spill into the Cs tweezer.

which is where the Rb atom spills into the Cs tweezer (Fig. 3.5(a)).

The key message of Fig. 3.6 is that taken together, these requirements are quite restrictive, and leave only a small range of viable $\lambda_{Cs}, \lambda_{Rb}$, indicated by the highlighted rectangle. In Fig 3.6(b) we show an enhanced view of ξ_{Cs} in this viable region, and in Fig 3.6(c) we show ξ_{Rb}. The white star indicates pair of tweezer wavelengths chosen in the experiment: $\lambda_{Cs} = 938$ nm and $\lambda_{Rb} = 814$ nm. Astute readers will notice that the white star lies outside of the viable region. Wavelength pairs in the blue-hatched region were excluded because $|\alpha_{Cs}(\lambda_{Rb})| > |\alpha_{Cs}(\lambda_{Cs})|$, causing the expulsion of Cs by the Rb tweezer. In reality, the relative power in the Cs tweezer can be increased, making the tweezer deeper and shifting the threshold so that the Rb repulsion is insufficient to cause loss. In practice, we use twice as much power

Table 3.1: Summary of the Cs and Rb scalar polarisabilities at 814 nm, 938 nm and 1064 nm.

Polarisability (a_0^3)	814	938	1064
Cs	-3220	2890	1170
Rb	4760	1030	680

in the 938 nm tweezer, expanding the viable region to encompass the white star.

The polarisabilities at the chosen tweezer wavelengths are summarised in Table 3.1. We also include the polarisabilities for a tweezer of wavelength 1064 nm. Although less species-selective, the spontaneous Raman scattering rate is reduced at this further detuning (see section 4.1.5). We make use of this suppression in Chapter 5 by transferring Cs atoms from a 938 nm tweezer to a 1064 nm tweezer.

3.4 Loading and Imaging Atoms in Tweezers

The tight confinement of the optical tweezers gives rise to the collisional blockade effect [98], where at most one atom can be loaded at a time. The underlying cause of this effect is the occurrence of rapid pairwise light-assisted collisions between atoms, driven by the MOT light [160, 178], resulting in radiative escape of both atoms from the tweezer [179]. Since the number of atoms loaded is either even or odd with equal probability, after radiative escape of atom pairs, the tweezer occupancy is zero or one atom with approximately 50 % probability. Since the outcome of a single run of the experiment is binary (there is one atom in the tweezer, or there isn't), the experiment must be repeated many times, producing an ensemble. This allows an average loading probability for the ensemble to be determined, with an error given by a binomial confidence interval.

3.4.1 Imaging Single Atoms

We use fluorescence imaging to detect single atoms which have been confined in the tweezers, utilising the same high-NA lens which focusses the tweezers. After the MOT and molasses stages, we use the MOT cooling and repump beams as imaging beams to apply a 20 ms pulse of light near-resonant with the atomic D_2 transition. Photons are spontaneously absorbed and the atom re-emits them approximately isotropically, with the photon scattering rate given by Eq. (3.7). The goal of fluorescence imaging is to produce and collect as many photons as possible, while minimising sources of noise, to produce a clear binary signal of zero or one atom at the camera.

Focussing the Imaging System

Firstly, the EMCCD must be positioned at the focus of the imaging system in order to maximise the signal on a subset of pixels. This is achieved by imaging the atomic PSF as a function of the EMCCD axial translation (along the E/W direction in Fig. 2.20). Example PSFs using Cs confined in a 938 nm tweezer are presented in Fig. 3.7(a)(i-v). The PSFs are fitted with a Gaussian function to measure the $1/e^2$ extent, which is plotted as a function of EMCCD position in Fig. 3.7(b) for Cs and Fig. 3.7(c) for Rb. The x (squares, solid) and y (circles, dotted) axes of the PSFs clearly focus astimatically. This effect arises due to curvature of the dichroic mirror which splits fluorescence into the imaging path. The circle of least confusion (COLC) is the midpoint of the foci, where the PSF is approximately circular (Fig. 3.7(a)(iii)). We estimate the position of the COLC from the intersection of the x and y parabolic fits. Necessary astigmatism correction of the optical tweezers is discussed in section 3.6.1, however it is not essential for the imaging path. We estimate a chromatic focal length shift $\Delta f_{\mathrm{im}} \approx 0.5$ mm in the imaging system by comparing the positions of the Rb and Cs COLCs (vertical lines). We set the camera to the intermediate position between the Rb and Cs COLCs (zero in figure).

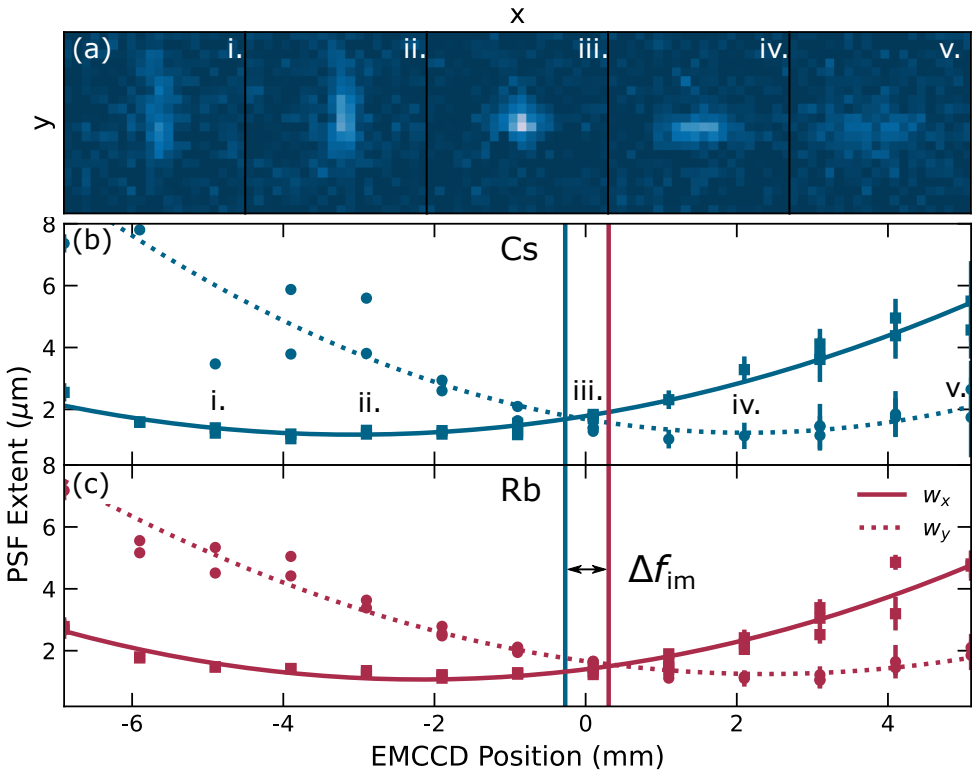

Figure 3.7: Focusing the imaging system using atomic fluorescence. (a) The atomic PSF imaged as the EMCCD is axially translated. Images (i-v) correspond to the marked points in (b) Cs $1/e^2$ PSF extent with EMCCD position extracted from a Gaussian fit. Astigmatism causes a differential focus of the x (solid squares) and y (dotted circles) PSF axes(c) Rb PSF extent. The vertical lines indicate the circles of least confusion used to estimate the CFLS.

Imaging System Efficiency

The total efficiency of the imaging system is the fraction of emitted photons which are counted by the EMCCD, and is the product of the collection efficiency and the detector efficiency.

The photon collection efficiency is primarily limited by the solid angle subtended by the high-NA lens. The objective subtends a solid angle of 1.02 steradians so that only 8 % of photons are captured. Further loss arises as the captured fluorescence propagates down the imaging optical path. These losses are due to imperfect reflection/transmission, and clipping off of mounting hardware. Fluorescent photons are separated into the imaging arm via a dichroic mirror and focussed on the EMCCD using a $f = 1000$ mm achromatic lens. Optical filters are required before the EM-

Table 3.2: Efficiency of the single atom imaging system for emission at 780 nm and 852 nm.

Imaging Element	**Efficiency**	
	780 nm	852 nm
Objective collection	0.08	
Objective transmission	0.954	0.977
Mirror clipping	0.83	
Dichroic reflection (×4)	0.997	0.990
808 nm notch filter	0.84(3)	0.98(1)
900 nm shortpass filter	0.95	0.8(1)
Quantum efficiency	0.78	0.53(4)
Total	0.039	0.027

CCD to block the small amount of tweezer photons which back-reflect into the imaging path. We use a shortpass filter[5] with cutoff wavelength of 900 nm to suppress 938 nm photons, and a notch filter[6] which blocks transmission at 808 ± 17 nm to suppress 814 nm photons.

The detector efficiency is given by the wavelength-dependent quantum efficiency $Q(\lambda)$. The number of photoelectrons N_e produced for N_p photons incident on the detector is $N_\mathrm{e} = Q(\lambda)N_\mathrm{p}$. The photoelectrons are converted to EMCCD counts via a pre-amp gain stage which is set to require 4.5 electrons per count. The contributions to the total efficiencies at 780 nm and 852 nm are summarised in Table 3.2.

Fluorescence Maximisation

Since in a given experimental shot the tweezer occupancy is either 0 or 1, over many experimental runs we accumulate the characteristic bimodal histogram of fluorescence counts which is typical of tweezer experiments. We present optimised histograms for Cs imaged in the 938 nm tweezer and Rb in the 814 nm tweezer in Fig. 3.8(a)&(b) respectively. The lower peak corresponds to experimental shots where zero atoms were loaded. Scattered light from

[5]Thorlabs FESH0900
[6]Thorlabs NF808-34

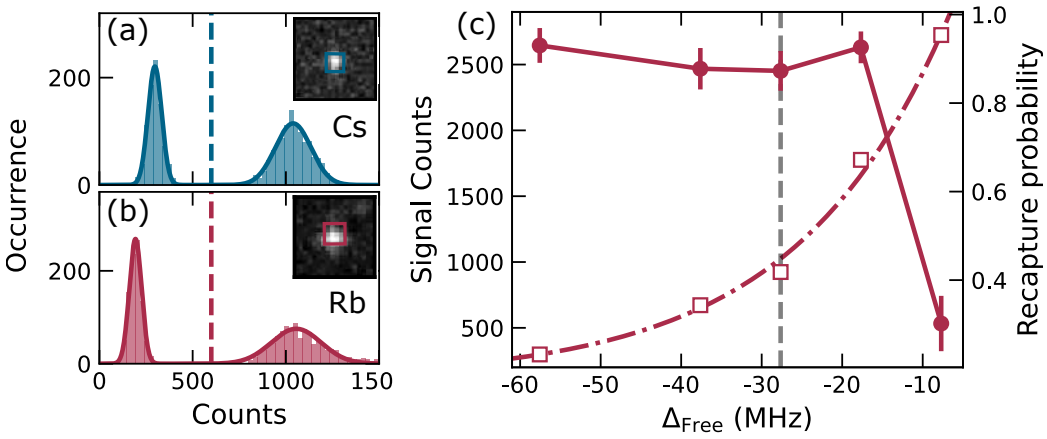

Figure 3.8: Fluorescence imaging single Rb and Cs atoms. (a) Histogram of fluorescence counts from fluorescence imaging Cs in the 938 nm tweezer. The inset shows a single atom image without pixel binning obtained from a single experimental shot. The outlined square shows the superpixel formed by binning 16 pixels. The dashed line indicates the threshold for atom detection. (b) Histogram of fluorescence counts from imaging Rb in the 814 nm tweezer. (c) Optimisation of the Rb imaging cool beam detuning in the 814 nm tweezer. The open squares show the separation between the histogram background and signal peaks. The circles show the single atom survival after a 1000 ms fluorescence pulse. The dashed grey line indicates the imaging detuning chosen. The red lines are guides to the eye.

the imaging beams and tweezers contribute to the background level which is the mean of the lower peak. The dashed line is a threshold. Counts above threshold correspond to shots where an atom was loaded into the tweezer. The insets show the atom image collected in a single shot of the experiment. The probability of loading an atom from the MOT is then the ratio of atoms with counts above threshold to the total number of shots taken. The error in the loading probability is calculated using a binomial confidence interval.

It is desirable to increase the separation between the two histogram peaks in order to reduce their overlap, and thus reduce the occurrence of false positives and negatives for experimental shots with counts close to threshold. The separation of the signal and background peak should be maximised while the peak widths should be minimised [180]. Tuning the imaging beam frequency closer to resonance results in a higher scattering rate, and so a greater number

of signal counts, as shown by the open squares in Fig. 3.8(c). Here, we optimise the Rb fluorescence imaging in a 814 nm tweezer of depth. The imaging cool beams each have a power of 400 μW and are red-detuned of the D_2 line. The detuning cannot be set arbitrarily close to resonance due to rapid recoil heating (see Eq. (3.6)), which begins to dominate over the Doppler cooling rate from the red-detuned beam. The closed circles show the probability to retain an atom after it is exposed to a 1 s pulse of imaging light. Close to resonance, recoil heating is sufficient to induce atom loss. The grey dashed line shows the selected imaging detuning of -28 MHz, which gives sufficient signal and little heating.

In a typical experiment, the probability of retaining a Rb or a Cs atom in the tweezer after fluorescence imaging is $> 99\,\%$ and $> 95\,\%$ respectively. Loss of Cs atoms from the 938 nm tweezer occurs during imaging because broadband emission from the bare laser diode optically pumps the atom from the $6^2P_{3/2}$ state to an untrapped state. We suppress this emission using narrowband laser-line filters as discussed in section 2.6, however the few nW power remaining is still sufficient to induce loss.

3.4.2 Tweezer Loading Probability Optimisation

The loading probability of atoms into the optical tweezers is saturated by overlapping the MOT with the tweezers, which maximises the atomic density at the position of the tweezer.

At the centre of the MOT coils, the quadrupole magnetic field passes though zero with a field gradient in the N/S direction of 8.5 G cm^{-1}. Applying an offset to the quadrupole field of e.g. 1 G then translates the field position of the field zero by 1/8.5 cm $\approx$ 1.2 mm. The magnetic field offset in the E/W, U/D and N/S directions can be independently set using the corresponding shim coil pair. The overlap is optimised by maximising the loading probability into the optical tweezer as a function of shim field. Fig. 3.9(a) shows the Rb loading probability into a 1 mK deep 814 nm tweezer as a function of applied shim field along the 3 cell axes. The Gaussian profiles reflect the Gaussian MOT distribution as it is swept through the delta function-like trap. The width (FWHM) of the features is around 0.15 G, corresponding

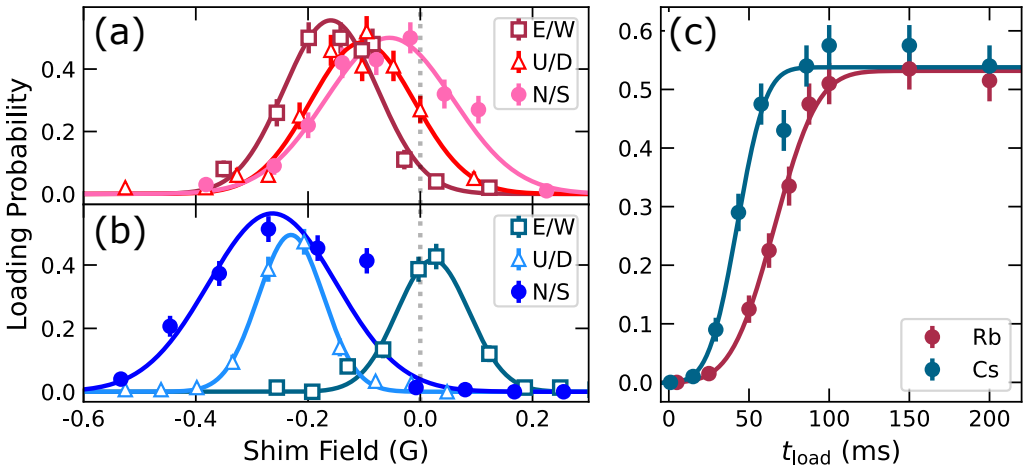

Figure 3.9: Optimisation of the single atom loading probability. (a) Overlap of the Rb MOT with the 814 nm tweezer using the 3 shim coil pairs. The overlap in each axis is independently optimised. The x-axis is the applied shim field with respect to zero field after bias cancellation. (b) Overlap of the Cs MOT with the 938 nm tweezer. The optimal shim parameters for Cs do not coincide with those for Rb due to differences in the MOT beam alignment. (c) Loading probability with MOT overlap time. The loading probability for both species reaches the saturated value of ~ 0.55 after 100 ms.

to a spatial extent of 180 μm, which is comparable to the spatial extent of the MOT. Fig. 3.9(b) shows the same shim optimisation for Cs in a 1 mK deep optical tweezer. It is clear that although the tweezers are only spatially separated by a few microns, significantly different shim fields are required for each species. For example the difference in optimal E/W fields (open squares) corresponds to an offset in the MOT centres of 200 μm, precluding the simultaneous loading of both MOTs.

Once the overlap has been set, we find a suitable overlap time with the MOT, as shown in Fig 3.9(c). To minimise the experiment run time, we choose the shortest time which saturates the loading probabilities in each tweezer. For a 1 mK deep tweezer, 100 ms is sufficient to saturate the loading into each tweezer. We note that the loading probability saturates to slightly more than 0.5. This is because a the kinetic energy is unevenly split in a light-assisted collision, so that for a fraction of cases, only one atom is lost from the tweezer.

Optimisation of the optical molasses stage is similarly achieved by finding the optimal shim fields. The molasses fields are set at a low tweezer depth, so that the loading is more sensitive to the atom temperature. The peak in

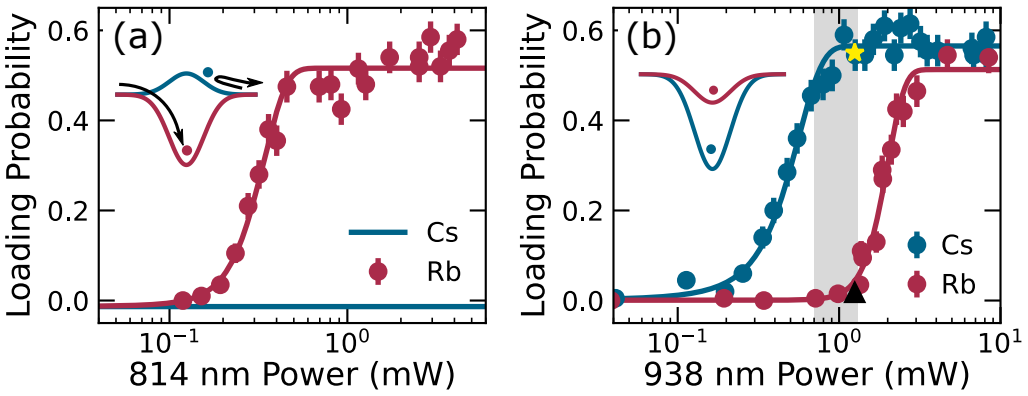

Figure 3.10: Atom loading into species-selective optical tweezers. (a) Rb loading probability as a function of 814 nm tweezer power. The 814 nm tweezer is repulsive for Cs (inset), so only Rb is loaded. (b) Loading probability of Rb and Cs as a function of 938 nm tweezer power. The tweezer is species-selective for the shaded band of powers. The yellow star and black triangle are 500-shot measurements of the loading into a 1.25 mW tweezer for Cs and Rb, respectively. The inset shows the relative potentials experienced by Rb (red) and Cs (blue).

the loading probability corresponds to the shim fields which yield the lowest atom temperature.

3.4.3 Loading Species-Selective Tweezers

With the MOT and tweezer beams overlapped, we now evaluate the species-selectivity of the tweezers, whose wavelengths were chosen in section 3.3.2.

We first examine the species-selectivity of the 814 nm tweezer in Fig. 3.10(a) by measuring the atom loading probability as a function of the tweezer power. The loading probability is sensitive to the trap depth; for insufficient depth the loading probability is poor. As expected, since the 814 nm tweezer potential is repulsive for Cs, no Cs atoms load at any power and the tweezer is perfectly species-selective. The Rb loading probability saturates at 0.52(1) for powers > 0.5 mW, corresponding to a trap depth of 0.33(2) mK. The behaviour of the 938 nm tweezer is very different, as it is attractive for both Rb and Cs. The loading probabilities for Rb (red) and Cs (blue) into the 938 nm tweezer as a function of tweezer power, P_{938}, are shown in Fig. 3.10(b). The Cs loading probability saturates at a lower power than the Rb loading prob-

ability because Cs experiences a deeper confining potential in the 938 nm tweezer. The Cs loading probability saturates at 0.57(1) for tweezer powers greater than 1 mW, corresponding to a trap depth of 0.30(2) mK. The Rb loading probability into the 938 nm tweezer saturates to 0.51(3) for powers greater than 3 mW, corresponding to a trap depth of 0.32(2) mK, in agreement with the Cs measurement. We note that the loading probabilities for Rb and Cs into both tweezers saturate at similar trap depths of around 0.32 mK due to the similar temperatures and densities of the MOTs. The 938 nm tweezer is species-selective for powers in the range 0.7 mW $< P_{938} <$ 1.3 mW (shaded grey), where the Cs loading probability is close to saturation and the Rb loading probability is close to zero. Specifically, for a tweezer power of 1.25 mW, we measure loading probabilities of 0.018(6) for Rb (black triangle) and 0.55(2) for Cs (yellow star) over 500 repetitions of the experiment. At this power, the tweezer can therefore be used to load a Cs atom selectively.

3.5 Atom and Tweezer Characterisation

It is necessary to characterise the optical tweezers and the properties of the atom trapped within them. While this was done *ex-situ* in section 2.7, an *in-situ* measurement using the atoms themselves is required to accurately parametrise the tweezers (it is also somewhat tricky to perform a knife-edge measurement inside a vacuum cell). We have found that such characterisation measurements must be done routinely for optimisation purposes, and to diagnose experimental issues. Given the frequency with which they are required, we take a more pedagogical approach in the following discussion, to serve as a reference for future experimentalists.

3.5.1 Atom Lifetime

A simple but useful measurement is of the atom lifetime in the tweezer. We simply measure the atom survival probability after a variable hold time t_{hold} in the tweezer. The lifetime is the hold time for which the recapture probability decreases to $1/e$ of its value measured at short times ($<$ 1 ms). Contributions to loss during t_{hold} include collisions with room-temperature

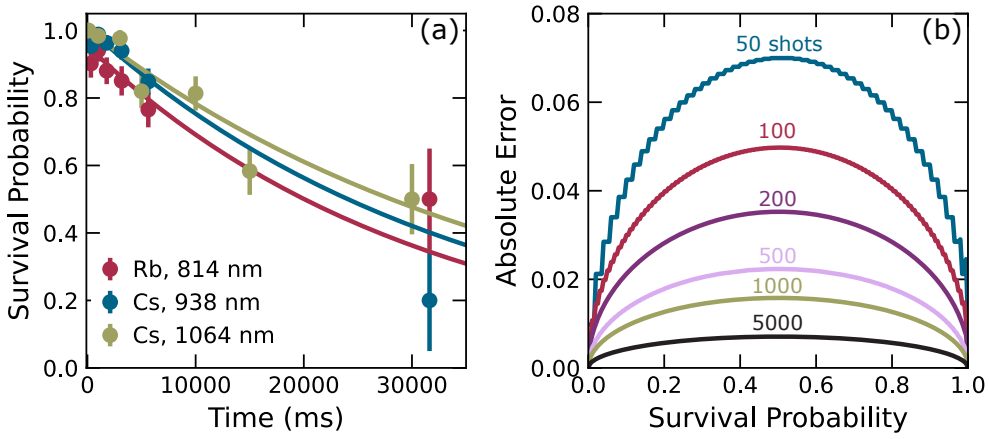

Figure 3.11: Single atom lifetimes and histogram error. (a) Lifetimes for Rb in the 814 nm tweezer, Cs in the 938 nm tweezer and Cs in the 1064 nm tweezer. (b) Absolute error in the survival probability calculated using a binomial confidence interval. The error is calculated as a function of the survival probability and the number of shots. More shots are required when $P \sim 0.5$, however the returns diminish quickly.

background gas atoms in the UHV cell, and heating of the atom through intensity and pointing instability of the tweezer. It is desirable to maximise the lifetime so that loss of single atoms is negligible for subsequent measurements. Empirically, we maximised the single atom lifetimes by elimination: we use sturdy optics mounts, and atom dispenser currents far below threshold. Lifetime curves for Cs in the 938 nm and 1064 nm tweezer, and Rb in the 814 nm tweezer are shown in Fig. 3.11(a). The tweezer depths are 1 mK, which is a typical depth used in an experiment. The solid lines are fits of exponential decay to the data, from which we extract $1/e$ times of $t_{\mathrm{Cs},938} = 41(7)$ s, $t_{\mathrm{Cs},1064} = 41(6)$ s and $t_{\mathrm{Rb},814} = 31(7)$ s. These times are all sufficiently long that single atom loss does not significantly impact further experiments. The large fitting errors on the lifetimes arise because the fit at long hold times is poorly constrained. The error bars at long t_{hold} are large because it is impractical to take the many shots necessary to resolve changes in the atom survival probability.

A reasonable question at this point is to ask how many shots are required per histogram? For a single experimental shot, the atom survival follows a binomial probability distribution. We can the therefore assign an error bar to

the survival probability using a binomial confidence interval [181], which we calculate using the `astropy` Python package with a Jeffrey's interval [182]. The confidence interval depends on the survival probability and the number of trials. To understand how many shots are required, we plot the absolute error calculated as a function of the survival probability in Fig 3.11(b).

Clearly, the error is greatest for intermediate probabilities $P \sim 0.5$. Significantly fewer shots are required when the probability is near an extreme[7], which can expedite the measurement if the shape of the expected survival probability curve is known. The absolute error decreases as more shots are taken and the mean value is better known. The returns are diminishing however, and unless good precision is required (for example to resolve a difference between two similar values), no more than 200 shots is usually sufficient.

3.5.2 Atom Temperature

It is important to know the temperature of the atoms trapped in the optical tweezers. The atom temperature affects the density and collisional loss rates, discussed in Chapter 5. It is also intimately related to the mean motional state n of the atoms in the tweezer. For eventual magnetoassociation of two atoms in a tweezer, *both* atoms must be in $n = 0$ for all three tweezer axes [71]. Quantifying the atom temperature is thus a critical goal, and a tool to measure a relative change in the temperature will prove very useful as a way to identify and minimise sources of heating experimentally.

How can we define the temperature of a single atom? After all, temperature in a bulk gas is usually thought of in terms of the width of the atomic velocity distribution. We recall that the atom prepared in each shot of the experiment is part of a thermal ensemble. The atom loaded into an optical tweezer is sampled from a MOT, where the atomic speeds follow a Maxwell-Boltzmann distribution. The probability for an atom to have a speed in the range $v + dv$ is given by [183]:

$$f(v)dv = 4\pi v^2 \left(\frac{m}{2\pi k_\mathrm{B} T}\right)^{3/2} \exp\left(-\frac{mv^2}{2k_\mathrm{B}T}\right) dv, \tag{3.8}$$

[7] The reason for this is intuitive: if a coin lands heads-up 10 times in a row, the chance the coin is fair is quite low.

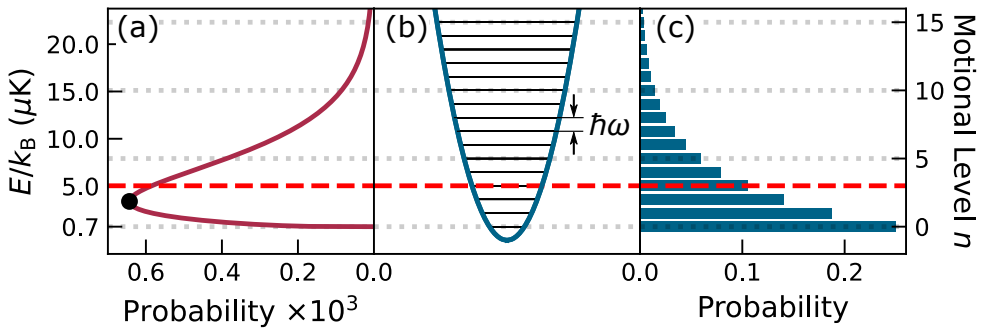

Figure 3.12: Motional state occupancy when loading an optical tweezer from an caesium gas with mean atom energy $E/k_B = 5$ μK. (a) 3D Maxwell-Boltzmann distribution of energies of the free gas. The most probable energy is indicated by the black point and corresponds to a motional level of $n_{MP} = 1.84$. (b) Harmonic energy levels in the tweezer. The mean motional state occupied for a trap frequency of 30 kHz is $\bar{n} = 3$ (dashed line). (c) The occupation probability of the tweezer motional states n reflects the Boltzmann factor (Appendix C).

where T is the temperature of the ensemble, m is the atomic mass, and k_B is the Boltzmann constant. We plot the 3D Maxwell-Boltzmann distribution for a free gas of Cs atoms in Fig 3.12(a). The distribution has been plotted as a function of temperature using equipartition, $\frac{3}{2}k_BT = \frac{1}{2}mv^2$. The red dashed line indicates the mean temperature of the cloud, 5 μK, which is typical after optimisation.

An atom in an optical tweezer is a quantum harmonic oscillator. The motional energy levels n in the tweezer have eigenenergies $E_n = \hbar\omega(n + \frac{1}{2})$, where $\omega/2\pi$ is the trap frequency, shown for one dimension in Fig. 3.8(b). Since the ensemble follows a distribution of energies, the atoms are mapped onto a distribution of motional states in the tweezer. The mean motional occupancy of the atomic ensemble $\bar{n}$, is related to the ensemble temperature by:

$$\bar{n}(T) = \frac{1}{e^{\hbar\omega/k_BT} - 1}, \tag{3.9}$$

which is derived in Appendix C. The probability of occupying a specific motional state n is:

$$P_n(\bar{n}) = \frac{\bar{n}^n}{(1+\bar{n})^{n+1}}. \tag{3.10}$$

In Fig. 3.8(c) we plot P_n for a Cs atom with $T = 5$ μK and $\omega/2\pi = 30$ kHz,

corresponding to $\bar{n} \approx 3$. Finally we are able to interpret the meaning of temperature for an atom in a tweezer. The "temperature" of a single-atom ensemble is simply the mean energy of the atoms in the ensemble, expressed in units of k_{B}, which from Eq. (3.9) corresponds to a mean motional level $\bar{n}(T)$. For a given experimental shot, the atom occupies a single motional level, and so does not possess a temperature distribution; in this case, discussion of an atom temperature is less meaningful.

It is possible to measure the classical average temperature of the atom, from which $\bar{n}$ can be inferred using Eq. (3.9). We use a method commonly referred to as release and recapture [184]. The idea is to briefly extinguish the trap for a release time t_{r}, as shown in Fig. 3.13(a), resulting in an amount of atom loss dependant on the atom velocity at the time the trap is extinguished. For a given t_{r}, there is a higher probability that an atom from an ensemble with a high mean T will be lost, compared to a colder ensemble.

We measure the recapture probability as a function of t_{r} for Rb in a 814 nm tweezer of power 1.60 mW, as shown in Fig. 3.13(b). The solid line is a fit of a Monte Carlo simulation to the data. In the simulation, the atom velocity is randomly selected from the Maxwell-Boltzmann distribution, and its position $\underline{r}$ in the trap randomly selected from a Gaussian distribution. After the release time the new atom coordinates are $\underline{r}' = \underline{r} + \underline{v}t_{\mathrm{r}}$. The kinetic energy of the atom is compared to the trap depth at $\underline{r}'$, and if $U(\underline{r}') < E_{\mathrm{kin}}$, the atom is lost from the trap. This binary simulation is repeated several thousand times to generate a recapture probability for each release time. An optimisation parameter of the fit is the ensemble temperature, which determines the mean $\underline{v}$ of the simulation. The temperature extracted from the least-squares fit is 28(2) μK. The temperature extracted is sensitive to the trap power. The energy of an atom in a given motional level n is dependent on the trap frequency, where $\omega \propto \sqrt{P}$. The extracted temperature must therefore be appropriately scaled if the tweezer power is later ramped adiabatically.

In Fig. 3.13(c), we present a temperature measurement of Cs in the 938 nm tweezer with power 3.63 mW. Here, we demonstrate the utility of this measurement technique for detecting changes in the atom temperature. Typically in an experimental sequence we apply a 5 ms pulse of cooling light to counteract heating after the first atom image. The temperature extracted in this

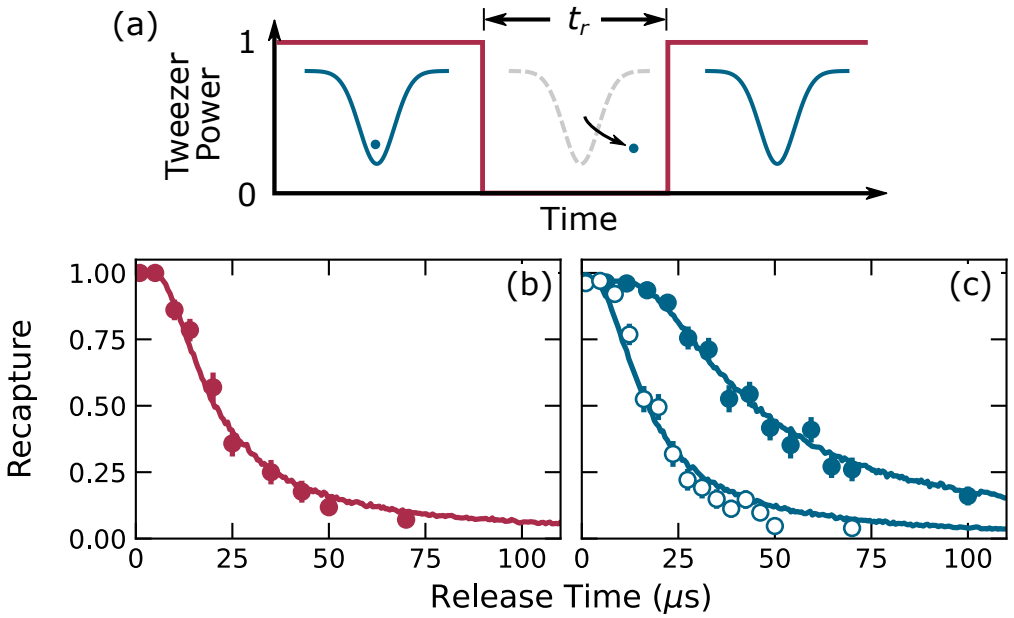

Figure 3.13: Measurement of the atom temperature distribution in an optical tweezer. (a) Tweezer power profile with time for a release and recapture measurement. The tweezer is switched off for a time t_r, causing some atoms in the ensemble to be lost. (b) Measurement of the ensemble temperature for Rb loaded into a 814 nm optical tweezer of power 1.60 mW. The single atom recapture probability decreases for longer t_r. The solid line is a Monte Carlo least-squares fit to the data. (c) Measurement of the Cs ensemble temperature in a 938 nm with power 3.63 mW. The closed and open circles respectively show the recapture with and without a cooling stage before the release step.

case (closed circles) is 15(1) μK. In contrast, the open circles show the recapture if the cooling pulse is omitted. The fitted temperature here is 65(5) μK, indicating that there is 50(5) μK of heating during the imaging time. If a fixed release time is included in a sequence, other parameters can be tuned to minimise heating by maximising the recapture probability.

It is important that the trap switches rapidly with respect to the atomic motion, so that the atoms experience an instantaneous vanishing of the potential[8]. We therefore use the AOMs in the tweezer beam paths to switch the beams, with have a rise time of ~ 60 ns, which is much less than a trap period ($\lesssim 10$ μs). The RF signal to the AOM is rapidly attenuated in 20 ns

[8]A lowering time comparable to the trap period would be somewhat adiabatic and modify the observed temperature of the atoms. Furthermore the comparison to the Monte Carlo simulation would be less accurate.

by a fast RF switch[9].

3.5.3 Light Shift

Similarly to the AC-stark shift experienced by an atom in the ground state (section 3.3.1), the other atomic states are also shifted by the tweezer. The light shift is the frequency shift Δ_{LS} of the atomic transition with respect to its free-space value ω_0, as illustrated in Fig. 3.14(a). The light shift can have a significant effect due to the tight waist of an optical tweezer: a typical shift of $\Delta_{\mathrm{LS}} \sim 10$ MHz is sufficient to detune imaging beams from resonance. Moreover, for some species, the tweezer loading can be affected if the light shift of the upper state is particularly repulsive [177]. The mismatch of ground- and excited-state potentials can also cause dipole force heating [185]. It is therefore useful to characterise the light shift between the relevant atomic states in a tweezer.

We examine the light shift of the Cs $f = 4 \rightarrow f' = 5$ cooling transition in an optical tweezer of wavelength 938 nm. The light shift is probed using a circularly-polarised pushout beam which is the same used for state-sensitive detection in section 4.1.2. The pushout beam drives σ^+ transitions with respect to a $\sim$ 2 G bias field applied by the N/S shim coil pair. When resonant with the $4 \rightarrow 5'$ transition, the pushout beam induces loss.

In Fig. 3.14(b), we show example loss features for tweezers of depth 0.5 mK (purple) and 4 mK (red). The survival probability is measured as a function of the probe detuning. We choose the probe pulse time and power at each trap depth to avoid saturating the loss feature. Typically $\sim$ 2 μW probe power and $\sim$ 2 ms probe time are sufficient. The solid lines are Lorentzian fits to the data, from which we extract the loss minima. The full-width at half maximum (FWHM) of the features is $\sim$ 5 MHz, which is consistent with the natural linewidth of the D_2 transition. The atoms are distributed across m_f states, so that the measured resonance positions are averages for the $f = 4 \rightarrow f' = 5$ transition.

In Fig 3.14(c), we plot the fitted resonance centres as a function of tweezer power. The dotted lines indicate the centres of the resonances plotted in

[9]Mini-Circuits ZASWA2-50DR-FA+

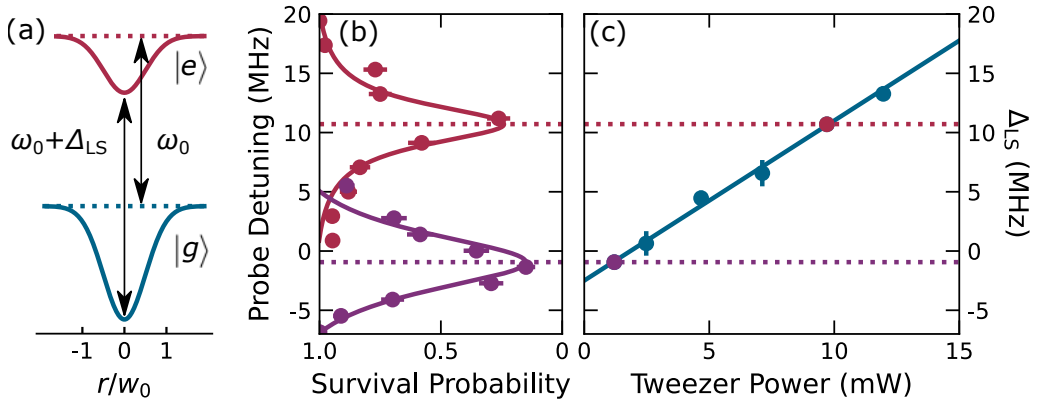

Figure 3.14: Measurement of the light shift of the $f = 4 \rightarrow f' = 5$ transition for Cs in a 938 nm tweezer. (a) A spatially varying light shift is induced by the tweezer, shifting the frequency separation of the ground and excited states $|g\rangle$ and $|e\rangle$ by Δ_{LS}. (b) Probe-induced loss as a function of detuning for tweezers of depth 0.5 mK (purple) and 4 mK (red). The pushout time is adjusted to avoid saturating the loss features. The solid lines are fits from which we extract the position of the light-shifted resonance. (c) Light shift as a function of tweezer power incident on the atoms. The data points correspond to the fitted centres of measurements as in (b). The solid line is a linear fit to the data, from which the power-dependent light shift is extracted.

Fig 3.14(b). The solid line is a linear fit to the data, from which we extract a light shift of $\Delta_{\mathrm{LS}} = 1.35(3)$ MHz/mW. This measured value is higher than the expected shift of the $f = 4 \rightarrow f' = 5$ transition, averaged over m_f states, of ~ 0.8 MHz/mW. The discrepancy is likely due to the incorrect assumption of equal m_f population. A better comparison to theory could be made by measuring the light shift of the spin-stretched $(3, 3) \rightarrow (4', 4')$ transition by incorporating the optical pumping scheme described in section 4.1.3. The value extracted depends on the trap waist, and increases as the trap waist is optimised, as discussed in the following sections. The new light shift can be estimated by scaling by the ratio of old and new waists: $\Delta'_{\mathrm{LS}} = (w_0/w'_0)^2 \Delta_{\mathrm{LS}}$. The extracted offset is $-2.5(2)$ MHz, which is much larger than the value of ~ 0.2 MHz expected from the Zeeman shift due to the bias field. We attribute this discrepancy to a drift in the laser frequency offset during this measurement.

3.5.4 Trap Frequency and Waist

The tweezer waist is a critical parameter to pin down, so that the tweezer intensity and potential depth can calculated with confidence. In a cylindrically symmetric tweezer, the radial x and y axes are degenerate and have the same trap frequency. The axial direction of the tweezer z is less confined, and related to the radial dimensions by a geometric factor. The trap frequencies in the radial and axial directions are related to the waists and Rayleigh range respectively by:

$$\omega_r = \sqrt{\frac{4U_0}{mw_0^2}} \qquad (3.11) \qquad \text{and} \qquad \omega_a = \sqrt{\frac{2U_0}{mz_R^2}}. \qquad (3.12)$$

Here, U_0 is defined as in Eq. (3.2), so that if the tweezer power incident on the atom is known, a measurement of the trap frequency can be used to infer the beam waist. The trap frequencies in units of Hz are $\nu_i = \omega_i/2\pi$.

In our system, it is important to note that the optical tweezers are asymmetric, possessing different waists along the orthogonal x and y axes of the trap. The source of the asymmetry is apodisation of the large-diameter tweezer beam on the main table, which is clipped by the limited clear aperture of the beam-shaping optics. The limiting clear diameter of the optics in the direction parallel to the table is ~ 30 mm, compared to ~ 50 mm in the vertical direction, corresponding to the x and y axes of the tweezers respectively. The asymmetry cannot be corrected at present, since it is a consequence of the objective requiring large-diameter input beams (see Fig. 2.16(c)), which necessitates overfilling the limited-aperture auxiliary optics. This issue could be resolved in future by switching to an objective of shorter effective focal length.

Release and Recapture

The first method we discuss for measuring the trap frequency is another release and recapture technique, where the tweezer is briefly extinguished *twice* for durations t_1 and t_2, as shown in Fig. 3.15(a). Fast switching of the trap is achieved in the same way as for the temperature measurements

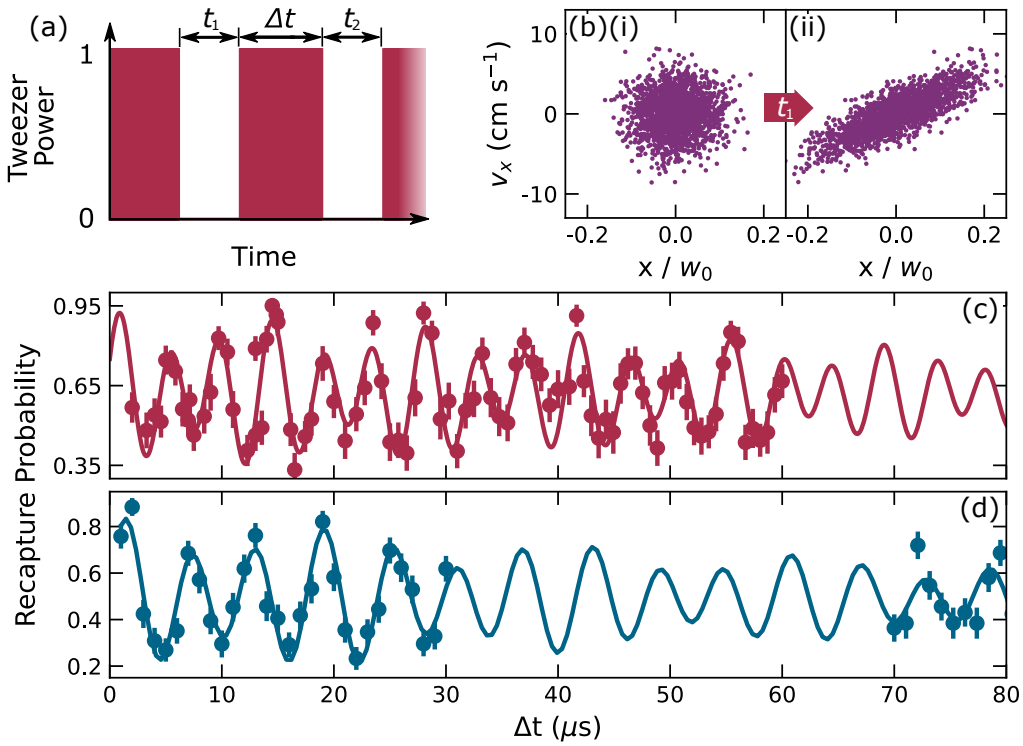

Figure 3.15: Measurement of the radial trap frequencies using release and recapture. (a) The tweezer temporal power profile. The tweezer is switched off for time t_1 to synchronise atom oscillation phases in the ensemble. The tweezer is jumped back on and the atoms oscillate for a time Δt. A second off-time t_2 probes the oscillation phase. (b) Modification of the phase-space distribution along the radial trap axes induced by the first off-step t_1. (i) Initially, the atoms positions and velocities follow a Gaussian distribution, with widths determined by their temperature. (ii) After t_1, the atoms have translated $dx = v_x t_1$ in free space, modifying the phase-space distribution. (c) Trap frequency measurement for Rb in the 814 nm tweezer. (d) Trap frequency measurement for Cs in the 938 nm tweezer. The solid lines are damped sinusoidal fits to the data.

discussed in section 3.5.2. The purpose of the first release for t_1 is most easily understood by considering a Monte Carlo simulation of the atom ensemble in phase space [186]. Fig. 3.15(b)(i) shows the phase space distribution along the x axis at the start of the experiment. The atoms follow a Gaussian distribution of positions, with thermal width given by $\sigma_x = \omega_x^{-1}\sqrt{k_B T/m}$ [97]. We assume a 1D Maxwell-Boltzmann distribution of velocities, where the v_x is related to the atom temperature by $\frac{1}{2}k_B T = \frac{1}{2}mv_x^2$. During the first release time t_1, the atoms travel a distance $dx = v_x t_1$ in free space. Fig. 3.15(b)(ii) shows that the effect of the travel time t_1 is to modify the

distribution in phase-space. As a result, when the trap is switched back on, the oscillation phase of the atoms in the ensemble becomes synchronised.

When the trap is switched back on, the now in-phase atoms in the ensemble undergo harmonic motion for a time Δt, where the kinetic and potential energies constantly interchange, visualised as a rotation of the phase-space ellipse with frequency ω [187]. The purpose of the second off-time t_2 is then to probe the oscillation phase of the ensemble, which is dependant on the experimentally varied Δt. If the atom phase had not been synchronised in t_1, the atom oscillations would average to zero.

Fig 3.15(c) shows the result of this technique for Rb in a 814 nm tweezer with power 1.7 mW, and Fig. 3.15(d) shows the result for Cs in a 938 nm tweezer with power 4.0 mW. Empirically, t_1 is set to optimise the contrast of the oscillation fringes; $t_1 = T/4$, with T the trap period, is usually suitable. t_2 determines the offset in the recapture probability, and is set by the atom temperature, requiring shorter times for a hotter ensemble. Due to the symmetry of oscillation in the trap[10], the atom recapture probability oscillates at twice the trap frequency.

The situation is slightly complicated by the asymmetry of the tweezer. Oscillations along the x and y axes at different frequencies may both be excited by the initial release time t_1. This gives rise to a beatnote in the measured survival probability. The solid lines are fits to the data, corresponding to the sum of sinusoidal oscillations at angular frequencies $2\omega_i$ along x and y, decaying with a $1/e$ time τ [188]:

$$P(t) = P_0 + e^{-t/\tau} \sum_{i=x,y} a_i \sin\left(2\omega_i t + \phi_i\right), \tag{3.13}$$

where a_i are the amplitudes of oscillation, ϕ_i are phases and P_0 is an offset.

For Rb, we extract trap frequencies $\{\nu_x, \nu_y\}_{\mathrm{Rb}} = \{74.0(9), 109.8(4)\}$ kHz, which are in the ratio 0.67(1). For Cs, we extract trap frequencies $\{\nu_x, \nu_y\}_{\mathrm{Cs}} = \{60.2(8), 83.9(3)\}$ kHz, which are in the ratio 0.72(1). The ratios are similar because the asymmetry of both tweezers is induced by the same optics.

[10] In a single trap period, the atom velocity is maximal and minimal twice.

The damping of the oscillation fringes is due to dephasing of the initially synchronised ensemble. This can arise from, for example, off-resonant scattering, or a slight motional state-dependent variation in the trap frequencies, caused by the thermal distribution of the atoms. Here, the damping time is relatively long ($\tau > 100$ μs), which we attribute to the low mean occupancy of the ensemble $\bar{n} \approx 3$, where the trap has little anharmonicity.

While experimentally simple, this method is limited to measurements of the radial trap frequencies. Since $\omega_r \gg \omega_a$, the longer t_1 required to synchronise axial oscillations would just result in loss of all atoms from the tweezer. To measure the axial trap frequencies, we turn to a second method of measuring the trap frequencies.

Parametric Modulation

A second method for measuring the trap frequency is via parametric modulation of the tweezer intensity. Fluctuations in the intensity contribute to heating of the trapped atom, which can escape the trap if it gains sufficient energy. This effect is especially significant when the frequency of the noise is resonant with a harmonic of the trap frequency. Deliberate modulation of the tweezer intensity essentially introduces intensity noise at a frequency ω_{mod} to the trap, which can be used to probe the trap frequency.

An atom in an intensity-modulated tweezer is a driven harmonic oscillator. Maximal heating of the atom occurs when ω_{mod} is resonant with twice the trap frequency [189], manifesting as a dip in the atom recapture probability as the modulation frequency is scanned through $2\omega_i$. The tweezer intensity is tuned by controlling the amplitude of an RF tone applied to an AOM in the beam path. We sinusoidally modulate the RF amplitude at a frequency $\omega_{\text{mod}} \sim 100$ kHz, producing a sinusoidal tweezer intensity profile with time.

The parametric loss spectrum for Cs in a 938 nm tweezer of power 2.6 mW is shown in Fig 3.16. We modulate the trap depth for 50 ms with a modulation amplitude of $h = 5$ % to probe the radial dimensions x and y. We observe two radial trap frequencies because the tweezer is strongly asymmetric as discussed in the previous sections. The radial trap frequencies extracted from Fig 3.16 are 49.2(3) kHz and 73.4(2) kHz, with a similar ratio to those

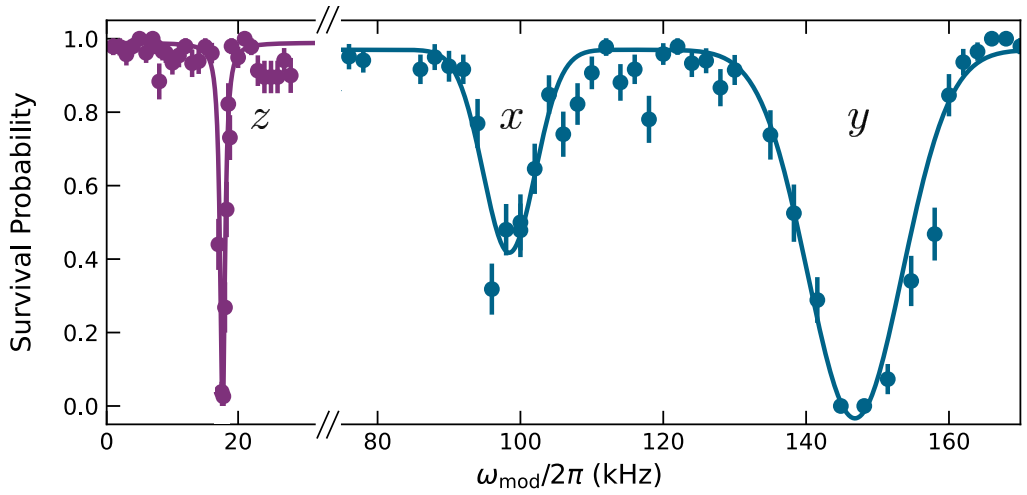

Figure 3.16: Parametric modulation spectroscopy of the three axes of the 938 nm tweezer using Cs. The solid lines are Gaussian fits to the data. Resonances shown in blue at 98.4(5) kHz and 146.8(3) kHz correspond to the x and y trap axes respectively. The solid lines are a Gaussian fit to the data. The axial trap resonance at 17.6(1) kHz is shown in purple, corresponding to the z axis of the trap. The resonances occur at twice the trap frequency.

extracted using release and recapture. The axial trap frequency is expected to be about 5 times lower than the radial trap frequencies (Eqs. (3.11) & (3.12)). Since the heating rate is proportional to square of the trap frequency [190], a larger modulation depth is required to induce loss at at axial resonance. We apply a modulation depth of $h = 18$ % for 50 ms to induce loss. The resonance feature coloured purple in Fig. 3.16 corresponds to the axial trap frequency, which from the fit is determined to be 8.82(2) kHz.

We use the measured trap frequencies and the known tweezer powers to calculate the tweezer waists using Eq. (3.11), which we tabulate in table 3.3. We have also measured the waists of the 814 nm tweezer using Rb, and the 1064 nm tweezer, using Cs. Both of these tweezers are asymmetric for the same reason as the 938 nm tweezer. The waists summarised in table 3.3 are finalised after the trap frequencies have been optimised, as discussed in the following section.

Table 3.3: Summary of the measured waists of the optical tweezers after optimisation, in units of μm. The asymmetric waists were measured by parametric modulation spectroscopy. There are two tweezer waists due to asymmetry of the tweezers. w_x is larger, and corresponds to the N/S direction in which the tweezers are apodised by the limited clear aperture of the optics. w_y corresponds to the E/W direction.

	Tweezer		
Waist (μm)	814	938	1064
w_x	1.11(3)	1.29(4)	1.58(3)
w_y	0.92(3)	1.06(4)	1.43(4)

3.6 Trap Frequency Optimisation

It is beneficial to minimise the waist of the optical tweezers. The tweezer depth scales as $\propto P/w_0^2$, so that a tighter tweezer requires significantly less optical power to achieve the same depth. A smaller waist therefore allows larger tweezer arrays to be achieved within the optical power budget. A second reason relates to the efficiency of Raman sideband cooling, for which it is desirable to maximise the axial trap frequency while minimising detrimental photon scattering.

In principle, the tightest possible waist is set by the diffraction limit. In practice, optical aberrations arising from misalignment and curvature of the optics result in waists slightly above the diffraction limit. Nevertheless it is possible to improve the waists of the tweezers, using the trap frequency as a diagnostic. Experimentally, we optimise the axial trap frequency, which scales as $\omega_{\mathrm{ax}} \propto 1/w_0^3$, since it is more sensitive to changes in the tweezer waist than the radial trap frequency, which only scales as $\omega_{\mathrm{r}} \propto 1/w_0^2$.

3.6.1 Astigmatism Correction

We identified the presence of large astigmatism of the tweezers. Astigmatism causes the orthogonal axes of the tweezer to focus at different positions along the optical axis. The circle of least confusion occurs midway between the two distinct foci. The atoms are trapped at the circle of least confusion since

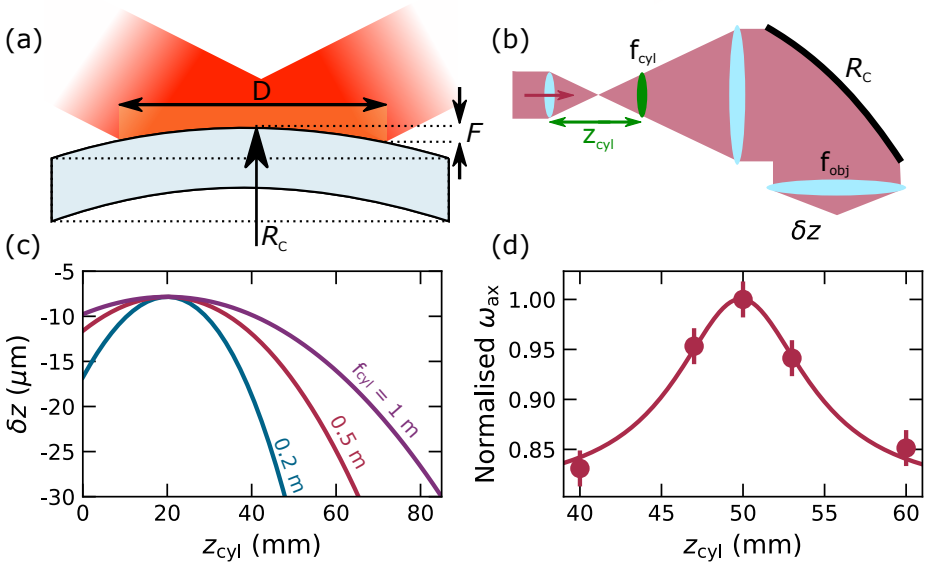

Figure 3.17: Astigmatism correction of the 814 nm tweezer using a cylindrical lens. (a) Stress-induced curvature of the dichroic mirror results in a parabolic surface with radius of curvature R_C and peak-valley flatness F across the illuminated diameter D. (b) Correction of the astigmatism introduced by the curved dichroic using a cylindrical lens (green). Fine adjustment of the lens position z_{cyl} tunes the divergence along one tweezer axis, adjusting the tweezer focus by δz. (c) Shift in the tweezer focus δz with z_{cyl} calculated using the ray transfer matrices. (d) Optimisation of the cylindrical lens position using parametric modulation.

the intensity is maximal, but since neither tweezer axis is well-focussed, the effective waist is large. We consider the 814 nm tweezer, which is reflected off a dichroic mirror[11] to overlap it with the 938 nm tweezer before the objective. The differential stress between the dichroic coating and substrate causes the mirror to become parabolic, with a radius of curvature R_C, illustrated in Fig. 3.17(a). For a beam incident at 45°, the symmetry of the parabolic mirror is broken. The orthogonal axes of the beam experience differential lensing, and focus at different positions along the optical axis.

The separation of the tangential and sagittal foci of the tweezer is given by $\Delta z = f_{obj}^2/(2R_C)$ [191], where f_{obj} is the effective focal length of the objective. R_C is related to the peak-valley flatness[12] F of the dichroic by $F = \frac{D^2}{8R_C}$, where D is the illuminated diameter of the dichroic. Since $R_C \propto$

[11] Thorlabs DMLP900L

[12] For a beam incident at 45°, the reflected wavefront error is $\sqrt{2}F$.

D^2, the astigmatism caused by the curvature of the dichroic is especially problematic in our system, where $D \sim 50$ mm. The dichroic has a reflected wavefront error (RWE) of $\sim 6\lambda$, causing the tweezer foci to be offset axially by $\Delta z > 6$ μm, which is larger than the Rayleigh range.

The astigmatism, which causes two distinct asymmetric foci to form, must be corrected for. We do this by inserting a cylindrical lens into the tweezer beam path, as shown in Fig. 3.17(b). This method has been used in other experiments to correct for astigmatism arising from different sources [192]. The cylindrical lens modifies the divergence along one beam axis, while preserving the divergence of the other. The cylindrical lens is placed in the $M = 25$ telescope of the 814 nm tweezer at a distance z_{cyl} from the first lens. The effect of the cylindrical lens on the focus displacement δz is shown in Fig. 3.17(c). The solid lines are calculations of δz using ray transfer matrices (see Appendix D) for cylindrical lenses of different focal lengths f_{cyl}. When the cylindrical lens is placed at the focus of the expansion telescope, there is no modification to the beam divergence. Either side, the effect is to pull the tweezer focus towards the objective lens, hence why $\delta z < 0$. We choose $f_{\mathrm{cyl}} = 1$ m because δz is less sensitive to the exact positioning of the cylindrical lens than for shorter focal lengths. A simulation using Zemax ray-tracing software verified this calculation.

The position of the cylindrical lens is optimised empirically by maximising the axial parametric resonance frequency. As the tweezer becomes more stigmatic, the measured axial trap frequency will increase due to the tighter waist. When the tweezer is stigmatic, the circle of least confusion will coincide with the tweezer focus. Fig 3.17(d) shows the normalised axial trap frequency as a function of z_{cyl}. The optimal position is at $z_{\mathrm{cyl}} = 49.9(4)$ mm, where the resulting δz is in agreement with expectation, in that it roughly cancels the focal shift due to the dichroic curvature. After optimisation, ω_{ax} was increased by a factor of $\times 2.0$ compared to without a cylindrical lens, corresponding to a 20 % reduction of waists. We have similarly inserted a cylindrical lens into the 938 nm tweezer path. We did not observe astigmatism on the 1064 nm tweezer, which is transmitted through all dichroic mirrors, and so does not require correction by a cylindrical lens.

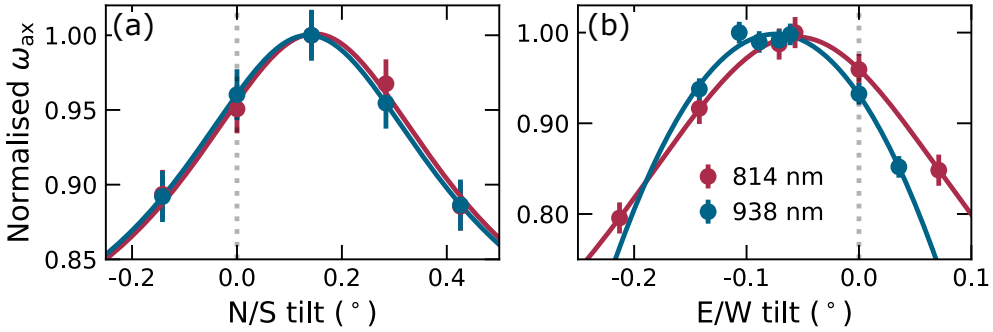

Figure 3.18: Optimisation of the objective lens alignment by maximising the axial trap frequency. The trap frequencies are measured using parametric modulation of the tweezer intensity. (a) Normalised axial trap frequency with N/S tilt. The dashed line indicates the initial lens angle before adjustment. The blue points are measured using Cs in the 938 nm tweezer. The red points are measured using Rb in the 814 nm tweezer. The two tweezers share a common N/S optimum. (b) Optimisation of the E/W tilt.

3.6.2 Objective Tilt

Further improvements to the trap waist can be made by optimising the tilt of the objective lens. Misalignments of this objective introduce aberrations which increase the waist of the optical tweezer. The angle of the objective can be adjusted along the N/S and E/W axes of the science cell using an adjustable kinematic mount. As before, we use a parametric measurement of the axial trap frequency to optimise the tilt of the objective, and find the optimal angle. One turn of an adjuster knob tilts the objective lens by 0.071 °. The focus of the tweezer is located $\sim$ 100 mm from the centre of rotation of the objective, resulting in transverse displacement of the optical tweezer of 200 μm per turn. This is comparable to the size of the MOT, therefore after each angular adjustment the shim fields must be reoptimised to keep the MOT and tweezer overlapped.

We present the axial trap frequency as a function of N/S tilt in Fig. 3.18(a) and as a function of E/W tilt in Fig. 3.18(b). We normalise the measured frequency values by the peak value for ease of comparison. The optimisation was done for both Cs in the 938 nm tweezer (blue) and Rb in the 814 nm tweezer. The solid lines are Gaussian fits used to extract an optimal value. The dashed lines indicate the starting angle of the lens, before adjustment. For both cases, the tweezer waist is less sensitive to misalignment in the

N/S direction, corresponding the clipped direction of the input beams. The tweezer waist scales weakly as $w_0 \propto 1/\omega_{\mathrm{ax}}^{1/3}$, so that the improvements correspond to modest reductions of ~ 2 % in w_x and w_y. The lens was finally set to the angles giving the maximal axial trap frequencies.

Chapter 4

Controlling Atoms in Tweezers

We have demonstrated that the apparatus presented in Chapter 2 can be used to prepare atoms in optical tweezers of several wavelengths, as discussed in Chapter 3. Having characterised the properties of the trapped atoms and the optical tweezers, we now turn to the task of extending our control over the isolated atoms, which broadly encompasses three categories. First, we consider manipulation of the internal state of the atoms (f, m_f) via optical pumping and microwave transfer. Second, we discuss control of the 3D position of the optical tweezers, which allows the atoms to be transported and for multiple atoms to be prepared in the same tweezers, as well as the production of optical tweezer arrays. The third area is control of the motional state n of an atom in a tweezer. Full control and preparation into $n = 0$ is possible using the technique of Raman sideband cooling, which is beyond the remit of this thesis, but discussed in the outlook (section 6.2.2).

4.1 Internal State Control

Atoms loaded into the optical tweezers from a MOT are distributed approximately evenly across the ground state f and m_f states. It is necessary to establish control of the internal state, preparing the atomic ensemble in specific (f, m_f) levels, since atomic properties such as the Zeeman splitting and the scattering length (section 5.1.1) depend on the internal state of the atom. Furthermore, the interspecies spectrum of Feshbach resonances

is state-dependent, and the well-established RbCs magnetoassociation technique we plan to use requires Rb and Cs atoms to be prepared in their maximal-m_f ground states $(f = 1, m_f = 1)$ and $(f = 3, m_f = 3)$ respectively [89, 193]. Control of the internal state of the atomic ensemble is therefore necessary. Preparation of the ensemble in a specific quantum state (f, m_f) may be achieved via optical pumping (OP), as described in the following sections, where we also discuss a state-selective imaging scheme and spontaneous Raman scattering, which is an obstacle for state preparation.

4.1.1 Atoms in a Magnetic Field

Optical pumping requires the application of an external magnetic field in order to define a quantisation axis. Atomic structure was reviewed in section 2.5.1. We now extend that discussion to the interaction of an atom in an applied magnetic field. Each hyperfine state f is has $(2f + 1)$ Zeeman sublevels labelled m_f, with values from $-f$ to f in integer steps of 1. In an external magnetic fields, the atom-field interaction causes the energies of the (f, m_f) states to shift.

For the special case of $j = 1/2$, which applies to the $n^2S_{1/2}$ ground states of Rb and Cs, the field-dependent energy shift of the (f, m_f) states is given analytically by the Breit-Rabi formula [194, 195]:

$$E(B) = -\frac{\Delta E_{\text{hfs}}}{2(2i+1)} + g_i \mu_{\text{B}} m_f B \pm \frac{\Delta E_{\text{hfs}}}{2}\left(1 + \frac{4m_f x}{2i+1} + x^2\right)^{\frac{1}{2}}, \qquad (4.1)$$

where i is the nuclear spin, $\Delta E_{\text{hfs}} = A_{\text{hfs}}(i + \frac{1}{2})$ is the hyperfine splitting with A_{hfs} the magnetic dipole constant, μ_{B} is the Bohr magneton, $x = \frac{\mu_{\text{B}}(g_j - g_i)B}{\Delta E_{\text{hfs}}}$ is the scaled magnetic field strength and g_i, g_j are Landé g-factors. The $\{+\}$ sign is taken for the upper f manifold and the $\{-\}$ sign for the lower. The energy splitting ΔE of a transition $(f, m_f) \rightarrow (f', m_f')$ is obtained by calculating $E(B)$ for each state and taking the difference.

The shifts $E(B)$ are plotted in Fig. 4.1 for the ^{87}Rb and Cs ground-state hyperfine manifolds. We calculate the shifts for fields up to 250 G using Eq. (4.1), with $A_{\text{hfs}}^{\text{Rb}} \approx h \times 3.41$ GHz and $A_{\text{hfs}}^{\text{Cs}} \approx h \times 2.30$ GHz [196]. The degeneracy of m_f sublevels is lifted in an external magnetic field, which at

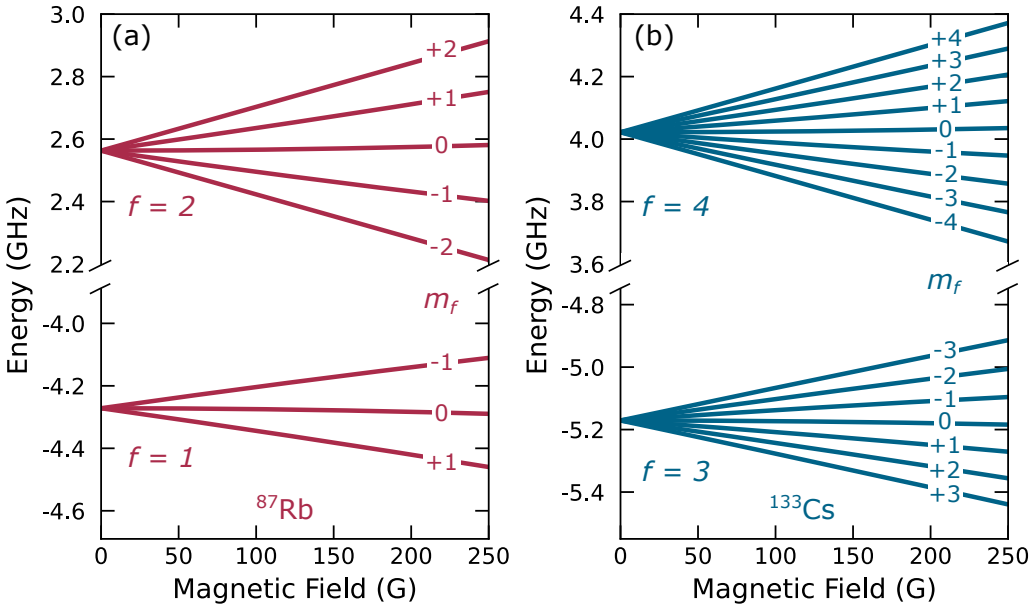

Figure 4.1: Energy shift of m_f sublevels in an external magnetic field calculated using the Breit-Rabi formula, Eq. (4.1), for (a) ^{87}Rb in $5^2S_{1/2}$ and (b) Cs in $6^2S_{1/2}$.

magnitudes of $\approx$ 10 G are separated by several MHz. With the degeneracy lifted, it is now possible to controllably transfer population between m_f states, as we discuss in the following sections.

4.1.2 Hyperfine Pumping and Internal State Detection

The simplest optical pumping scheme is to prepare the ensemble in either the upper or lower hyperfine manifold (but no specific m_f), which can be achieved using the 6 MOT beams. Using Cs in the 938 nm tweezer as an example, the atomic population can be pumped to the lower $f = 3$ manifold by applying a pulse of cooling light resonant with the $f = 4 \rightarrow f' = 5$ transition, which clears population from the $f = 4$ manifold, taking advantage of the small $\approx 1/10^4$ probability for atomic population to leak from the cooling cycle. Atoms may instead be transferred to the upper $f = 4$ manifold using a pulse of repump light resonant with the $f = 3 \rightarrow f' = 4$ transition, which clears the population from the $f = 3$ manifold. In both cases, a pulse with $\sim$ 200 μW per beam lasting 5 ms is sufficient to saturate the state preparation fidelity.

To quantify and optimise the OP efficiency, it is necessary to develop a

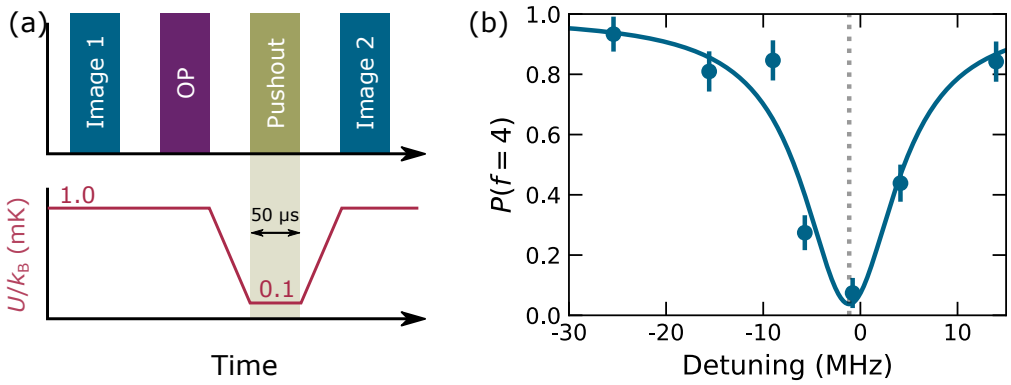

Figure 4.2: State-selective imaging. (a) Timing diagram: after verifying the tweezer occupancy in Image 1, the internal state is prepared using an optical pumping pulse. The trap depth is lowered by a factor of 10, whereupon the pushout beam expels atoms in the upper hyperfine manifold. Image 2 maps the hyperfine state onto a binary survival event. (b) Optimisation of the Cs pushout beam detuning from the $f = 4 \rightarrow f' = 5$ transition for a 938 nm tweezer of depth 100 μK. The detuning is defined with respect to the field-free $4 \rightarrow 5$ transition.

method for probing the internal state of an atom. Such a method will be also useful for detecting subsequent changes in the internal state after optical pumping (see 4.1.5). We utilise a 'pushout' detection scheme to measure the fraction of Cs atoms populating the lower $f = 3$ manifold [197]. A circularly polarised pushout beam, roughly aligned (see Fig. 2.19) to an external magnetic field and resonant with the $f = 4 \rightarrow f' = 5$ transition, is used to eject any atom in $f = 4$, while preserving those in $f = 3$ which are ≈ 9.2 GHz detuned and so dark to the pushout beam. The external magnetic field of 4.78 G defines a quantisation axis along the $+x$ (+N/S) direction. The pushout beam induces loss through a combination of the radiation pressure force and recoil heating. When the atom is fluorescence imaged at the end of the sequence, population in $f = 3$ is mapped onto atom survival and population in $f = 4$ is mapped onto atom loss. The pushout protocol for Rb is similar, sharing the same optical path, and ejecting atoms from $f = 2$.

The pushout beam must induce rapid loss to avoid off-resonant scattering of pushout photons, which can cause transfer between hyperfine manifolds, reducing the pushout detection fidelity (section 4.1.5). To this end, the 938 nm tweezer is lowered to a depth of $U/k_B \sim 100$ μK. Furthermore, the scattering rate of the pushout beam is maximised by setting the frequency

Table 4.1: Hyperfine optical pumping fidelity. The survival probabilities are calculated over 300 shots of the experiment. With the pushout beam applied, the high survival probability of $f = 3$ atoms, but low survival of $f = 4$ atoms, confirms that the pushout beam is dark to the $f = 3$ state and ejects most of the $f = 4$ population.

Manifold	Pushout	Survival Probability
$f = 3$	On	$0.97^{(+0.03)}_{(-0.03)}$
$f = 3$	Off	$0.98^{(+0.02)}_{(-0.03)}$
$f = 4$	On	$0.02^{(+0.03)}_{(-0.02)}$
$f = 4$	Off	$1.00^{(+0.00)}_{(-0.03)}$

resonant with the $f = 4 \rightarrow f' = 5$ transition, as shown in Fig. 4.2(c) for atoms optically pumped to $f = 4$. The optimal free-space detuning is $-1.0(1)$ MHz, consistent with the expected light shift for a 938 nm tweezer with depth 100 μK. The pushout beam has a $1/e^2$ waist $w_0 = 0.95$ mm, with an optical power of 50 μW and is applied for 500 μs.

The Cs hyperfine OP fidelity is verified using the pushout beam. The ensemble is pumped to $f = 3$ or $f = 4$ and the survival probability is measured with and without a pushout pulse. The results, presented in table 4.1, confirm the expectation that loss only occurs for atoms optically pumped to $f = 4$ when a pushout pulse is applied, and verify the efficacy of both the pushout and hyperfine OP pulses.

4.1.3 Optical Pumping to a Specific m_f State

It is necessary to extend the optical pumping techniques described above to prepare atoms in a specific m_f state within a hyperfine manifold f. Optical pumping to a specific m_f state relies on repeated cycles of absorption of polarised photons, which bias the change in m_f state, and spontaneous emission, to accumulate population in a target state. Typically the maximal-m_f or $m_f = 0$ states are targeted because experimentally they can be made dark to the pumping light with an appropriate optical pumping arrangement

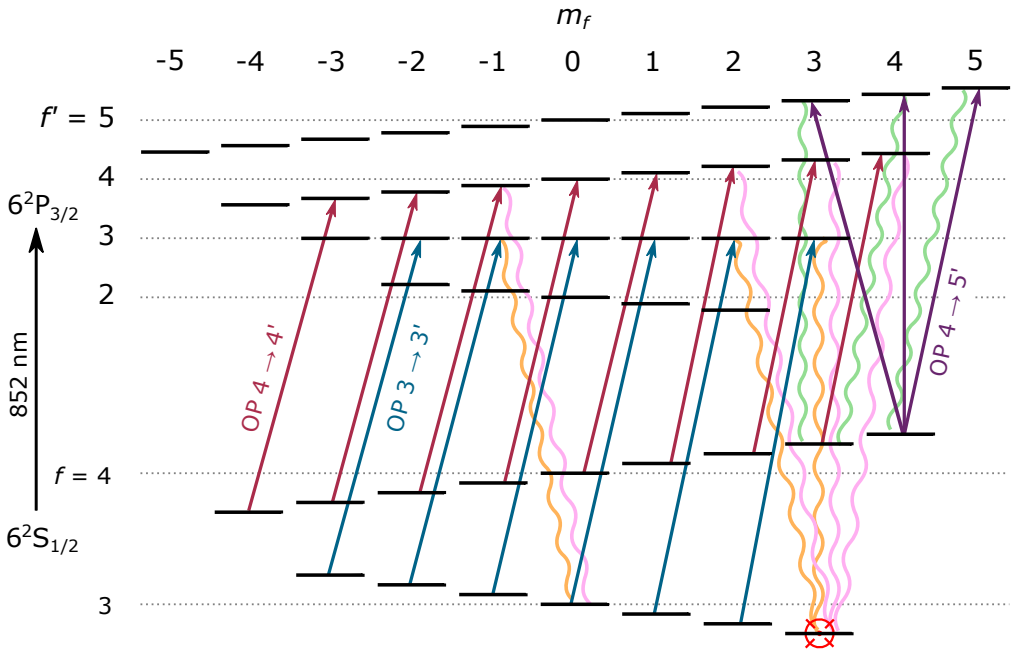

Figure 4.3: Optical pumping scheme for preparing Cs in the lowest-energy internal state ($f = 3, m_f = 3$) (red target). The Zeeman splitting of energy levels is shown qualitatively. Three OP frequencies are used (solid lines). The wavy lines indicate spontaneous decay channels, which for clarity are not all shown. OP to ($f = 3, m_f = -3$) proceeds similarly, but with the direction of the magnetic bias field reversed, or the handedness of the circularly polarised OP beams inverted.

[197, 198].

We present our scheme for optical pumping of Cs to the maximal-m_f state ($f = 3, m_f = 3$) as an example, since it is relevant to the measurements of the next chapter. A diagram of the OP scheme used is presented in Fig. 4.3, where the straight arrows represent absorption of an OP photon and wavy lines indicate spontaneous emission. For clarity, not all spontaneous emission lines are drawn. A magnetic bias field of $B_x = 4.78$ G is applied along the $+x$ axis using the N/S shim coil pair, setting the quantisation axis and lifting the degeneracy of the Zeeman sublevels. The OP beam propagates parallel to B_x (Fig 2.19) and is circularly polarised with respect to the quantisation axis. The handedness is set using a quarter waveplate so that the OP beam drives σ^+ transitions ($\Delta m_f = +1$).

The OP beam is composed of two overlapped laser frequencies launched from the same optical fibre. Preparation of the laser frequencies was de-

scribed in section 2.5.3. The first frequency (blue arrows) is resonant with the $f = 3 \rightarrow f' = 3$ transition, exciting atoms from $f = 3$ and increasing m_f by 1. Selection rules allow spontaneous decay back to $f = 3$, where the OP cycle repeats or to $f = 4$. The second OP frequency (red arrows) is resonant with the $f = 4 \rightarrow f' = 4$ transition and excites atoms from $f = 4$, increasing m_f by 1. Again, selection rules allow decay to $f = 3$ or $f = 4$. Applied continuously together, these beams transfer the atom to the maximal-m_f states $(f = 3, m_f = 3)$ and $(f = 4, m_f = 4)$, which are dark to the OP light, since the optical pumping light cannot induce σ^+ transitions from these states. To clear the population from $(f = 4, m_f = 4)$, we use the 6 MOT beam paths to apply light resonant with the $f = 4 \rightarrow f' = 5$ transition. Since the polarisation is not well-defined with respect to the quantisation axis π, σ^+ and σ^- transitions to $f' = 5$ may all occur (purple arrows), whereafter the atom may decay to $(f = 4, m_f \neq 4)$ and subsequently be optically pumped to $(f = 3, m_f = 3)$.

The OP beam focuses to a $1/e^2$ waist of $w_0 = 0.6$ mm at the optical tweezers and contains 3 μW of OP light resonant with the $f = 3 \rightarrow f = 3'$ transition and 9 μW of repumping light resonant with the $f = 4 \rightarrow f' = 4$ transition. 200 μW of $4 \rightarrow 5'$ repumping light is used per MOT beam.

Optical pumping to the $(f = 3, m_f = 3)$ state is optimised using 'depump'-type measurements. In such measurements, after the OP stage to $(f = 3, m_f = 3)$, a pulse of 'depump' OP light resonant with only $f = 3 \rightarrow f' = 3$ is applied, followed by a pushout pulse. This tests the darkness of the target state to the OP light: for example, if the OP polarisation is impure, there will be some probability to drive σ^- and π transitions, causing depumping from $(f = 3, m_f = 3)$ and some population to accumulate in $f = 4$. Purer polarisation and better alignment of the OP beam to the magnetic field results in a darker $(3, 3)$ state which maps onto a higher survival probability after the pushout pulse.

In Fig. 4.4(a) the U/D and E/W shim fields are varied for a depumping time of 1.6 ms. When the fields are optimal, corresponding to cancellation of stray fields and good alignment of the bias field B_x to the OP beam, the $(3, 3)$ state is dark to the OP light and the survival probability peaks. Similarly, the survival probability peaks when the quarter waveplate angle of

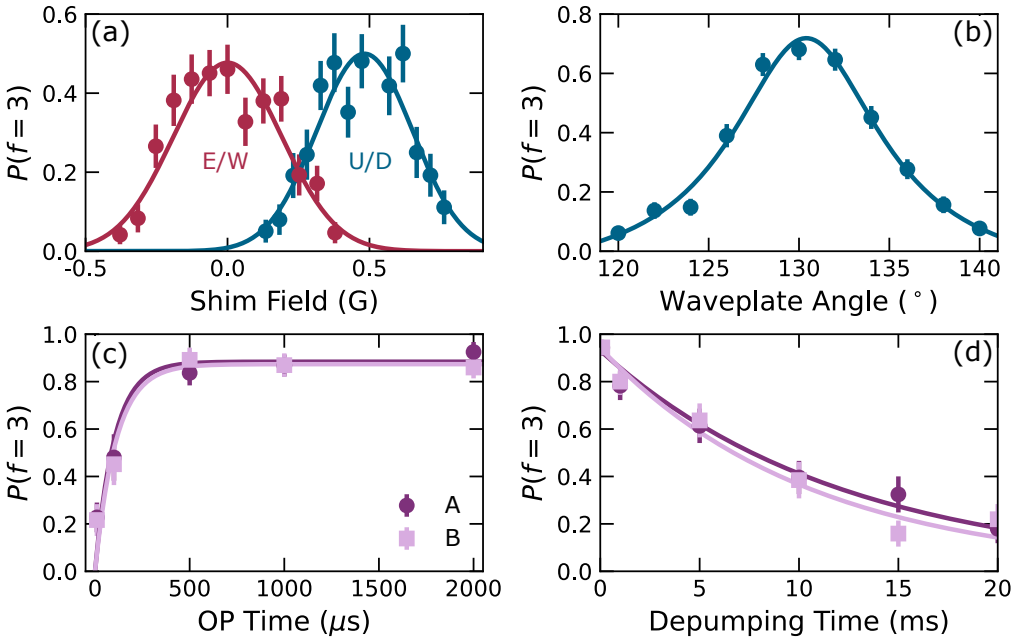

Figure 4.4: Optimisation of optical pumping to $(f = 3, m_f = 3)$. (a) Cancellation of external fields along the E/W and U/D axes of the chamber (y and z axes respectively). (b) Alignment of the OP beam quarter waveplate. (c) Measurement of the optical pumping time after optimisation. (d) Measurement of the depumping time after optimisation.

the OP beam is optimal, shown in Fig. 4.4(b), corresponding to pure circular polarisation.

Measurements of the optical pumping time and depumping time after optimisation are shown Fig. 4.4(c)&(d) respectively. The measurement was performed simultaneously for an array of two tweezers labelled A and B separated by 4.5 μm (see section 4.2.3). The optically pumped fraction $P(f = 3)$ saturates to less than one because of spontaneous Raman scattering of tweezer photons (section 4.1.5) which occurs before pushout. When optimal, the optical pumping rate is much greater than the depumping rate. The average $1/e$ OP and depump times extracted from the exponential fits are $\tau_{\mathrm{OP}} = 0.11(4)$ ms and $\tau_{\mathrm{DP}} = 12(1)$ ms respectively. In the steady state, depumping competes against optical pumping, so that the state preparation fidelity is given by the ratio $(1 - \tau_{\mathrm{DP}}/\tau_{\mathrm{OP}})$. We determine an OP fidelity to prepare one atom in $(3, 3)$ of 0.99(1) and a probability to prepare both simultaneously of 0.98(2).

Optical pumping to $(f = 3, m_f = -3)$ is achieved by inverting the direc-

tion of the magnetic field, or by reversing the handedness of the circularly polarised OP beam, so that $\Delta m_f = -1$ transitions are driven instead. Pumping instead to $(f = 4, m_f = 4)$ can be implemented by replacing the $4 \rightarrow 5'$ cooling beams with the repump beams which drive $f = 3 \rightarrow f' = 4$ transitions instead. The OP scheme to pump ^{87}Rb to the maximal-m_f states $(f = 1, m_f = 1)$ and $(f = 2, m_f = 2)$ is very similar, with a change of laser wavelength to $\sim$ 780 nm. Pumping to $m_f = 0$ states has also been demonstrated, which is desirable for applications where Zeeman-insensitivity is required [198]. Pumping to $m_f = 0$ is achieved using two linearly polarised beams. Since optical transitions with $\Delta m_f = 0$ are forbidden by selection rules, the $m_f = 0$ sublevel of the lower hyperfine manifold is a dark state.

4.1.4 Microwave Control

The ground-state hyperfine manifolds of Rb and Cs have a frequency separation of 6.8 GHz and 9.2 GHz, which allows transitions between them to be driven using microwave radiation. Microwave transfer is useful for probing states that are not directly accessible by optical pumping (i.e. states where $|m_f| \neq 0, f$). Furthermore, since the microwave frequency is electronically generated, it is well known and so can be used to measure magnetic field-dependent hyperfine transition frequencies to high precision, in turn allowing precise calibration of magnetic field coil pairs.

Resonant microwave radiation satisfying the selection rules will couple two hyperfine states $|1\rangle = |f, m_f\rangle$ and $|2\rangle = |f', m_f'\rangle$, inducing Rabi oscillations of the atomic population between them. When the microwaves are tuned to resonance, the atom-field coupling strength is described by the Rabi frequency Ω_R, which is the frequency of oscillation of the population [174, 195]:

$$\Omega_\mathrm{R} = \sqrt{\frac{I_\mathrm{MW}}{c\epsilon_0\hbar^2}} \langle 2| \mathbf{d} \cdot \hat{\sigma}_q |1\rangle , \tag{4.2}$$

where I_MW is the microwave intensity incident on the atom, and $\langle 2| \mathbf{d} \cdot \hat{\sigma}_q |1\rangle$ is the electric dipole matrix element of the transition, explained further in section 4.1.5.

The length scale of the science cell and surrounding apparatus is comparable

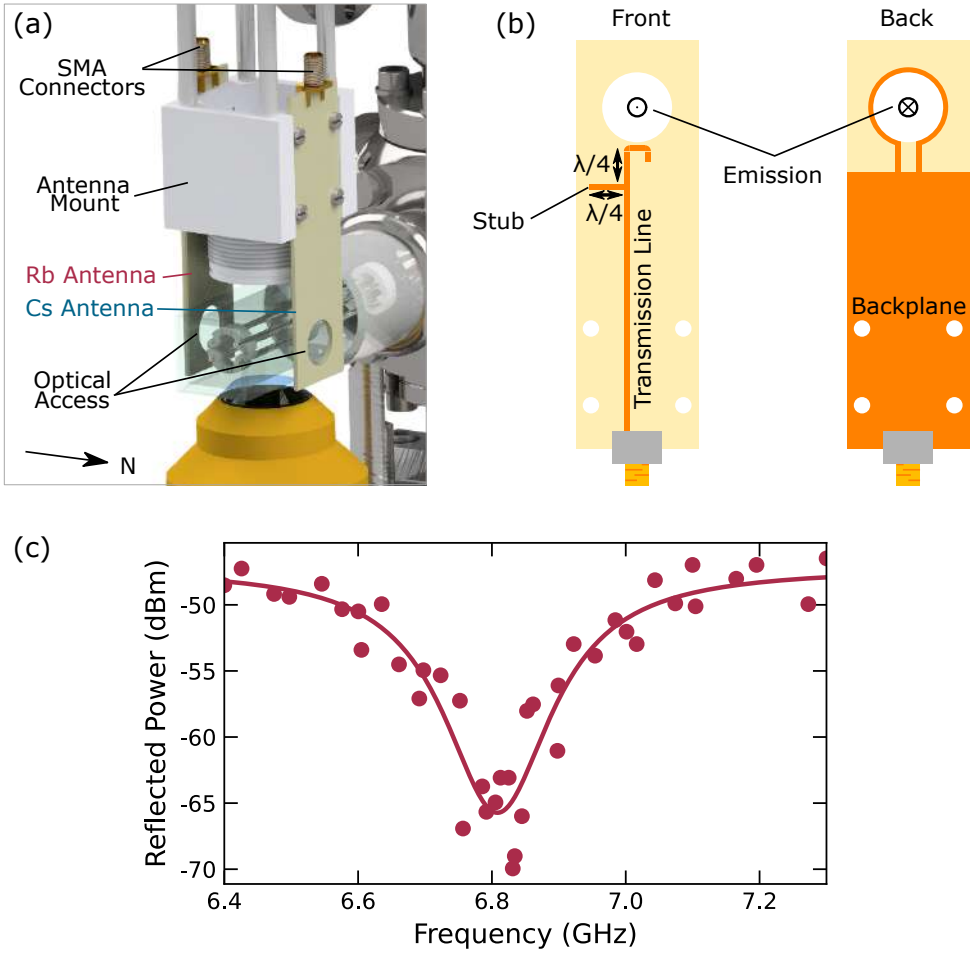

Figure 4.5: Microwave antennas used in the experiment. (a) Render of the antennae configuration. The holes in each antenna allow for optical access along the N/S axis of the cell for the MOT, OP and pushout beams. Emission of circularly polarised microwaves is centred on the holes, which are centred on the N/S axis. (b) Schematic of an antenna. Microwave power is fed to the antennas via GHz-frequency SMA cables. Interference from stub reflections results in circular polarisation. The copper backplane enhances the directionality of emission out of the front side of the antenna. (c) Microwave reflectance spectrum after stub-tuning the Rb antenna to a resonance frequency of 6.8 GHz.

to the microwave wavelength, and modelling of antenna near-field emission profiles is a complex affair [199], so estimation of the effect on I_{MW} of microwave reflection, absorption and interference in our system is intractable. The goal is therefore to maximise Ω_{R} by maximising the intensity output by an antenna. The output intensity increases with the input power from the microwave source and diminishes with distance from the antenna. The effective

intensity depends on the microwave polarisation, since the narrow linewidth means that only those microwaves with the correct polarisation will be resonant with a hyperfine transition. An antenna must therefore be situated as close to the science cell as possible and produce majority-circularly-polarised microwaves with good output coupling.

We use separate antennas for Rb and Cs. Their design is based on those presented in refs. [200, 201]. The planar shape allows for the antennas to be mounted close ($\approx$ 2 mm) to the science cell and $\approx$ 12 mm from the optical tweezers, as shown in Fig. 4.5(a). The design is only feasible due to large 12 mm-diameter holes in the antennas which provide optical access for the MOT, OP and pushout beams. A schematic of the antenna design is presented in Fig. 4.5(b). The antennas are manufactured from standard printed circuit board (PCB), where the designs are produced by milling away the thin copper layers on either side. A copper wire stub of length $\approx \lambda/4$ is soldered onto the transmission line at a distance $\approx \lambda/4$ from the hook, where λ is the microwave wavelength. Interference of signals reflected from the stub and the hook produces circularly polarised microwaves [202, 203] which are emitted from the antenna, centred on the hole. The copper backplane reflects microwaves so that emission is directed out of the front face, which points towards the atoms.

Each antenna is stub-tuned to maximise microwave emission at the desired frequency. The stub length is adjusted while monitoring the power reflected from the antenna on a spectrum analyser. Low reflectance indicates better outcoupling of microwaves from the antenna. A measurement of the microwave reflectance profile is presented in Fig. 4.5(c) for the Rb antenna after optimisation by stub-tuning. The feature centre of 6.808(6) GHz indicates maximum emission occurs at frequencies resonant with the Rb $5^2S_{1/2}$ hyperfine splitting, and the bandwidth of 0.20(3) GHz is sufficiently broadband to access the different m_f states in bias fields up to $\approx$ 50 G. The Cs antenna is similarly stub-tuned to a frequency of 9.2 GHz.

The antennas are driven using an Agilent N5183B analogue microwave source connected to a Mini-Circuits ZVE-3W-183+ amplifier which amplifies the signal to around 34 dBm. The frequency resolution of the source is 1 mHz.

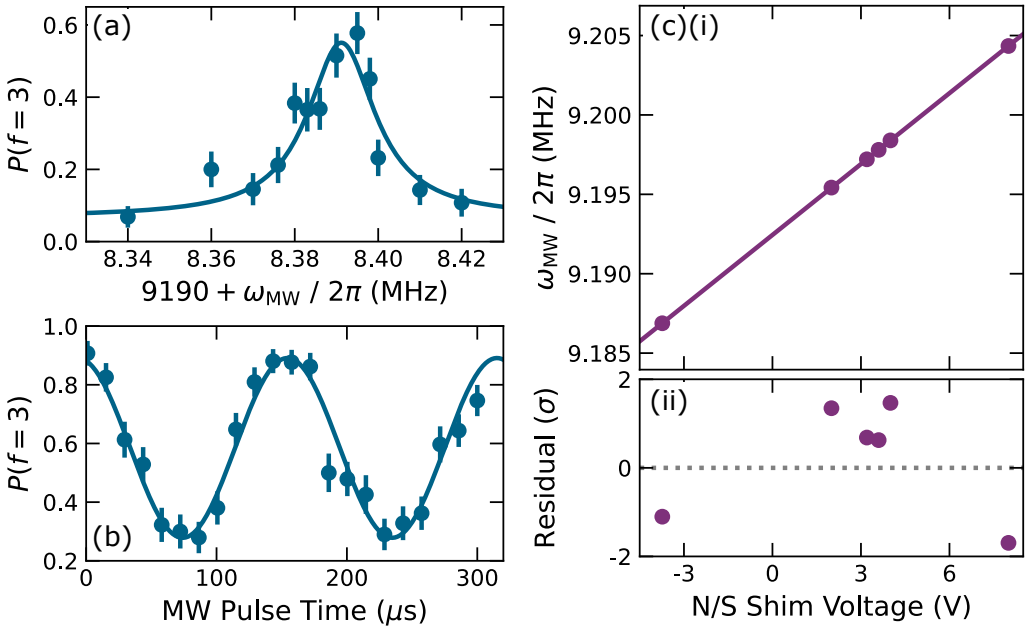

Figure 4.6: Microwave transfer of Cs. (a) Location of the Cs $(3,3) \rightarrow (4',4')$ spin-stretched transition. (b) Microwave Rabi oscillations on the $(3,3) \rightarrow (4',4')$ transition. (c)(i) Calibration of the North/South shim coil pair. The solid line is a plot of the Breit-Rabi formula. (ii) Residual of the data and Breit-Rabi formula.

The source, antenna and amplifiers are connected using coaxial cables[1] rated for frequencies up to ≈ 20 GHz to mitigate power loss.

Microwave transfer of Cs in a 938 nm tweezer is demonstrated in Fig. 4.6(a) at a magnetic bias field of 2.35 G applied along the +N/S axis. After optically pumping to $(f = 4, m_f = 4)$, a 5 ms microwave pulse is applied, followed by a pushout pulse which ejects $f = 4$ atoms. When tuned to resonance, the microwaves induce Rabi oscillations on the $(3,3) \rightarrow (4',4')$ spin-stretched transition. The pulse time is sufficiently long that any Rabi oscillations dephase, distributing the ensemble approximately equally across hyperfine manifolds. The pushout pulse maps any resonant oscillations onto an increase in the survival probability. The centre of the feature is known to 1 kHz from the Lorentzian fit and the width is 19(1) kHz. The width indicates magnetic field noise of ~ 8 mG, or 0.3 %.

Setting the frequency of the microwave source to resonance, in Fig. 4.6(b)

[1]Such as Minicircuits 141-1.5MSM+

we demonstrate Rabi oscillations between the maximal-m_f states $(3,3)$ and $(4',4')$. We extract a Rabi frequency driven with the PCB antenna of $\Omega_R/2\pi = 6.3(1)$ kHz with a $1/e$ damping time of > 1 ms. Damping of the oscillations is due to decoherence of the single-atom ensemble which can be caused by effects such as magnetic field noise, differential Rabi frequencies depending on the motional level [197] and spontaneous Raman scattering (section 4.1.5). The contrast of the Rabi oscillations is less than the value expected from the OP fidelity because of spontaneous Raman scattering from the 938 nm tweezer occurring between the OP and microwave transfer stages.

We use the well-known frequency of the applied microwaves to calibrate the N/S shim coils, as shown in Fig. 4.6(c). The frequency measurement of the Cs $(3,3) \rightarrow (4',4')$ transition presented in subplot (a) is repeated as a function of the voltage set-point applied to the bipolar current source driving the N/S shim coils. The frequency measured is converted to a magnetic field at the tweezers using the Breit-Rabi formula presented in Eq. (4.1). From the fit, we determine that the coils produce 0.6068(2) G V^{-1} with a field offset of $-0.0784(1)$ G. We note that the bias and jump coils were similarly characterised, although instead using Raman spectroscopy to measure the splitting of the $(3,3) \rightarrow (4',4')$ transition (section 2.4).

4.1.5 Spontaneous Raman Scattering

Atoms confined in a far-detuned optical tweezer experience spontaneous photon scattering of the tweezer light. In this process, a tweezer photon is absorbed, promoting the atom to a virtual excited state (black arrow in Fig. 4.7(a)), before the atom decays and re-emits a photon. If the atom decays to its original state, emitting a photon of the same energy as the absorbed photon, it is termed Rayleigh scattering (green arrow in Fig. 4.7(a)). If instead the atom decays to a state of different f and/or m_f quantum number, emitting a photon of different wavelength, it is termed Raman scattering (red arrows). Photon recoil from both processes results in recoil heating. At large detunings Δ from any atomic resonance, Rayleigh scattering dominates since it scales as $1/\Delta^2$ compared to Raman scattering, which scales as $1/\Delta^4$ [97, 204]. It is desirable to suppress Raman scattering because it effectively

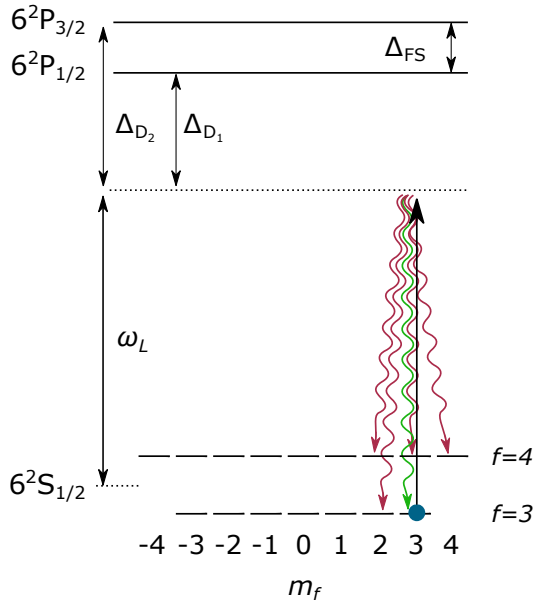

Figure 4.7: Photon scattering of a Cs atom prepared in the $(3, 3)$ state. Absorption of a photon (black arrow) causes excitation to a virtual level (dotted line), and results in Rayleigh scattering back to the initial state (green arrow) or Raman scattering to a different final state (f', m'_f) (red arrows).

reduces the state preparation fidelity, with a probability to change (f, m_f) that increases with the hold time in the tweezer.

When the laser is far-detuned with respect to the excited state hyperfine splitting Δ_{HFS}, spontaneous Raman scattering of an atom in an initial state $|f, m_f\rangle$ to a final state $|f', m'_f\rangle$ may occur via several pathways, so that the transition amplitude must be summed over the intermediate excited states $|i\rangle$. The scattering rate summed over all pathways can be calculated using the Kramers-Heisenberg formula[2] [175, 204, 205]:

$$\Gamma_{|f,m_f\rangle\to|f',m'_f\rangle} = \frac{1}{c\epsilon_0\hbar}\frac{I}{\mu_{\mathrm{ss}}^2}\left|\sum_{i=D_1,D_2}\sum_q \sqrt{\Gamma_i}\frac{\langle f', m'_f|\,\mathbf{d}\cdot\hat{\sigma}_q\,|i\rangle\,\langle i|\,\mathbf{d}\cdot\hat{\sigma}_{q=0}\,|f, m_f\rangle}{\Delta_i}\right|^2, \tag{4.3}$$

where Δ_i is the tweezer detuning from the intermediate state, Γ_i is the radiative linewidth of the intermediate state, and I is the laser intensity. The terms

[2]The Kramers-Heisenberg formula is an extension of Fermi's Golden Rule to second-order processes (i.e. 2-photon transitions), see ref. [205].

$\langle f, m_f | \, \mathbf{d} \cdot \hat{\sigma}_q \, | f', m'_f \rangle$ are dipole matrix elements, with $\mathbf{d}$ the electric dipole operator. $\hat{\sigma}_q$ denotes the polarisation of light with respect to a magnetic bias field, where $q = 0, +1, -1$ for linear, right circular and left circular polarisation respectively. $q = 0$ for the initial excitation, but must be summed over for decays from the intermediate state. $\mu_{\text{ss}} = \langle 3, 3 | \, \mathbf{d} \cdot \hat{\sigma}_{-1} \, | 4, 4 \rangle$ is the dipole matrix element for the spin-stretched transition.

The total scattering rate of an atom prepared in an initial state $|f, m_f\rangle$ to any other state is obtained by summing Eq. (4.3) over all final states, $\Gamma_{\text{tot}} = \sum \Gamma_{|f,m_f\rangle \to |f',m'_f\rangle}$. The total scattering rate calculated in this way agrees to within 0.5 % with the rate obtained using Eq. (3.7). The total scattering rate is the sum of the Rayeigh and Raman scattering rates:

$$\begin{aligned} \Gamma_{\text{tot}} &= \Gamma_{\text{Rayleigh}} + \Gamma_{\text{Raman}} \\ &= \Gamma_{\text{Rayleigh}} + (\Gamma_{\text{Raman}}^{\Delta f = 0} + \Gamma_{\text{Raman}}^{\Delta f \neq 0}). \end{aligned} \tag{4.4}$$

In the second line, the Raman scattering rate has been separated into the fraction of Raman scattering events which result in a change in f, and the remainder where only m_f is changed. Decomposition of the spontaneous Raman scattering rate is useful, because experimentally only changes in f can be detected using the state-sensitive detection scheme described in section 4.1.2. Spontaneous Raman scattering causing a change of f results in so-called "spin-relaxation", which is a time-dependent redistribution of the ensemble's hyperfine quantum number [206].

To calculate the Rayleigh or Raman scattering rates for an atom prepared in (f, m_f), Eq. (3.7) is summed over all final states which fulfil the conditions on f and m_f. The decomposed rate is presented in table 4.2 for a Cs atom in a 938 nm tweezer of measured waists $\{w_x^{938}, w_y^{938}\} = \{1.29(4), 1.06(2)\}$ μm and power of 1 mW. For an atom prepared in the maximal-m_f state, it can be seen that ≈ 10 % of events are Raman scattering, of which ≈ 90 % result in a change in f. For an atom prepared in $f = 3$ but no specific m_f, we calculate the rates by averaging over an evenly-weighted m_f distribution. In this case, only the fraction of f-changing to f-preserving Raman transitions is modified. $\Gamma_{\text{Raman}}^{\Delta f \neq 0}$ is highest for the maximal-m_f states: the $|m_f| = 0, 1$ contributions are much lower, therefore reducing the average rate.

Table 4.2: Decomposition of the total calculated scattering rate into Rayleigh and Raman scattering fractions, for Cs in a 938 nm tweezer. The Raman scattering rate is further separated into rates for which $f' = f$ and $f' \neq f$. In the first column, the rate is calculated for a Cs atom prepared in $|f = 3, m_f = 3\rangle$. In the second, the average scattering rates for the $f = 3$ hyperfine manifold are calculated by averaging the rates for each m_f, assuming an equal weighting. The errors are calculated using the measured uncertainties on the beam waists.

	Rate (Hz)	
Scattering	$\|f = 3, m_f = 3\rangle$	$f = 3$
Γ_{tot}	8.9(5)	8.9(5)
Γ_{Rayleigh}	8.0(4)	8.0(4)
Γ_{Raman}	0.93(5)	0.93(5)
$\Gamma_{\text{Raman}}^{\Delta f=0}$	0.09(5)	0.23(1)
$\Gamma_{\text{Raman}}^{\Delta f\neq 0}$	0.84(4)	0.70(3)

For detunings much larger than the fine and hyperfine splittings, the Raman scattering amplitudes via the $6^2P_{1/2}$ and $6^2P_{3/2}$ states in Eq. (4.3) nearly cancel, whereas the amplitudes of Rayleigh processes sum [175]. This results in the respective $1/\Delta^2$ and $1/\Delta^4$ scalings of the Rayleigh and Raman scattering. Increasing the tweezer detuning therefore reduces the recoil heating rate and the spin-redistribution rate.

A measurement of the spin redistribution time for Cs confined in a 938 nm tweezer is presented in Fig. 4.8(a). After optically pumping (section 4.1.2) the ensemble to $f = 3$ (red squares) or to $f = 4$ (blue circles), the atom is held for a variable time in the tweezer before a pushout pulse ejects atoms in $f = 4$, preserving the $f = 3$ population. Spontaneous Raman scattering from the optical tweezer results in decay of atoms from the initial hyperfine manifold with an exponential dependence. At long hold times both curves, which measure *only* the $f = 3$ population, are expected to saturate to $7/16 = 0.44$ (dotted line) in the absence of background loss, which is estimated by considering the ratio[3] of m_f levels in each hyperfine manifold. The average of the fitted $1/e$ decay times (solid lines) is 0.5(1) s.

[3]There are $(2f + 1)$ Zeeman sublevels (m_f) available per f manifold.

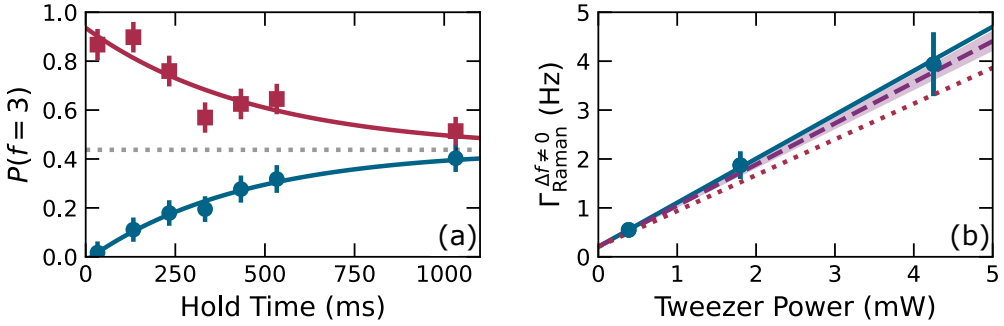

Figure 4.8: Spontaneous Raman scattering of Cs in a 938 nm optical tweezer (a) Spin redistribution of Cs in a 938 nm tweezer. (b) Measured rate of f-changing spontaneous Raman scattering as a function of tweezer power (blue points). The dashed line shows the expected rate for atoms in $(f = 3, m_f = 3)$, where the shaded region is the error estimated using the error on the tweezer waists. The dotted line shows the expected rate for an ensemble pumped to $f = 3$ and equal population in each m_f. Both theory lines are adjusted to match the non-zero offset of the data.

We investigate the power-dependence of $\Gamma^{\Delta f\neq 0}_{\text{Raman}}$ in Fig. 4.8(b) by performing the redistribution measurement of (a) for atoms pumped to $f = 3$ at multiple tweezer powers. $\Gamma^{\Delta f\neq 0}_{\text{Raman}}$ is given by the inverse of the fitted $1/e$ lifetime and exhibits a linear dependence on the power, with a gradient of 0.90(3) Hz per mW (solid line). The zero-offset of 0.21(2) Hz may be due to the lifetime of an atom in the tweezer and scattering of small quantities of light from other beams. The dotted line shows the expected rate for $f = 3$ atoms evenly distributed across m_f states, calculated using Eq. (4.3). The dashed line shows the expected rate for atoms prepared in the $(f = 3, m_f = \pm 3)$ states. The better agreement with the latter expectation indicates a bias in the hyperfine optical pumping to maximal-m_f states, which is unsurprising given that the 6 circularly polarised MOT beams were used to perform the optical pumping.

While useful for species-selective loading, the relatively high spontaneous Raman scattering in a 938 nm tweezer is problematic because it introduces a time-dependent decay in the state preparation fidelity. Using Eq. (4.3), we expect the Rayleigh and Raman scattering rates to be suppressed more than 100-fold in a further red-detuned 1064 nm optical tweezer, due to the favourable scaling of the rates with the detuning. In separate spin-redistribution measurements using Cs in a 1064 nm tweezer we did not resolve

state decay after a seconds-long hold time, with longer measurements limited by the finite trap lifetime. To leverage this reduction in the Raman scattering rate, we transfer Cs atoms from a 938 nm tweezer to a 1064 nm tweezer for the Feshbach spectroscopy measurements presented in the following chapter. We observed negligible spin redistribution for Rb in a 938 nm tweezer, since it is much further detuned from the Rb D_2 line.

4.2 Position Control of Tweezers & Arrays

While control and manipulation of a single atom is itself interesting, richer physics and applications may be accessed by extending the techniques described thus far to arrays of optical tweezers. Arrays of optical tweezers have been produced experimentally via several routes [9], of which two are directly relevant to this work.

Firstly, as used in this experiment, an acousto-optic deflector (AOD) may be used to split a beam into several diffracted orders [51, 102, 107, 112, 207]. 2D arrays may be achieved using a crossed pair of AODs [208–210], however only square arrays may be produced, whose sites may not be independently extinguished due to contributions from both AODs to a single tweezer. The differential frequency shift of tweezers in such an array ($\approx$ 10 MHz) can introduce an additional dephasing mechanism to some quantum metrology applications [211]. Despite these drawbacks, the short rise time ($<$ 100 ns) and position resolution afforded by AODs has made them the tool of choice for single-particle transport [103, 114, 173, 212, 213].

Spatial light modulators (SLMs) provide an alternative route to the production of truly arbitrary arrays. An SLM can imprint a phase pattern upon a beam, such that upon Fourier transformation by the tweezer objective lens [152], an arbitrary array of tweezers is formed at the focus. Several groups use an SLM to produce arbitrary 2D arrays of optical tweezers [103, 214]. Furthermore, the incredible flexibility afforded by full control of the phase profile can be used to correct aberrations and to increase the axial trap frequency of the tweezers [215]. Production of 3D arrays has even been demonstrated [104]. The principle drawback of using SLMs is their slow refresh

rate ($\approx$ 60 Hz), meaning that the arbitrary arrays may not be dynamically adjusted in real time. To circumvent this issue, several groups use a hybrid SLM / AOD scheme to shuttle atoms between SLM array sites [103, 216].

Other techniques have been used to produce arrays, such as using a digital micromirror device (DMD) to apply binary holograms to a beam [217], which achieves a similar effect to an SLM, and using a microlens array to produce grids of thousands of tweezers [218].

In this section we discuss production of a modest 1D array using an acousto-optic deflector driven by an arbitrary waveform generator. We discuss positional sweeps of the tweezers and demonstrate rearrangement of the array to enhance the loading probability for a subset of array sites.

4.2.1 The Acousto-Optic Deflector

We achieve rapid steering of a single tweezer and production of arrays of optical tweezers using an acousto-optic deflector (AOD). An AOD consists of an acoustic crystal to which a piezo-electric transducer (PZT) is bonded, as shown in Fig. 4.9(a). The transducer is driven at radio frequencies (RF) of $f_{\mathrm{RF}} \approx 100$ MHz to inject the crystal with an RF acoustic wave of wavelength Λ. The longitudinal wave produces wavefronts of compression and rarefaction within the crystal, resulting in a spatially modulated index of refraction [219].

An optical beam of wavelength λ is reflected from the successive acoustic wavefronts. When the beam is aligned to the Bragg angle θ_{B}, the path length between successive reflected rays is equal to an integer number of wavelengths and the paths constructively interfere, described by the equation [220, 221]:

$$2\Lambda \sin\theta_{\mathrm{B}} = n\lambda. \tag{4.5}$$

The incident beam experiences Bragg diffraction into multiple orders $n = 0, \pm1, \pm2, ...$ The AOD is angle-tuned to maximise power diffracted into $n = 1$, and the $n \neq 1$ orders are dumped. The fraction of optical power diffracted into the first order is termed the diffraction efficiency (DE).

The deflection of the first order beam with respect to the undeflected zeroth order beam, Θ, is twice the Bragg angle. It is typically small ($\sim$ 20 mrad)

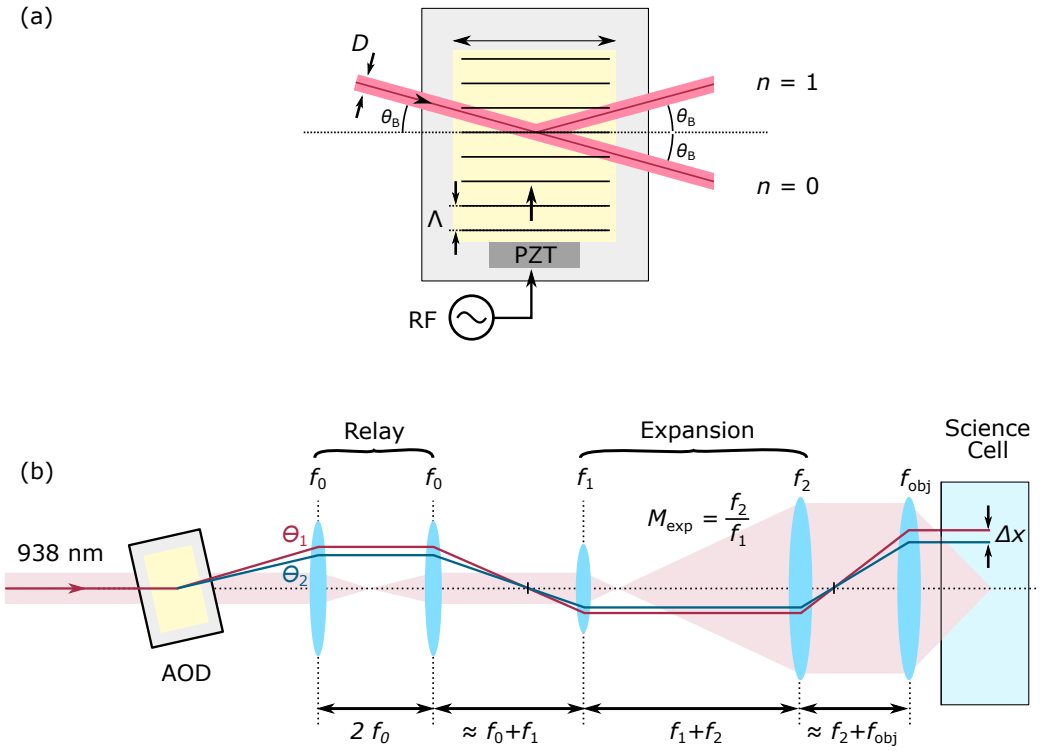

Figure 4.9: Deflection of a beam by an acousto-optic deflector. (a) Radio-frequency acoustic waves coupled into the crystal by a piezo-electric transducer (PZT) cause Bragg deflection of a transmitted laser beam. (b) Change in position of an optical tweezer caused by driving at two different RF tones (solid lines). The difference in Bragg angle maps onto the spatial separation of the tweezers Δx in the science cell. The shaded region indicates the modification to the Gaussian beam profile due to the beam-shaping optics.

so can be written:

$$\Theta \approx \frac{\lambda}{\Lambda} = \frac{\lambda}{v_s} f_{\mathrm{RF}}, \tag{4.6}$$

where in the second equality the acoustic wavelength is related to the applied RF frequency by the speed of sound in the crystal v_s. For small deflections, $\Theta \propto f_{\mathrm{RF}}$ so that the beam pointing of the first order may be controlled dynamically tuning the frequency of the RF tone.

The angular deviation imparted by the AOD results in a displacement of the optical tweezers in the focal plane Δx, which can be understood from Fig. 4.9(b). The red and blue rays indicate the path of the first order diffracted beam at two different RF frequencies, resulting in a differential deflection $\Theta_2 - \Theta_1$. The lenses with focal lengths f_1 and f_2 form a telescope

which magnifies the deflected beam by $M_{\text{exp}} = f_2/f_1$; this expansion is required to fill the objective and produce tweezers with tight waists. The relay telescope with a magnification $M_{\text{rel}} = 1$ downscales deviation from the optical axis of the angled beam incident on lens f_1, thereby reducing aberration from the lens curvature. Δx can be derived using the ray transfer matrices (see Appendix D), yielding:

$$\Delta x = \frac{\lambda f_{\text{obj}}}{v_{\text{s}} M_{\text{exp}}} \Delta f_{\text{RF}}, \tag{4.7}$$

where Δf_{RF} is the frequency difference between adjacent RF tones.

Eq. (4.7) restricts the choice of AOD: λ is set by the atomic polarisabilities as discussed in section 3.3.2, and M_{exp} and f_{obj} are fixed by the objective lens. The only flexibility is in v_s - but how should this choice be made? A suitable value may be determined by considering the long-term requirements of inducing a dipole-dipole interaction between RbCs molecules prepared in adjacent optical tweezers. In this future scenario, the tweezer spacing must be $\lesssim 1$ μm in order to achieve dipole-dipole interaction energies of $\sim h \times 1$ kHz between neighbouring molecules [3]. This close spacing requires the AOD to be driven with several tones close in frequency, which results in a frequency beat note that modulates the trapping potential. If this modulation frequency is comparable to the trap frequencies, parametric heating of the trapped atoms or molecules will occur [102], similarly to the parametric modulation measurement described in section 3.5.4.

The AOD used in this experiment is an IntraAction ATD-1803DA2.850 longitudinal-mode[4] AOD utilising a Tellerium Dioxide crystal (TeO_2), for which the speed of sound is $v_s = 4200$ m s^{-1}. This relatively high speed of sound ensures that adjacent tweezers can be spaced ~ 1 μm for a frequency spacing of ~ 3 MHz between the RF tones. This is sufficiently large with respect to the trap frequencies ($\lesssim 100$ kHz) that parametric heating is negligible (see section 4.2.5). The AOD has a nominal centre frequency of 180 MHz and a large frequency bandwidth[5] of 90 MHz.

[4]AODs more commonly operate in the shear mode, whose lower speed of sound yields higher deflections for lower Δf_{RF}. For precise control during merging, and to avoid beating, we desire *small* deflections for relatively high Δf_{RF}.

[5]The operational range of the AOD is nominally in the band 180 ± 45 MHz, beyond

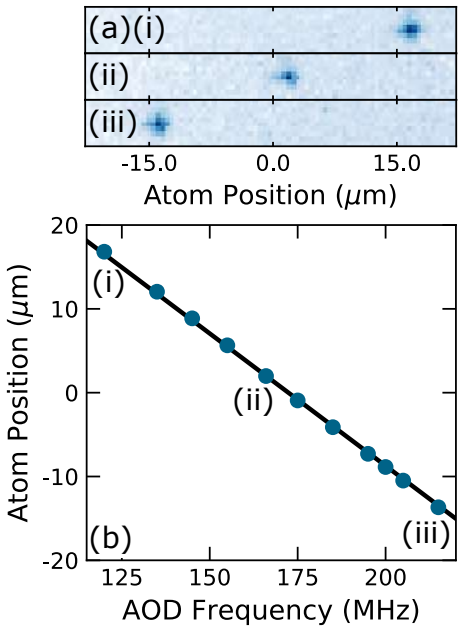

Figure 4.10: Positional control of a 938 nm optical tweezer. (a) The point-spread function observed on the EMCCD by fluorescence imaging shift position with f_{RF}. (b) Gaussian fits to the PSFs reveal a linear dependence on f_{RF}. The black line is expected dependence calculated using Eq. (4.7).

In Fig. 4.10, we demonstrate control of the tweezer position by tuning f_{RF} and verify Eq. (4.7). The position of the optical tweezer is determined by fitting a Gaussian function to a fluorescence image of a Cs atom trapped in the 938 nm tweezer, which shifts as a function of f_{RF}, as shown in Fig. 4.10(a). The fitted centres are plotted as a function of f_{RF} in Fig. 4.10(b). The points labelled (i-iii) correspond to the images in (a). The fitted dependence of the tweezer displacement on the RF frequency is 0.322(1) μm MHz^{-1}. This is similar to the value of 0.315 μm MHz^{-1} expected from Eq. (4.7), indicated by the solid line in Fig. 4.10(b). The slight discrepancy can be attributed to uncertainty in M_{exp} arising from uncertainty in the spacing of the expansion telescope.

The diffraction efficiency of the AOD varies with f_{RF}, due to deviation from the optimal Bragg angle as Θ is varied. Correspondingly, the tweezer depth will also vary with f_{RF}, leading to non-uniform arrays (section 4.2.3) and intensity modulation during sweeps of the tweezer position (section 4.2.4).

which the diffraction efficiency quickly falls to zero.

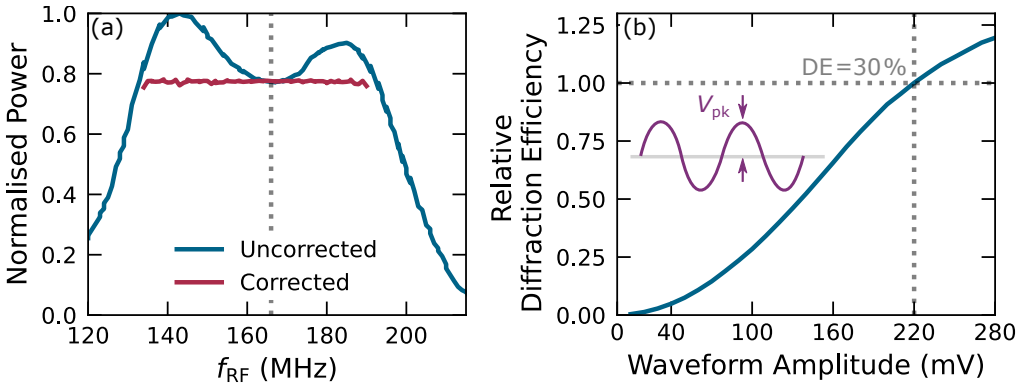

Figure 4.11: Diffraction efficiency (DE) correction of the AOD. (a) Uncorrected, the DE varies around ±10 % in the range 135 to 190 MHz. After correction, the DE is matched to the value at 166 MHz (dotted value), which is 77 % of the maximal value occurring at 142 MHz. In the range *df* the corrected diffraction efficiency fluctuates ≈ ±1 %. (b) DE at 166 MHz with waveform amplitude V_{pk} relative to the DE at 220 mV (dotted lines). Inset: definition of the waveform amplitude V_{pk}.

Nominally this effect is corrected for by the design of the AOD crystal, which is cut to produce a phased-array, so that the acoustic wavefronts are rotated as f_{RF} is varied [221]. However, it can be seen from Fig. 4.11(a) that in the frequency range 135 to 190 MHz there is still variation of ±10 % about the mean value, determined using a photodiode to measure the tweezer power transmitted through the cell. Furthermore, it can be seen that the centre frequency is offset from the expected value and is closer to $f_c' = 166$ MHz.

Inhomogeneities in the diffraction efficiency profile are corrected by tuning the amplitude of the waveform V_{pk} at discrete f_{RF}, flattening the DE response. V_{pk} is tuned at each point to match the diffraction efficiency at f_c' across the range 135 to 190 MHz. The diffraction efficiency at 166 MHz as a function of V_{pk} is shown in Fig. 4.11(b), relative to the DE for an amplitude of 220 mV, which corresponds to an absolute diffraction efficiency of 30 % (dotted lines). After correction the diffraction efficiency is significantly improved, fluctuating by ≈ ±1% (red line, Fig. 4.11(a)). This process is repeated for multiple absolute diffraction efficiencies, with the results combined to create a 2D lookup table of V_{pk} for producing flattened DE curves at each value. Intermediate V_{pk} are determined by interpolating between the measured values.

This method is effective for a single tweezer. However, when generating several tweezers intermodulation can introduce new inhomogeneities across the array [102], requiring further correction. Equalisation of tweezer arrays is discussed in section 4.2.3, where the atom response is used to iteratively tune the trap depths.

4.2.2 The Arbitrary Waveform Generator

The RF tones used to drive the AOD are produced using an arbitrary waveform generator (AWG). The AWG is used to produce time-varying waveforms which are more complex than a simple sine wave.

We use a Spectrum Instrumentation model M4i.6622-x8 AWG which is installed in a PCIe-x8 slot on the Hardware computer. There are $n_c = 4$ independently variable output channels, which may each output a digitally constructed waveform with a sample rate of up to $S_r = 6.25 \times 10^8$ samples/s (equivalently, sampling once every 1.6 ns). This is sufficient to generate frequencies near the AOD centre frequency of 180 MHz and within the operational bandwidth[6]. At present, only a single channel is used, however in future the remaining channels will be employed to drive AODs placed in the 814 nm and 1064 nm tweezer paths and to deflect a tweezer in two dimensions using a crossed AOD configuration [103].

The AWG may be operated in one of several modes, however we exclusively use "sequence replay" mode, which affords the most flexibility. In this mode, the 4 Gb total internal memory across all channels is divided into N_{seg} equally sized *segments*, where N_{seg} is restricted to be a power of 2. Each segment may be programmed independently with a time-varying waveform, as illustrated in Fig. 4.12(a). The full memory of any segment need not be used, and unused memory will be ignored during playback. The maximum possible segment duration in seconds is given by:

$$t_{\max} = \frac{4 \times 10^9}{2 \times S_r \times N_{\text{seg}} \times n_c}. \tag{4.8}$$

[6]From the Nyquist-Shannon sampling theorem [222], the sampling rate should be greater than twice the desired frequency to avoid aliasing, which is indeed the case here.

The factor of 2 arises because each sample occupies 2 bytes of memory. For a typical number of segments, $N_{\text{seg}} = 20$, $t_{\max} = 160$ ms and is not limiting. We measure a linear dependence of the upload time to the AWG on the segment duration, finding that it takes 3.83(7) ms time per ms segment length.

The waveforms assigned to each segment are generated in Python using a home-written script hosted on the Hardware computer (see section 2.9). A waveform is constructed in the time domain by assigning a voltage of up to ±2 V to each sample, with 16-bit resolution. For example, a sinusoidal wave is digitally constructed from discrete samples which are assigned voltages according to:

$$V_j(t_j) = V_{\text{pk}} \times \sin\left(2\pi f_{\text{RF}} t_j + \phi_0\right), \tag{4.9}$$

where $t_j = n_j/S_r$ is the discretised time step corresponding to the n_j'th sample, ϕ_0 is a phase and V_{pk} is the peak voltage. More complex waveforms are similarly generated in the time-domain, sampled at discrete times t_j. In the following discussion we omit the discrete sampling of the time steps for simplicity and work in terms of a continuous time variable t.

For a simple sine wave, V_{pk} is related to the root-mean-squared (RMS) voltage of the waveform by $V_{\text{pk}} = \sqrt{2} \times V_{\text{RMS}}$. The power of the RF signal is related to the RMS voltage by:

$$P_{\text{W}} = \frac{V_{\text{RMS}}^2}{R}, \tag{4.10}$$

where R is the impedance. For the AWG, amplifier, AOD and cables, $R = 50\ \Omega$.

The signal from the AWG is passed to an amplifier[7], which amplifies it by 35 dB (saturating at 34 dBm) before the signal is coupled into the AOD crystal. All components are connected by SMA cables rated for good transmission at frequencies up to several GHz. The AOD is rated for RF powers up to 2.5 W, so to protect it from excess RF powers[8] we limit the amplitude of the waveform output by the AWG to $V_{\text{RMS}} = 200$ mV.

In many experiments, controlled time-variation of the tweezer position and/or power is desired, requiring sequential playback of the waveforms

[7] Opto-Electronics AMPA-B-34-20.425.

[8] A typical failure mode caused by overdriving AODs is detachment of the PZT from the acoustic crystal.

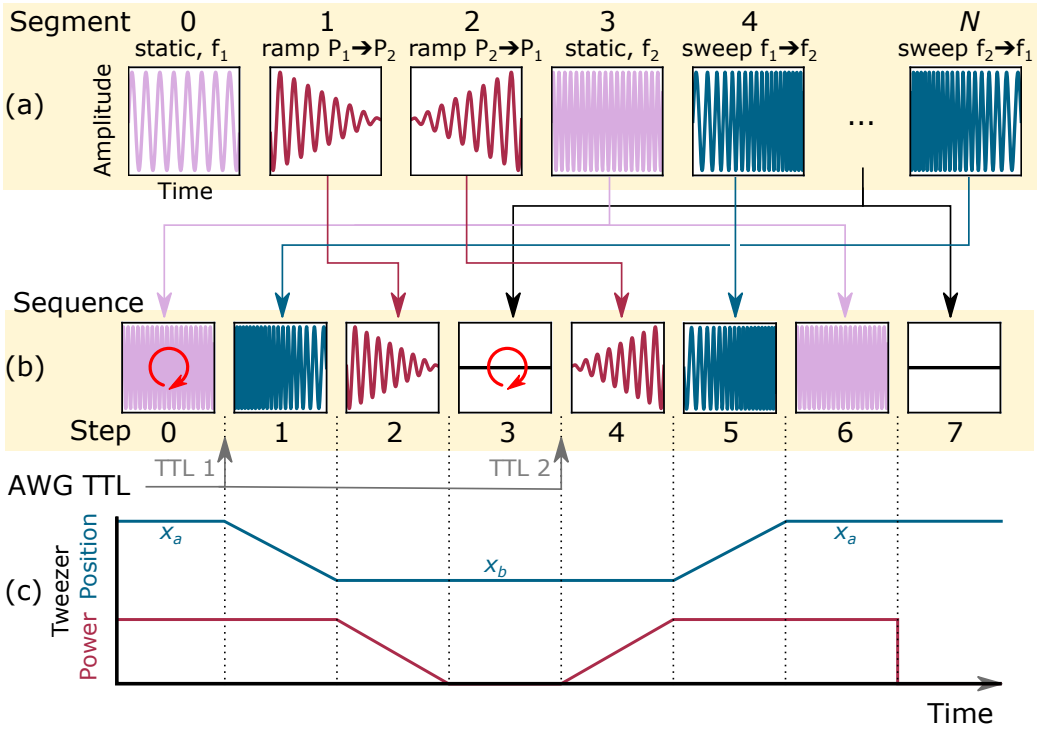

Figure 4.12: Programming of AWG segments and assembly of a waveform sequence. (a) The AWG memory is subdivided into N segments which may have different durations. The segments are independent and hold arbitrary digital waveforms. (b) Waveform sequence output by AWG. Segments are assigned to steps to form a sequence, and may be assigned to multiple steps. This 8-step example sequence shows a sequence for transferring an atom from a single tweezer into a different tweezer, not controlled by the AWG, and then retrieving it. The red arrows indicate that the corresponding segment is looped until a TTL signal is received by the AWG. (c) Position and power of the optical tweezer as a function of time induced by applying the sequence shown in (b) to the AOD.

stored in different segments. An AWG *sequence* is constructed by combining segments together in a string of *steps*, as shown in Fig. 4.12(b). A sequence may contain up to 4096 steps which may play back any of the N predetermined segments. The AWG will automatically move through the list of steps, unless it is instructed to await a TTL trigger before proceeding. In this case, the current step will be looped continuously until the TTL trigger is received.

The sequence shown in Fig. 4.12(b) results in the tweezer position and power variation sketched in Fig. 4.12(c). This sequence is an example of the merging

sequence described in section 4.3.1. On receipt of a TTL trigger, the position of a tweezer is swept from $x_a \to x_b$ by tuning the frequency of the RF tone, and then the amplitude of the tone is ramped to zero, extinguishing the tweezer. After a variable hold time which ends on a second TTL trigger, the sequence is reversed.

4.2.3 Arrays of Optical Tweezers

A static array of optical tweezers can be produced by driving the AOD with a multi-tone waveform composed of a sum of different-frequency sine waves. Each sine wave results in diffraction into the first order at slightly different Θ. The maximal possible spatial extent of the array is given by the product of the AOD bandwidth and the measured $\Delta x/\Delta f_{\mathrm{RF}}$, yielding 29 μm. The multitone RF waveform may be written as the sum of individual tones indexed by i:

$$\Psi(t) = \sum_i \psi_i(t) = \sum_i a_i \sin \phi_i(t), \tag{4.11}$$

where each tone has amplitude a_i and $\phi_i(t)$ is its time-dependent phase. For a static array the phase of each tone is simply given by $\phi_i(t) = (2\pi f_{\mathrm{RF},i})t + \phi_{0,i}$, where $0 < \phi_{0,i} < 2\pi$ is a constant phase offset.

We demonstrate production of 1D arrays of regularly-spaced optical tweezers using the AOD in Fig. 4.13(a), which shows fluorescence images of confined Cs atoms averaged over 200 experimental shots. In descending order we increment the number of tones in the waveform, adding an additional tweezer in each panel. The frequencies of the RF tones are spaced by 14 MHz, yielding trap spacings of 4.5 μm.

When driving the AOD with a multitone waveform, the RF power must still be set below the damage threshold of the AOD. For a complex sinusoid, $V_{\mathrm{pk}} \neq \sqrt{2} \times V_{\mathrm{RMS}}$, however Eq. (4.10) still holds true. The RMS voltage of a composite waveform is the sum of the RMS voltages of each tone. This introduces a constraint on the diffraction efficiency per tweezer, since the power of each tone must be divided by the number of tones to keep the power of the composite waveform below the damage threshold. Furthermore

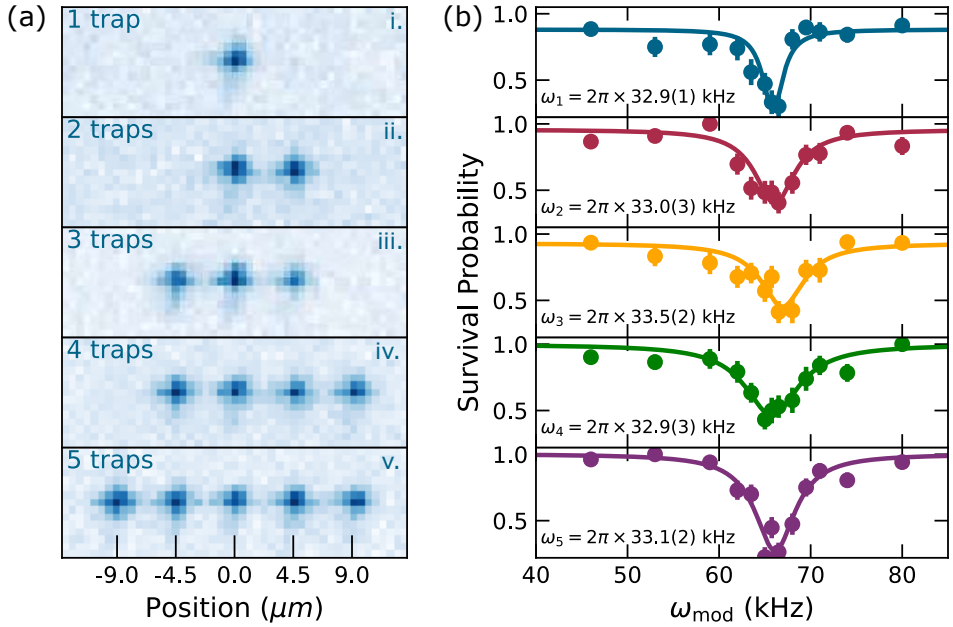

Figure 4.13: 1D array of Cs atoms in optical tweezers. (a) Images of 1D arrays of Cs atoms in optical tweezers averaged over 200 experimental shots. In the first panel, the AOD is driven at a single tone. In successive panels, a further tone is added to the composite waveform, introducing additional trapping sites. (b) Simultaneous parametric trap frequency measurement of an array of 5 iteratively balanced tweezers. Top-to-bottom correspond to the sites left-to-right in the lower panel of (a). The annotation shows the trap frequency extracted from the fit.

we set the phases of each tone to minimise the crest factor[9] of the waveform, reducing spikes in the instantaneous power [223, 224]. For the array of 5-tweezers shown in Fig. 4.13(a), the diffraction efficiency per tweezer is limited to 8 %. At present only five 938 nm tweezers can be produced using the AOD, limited by the optical power produced by the diode laser. Nevertheless, the trap depth of each array site is 0.35 mK which is sufficient to saturate the loading probability to ≈ 50 %.

For many applications with a dependence on the tweezer trap frequencies (such as RSC) it is important to equalise the powers of the tweezers in the array. Variations in the diffraction efficiency were corrected for a single tweezer in section 4.2.1. However, when producing multiple tweezers a second source of inhomogeneities becomes apparent. The AOD may act as a frequency

[9]The crest factor is simply the ratio $V_{\mathrm{pk}}/V_{\mathrm{RMS}}$, and quantifies the relative magnitude of peaks in a waveform and gives a measure of its quality.

mixer for the RF tones, producing sum and difference tones at $f_i \pm f_j$, which may mix again to produce subsequent higher-order tones [102, 112]. This "intermodulation" phenomenon can cause interference with the amplitudes of the principal tones. Intermodulation can reduce the homogeneity of an array, and in extreme cases of many tweezers may result in full extinction of trapping sites.

Site-dependent intensity variations may be corrected for by iteratively adjusting the RF amplitudes of each tweezer tone. While this can be done by imaging the array onto a camera, a more accurate method is to optimise the depths using a power-dependent atom-loss response such as the light shift Δ_{LS} or the trap frequency ω of atoms confined at each site (see Chapter 3). Since $\Delta_{\mathrm{LS}} \propto P$ and $\omega \propto \sqrt{P}$, one might expect the light shift to be the more sensitive measurement. However, in the particular case of a 938 nm tweezer, the wavelength is close to a magic trapping wavelength for the Cs^{10} D_2 transition at 932 nm [170], where $\Delta_{\mathrm{LS}} \to 0$. Many shots would then be required to distinguish small variations in Δ_{LS}, so we instead equalise the tweezer depths using the parametric modulation to measure trap frequencies.

Fig. 4.13(b) shows a simultaneous measurement of the radial trap frequencies of sites in the 5-trap array shown in (a)(v). Parametric modulation with amplitude 8 % is applied digitally by the AWG, beginning on receipt of a TTL trigger and lasting 50 ms. The trap powers have been iteratively tuned three times by adjusting the amplitudes of the RF tones corresponding to each site. The values ω_i shown are the trap frequencies measured at each site. The quoted uncertainties are the least-squared fitting errors from the Gaussian fits (solid lines). The mean trap frequency is 30.0(2) kHz, corresponding to a standard deviation of 0.5 % in the tweezer powers after iterative equalisation. This level of uniformity is expected to be sufficient for simultaneous RSC of atoms in an array, which is we expect to be tolerant to fluctuations in the trap frequency up to ≈ 10 % (see chapter 6).

As an interesting aside, rather than applying a composite waveform, it is possible to rapidly cycle through the individual RF tones to produce a time-

[10] Although 938 nm is not close to a magic wavelength for Rb, we did not use Rb for these experiments, because the polarisability is much lower than for Cs (see section 3.3.2), so a 5-trap array would not be possible using the limited optical powers at present.

averaged 'painted potential' [225–227]. A full cycle must occur faster than a tweezer oscillation period, otherwise atom loss occurs while a given site is pulsed off. The cycling frequency must also be greater than twice the trap frequency to avoid parametric heating [190]. This limits the technique to a small number of static traps due to the high radial trapping frequencies in a tweezer. By square-modulating both channels of a MOGlabs XRF agile synthesiser and combining the channels on a power splitter before applying to the AOD, it was possible to generate an array of four tweezers. Loading of Cs was observed for modulation frequencies ω_{mod} from 40 MHz to as low as 400 kHz, dropping to zero as the cycling frequency approached a parametric resonance.

4.2.4 Moving Tweezers

The position of a given tweezer in an array may be swept by tuning the frequency of the corresponding AWG tone during an experimental cycle. Experimentally, this occurs by progressing from an AWG segment containing a static RF tone to a segment containing an RF tone with varying f_{RF}.

The functional form of $f_{\mathrm{RF}}(t)$ in the time domain determines the trajectory of the tweezer $x(t)$. A single RF tone is given in the time domain by $\psi(t) = a \sin \phi(t)$. The angular frequency of the sinusoid is the time derivative of the phase: $\frac{d\phi(t)}{dt} = 2\pi f_{\mathrm{RF}}$. Therefore, $\phi(t)$ must vary as the *integral* of the desired frequency sweep profile:

$$\begin{aligned} \psi(t) &= a \sin \phi(t) \\ &= a \sin \left[\phi_0 + 2\pi \int_0^t f_{\mathrm{RF}}(\tau) d\tau \right]. \end{aligned} \tag{4.12}$$

It can easily be seen now why the phase for a static tweezer should be $\phi(t) = 2\pi f_{\mathrm{RF}} t$. An array of tweezers may be simultaneously swept by summing over tones i with arbitrary temporal profiles given by Eq. (4.12).

The simplest trajectory is a linear sweep $x_{\mathrm{lin}}(t)$, where a tweezer is moved at a constant velocity between two points, which can be achieved using a phase $\phi(t) \propto \frac{df_{\mathrm{RF}}}{dt} t^2$ (red in Fig. 4.14(a)). Although straightforward and functional, a linear sweep is problematic because it can introduce heating through two

technical effects.

Firstly, the large instantaneous acceleration at the start and end of a sweep may cause an increase in the motional state n. This effect may be suppressed by using a "minimum-jerk" (MJ) trajectory[11], which is used in similar experiments to minimise heating while sweeping the tweezer position [128]. For a sweep over distance d in a total time τ_{sw}, the minimum-jerk trajectory is plotted in blue in Fig. 4.14(a) and follows the temporal profile given by [128, 228]:

$$x_{\mathrm{MJ}}(t) = d\left[10\left(\frac{t}{\tau_{\mathrm{sw}}}\right)^3 - 15\left(\frac{t}{\tau_{\mathrm{sw}}}\right)^4 + 6\left(\frac{t}{\tau_{\mathrm{sw}}}\right)^5\right]. \tag{4.13}$$

The second potential source of heating arises due to the AOD crystal acting as an acoustic etalon, which may result in parametric heating at certain sweep speeds. The etalon has a free spectral range (FSR) $\nu_{\mathrm{FSR}} = v_{\mathrm{s}}/2L$, where L is the length of the acoustic cavity [128]. The tweezer intensity is modulated by ≈ 1 % as the RF frequency is scanned through successive etalon peaks spaced by the FSR. As discussed in section 3.5.4, intensity modulation at twice the trap frequency, $2\nu_{\mathrm{trap}}$, results in parametric heating. Parametric heating will occur if:

$$\begin{aligned}\frac{df_{\mathrm{RF}}}{dt} &= \frac{\nu_{\mathrm{FSR}}}{T/2} \\ &= 2\nu_{\mathrm{FSR}}\nu_{\mathrm{trap}},\end{aligned} \tag{4.14}$$

i.e. if f_{RF} is swept by one FSR in a time $T/2$, where $T = 1/\nu_{\mathrm{trap}}$ is the trap oscillation period. Both radial and axial resonances may be targeted, as well as weaker resonances corresponding to other harmonics of the trap frequency.

To estimate the position of parametric resonances to be avoided, we measure the FSR of the acoustic cavity. The optical power diffracted into the first order is measured as a function of f_{RF}, which is swept by 1.05 MHz near the centre frequency as shown in Fig. 4.14(b). The slow (approximately linear) background variation in intensity caused by the variable diffraction efficiency has been subtracted. From the sinusoidal fit we extract a FSR of 196 kHz, which is consistent with $v_s = 4200$ m s^{-1} and $L \approx 10$ mm.

[11] Jerk is the time derivative of acceleration, $j(t) = \dot{a}(t) = \dddot{x}(t)$.

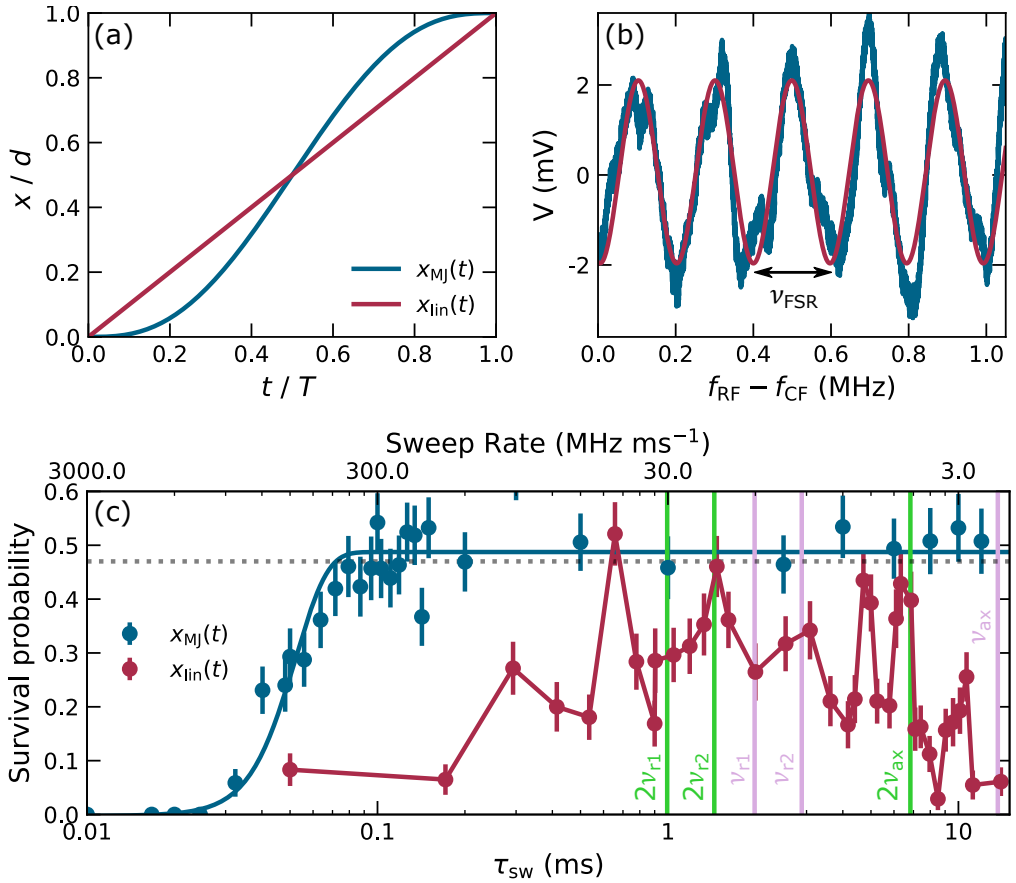

Figure 4.14: Sweeping the position of an optical tweezer. (a) Linear to minimum-jerk tweezer sweep trajectories. (b) An acoustic etalon formed in the AOD crystal results in period modulation of the diffraction efficiency as the drive frequency is swept, measured in units of milliVolts on a photodiode. (c) Comparison of heating from sweeping a tweezer tone by 30 MHz following linear (red) and minimum-jerk (blue) trajectories, as a function of the sweep time. The green (pink) lines are the estimated positions of parametric resonances at two (one) times the trap frequencies $\{\nu_{r1}, \nu_{r2}, \nu_{ax}\}$.

We examine the atom heating resulting from a linear trajectory compared to a minimum-jerk trajectory in Fig. 4.14(c). The tweezer is swept 30 MHz (9.7 μm) from its initial position in time τ_{sw} and then back in the same time. Heating induced by the sweep is mapped onto atom loss using a 40 μs release time, where the dotted line shows the background survival probability when the tweezer is not swept. In this experiment, $U/k_B = 1$ mK and the trap frequencies were $\nu_{trap,i} = \{\nu_{r1}, \nu_{r2}, \nu_{ax}\} = \{77, 53, 11\}$ kHz. For a linear sweep (red), we observe significant heating at most sweep rates probed. The vertical lines indicate the positions of resonances at $2 \times \nu_{trap,i}$ (green) and

lower harmonics resonant with $1\times\nu_{\mathrm{trap},i}$ (pink), estimated using the measured FSR. The densely-packed resonances make it difficult to select a suitable sweep speed absent of heating. In contrast, no heating is apparent using a minimum-jerk trajectory until the position is swept in times < 0.1 ms.

During a minimum-jerk sweep, the variable df_{RF}/dt means that some parametric resonances will likely be addressed. The lack of loss using a minimum-jerk sweep therefore indicates that heating for a linear trajectory is dominated by the instantaneous acceleration at the start and end of the sweep. In an independent measurement we found that for a minimum-jerk sweep in $\tau_{\mathrm{sweep}} = 0.2$ ms there was no heating for trap depths as low as 0.1 mK. Furthermore, we have measured a negligible probability of atom loss during a sweep of $P < 1/3000$. It was later found using the more precise method of Raman sideband spectroscopy [125] that a Cs atom in a 938 nm tweezer gains 0.02(2) quanta in both the axial and radial directions from a single minimum-jerk sweep [229], which is below the detection resolution of, and thus consistent with, the method presented here. Better control of the sweep rate may be achieved by implementing a "hybrid-jerk" trajectory, which may be constructed using the piecewise expression given by Liu *et al.* [128].

4.2.5 Tweezer Beating

We are now in a position to investigate the beating of RF tones which was briefly mentioned in section 4.2.1. The RF tones of two tweezers in an array will interfere if the tones are similar in frequency, beating at a frequency given by their frequency difference Δf_{RF}. If Δf_{RF} is resonant with a harmonic of a radial or axial trap frequency, parametric heating will occur (seen already in sections 3.5.4 & 4.2.4). This effect sets a lower bound on the spacing of tweezers in an array.

To probe beatnote heating, we prepare an atom in a tweezer and sweep it to a variable separation Δx from a second tweezer, where it is held for 30 ms. Heating is mapped onto loss using a 20 μs release time before probing to detect the survival probability, shown in Fig. 4.15(a). The dotted line indicates the background survival due to the release time, in the absence of a sweep. The separations Δx are scaled to the trap waist $w_0 = 1.26$ μm of the

938 nm tweezer along the sweep axis. The high survival for $\Delta f_{\mathrm{RF}} > 1$ MHz indicates little heating at larger frequency separations. For $\Delta f_{\mathrm{RF}} < 250$ kHz, there is significant heating due to beating. At these frequencies loss occurs due to parametric modulation at the closely-spaced radial and axial trap frequencies. The vertical lines show the expected resonances at twice the trap frequency $2\nu_{\mathrm{trap},i}$ (green), and at the trap frequency $\nu_{\mathrm{trap},i}$ (pink), where $\nu_{\mathrm{trap},i} = \{77, 52, 11\}$ kHz.

The expected positions of the resonances are scaled according to Fig. 4.15(b), which shows the variation in the trap frequency experienced by an atom as the two tweezers begin to overlap. The trap frequency is calculated by fitting the curvature of Gaussian double-well potentials as a function of the well separation separation. At large separations (iii), the trap frequency is ω_0, when the tweezers are overlapped (i), the intensity at the atom is double, so that the trap frequency is $\omega = \sqrt{2}\omega_0$. The minimum observed when the tweezers are spaced by one trap waist corresponds to a flat-bottomed tweezer (ii). In our system, separations < 4 MHz correspond to the two tweezers forming a single-well potential.

Interestingly, in Fig. 4.15(a) it can be seen that as $\Delta f_{\mathrm{RF}} \to 0$, the increased survival indicates a reduction in the heating rate. This is because the tweezer tones are nearly identical, so that the beatnote is low enough to avoid axial parametric resonances. The additional feature at 0.56(2) MHz may occur due to resonances with higher harmonics or to technical noise arising from e.g. the AWG. From this measurement, we determine that separations ≥ 1 MHz should be sufficient to mitigate beating. However, from Fig. 4.15(b) we determine that two tweezers should be spaced by more than at least $1w_0$ to yield distinct trapping sites. In fact, the tweezers should ideally be spaced by at least $2w_0$ (8 MHz in our system) to saturate the trapping frequencies.

4.2.6 Rearrangement of Tweezer Arrays

Rearrangement is a commonly used technique to combat the stochastic loading of a single optical tweezer [9]. The sites of a randomly loaded initial array are moved to produce a target array. By loading more tweezers than necessary, the correct initial conditions can be achieved in more experimental

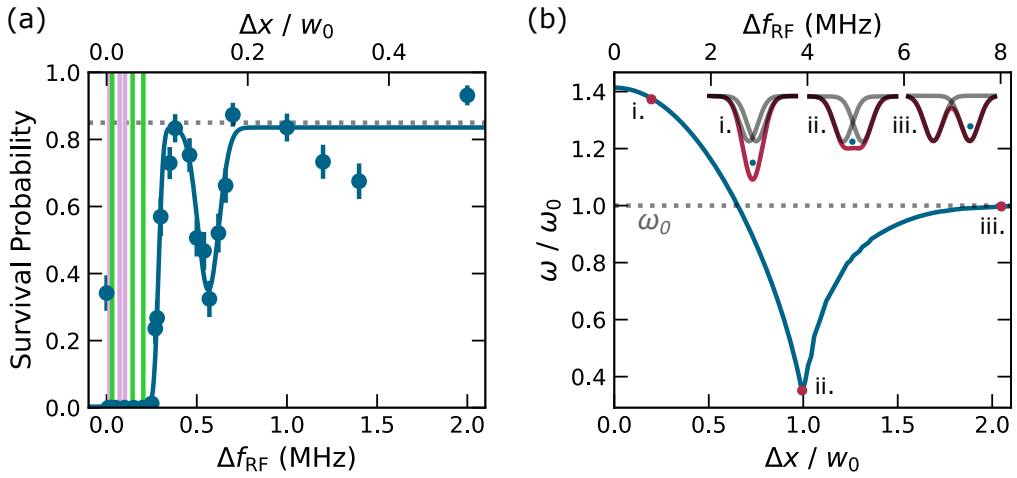

Figure 4.15: Measurement of beating between two tweezers. (a) Atom heating due to beating between two tweezers as a function of their spacing Δf_{RF}. The vertical lines indicate resonances at $\nu_{\mathrm{trap},i}$ (pink) and $2\nu_{\mathrm{trap},i}$ (green), where $\nu_{\mathrm{trap},i} = \{\omega_{\mathrm{r1}}, \omega_{\mathrm{r2}}, \omega_{\mathrm{ax}}\}/(2\pi)$. (b) The trap frequency ω as two tweezers are brought into proximity. (i) When the traps are near-overlapped, the trap frequency approaches $\sqrt{2}\omega_0$. (ii) A minimum in the trap frequency occurs when the tweezers are separated by one trap waist $\Delta x = w_0$, corresponding to a flat-bottomed tweezer. (iii) ω is normalised to the trap frequency ω_0 at large separations (dotted line).

shots, thus increasing the duty cycle of the experiment. Here we demonstrate rearrangement of a 5-site array of Cs atoms using the AOD.

A timing diagram for a sequence incorporating rearrangement is shown in Fig. 4.16(a). Rearrangement is encoded into the first 3 segments of a sequence (grey and red in diagram). The initial array consisting of 5 sites is generated by a looped AWG segment containing 5-tone waveform. After the array is loaded from the MOT, fluorescence imaging (Image 0) is used to determine the occupancy of each site, producing a binary string of occupancies, e.g. 00101. This information is used to select the multitone frequency sweeps required to rearrange to the target array. The waveforms are selected from a precalculated list of sweeps to eliminate the waveform generation time. Once selected, the the sweep step (red block) is overwritten with the new segment and the AWG is triggered to enact the rearrangement.

On receipt of the TTL, sites containing no atoms are extinguished. If more than the target number of atoms is loaded, sites containing excess atoms are extinguished. The frequencies of the remaining occupied sites are simul-

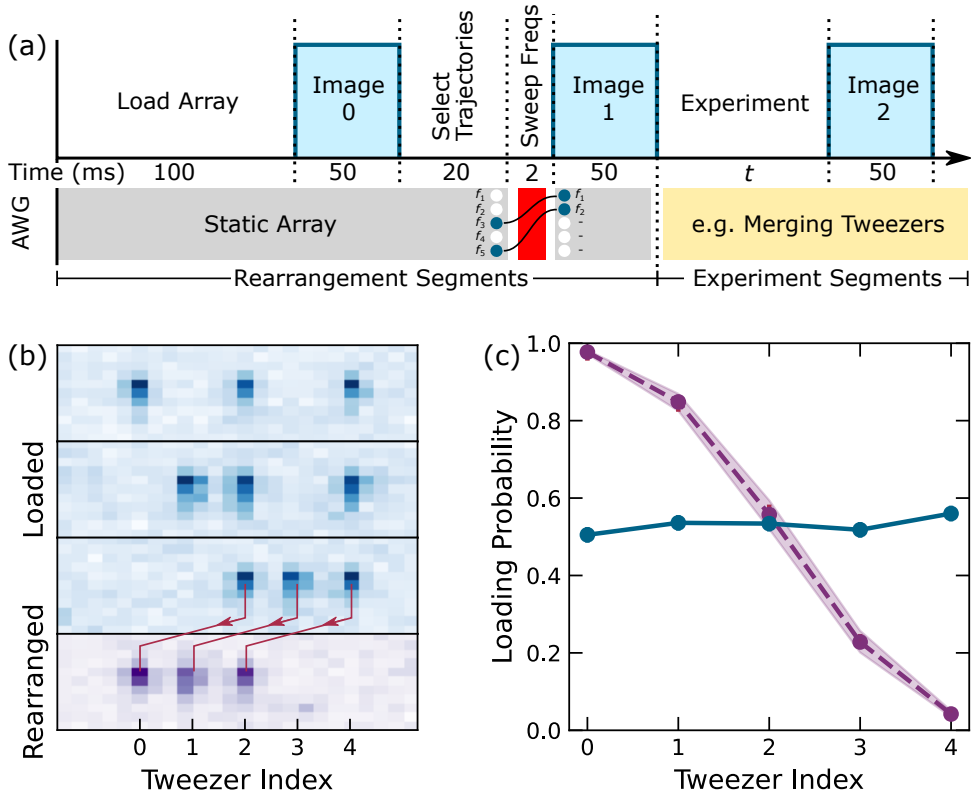

Figure 4.16: Rearrangement of a 1D array of Cs atoms. (a) Rearrangement timing diagram. The red block indicates the frequency sweep segment responsible for rearranging the occupied tweezers. (b) Fluorescence images before (blue) and after (purple) rearrangement. The atoms are shuttled from right to left in the image (red arrows). (c) Occupation probability after rearrangement of a 5-site array (purple points). The dashed line shows the expected probability, calculated using the cumulative binomial probability, Eq. (4.15); the shaded area shows the uncertainty on the expectation. The blue points show the loading probability of each site from the MOT.

taneously swept in a minimum jerk trajectory lasting 2 ms to produce the target array, produced by a looping static segment. The atoms are reimaged (Image 1) to verify successful rearrangement, and the experiment proceeds as normal. The rearrangement segments (grey) can be combined with arbitrary AWG sequences (yellow), such that after array rearrangement using the AWG, the tweezer positions may be swept again, e.g. for merging tweezers. If the AOD is not required after the initial rearrangement, the final static array may be looped instead until the end of the experimental sequence.

Fluorescence images showing a 5-site array before (blue) and after (purple)

rearrangement are presented in Fig. 4.16(b) for the initial loading of 3 atoms. Each site is assigned a region of interest which is used to calculate loading probabilities (from Image 0) and survival probabilities (from Images 1 and 2).

Loading of two or three Cs atoms is required for the Feshbach resonance study of Chapter 5. Without rearrangement, the probability to load two atoms into two tweezers is ≈ 0.25, and the probability to load three atoms into three tweezers is ≈ 0.125. Rearrangement significantly enhances these probabilities, as shown in Fig. 4.16(c). The blue data points show the loading probability per site, which has a mean value of 0.53(1). The purple data points show the site occupation probability after rearrangement, measured over 700 shots of the experiment. Here, any loaded atoms are shuttled to the end of the array to fill empty sites with a lower index. For a mean loading probability p across a tweezer array of n sites, the probability that no tweezer is loaded is given by $(1-p)^n$. By similar reasoning, the probability P that at least m tweezers are loaded is given by the cumulative binomial probability:

$$P_{n,m}(p) = \sum_{j=m}^{n} C_j^n p^j (1-p)^{n-j}, \tag{4.15}$$

where j is a summation index and C_j^n is the combinatorial of n and j. $P_{n,m}(p)$ can be improved either by increasing p, e.g. through optically-enhanced loading techniques [181, 230], or else by increasing the size of the initial array.

The measured probabilities are in excellent agreement with the binomial expectation (dashed line). We measure a probability to load two atoms of 0.84(2), and to load three atoms of 0.56(2). This constitutes a significant improvement over the base loading probability, and will significantly expedite the data collection rate by reducing the number of shots with insufficient atoms. The probability to load two atoms is expected to exceed 0.95 for $n \geq 7$ array sites. At present, the number of sites is limited by the available optical power. In future, the AOD bandwidth and imaging resolution could pose a more fundamental limit of $n \approx 11$, assuming the array sites are spaced by two tweezer waists, $2w_0 \approx 3$ μm.

4.3 Merging Species-Selective Tweezers

Magnetoassociation to form a RbCs molecule requires exactly one Rb and one Cs atom to be localised to the same optical tweezer. Similarly, a pair of Cs atoms must be prepared in the same optical tweezer for the Feshbach study of the next chapter. To this end, it is essential to develop robust transfer of atoms between tweezers.

4.3.1 Transferring Rb and Cs into a Single Tweezer

Exactly one Rb and one Cs atom are prepared in the 938 nm tweezer by merging the 938 nm tweezer (containing Cs) with the 814 nm tweezer (containing Rb), and adiabatically ramping off the 814 nm tweezer, as illustrated in Fig. 4.17(a). Merging during an experimental sequence is achieved by sweeping the AOD to adjust the 938 nm tweezer position. For this process to be efficient, the two tweezers (of volume $\approx 1\ \mu\text{m}^3$) must be well-overlapped in 3D for a specific AOD frequency when the 814 nm tweezer is ramped off.

Overlapping the 814 nm and 938 nm Tweezers

Overlap in the y radial direction is achieved using the 2-axis piezo-electric mirror (PZM) in the 814 nm path (see Fig. 2.20). The PZM angle is adjusted by ratcheting a motor in discrete steps controlled by an open-loop driver. Each voltage step increments the mirror angle by 0.14 arcseconds. In the atom plane, the measured displacement of the tweezer is 1.34(7) μm per 1000 steps. To overlap the tweezers in the y direction, we exploit the repulsion of Cs by the 814 nm tweezer. After a Cs atom is loaded into the 938 nm tweezer, the AOD is used to sweep the position of the 938 nm tweezer through 10 μm and back to the starting position in 40 ms, translating it through the x-coordinate of the 814 nm tweezer. The PZM angle is varied so that the y position of the 814 nm tweezer is stepped through the scanning 938 nm tweezer. By setting the tweezer powers such that $|U_{\text{Cs}}(\lambda_{814})/k_{\text{B}}| > |U_{\text{Cs}}(\lambda_{938})/k_{\text{B}}|$, we ensure that the Cs atom in the 938 nm tweezer is expelled when the tweezers overlap, as shown in Fig. 4.17(b). From this measurement, the PZM is set to the optimal y overlap, which is known from the fit to within a 1σ uncertainty

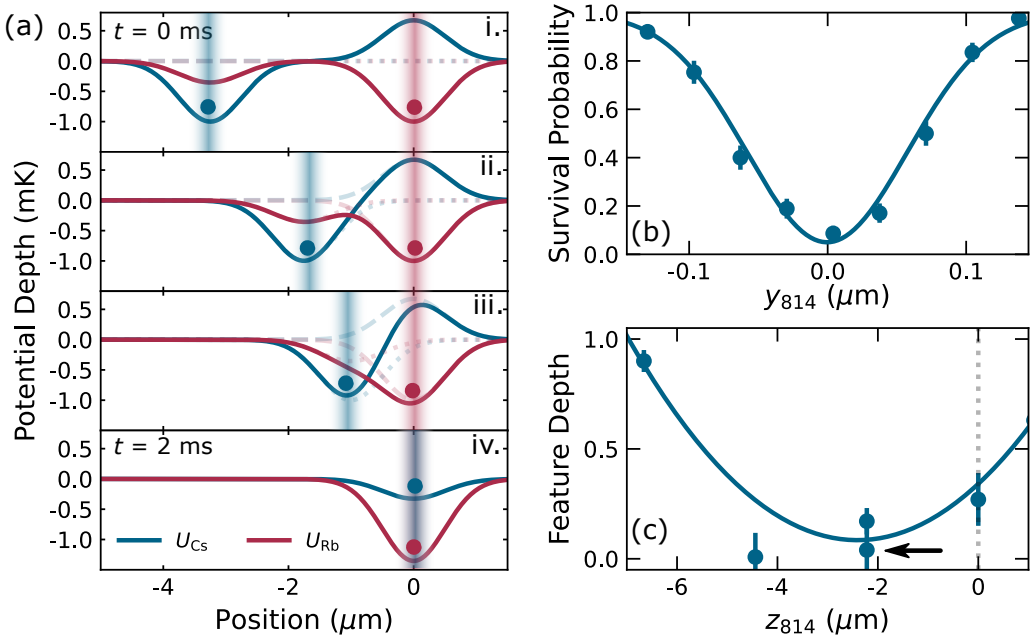

Figure 4.17: Overlap optimisation of a 814 nm and a 938 nm tweezer. (a) Species-selective potentials experienced by Rb and Cs during the merging sequence. The solid lines show the total potential experienced by each atom from both tweezers. The vertical bars show the 814 nm (red) and 938 nm (blue) tweezer positions. The dashed lines show the contribution from the 814 nm tweezer and the dotted lines show the contribution from the 938 nm tweezers. (b) y overlap of the 814 nm tweezer with the 938 nm tweezer using the PZM. Loss of a trapped Cs atom is induced by the repulsive 814 nm potential. (c) Fitted depth of the loss feature in (b) as a function of the 814 nm axial displacement. The dotted line shows the starting axial position. The arrow indicates the point corresponding to the plot in (b).

of 20 nm. Coarse overlap in the x radial direction is similarly achieved using the PZM. We have observed an hour-scale drift in the radial overlap of less than 150 nm, and a 200 nm drift over one month.

Overlap in the z direction is performed by repeating the measurement in Fig. 4.17(b) for several axial displacements of the focus of the 814 nm tweezer. When the axial overlap of the two tweezers is optimal, the depth of the loss feature in Fig. 4.17(b) is maximised since the increase in 814 nm intensity causes a stronger repulsion of the Cs atom. The fitted feature depth as a function of the 814 nm axial displacement is shown in Fig. 4.17(c). The Rayleigh range of the 814 nm tweezer is ≈ 3 μm, and the axial position of the 814 nm tweezer can be set to within 0.5 μm of the 938 nm tweezer using

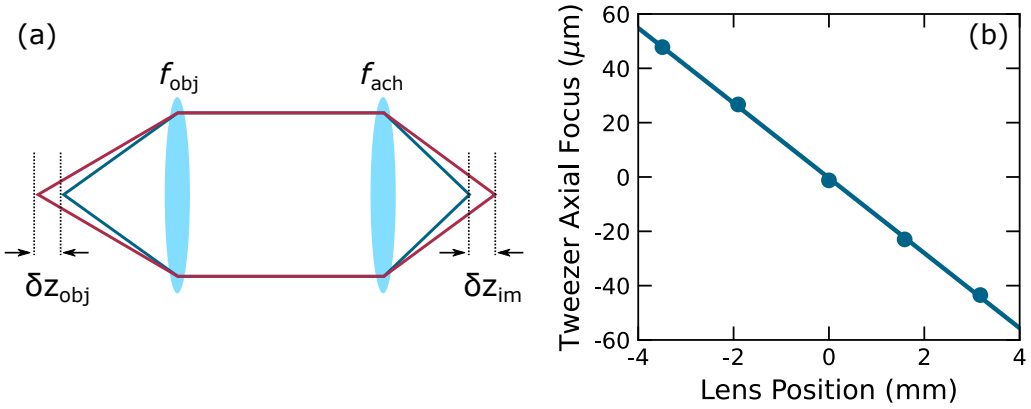

Figure 4.18: Tweezer axial focus adjustment (a) The axial position of the imaging system focus is modified by δz_{im} when the object is displaced axially by δ_{obj}. (b) Displacement of the 938 nm tweezer axial focus δz_{obj} when the expansion telescope spacing is varied.

this method.

The axial position of the focus of the 814 nm and 938 nm tweezers is set by varying the spacing of the $M = 25$ expansion telescope in the corresponding beam path (see Fig. 2.20). This modifies the beam divergence, which alters the position of the focus. The second lens of each expansion telescope is mounted in a threaded mount[12] which allows the lens position to be translated axially along the beam path. We calibrate the tweezer displacement as a function of the expansion telescope spacing by measuring the axial focus of the imaging system (as in Fig. 3.7) as the telescope lens is varied. We then infer the displacement of the tweezer using the longitudinal magnification of the imaging system shown in Fig. 4.18(a). The longitudinal magnification $\mathcal{M}$ gives the conversion from object plane to image plane displacement: $\delta z_{\mathrm{im}} = \mathcal{M}\delta z_{\mathrm{obj}}$, where $\mathcal{M} = M^2 = (f_{\mathrm{ach}}/f_{\mathrm{obj}})^2 = 28.6^2$.

In Fig. 4.18(b), we present the results of this calibration for a 938 nm tweezer. The gradient of the straight line fit is $-13.8(2)$ μm shift per 1 mm of lens displacement. The resolution of the threaded mount is 80 turns per inch, so that a single turn modifies the expansion telescope by 0.3 mm and displaces the tweezer focus by ~ 4 μm.

[12]Newport LP-2A-XYZ

Merging Rb and Cs into a 938 nm Tweezer

With the tweezers aligned in the y and z axes, we perform merging of Rb and Cs into the same tweezer along the x direction using the experimental sequence shown in Fig. 4.19(a). The tweezers are loaded and imaged to check for atom occupancy (shaded region labelled Image 1). The AOD frequency is set to 140 MHz and the 938 nm tweezer power is held at 3.13 mW. The 814 nm tweezer is loaded at a power of 1.38 mW. For these powers, the potential depths experienced by each species are: $\tilde{U}_{\mathrm{Cs}}(\lambda_{938}) = 0.95$ mK, $\tilde{U}_{\mathrm{Cs}}(\lambda_{814}) = -0.62$ mK, $\tilde{U}_{\mathrm{Rb}}(\lambda_{814}) = 0.92$ mK and $\tilde{U}_{\mathrm{Rb}}(\lambda_{938}) = 0.34$ mK, yielding combined trap depths of $\tilde{U}_{\mathrm{Cs,merged}} = 0.33$ mK and $\tilde{U}_{\mathrm{Rb,merged}} = 1.26$ mK. Crucially, for the 814 nm power used, the anti-trapping potential applied to Cs is insufficient to eject it from the 938 nm tweezer when the tweezers are overlapped. The AOD frequency is then swept to a target frequency in 10 ms, translating the x position of the 938 nm tweezer to a distance Δx from the 814 nm tweezer. The power of the 814 nm tweezer is then adiabatically ramped to zero in 5 ms. If the overlap between the tweezers is good, the Rb atom is transferred into the 938 nm tweezer; if there is insufficient overlap, the Rb atom is lost and not recaptured into the 814 nm tweezer.

After a time $t_{\mathrm{hold}} = 10$ ms, the sequence is reversed and the occupancy of each tweezer is probed again (shaded region labelled Image 2). Due to the species-selectivity of each tweezer, when the tweezers are separated, each atom returns to its original tweezer. In Fig. 4.19(b) we present the Cs and Rb single atom survival probabilities as a function of Δx. When the tweezers are overlapped to within 2 μm along x, the Rb atom is retained with > 0.90 probability. At the optimal overlap, which occurs at an AOD frequency of 163.3 MHz, the Cs survival probability is $0.99^{(+0.01)}_{(-0.02)}$ and the Rb survival probability is $1.00^{(+0.00)}_{(-0.01)}$, yielding a combined merging and separation survival probability of $0.99^{(+0.01)}_{(-0.02)}$. The asymmetry of the survival probabilities about $\Delta x = 0$ is due to the directionality of the tweezer sweep, which always originates at -7.5 μm, so that for values $\Delta x > 0$ the 938 nm tweezer is swept twice through the 814 nm tweezer. The tweezer sweep speed is not kept constant, so that intensity modulation from the crystal etalon (section 4.2.4)

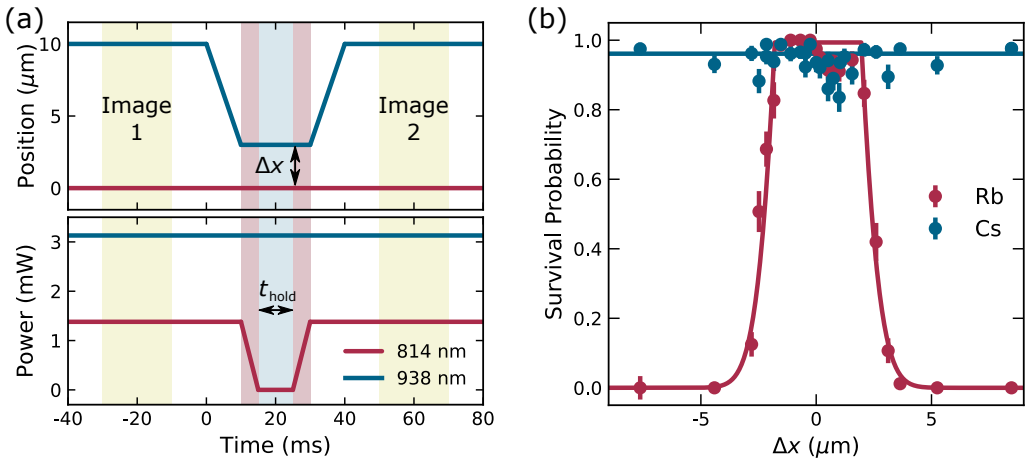

Figure 4.19: Merging Cs and Rb into a single optical tweezer. (a) Timing diagram for the tweezer merging sequence. After both tweezers are checked for atom occupancy (Image 1), the AOD frequency is ramped to overlap the 938 nm optical tweezer with the 814 nm tweezer (red-shaded region). The 814 nm tweezer is ramped off so that both atoms are confined in the 938 nm tweezer (blue-shaded region). After a hold time, the sequence is reversed, and the atom occupancy is again probed (Image 2). (b) Survival probability of Cs in the 938 nm tweezer (blue)vand Rb in the 814 nm (red) tweezer after the merging sequence in (a) for a variable Δx and $t_{\text{hold}} = 10$ ms. For a range $-2\ \mu\text{m} < \Delta x < 2\ \mu\text{m}$ there is good transfer of the Rb atom between the tweezers.

may also contribute to loss.

Merging Non-Selective Tweezers

The merging protocol described thus far has dealt with species-selective tweezers, which had two benefits. Firstly, both atoms experienced a deeper potential in their starting tweezers, which suppressed atom heating by "spilling" as the tweezers were merged. Secondly, the atoms could easily be separated for imaging.

Preparation of homonuclear atom pairs and triplets in the same tweezer is complicated by the fact that all atoms experience the same attractive trapping potentials. This can result in additional heating during merging, and makes imaging more challenging. As we shall see in the following chapter, where we transfer up to three Cs atoms to the same tweezer, solutions to these issues can be found by carefully balancing the tweezer depths.

Chapter 5

Two-Atom Collisions and Feshbach Resonances

The preparation of pairs of atoms in a single optical tweezer provides a unique platform for the study of ultracold collisions. Historically, collisions have been studied in bulk gases, where attribution of loss to specific channels can be challenging. The exact control of the number and internal state of colliding participants in a tweezer can be leveraged to study 2-body and 3-body processes explicitly. In this chapter, we present Feshbach spectroscopy performed pairs of Cs atoms, and measurements of collisions between single Rb and Cs atoms. We start with a review of ultracold scattering, before proceeding to discuss the experiments performed.

5.1 Ultracold Scattering

Interatomic collisions will be detected through measurements of the loss of pairs of atoms from the optical tweezers. We must therefore understand how the underlying atom scattering properties map onto experimental observables such as atom loss. In the following, we give an overview of the basics of scattering theory which are relevant to understand the results of this chapter. More thorough treatments and derivations can be found, for example, in refs. [231–236].

5.1.1 Scattering Theory

In an ultracold collision, we consider a plane wave incident along z which is scattered by a potential to produce a spherical scattered wave. The collision wavefunction is the sum of the incoming and outgoing waves, expressed in terms of the internuclear separation r:

$$\psi(k, r, \theta) \sim e^{ikz} + f(k, \theta)\frac{e^{ikr}}{r}, \tag{5.1}$$

where $k = \sqrt{2mE}/\hbar$ is the scattering wavevector with collision energy E and $f(k, \theta)$ is the scattering amplitude. The scattering amplitude quantifies the amount of scattering into the direction θ. The total cross-section is the sum of all scattering across a unit sphere, encapsulated by the integral:

$$\sigma_{\text{tot}} = \int_{\text{sphere}} |f(k, \theta)|^2 d\Omega, \tag{5.2}$$

where $d\Omega$ is an infinitesimal solid angle. For a central potential[1] the scattering is spherically symmetric, so the wavefunction can be decomposed into a sum of *partial waves* of angular momentum l:

$$\psi(k, r, \theta) = \sum_{l=0}^{\infty} R_l(k, r) P_l(\cos\theta). \tag{5.3}$$

Each partial wave in the sum is the product of a radial part $R_l(k, r)$ and an angular part given by the Legendre polynomials $P_l(\cos\theta)$. Since $f(k, \theta)$ contains the angular scattering information, it too can be expressed as a sum of $P_l(\cos\theta)$. Performing the integral for σ_{tot} with $f(k, \theta)$ written as a sum of Legendre polynomials yields the total cross section [233]:

$$\sigma_{\text{tot}}(k) = \frac{4\pi}{k^2}\sum_{l=0}^{\infty}(2l + 1)\sin^2\delta_l(k). \tag{5.4}$$

The sum is across partial waves of angular momentum $l = 0, 1, 2, 3\ldots$, which are also referred to using the spectroscopic notation s-, p-, d-, f-wave and so on. $\delta_l(k)$ is the phase shift of the partial wave l (induced by the scattering

[1] One where the potential is spherically symmetric, depending only on r.

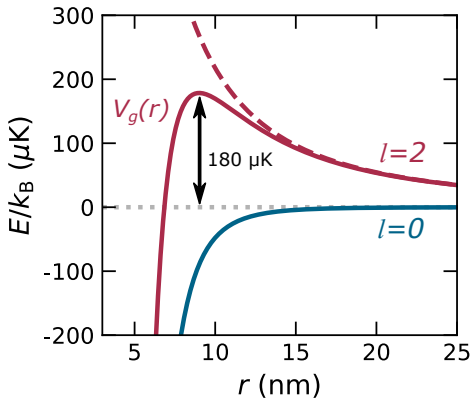

Figure 5.1: ^{133}Cs d-wave centrifugal barrier. The van der Waals contribution $-C_6/r^6$ is shown by the blue line. For $l = 0$ there is no barrier to s-wave scattering. The dashed line indicates the centrifugal contribution for $l = 2$. The solid red line shows the sum of the van der Waals and $l = 2$ centrifugal term, resulting in a potential barrier with height $E/k_B = 180$ μK.

potential) with respect to the incident wave.

The contribution of higher partial waves with $l > 0$ to $\sigma_{tot}(k)$ can be neglected as $k \to 0$. The radial Schrödinger equation, which $R_l(k, r)$ must satisfy, contains the effective potential $V_g(r)$. For two atoms in the ground state, the long-range potential as a function of internuclear separation r is given by [70]:

$$V_g(r) = -\frac{C_6}{r^6} + \frac{\hbar^2}{2\mu}\frac{l(l+1)}{r^2}, \tag{5.5}$$

where C_6 is the van der Waals dispersion coefficient and μ is the reduced mass. The left-hand term represents an attractive van der Waals interaction. The right-hand term constitutes a centrifugal barrier term for partial waves with $l > 0$ [237]. If a given partial wave has an energy much less than the barrier height E_b/k_B, its contribution to the scattering cross-section is small[2].

For identical bosons, such as for the case of the Cs+Cs scattering discussed in this chapter, only even-l partial waves contribute to the total cross section, so that the lowest centrifugal barrier for Cs is d-wave. To see why, consider interchanging the coordinates of the two indistinguishable colliding atoms

[2]This is true, except near a *shape resonance* [238], which can occur when the potential formed by the centrifugal barrier supports a quasi-bound state. A shape resonance can greatly enhance the contribution of higher partial waves, if the incident wave is close in energy to the quasi-bound state [234, 239].

$\mathbf{r_1} \leftrightarrow \mathbf{r_2}$, which for a given partial wave is equivalent to:

$$P_l[\cos(\pi - \theta)] = (-1)^l P_l(\cos\theta). \tag{5.6}$$

The wavefunction for identical bosons must be symmetric under interchange[3], which is only the case when l is even in the above expression. As a result, only even-l partial waves can contribute to the cross-section. There is no $l = 1$ p-wave contribution for identical bosons, and hence the lowest centrifugal barrier is d-wave.

The d-wave centrifugal barrier $V_g(R)$ for collisions of identical Cs atoms is shown in Fig. 5.1. For caesium, $C_6 = 6890\ E_\mathrm{h}\ a_0^6$, where E_h is the Hartree energy [240]. The centrifugal barrier maximum occurs at an interatomic separation R^l_max where the barrier height is E^l_b, given respectively by [237]:

$$R^l_\mathrm{max} = \left(\frac{6\mu C_6}{\hbar^2 l(l+1)}\right)^{\frac{1}{4}}, \tag{5.7}$$

$$E^l_b = \frac{\hbar^2 l(l+1)}{3\mu (R^l_\mathrm{max})^2}. \tag{5.8}$$

For $l = 2$, the barrier height is $E_b/k_\mathrm{B} = 180\ \mu$K. The barrier heights of further partial waves are even higher since $E^l_b \propto l^2$. The Cs+Cs collisions discussed in this chapter occur at energies $E/k_\mathrm{B} < 2\ \mu$K, which is much less than the d-wave barrier height. d-wave contributions are generally small for $E/k_\mathrm{B} < 50\ \mu$K [241], so we neglect scattering of partial waves with $l > 0$ and consider just s-wave scattering[4].

For collisions of non-identical bosons, such as the Rb+Cs collisions discussed in this chapter, *all* partial waves contribute. The p- and d-wave barrier heights in thermal units are $E_b/k_\mathrm{B} = 54\ \mu$K and $E_b/k_\mathrm{B} = 282\ \mu$K respectively. The Rb+Cs collisions relevant in this chapter occur at collision energies $E/k_\mathrm{B} < 5\ \mu$K. Again, we will neglect scattering of higher partial waves and assume only s-wave scattering.

In the limit $k \to 0$, scattering is parametrised by the s-wave scattering length

[3] For fermions, the wavefunction must be antisymmetric under interchange, requiring that l be odd so that only odd-l partial waves contribute.

[4] A more complete theoretical treatment should still consider the relatively small contribution of higher partial waves.

a, which is defined as [234]:

$$a = -\lim_{k\to 0} \frac{\tan \delta_0(k)}{k}. \tag{5.9}$$

Here, $\delta_0(k)$ is the phase shift of the scattered s-wave relative to the incoming wave. The scattering length can be interpreted as the zero-crossing of the asymptotic scattered wavefunction. In a BEC, a negative scattering length gives rise to attractive interactions within the condensate, and a positive scattering length induces repulsive interactions [232]. Since we will deal with thermal states in our study of collisional loss, we are instead interested in how the value of a will impact the elastic and inelastic collision cross-sections.

The total s-wave cross-section for *distinguishable* particles is obtained by substituting the effective range formula[5] into Eq. (5.4) for $l = 0$. After neglecting terms in r_e, the cross section is given by [233, 234]:

$$\sigma_{\mathrm{s}}(k) = \frac{4\pi a^2}{1 + k^2 a^2}. \tag{5.10}$$

There are two limiting cases to this equation. The first is the ultracold limit, when $k \to 0$ so that $\sigma_{\mathrm{s}} \sim 4\pi a^2$. The second is the unitarity limit, when $a \to \infty$ so that the cross-section saturates to a temperature-limited value $\sigma_{\mathrm{s}}(k) \sim 4\pi/k^2$. This expression is correct for Rb+Cs collisions, however for the case of identical bosons in Cs+Cs collisions, the factor of 4π is replaced with 8π due to the indistinguishability of identical bosons[6] [233, 236].

One can conclude from Eq. (5.10) that if a could be controlled, it would be possible in turn to control the atomic scattering properties.

5.1.2 Feshbach Resonances

Feshbach resonances allow for the sign and magnitude of the scattering length to be tuned. Briefly put, a Feshbach resonance occurs when a quasi-bound state is tuned to the same energy as the scattering state. If there is cou-

[5] The effective range formula is $k \cot \delta_0(k) = -\frac{1}{a} + \frac{1}{2} r_e k^2$, where r_e is the effective range, and is valid for short-ranged potentials.

[6] For identical particles, quantum interference between the $f(k, \theta)$ and $f(k, \pi - \theta)$ amplitudes results in an extra factor of 2 compared to non-identical particles.

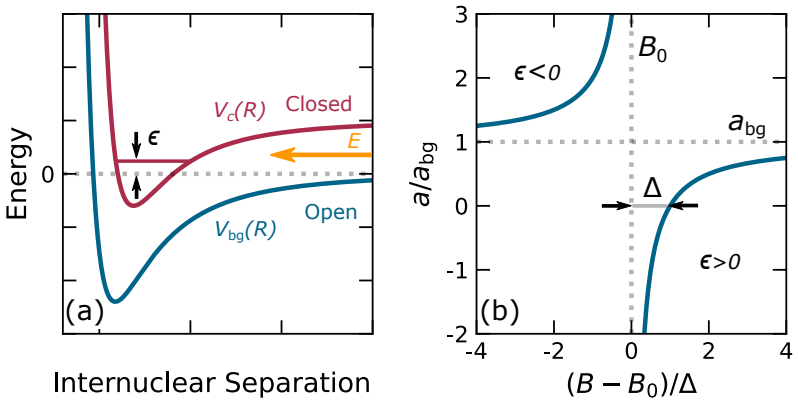

Figure 5.2: Principle of a Feshbach resonance illustrated for two channels. (a) The potentials V_{bg} and V_c of the open and closed channels as a function of the atom separation R. The closed channel bound state can be tuned into resonance with the open channel ($\epsilon \to 0$), inducing coupling. (b) Plot of the equation described in the text. When the bound state lies above threshold and $\epsilon > 0$, the scattering length is negative. a grows sharply as the B field is swept through the resonance at B_0, and changes sign when $\epsilon < 0$.

pling between the two, the scattering wavefunction is modified, altering the zero-crossing of its asymptote and correspondingly modifying the scattering length.

To understand how this works, consider a two-channel model shown in Fig. 5.2(a). Two atoms approach each other with collision energy E, indicated by the yellow arrow. The lower potential $V_{\rm bg}(R)$ supports the *open* (or *entrance*) channel[7], so-called because it lies below E, and therefore is energetically accessible to the unbound atoms. The upper potential $V_c(R)$ is called the *closed* channel, because the atoms would require more than their energy E to access it. $V_c(R)$ supports bound states. The energy of the least-bound state with respect to the atomic threshold is ϵ. If ϵ is small, the colliding atoms can resonantly couple to the bound state. This coupling occurs only when the selection rules of the coupling mechanism are satisfied. If there is coupling between the two states, the channels are mixed, which alters the scattering wavefunction. As a result, the zero-crossing of the asymptotic wavefunction, identified above as the scattering length, is shifted. Experimentally, ϵ can be tuned by applying a magnetic field, pro-

[7]The atom states before and after the collision, including free-atom states and bound states are referred to as *channels* in the context of scattering.

vided that the open and closed channels have a differential magnetic moment $\delta\mu = \mu_{\text{atoms}} - \mu_{\text{bound}}$. The resulting differential Zeeman shift between the two channels allows ϵ to be tuned to zero.

Near a Feshbach resonance, the scattering length as a function of magnetic field is given by [242]:

$$a(B) = a_{\text{bg}} \left(1 + \frac{\Delta}{B - B_0}\right). \tag{5.11}$$

We plot this expression in Fig. 5.2(b). B_0 is the position of the resonance pole (vertical dotted line), corresponding to $\epsilon \approx 0$. Δ is the resonance width, defined as the difference between B_0 and the position of the zero-crossing. The width scales as: $\Delta \propto 1/\delta\mu$, and is also proportional to the coupling strength of the free and bound states [236]. The horizontal dotted line indicates the background scattering length a_{bg} which is the slowly-varying contribution of all other off-resonant bound states. When the bound state is above threshold, the scattering length is negative (right side of Fig. 5.2(b)). As $\epsilon \to 0$ and the channels are tuned to resonance, the scattering length increase sharply (with a pole as $B \to B_0$). The change in sign as the bound state moves below threshold (left side of figure) corresponds to the addition of a new node to the scattering wavefunction [232]. Pairs of atoms may be transferred to the bound state if the magnetic field is adiabatically ramped through threshold in a process termed magnetoassociation, which is discussed further in section 6.2.3.

For real alkali atoms such as ^{133}Cs, the resonance spectrum is more complex than the two-channel model discussed above. A plethora of bound states leads to a rich Feshbach spectrum as a function of magnetic field for Cs polarised in a given (f, m_f). Feshbach resonances are labelled by the quantum number of their associated bound state: $n(f_1 f_2)FL(M_F)$ [240]. n is the molecular vibrational level, labelled with respect to the dissociation threshold, with $n = -1$ being the least-bound state. f_1 and f_2 are the hyperfine levels of each atom, which for Cs can be 3 or 4. F is the resultant of f_1 and f_2, $M_f = m_1 + m_2$ and L is the rotational angular momentum of the bound state.

5.2 Cs + Cs Feshbach Resonances

Feshbach resonances are a valuable tool for controlling ultracold systems. As such, there is interest in studying and characterising them. We give an overview of some major developments to motivate our study, before discussing the Feshbach spectroscopy performed in this work. The results presented here follow work the discussion of ref. [243].

5.2.1 Motivation

Feshbach resonances are utilised in many modern experiments to exert control over cold atoms and molecules [79]. Magnetic Feshbach resonances enable control of the atomic scattering length via an externally applied magnetic field [244, 245]. In this way, the atomic intra- and inter-species scattering properties can be tuned precisely in experiments, leading to many notable results. The ability to tune the scattering length was instrumental in the production of Bose-Einstein condensates (BECs) of ^{85}Rb [73], ^{133}Cs [74, 246] and ^{39}K [75]. Tuning the scattering length of fermionic species was used to study the BEC-BCS crossover and create molecular BECs [247–249]. Further manipulation of the BEC scattering length has allowed the study of bright-matter solitons [250, 251]. Interesting BEC phenomena such as *Bosenova* arise when the sign of the scattering length is quickly changed [252]. Tuning of the scattering length in Cs allowed for the first observation of Efimov physics [253] and identification of a minimum in the three-body recombination rate at ≈ 22 G [254], which is often used for evaporative cooling.

Furthermore, Feshbach resonances are necessary for the production of many species of ultracold molecules. By sweeping a magnetic field through a Feshbach resonance, pairs of atoms are made to follow an avoided crossing and are magnetoassociated to form weakly-bound molecules [71]. Intra-species resonances have been used to produce the homonuclear molecules including $^{133}Cs_2$ [87], $^{87}Rb_2$ [88], Na_2 [255]. Inter-species resonances have been used to produce the bialkali molecules ^{40}K^{87}Rb [82, 83], ^{23}Na^{40}K [84, 85], ^{23}Na^{6}Li [86], ^{87}Rb^{133}Cs [89, 90] and ^{23}Na^{87}Rb [91]. Given the broad utility of Feshbach resonances, there is considerable interest in studying them. Feshbach

spectroscopy, the measurement of Feshbach resonances, can shed light on the underlying molecular structure [240, 256].

Tightly-confining traps such as optical tweezers provide a new platform for studying Feshbach resonances. Conveniently, the exact number of collision participants is known, so that 2- or 3-body processes can be explicitly studied, while avoiding complications from loss via extraneous pathways. Production of Li_2 molecules from fermionic ^{6}Li in a tweezer was observed in a tight microtrap [257]. Interspecies Feshbach resonances have been detected in a tweezer using inelastic loss [111] and by the production of molecules via magnetoassociation [110]. It has been proposed that a double-well tweezer potential could be used as a tool to detect narrow Feshbach resonances and precisely measure their strength [258]. The prospect of using three atoms prepared in a tweezer to study Feshbach resonances has also been raised [213]. The message is clear, as stated in Ref. [258]: resonance spectroscopy of trapped isolated atoms is becoming the state of the art [for characterising Feshbach resonances].

A great deal of work exists concerning the characterisation of Cs Feshbach resonances, initially spurred by the quest for BEC. Early studies investigated collisions and evaporative cooling in a magnetically trappable states of Cs [259–263]. BEC was achieved using the $(f = 3, m_f = 3)$ state [74], after limitations due to two- and three- body loss were overcome [254] by taking advantage of an Efimov minimum in the three-body recombination rate [253]. Chin *et al.* measured and tabulated over 60 Cs resonances [256, 264] using elastic, inelastic and radiative Feshbach spectroscopy. Berninger *et al.* fitted Cs $(3, 3)$ resonances for fields up to 1000 G to precisely determine the Cs_2 singlet and triplet potentials [240]. At the time of writing, these are the most up to date interaction potentials that have been calculated.

In the following sections, we use the apparatus described thus far to measure Cs+Cs Feshbach resonances. In future work, these searches could be extended to other m_f states of Cs [241] and interspecies resonances [111].

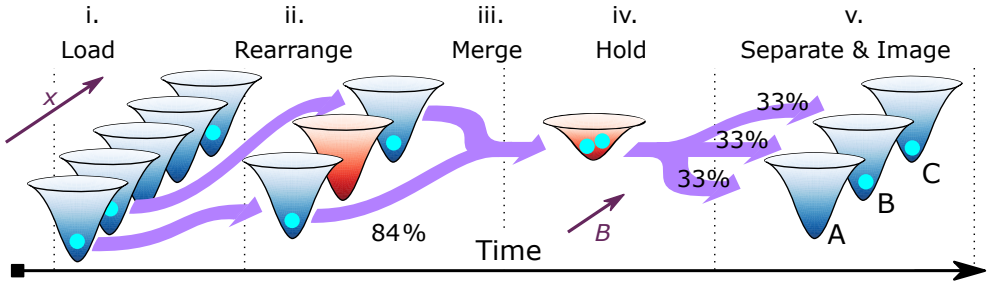

Figure 5.3: Preparation of atom pairs and detection of loss. (i) Atoms are loaded into 5 tweezers of wavelength 938 nm, with a mean probability of 0.53(1) per tweezer. (ii) Following tweezer rearrangement, pairs of Cs atoms are prepared in 84(2) % of experimental runs. (iii) Cs pairs are merged into a 1064 nm tweezer (red). (iv) The 1064 nm tweezer is down ramped to a depth of 30 μK for a hold time at a magnetic bias field B, where inelastic collisions induce loss. (v) The atoms are imaged by separating them into 3 traps with a final occupancy per site of 33 %.

5.2.2 Overview of Measurement Sequence

As in other experiments, the signature of a Feshbach resonance will be the enhancement of 2-body loss from the tweezers. We will prepare exactly two atoms, so that the loss will be observed as a minimum in the two-atom survival probability. We study previously measured Cs Feshbach resonances in the $(f = 3, m_f = -3)$ state using inelastic loss spectroscopy [264] and resonances in $(3, 3)$ using radiative loss spectroscopy [264, 265].

The experimental sequence used to detect Cs Feshbach resonances is shown in Fig 5.3. We reliably prepare pairs of Cs atoms in 84(2) % of experimental shots using the AOD to rearrange five 938 nm tweezers to 2 sites, discarding excess atoms as explained in section 4.2.6. After optical pumping, both atoms are simultaneously prepared in either $(3, -3)$ or $(3, 3)$ with a probability of 0.96(4), as explained in section 4.1.3. To suppress changes in f and m_f from spontaneous Raman scattering during the collision time, we merge the two 938 nm tweezers into a single 1064 nm "collision" tweezer (see section 4.1.5). The collision tweezer is ramped down to a depth of $U/k_\mathrm{B} = 30$ μK in 5 ms and the atoms are held for a time t, before being separated and probed for loss. We now discuss these steps in more detail.

5.2.3 Preparing Cs Atom Pairs Without Heating

The tweezers must be merged without heating the atoms, which requires that the trap depths be similar. If there is an imbalance in the trap depths, one atom is spilled along the merge direction into the deeper trap, gaining energy in that direction approximately equal to the difference in trap depths [213]. This heating mechanism was precluded for Rb+Cs by the choice of species-selective potentials in Chapter 3.

Heating is undesirable because it results in a reduction of the atom density. The pair density of a homonuclear atom pair in a single tweezer is given by:

$$\bar{n}_2 = \left(\frac{m\bar{\omega}^2}{4\pi k_{\mathrm{B}} T} \right)^{\frac{3}{2}}, \tag{5.12}$$

where $\bar{\omega}$ is the mean trap frequency, m is the atomic mass and T is the mean temperature of the pair. We derive this expression in Appendix E.

The heating caused by imbalanced tweezers is quantified in Fig. 5.4(a). An atom is loaded into either a 938 nm tweezer (blue) or the 1064 nm tweezer (red) at an initial temperature of 5 μK. The 1064 nm tweezer is ramped to a variable depth, and the 938 nm tweezer is ramped to a depth of $U/k_{\mathrm{B}} = 0.25$ mK. Next, the AOD is used to merge the 938 nm tweezer into the 1064 nm tweezer in 2 ms before being adiabatically ramped off in 3 ms. The atom energy E/k_{B} after the merge sequence is probed by performing a standard release and recapture measurement in the 1064 nm tweezer.

An atom loaded into the 938 nm tweezer is heated if the ratio of trap depths $U_{1064}/U_{938} > 1$ because it non-adiabatically spills into the deeper 1064 nm tweezer and increases its motional level. If $U_{1064}/U_{938} < 1$, its motional level is unchanged. Similarly, an atom loaded into the static 1064 nm tweezer is also heated if $U_{1064}/U_{938} < 1$ because it first spills into the deeper 938 nm tweezer before transferring back to the 1064 nm tweezer as the 938 nm tweezer is ramped off.

In principle the energy gain is along the merge axis x, however in reality misalignment of the tweezers results in some heating in the y and z axes. As a result there is a degree of inaccuracy on the temperature fitted by

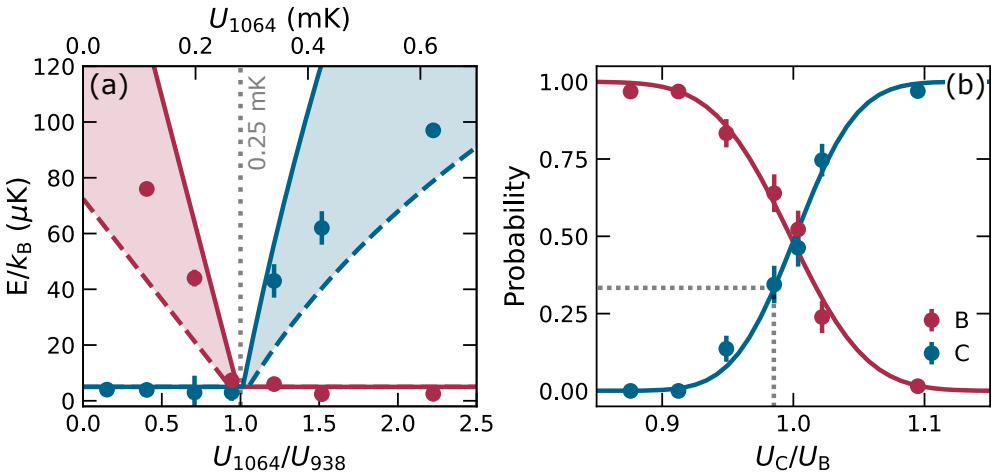

Figure 5.4: Merging and separating Cs atom pairs. (a) Heating of an atom prepared in the 1064 nm trap (red) or the 938 nm trap (blue) caused by a trap depth imbalance when the 938 nm tweezer is merged into the 1064 nm tweezer. The solid lines indicate the atom energy that would be expected if heating occurred only along x. The dashed lines indicate the expected energy assuming the energy gained is divided equally in all 3 axes. (b) Atom splitting probability between tweezers C and B with trap depth ratio. The tweezer depths are balanced where the curves cross. The dotted lines show the ratio for which 33 % of atoms are split into trap C.

the release and recapture Monte Carlo simulation[8], which assumes the atom energies along all trap axes are in thermal equilibrium. The shaded regions indicate the expected atom energy E/k_B measured after merging due to an imbalance in the trap depths, and is bounded by two extreme cases. The upper bound shown (solid lines) assumes the energy is gained along a single trap direction. The fitted temperature is overestimated because the release and recapture measurement is sensitive to the axis with most kinetic energy. The lower bound (dashed lines) assumes that energy gained is shared equally across trap axes. The measured data lie in the shaded regions between these two limiting cases.

Naturally, the 938 nm and 1064 nm tweezer depths are set equal during merging (to $U/k_B = 560$ μK) to avoid this heating effect. In the following measurements, the two Cs atoms are prepared in the 938 nm tweezers at temperatures of 6(1) μK and 8(1) μK respectively. They are transferred to

[8]Attempting to account for experimental imperfections in the simulation adds significant complexity, and it is unclear if the result is any more reliable.

the 1064 nm tweezer (without heating), which is then ramped to a depth of $U/k_{\mathrm{B}} = 30$ μK. Since the harmonic oscillator energy scales as $E_n \propto \sqrt{U/k_{\mathrm{B}}}$, the depth reduction results a mean atom temperature in the collision tweezer of 1.7(3) μK. The trap frequencies $\nu_{i=x,y,z}$ in the shallow collision tweezer are estimated by scaling the trap frequencies measured in a deeper 1064 nm trap by the relation $\nu \propto \sqrt{U}$, yielding $\{\nu_x, \nu_y, \nu_z\} = \{7.4, 9.1, 1.3\}$ kHz. In the collision tweezer, we estimate a corresponding pair density of $\bar{n}_2 = 5(2) \times 10^{11}$ cm^{-3}.

5.2.4 Imaging Homonuclear Atom Pairs

In the case of Rb+Cs, we were able separate the atoms back to their starting tweezers by leveraging the species-selectivity of the tweezer potentials. This is not possible for a homonuclear Cs pair, since both atoms experience the same attractive potential. While it is possible to observe multiple particles in the same optical tweezer [51, 266, 267], these methods are precluded in our system due to rapid light-assisted collisions during imaging originating from the tight waists of the optical tweezers[9]. As a result, we developed a splitting method which expands on the detection technique discussed in ref. [114].

The principle of the imaging scheme is to repeatedly subdivide the collision tweezer into several tweezers for imaging. After a hold time, the 938 nm tweezer is ramped on and the 1064 nm collision tweezer is ramped off. Any atoms are then confined in a tweezer, labelled B. The AOD is used to repeatedly subdivide tweezer B by splitting off a second tweezer and sweeping its position. This process is repeated multiple times to produce a 1D "imaging array" of N tweezers which are fluorescence imaged. The results of the imaging procedure are binned according to whether 0, 1 or 2 atoms were detected.

The probability of atom transfer, P_{split}, is set using the AOD to tune the relative depth of the two tweezers. We split into $N = 3$ imaging tweezers, labelled A, B and C. First C is split off from B, and then A is split off. P_{split} is chosen in each splitting event so that the occupation probability of the sites

[9] Additionally, these methods were impractical to introduce in our experiment at the time of measurement.

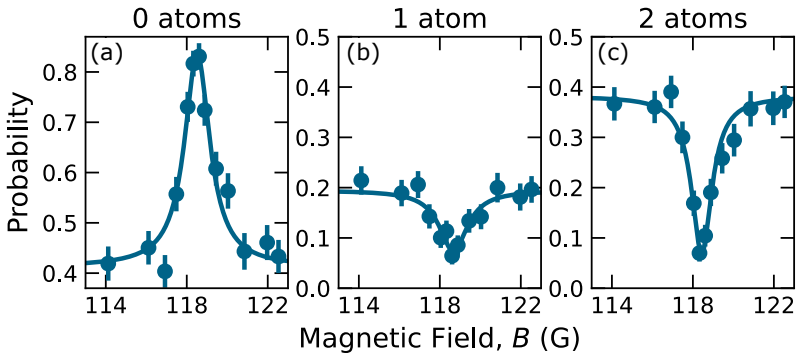

Figure 5.5: Detection of a Cs+Cs Feshbach resonance using the resonance feature at ~ 118 G for Cs in $(f = 3, m_f = -3)$ as an example. (a) Probability of detecting no atoms after the hold time of 50 ms. (b) Probability of detecting one atom. (c) Probability of detecting two atoms.

is $\sim 1/3$. A measurement of the splitting probability between two tweezers as a function of their relative depth is presented in Fig. 5.4(b).

For a tweezer split into N traps with equal final occupation, the probability that both atoms will occupy the same final trap is $1/N$. It is therefore desirable to use higher N in order to reduce the probability that two atoms occupy the same imaging tweezer, where they would be subject to light-assisted loss. As we discuss in section 5.2.5, light-assisted collisions can induce loss of one or both atoms from the tweezer and complicate the detection process. Splitting is currently limited to $N = 3$ because P_{split} depends on the temperature-dependent diffraction efficiency response of the AOD. The changing duty cycle of the AOD as the collision time is varied thus affects the splitting probabilities, requiring rebalancing of the depths which becomes burdensome as N is increased.

5.2.5 Detecting Two-Body Loss

During the collision time, the atom pairs are held in the 1064 nm tweezer at a bias field B. The bias field is applied in the x direction, corresponding to the N/S axis of the cell. The bias field is produced using a combination of the N/S shim coils and the bias coils, and ramped up to the target value during the merge step of the sequence.

Two-body collisions between atom pairs can result in pairwise loss. The cause

of loss is the release of internal energy, which is converted to kinetic energy that is shared between the atoms. Whether the atoms are lost from the tweezer depends on the amount of energy released. Cs atoms prepared in the lowest state ($f = 3, m_f = 3$) cannot release energy through hyperfine or m_f-changing collisions, and so do not exhibit 2-body loss. For Cs pairs prepared in $f = 4$, the energy released due to f-changing collisions is equal to the ground state hyperfine splitting energy $E/h = 9.19$ GHz. In such collisions the energy shared is vastly greater than the trap depth and both atoms are lost. f-changing collisions do not occur for pairs prepared in $f = 3$, however inelastic collisions can occur if the atoms are prepared in a Zeeman sublevel ($f = 3, m_f \neq 3$). The energy released is related to the Zeeman shift induced by the bias field $E = \Delta m_f \times \mu_B g_f B$, which was given previously in Eq. (2.2). For $\Delta m_f = 1$, the energy released for Cs is $dE/dB = 0.35$ MHz G^{-1}. The shallow trap depth of $U/k_B = 30$ μK ($U/h \approx 0.6$ MHz) is chosen so that m_f-changing collisions are expected to cause pairwise loss even at low bias fields.

When the magnetic field is tuned to a Feshbach resonance, the collision rate is enhanced, leading to faster 2-body collision rate which is maximal on resonance. For Cs optically pumped to $(3, -3)$, in Fig 5.5 we present an example Feshbach resonance near $\sim$ 118 G, measured using our detection scheme. At 118 G, the energy released is $\sim$ 41 MHz, so that any collision is expected to induce loss. In order to observe an unsaturated loss feature, we tune the hold time in the tweezer, which for the measurement shown is 50 ms. We are able to post-select experimental shots where zero, one or two atoms were detected after the collision time, as shown in Fig. 5.5(a-c) respectively. As expected, the probability of observing zero atoms after the hold time is maximal on resonance, correlated with a minimum in the two-atom survival. From this, we conclude that two-body collisions are indeed occurring.

Since collisions are expected to induce pairwise loss, the one-atom feature in Fig. 5.5(b) is perhaps surprising. Two atoms are only detected when they are trapped in separate imaging tweezers. In cases where two atoms end in the same imaging tweezer, rapid light-assisted collisions during imaging induce either $2 \to 0$ loss with probability $P_{2\to0}$, or $2 \to 1$ loss with probability $P_{2\to1} = 1 - P_{2\to0}$, contributing to the observed background in these detection

channels. In independent measurements, we measured the probability of $2 \rightarrow 1$ and $2 \rightarrow 0$ loss during imaging, finding respectively $P_{2\rightarrow1} = 0.36(2)$ and $P_{2\rightarrow0} = 0.64(2)$. In the remaining Feshbach spectroscopy, we use the zero-atom feature to characterise the Feshbach resonances, because it is insensitive to the complex $2 \rightarrow 1$ loss that arises during imaging.

5.2.6 Inelastic Feshbach Spectroscopy of $(3, -3)$

We measure five inelastic pair loss features for Cs optically pumped to $(f = 3, m_f = -3)$ using the methods outlined in the preceding sections. Fig. 5.6(a) shows the $(f = 3, m_f = -3)$ scattering length as a function of magnetic field. The scattering length data is obtained from ref. [241], which uses the most recent Cs potentials [240] to calculate the resonance positions. The vertical lines mark the fitted centres of the features shown in Fig. 5.6(b-f), which show the probability of observing loss of both atoms. We fit the loss features with a Lorentzian function to extract the feature centre and full-width at half maximum (FWHM).

The doubly-peaked feature shown in (b) corresponds to two closely-spaced resonances with fitted centres at 30.1(2) G and 34.1(8) G which are caused by the threshold crossing of the $6d(-6)$ and $6d(-4)$ bound states respectively [264]. The resonances presented in (d-f) correspond to the bound states $-7(4,4)8d(-7)$, $-7(4,4)8d(-6)$ and $-7(4,4)8d(-5)$ [264]. The centres and widths of the features, extracted from a least-squares fit, are presented in table 5.1.

The measured loss features corresponding to resonances are shifted from the poles in the scattering length shown in Fig. 5.6(a), which are calculated for $E_{\text{coll}} \rightarrow 0$. This is because the position of the measured features depends on the loss rate coefficients k_2, which are dependent on E_{coll}. The loss rates measured experimentally are related to k_2 by $\Gamma_2 = \bar{n}_2 k_2$. For these experiments, $E_{\text{coll}}/k_{\text{B}}$ is determined by a thermal distribution with $T = 1.7(3)$ μK, reduced from 5 μK by the adiabatic lowering of the collision tweezer to $U/k_{\text{B}} = 30$ μK depth, as described in section 5.2.3. For inelastic scattering, the s-wave con-

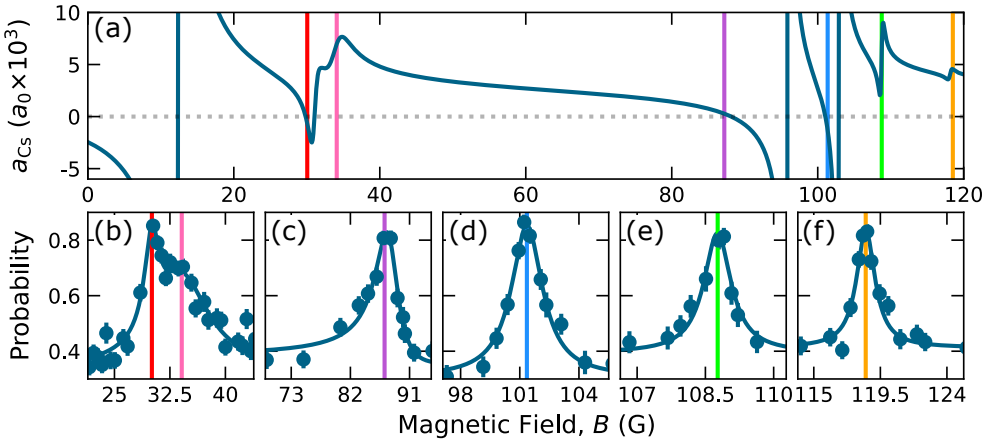

Figure 5.6: Inelastic Feshbach spectroscopy of Cs atom pairs prepared in $(f = 3, m_f = -3)$. (a) Real part of the Cs s-wave scattering length with external magnetic field for the $(3, -3)$ state (Theory from [241]). The coloured lines correspond to the features measured in (b)-(f). (b) Probability of observing zero atoms after a hold time at B. Resonances at 30.1(2) G and 34.1(8) G. (c) Loss feature arising from the zero in the scattering length at 88.0(3) G. (d) Resonance at 101.4(1) G. (e) Resonance at 108.77(6) G. (f) Resonance at 118.51(5) G. The uncertainties quoted are calculated from the fit and calibration errors added in quadrature.

tribution to the k_2 two-body loss coefficient is given by [241]:

$$k_2 = \frac{4\pi\hbar\beta/\mu}{(1 + k^2|a|^2 + 2k\beta)}, \tag{5.13}$$

where μ is the reduced mass, $k = \sqrt{2\mu E_{\text{coll}}}/\hbar$ is the incoming wavevector and $a(k, B) = \alpha(k, B) - i\beta(k, B)$ is the complex energy-dependent scattering length. The imaginary part of the scattering length β peaks at the position of the resonance while the real part of the scattering length α exhibits a dispersive pole through the resonance [235].

For $k \to 0$, the denominator of Eq. (5.13) approaches unity and the peak in the loss rate coincides with the position of the resonance. Experimentally, the atom temperature is finite and $k \neq 0$, so the a and β terms in the denominator cause a suppression of k_2. This suppression is observed as a shift in the observed loss peaks from the maximum of $\beta(B)$ to the zero of $\alpha(B)$ as E_{coll} is increased.

In Fig. 5.7 we compare the centres of the measured features to theoretical k_2 values. The loss rate curves shown were calculated by Matthew Frye and

Table 5.1: Centres and widths extracted from Lorentzian fits of the observed Cs ($f = 3, m_f = -3$) loss features. The final entry shows the centre extracted for the zero in the scattering length. The reported width is a FWHM extracted from the Fano-type fit.

Bound State	Centre (G)	Γ (G)
$6d(-6)$	30.1(2)	2.4(8)
$6d(-4)$	34.1(8)	9(3)
$-7(4,4)8d(-7)$	101.4(1)	1.9(2)
$-7(4,4)8d(-6)$	108.77(6)	0.7(1)
$-7(4,4)8d(-5)$	118.51(5)	1.5(2)
—	88.0(3)	4.6(3)

Jeremy Hutson, as discussed in ref. [243]. Due to the relatively large d-wave barrier for Cs discussed in section 5.1.1, only s-wave contributions are included. Each line corresponds to a single collision energy, i.e. the thermal distribution of the ensemble has been neglected. The solid lines correspond to the $E_{\mathrm{coll}}/k_{\mathrm{B}}$ listed in the legend. The dashed (dotted) lines of the same colour correspond to two (five) times the collision energy listed (e.g. 1 nK, 2 nK, 5 nK). The subplots (b-c) show zoomed views of the main figure.

We first discuss the features corresponding to Feshbach resonances (Fig. 5.7(b) & (d)). The measured position of the feature at 30.1 G is in line with the expectation for a collision energy of 1 nK to 2 μK. In independent measurements, we measured Γ_2 near-resonance at 31 G and off-resonance at 21 G. Using the known $\bar{n}_2$, we estimate $k_2(31\ \mathrm{G}) = 8(3) \times 10^{-11}\ \mathrm{cm^3 s^{-1}}$ and $k_2(21\ \mathrm{G}) = 8(3) \times 10^{-12}\ \mathrm{cm^3 s^{-1}}$, marked by the black circle and cross respectively. These values both lie close to the line corresponding to $T = 2\ \mu$K (thick dashed green), which is most similar to the measured ensemble temperature.

The vertical lines correspond to the feature centres extracted in Fig. 5.6, where the shaded regions indicate the 1 σ error. The features at 30.1 G and 34.1 G are within error of the expected feature positions for an ensemble temperature of $\sim 1\ \mu$K. The remaining features at 101.4 G and 108.77 G are within error of the expectation for lower ensemble temperatures. We note

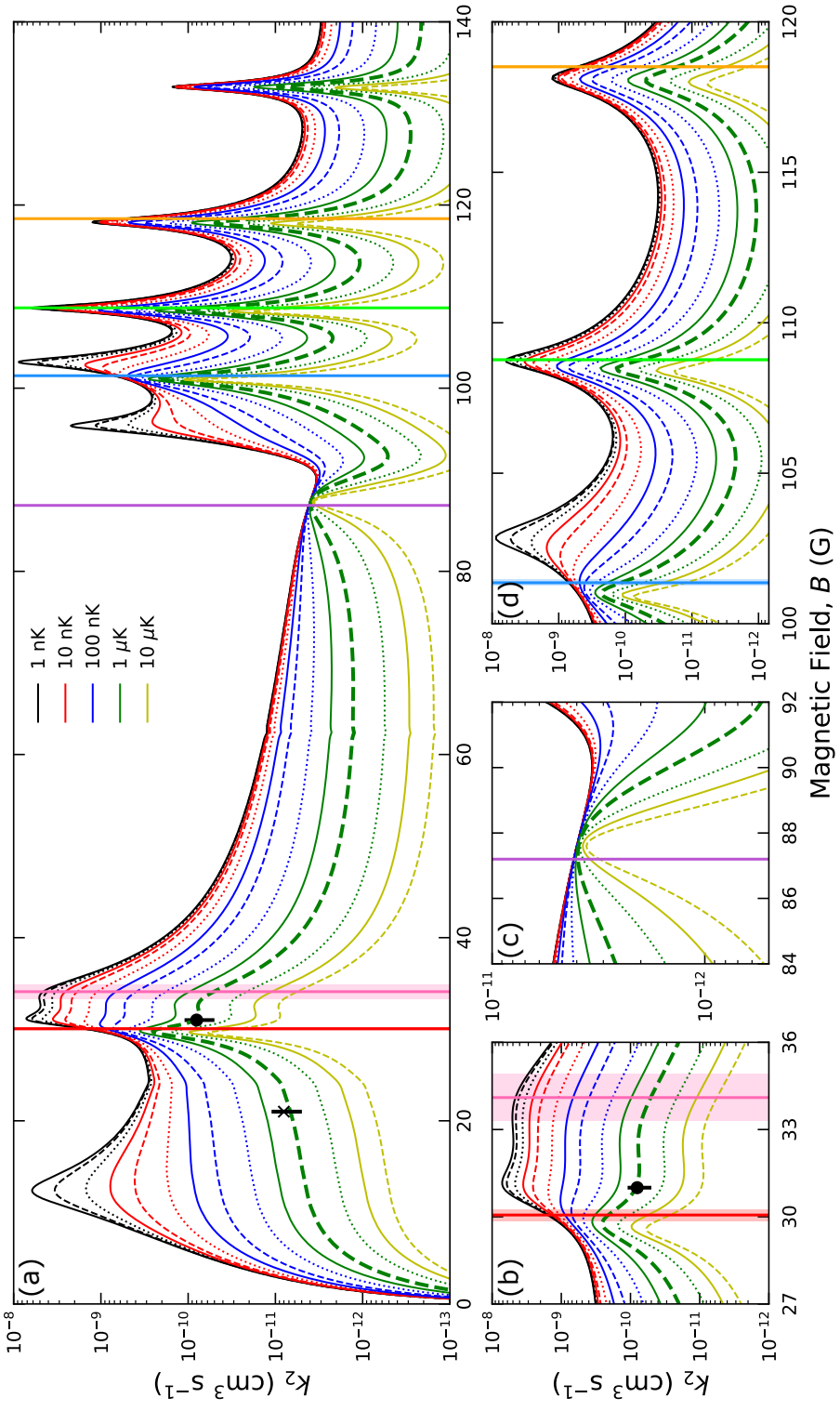

Figure 5.7: Theoretical k_2 loss rate coefficients for the ($f = 3, m_f = -3$) state of Cs as a function of magnetic field. The solid lines correspond to the collision energies listed in the legend. The dashed (dotted) lines of the same colour correspond to two (five) times the collision energy. The thick dashed green line is closest to the measured ensemble temperature. The vertical lines indicate centres of the loss features measured in the experiment. Subfigures (b-d) show zoomed views of the features. The black cross and circle are measurements of k_2 as described in the text.

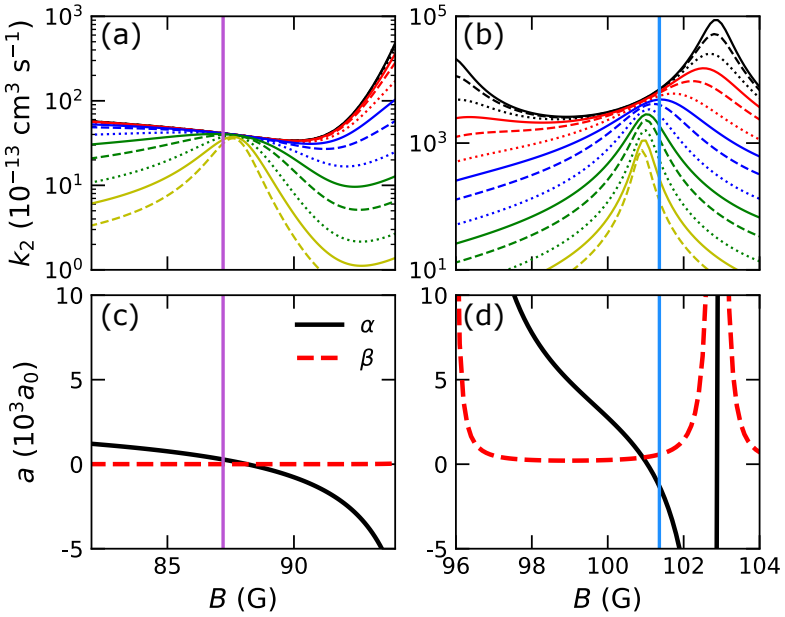

Figure 5.8: Shift of loss features at finite temperatures from peaks in β to zeroes in α for two example features. (a-b) Zooms of k_2 from Fig. 5.7(a). (c-d) Components of the complex scattering length $a = \alpha - i\beta$ at limitingly low energy. The vertical coloured lines correspond to resonances observed in Fig. 5.6. See ref. [243] for a fuller treatment of all features.

that the strong shift in the feature at 101.4 G from the resonance position at 103 G is due to the zero in α which occurs at 101 G (see Fig. 5.8(d)). The feature at 118.5 G is shifted from the expectation by ~ 0.5 G, which may be due to the uncertainty on the bias coil calibration of ~ 0.5 mG per Gauss applied. However, this is insufficient to fully explain the shift and suggests another contribution to the field offset during these measurements.

We were not able to resolve a feature corresponding to the resonance at 12 G. From Fig. 5.7(a), it is clear that at the collision energies used in our experiment, k_2 is strongly suppressed. An ensemble temperature of $\lesssim 50$ nK would be required to observe the feature, which would be challenging to achieve in a tweezer. We note that this suppression has also been observed in other experiments [263].

Finally, the loss feature we have measured in Fig. 5.6(c) does not correspond to the threshold-crossing of a bound state resonance. The feature corresponds to a zero-crossing in the real part of the scattering length. At finite E_{coll}, k_2 is more suppressed at neighbouring magnetic fields than at $\alpha \sim 0$, so a

peak is observed. This can be better understood by considering Fig. 5.8, which shows the real and imaginary parts of the complex scattering length $a = \alpha - i\beta$, calculated at limitingly low energy. As discussed in ref. [243], at limitingly low energy the observed loss features are expected to occur at peaks in β. However, at our finite experimental energies, where $k \neq 0$, if α or β are greater than zero, they cause a suppression in k_2, as seen from Eq. 5.13. The value of k_2 therefore tends to shift to zeros in α, where the suppression is somewhat lifted. Notably, the feature at ~ 88 G is shifted far from any peak in β, and coincides with the zero-crossing of α, seen in Fig. 5.8(c). Other features are similarly shifted towards zeros in α; for example the feature measured at 101.4(1) G is shifted 1.5 G from the peak in β at ~ 103 G.

The asymmetric feature corresponding to the zero in α is conveniently fit by a function with the form of a generalised Fano profile, from which we extract a centre of 88.0(3) G. Strikingly, k_2 is several orders of magnitude less than for the loss features attributed to Feshbach resonances. This is reflected in the parameters of the measurement, which were adjusted to increase the effective number of collisions measured by a factor of 30. A hold time of 250 ms was used, which is a factor of five longer than for the other features. Furthermore, we used a collision tweezer of depth ~ 330 μK, which is a factor of 11 greater than for the other measurements. Since $\bar{n}_2 \propto P^{3/4}$, the density was increased by a factor of six to $\approx 3 \times 10^{12}$ cm^{-3}.

5.2.7 Radiative Feshbach Spectroscopy of $(3, 3)$

The Cs ground state is $(f = 3, m_f = 3)$. Since there is no state of lower energy, inelastic f- and m_f-changing collisions do not occur, and so the two-body inelastic loss spectroscopy presented above cannot be used to detect resonances. Typically, resonances in the $(3, 3)$ state are measured by detecting three-body loss in a gas, or through thermalisation measurements [269].

Alternatively, radiative loss spectroscopy can be used to observe Feshbach resonances for Cs prepared in $(3, 3)$ [79, 265, 270]. This technique exploits the coupling of the scattering continuum to the bound state near a Feshbach resonance, as illustrated in Fig 5.9. When the magnetic field is tuned near

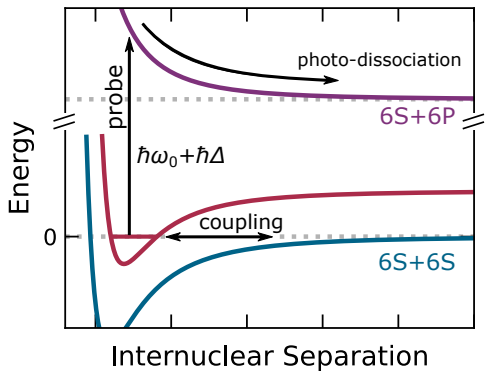

Figure 5.9: Radiative loss mechanism used to probe ($f = 3, m_f = 3$) Feshbach resonances. The magnetic field is tuned so that the free atom pairs (blue) are coupled to a weakly-bound Feshbach state (red). A probe beam is blue-detuned by a frequency $\Delta/2\pi = 47.2$ GHz with respect to the Cs D_2 transition. The molecular population is excited by the probe beam to a repulsive $1/r^3$ potential (purple), where it gains kinetic energy up to $\hbar\Delta$. When the molecule photo-dissociates, the imparted kinetic energy is enough to induce loss of both atoms from the $U/k_B = 30$ μK tweezer.

to a Feshbach resonance, some of the atomic population is coupled into the weakly-bound Feshbach state (red). The idea is to induce loss of the molecular population using a probe beam which is blue-detuned with respect to the Cs D_2 line. The probe beam couples the Feshbach molecules to a repulsive excited-state potential with a $1/r^3$ dependence due to the dipole-dipole interaction (purple). Excitation to the excited state occurs at the Condon radius R_C, given by $\hbar\Delta \approx C_3/R_C^3$ [271], where C_3 is the resonant dipole coefficient [70], calculated in ref. [272]. The detuning is chosen so that excitation by the probe beam occurs at extremely short interatomic distances, thereby affecting only the molecular population and not the unbound atoms. The excited molecules follow the repulsive potential and gain kinetic energy $\approx \hbar\Delta$. When the molecule photo-dissociates, the atoms are lost from the tweezer[10].

We induce loss of the Feshbach molecules using a probe beam aligned to the E/W axis of the cell, applied for the duration of the collision time. The probe is blue-detuned $\Delta/2\pi = 47.2$ GHz from the Cs D_2 line, conferring sufficient energy that both atoms are lost from the $U/k_B = 30$ μK collision tweezer. For Cs at this detuning, $R_C \approx 60$ Å. The probe beam is derived

[10]This is similar in concept to the enhanced loading of optical tweezers using blue-detuned light [230].

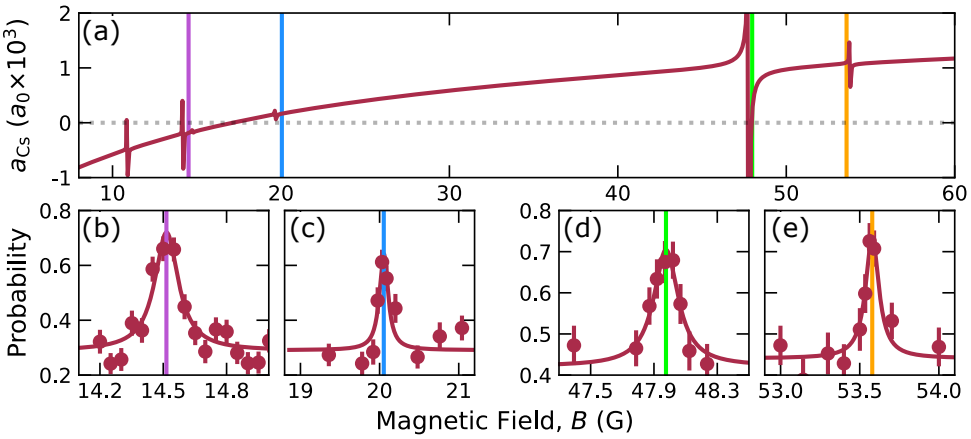

Figure 5.10: Radiative Feshbach spectroscopy of atom pairs prepared in the state ($f = 3, m_f = 3$). (a) Real part of the s-wave scattering length with external magnetic field for the Cs atoms prepared in $(3, 3)$. (Theory from [241]) The coloured lines correspond to the loss features measured in (b)-(e). (b) A beam blue-detuned by 47.2 GHz induces loss of molecules during a hold time at B. The probability of observing zero atoms is plotted. Resonance at 14.52(5) G. (c) Resonance at 20.05(2) G. (d) Resonance at 47.98(2) G. (e) Resonance at 53.58(2) G. The uncertainties quoted are calculated from the fit and calibration errors added in quadrature.

from an interference filter external cavity diode laser (IFECDL) [273] that is primarily used for RSC (section 6.2.2).

The resonances measured using this method are presented in Fig. 5.10. The scattering length for the Cs $(3, 3)$ state is shown in Fig. 5.10(a). Again, the scattering length data is obtained from ref. [241]. The vertical lines indicate the positions of the observed resonances, which are plotted in Fig. 5.10(b-e). The features plotted use the probability of observing zero atoms after the hold time. These resonances have previously been measured [264, 274], yielding narrow widths < 15 mG which result from relatively weak higher-order spin-orbit coupling [275].

The measured resonances are thermally broadened at the collision energy used in these experiments. We fit the features using a Lorentzian function to capture the feature centre and the FWHM. A more physically meaningful fit would be a Boltzmann profile, representing the thermal distribution, convolved with a narrow Lorentzian, capturing the transition linewidth [70, 265]. However, we have found that it is not possible to extract a useful information concerning the widths, since the Lorentzian and Boltzmann widths are

Table 5.2: Centres and widths of the extracted from Lorentzian fits to the observed Cs ($f = 3, m_f = 3$) loss features.

Bound State	Centre (G)	Γ (G)
$-2(33)4g(3)$	14.52(5)	0.14(3)
$-2(33)4g(4)$	20.05(2)	0.13(6)
$-2(33)4d(4)$	47.98(2)	0.19(5)
$x2g(2)$	53.58(2)	0.10(3)

highly covariant.

The features presented in Fig. 5.10(b-e) correspond to the bound states $-2(33)4g(3)$, $-2(33)4g(4)$, $-2(33)4d(4)$ and $x2g(2)$[11] [240]. We list the fitted centres and widths in table 5.2. The fitted centres of the features are similar to those previously measured [264], however as can be seen from Fig. 5.10(a), they are significantly shifted from the theoretical zero-energy resonance positions. This shift can likely be attributed to the fact that the theoretical resonance positions are not as accurately known for $(3, 3)$ as for $(3, -3)$, since they are calculated using Cs potentials determined from measurements of the $(3, -3)$ state [240, 268].

5.2.8 Three-Body Collisions

A natural extension to the two-body measurements presented thus far is to prepare three atoms in a single tweezer and search for evidence of three-body collisions. Making use of the atom number-control in the tweezers, loss from one-, two- and three-body processes can be individually resolved. Collisions of three ^{85}Rb atoms in a single optical tweezer have previously been investigated by Reynolds *et al* [213]. Such a scheme could be used, for example, to investigate Efimov physics [253, 276, 277]. Feshbach resonances of Cs in the $(3, 3)$ ground state are usually detected in a bulk gas by enhancement in the three-body recombination rate [79].

Three-body recombination occurs when three atoms interact to produce a

[11] x denotes that this bound state is of mixed $n(f_1 f_2)$ character, see ref. [240]

diatomic molecule and an atom. Near a Feshbach resonance, the three-body recombination rate is enhanced, scaling as a^4 [278]. The molecular binding energy E is released as kinetic energy, which is shared amongst the molecule and atom in the ratio $\frac{E}{3} : \frac{2E}{3}$. The enhancement in the three-body recombination rate can cause increased atomic loss near a resonance.

The energy released is dependent on the bound state formed in the recombination process, which depends on the scattering length. For recombination at $a > 0$, the near-threshold binding energy of the weakly-bound s-wave dimer formed is $E = \hbar^2/(\mu a^2)$, where μ is the reduced mass and a is the scattering length [279]. For $a < 0$, no weakly-bound state exists so that only recombination to a deeply-bound molecular state may occur [280]. As a result, the binding energy released is expected to be much larger than for recombination when $a > 0$. Atom loss may occur if the energy imparted to either recombination product is greater than the trap depth.

To investigate collisions of three atoms, we straightforwardly extend the scheme presented in Fig. 5.2. We use rearrangement to prepare 3 atoms in 56(2) % of experimental shots, which we merge into a single 1064 nm collision tweezer of depth $U/k_\mathrm{B} = 30$ μK without significant heating from trap imbalance. The tweezer subdivision imaging scheme remains the same. We prepare 3 Cs atoms in the internal ground state ($f = 3, m_f = 3$). In this lowest-energy state, two-body collisions are suppressed, so that the presence of three-body collisions should not be masked by extraneous loss processes. Loss is probed by measuring the one-, two- and three-atom survival probabilities as a function of the hold time in the collision tweezer.

We search for evidence of three-body loss at a magnetic field of 14.5 G, corresponding to the position of the Feshbach resonance identified in Fig. 5.10(c). Near 14.5 G, the background scattering length is negative, so that a deeply-bound dimer is expected to form during three-body recombination with a kinetic energy release much greater than the tweezer depth. We estimate the binding energy of the deeply-bound state to be $\sim$ 100 MHz, using the size of the below-threshold "bin" in which the molecular level lies [240]. A recombination event is therefore expected to induce loss of all three atoms from the shallow tweezer.

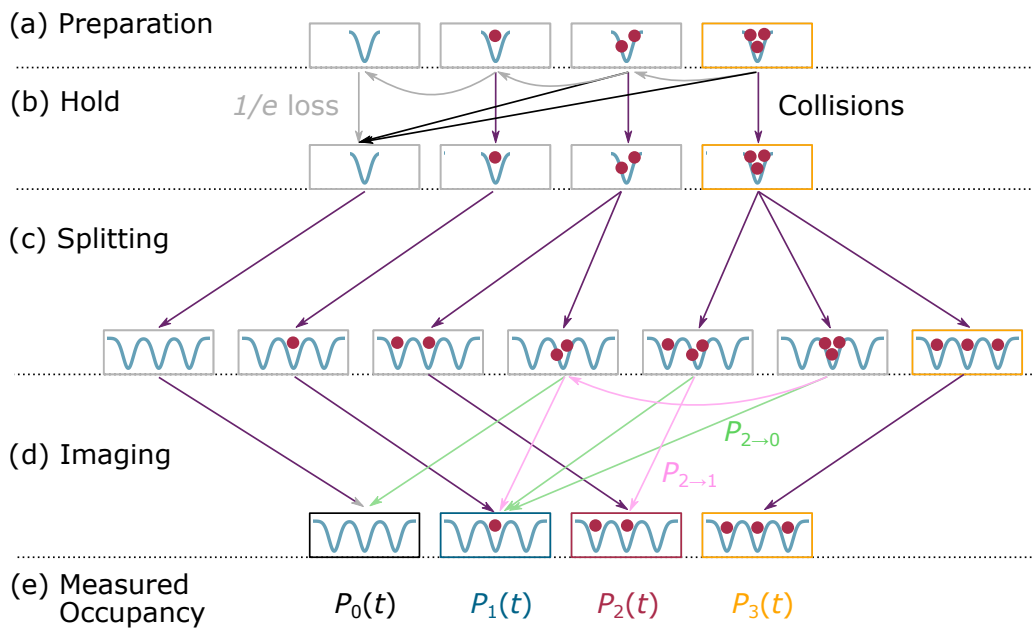

Figure 5.11: Probability tree of measurement outcomes evaluated by the Monte Carlo simulation. (a) The initial atom number is specified. (b) Atoms are lost through collisions or $1/e$ decay. Collisions are assumed to eject all atoms. (c) The atoms are split into the imaging array with many possible outcomes. Each splitting outcome is weighted by a combinatorial factor. (d) The imaging pulse induces light-assisted loss with probabilities $P_{2\to1}$ and $P_{2\to0}$, mapping the true survival probability onto a detected survival. Three atoms in the same tweezer may undergo consecutive light-assisted collisions, starting with $2 \to 1$ loss. (e) The probabilities P_0, P_1, P_2 and P_2 are those measured in the experiment.

The measurement is complicated by the probability for two or three atoms to end in the same tweezer after they are split for imaging, similarly to the discussion in section 5.2.5. Again, the effect of light-assisted collisions during imaging, inducing $2 \to 1$ or $2 \to 0$ loss, must be accounted for. For the case of three atoms split into the imaging array, there are many more possible outcomes, which form a large probability tree. Due to this complexity, we compare the measured time-dependent survival probabilities to a Monte Carlo simulation.

A simplified probability tree of outcomes evaluated by the simulation is presented in Fig. 5.11. During the hold time in the collision tweezer, a collision may occur (black arrows), which is assumed to eject all atoms. Loss may also occur due to the finite atom $1/e$ lifetime τ_1 (grey arrows). All atoms

survive if there is no loss (purple arrows). When the tweezers are split, there are several possible outcomes weighted by the factor which accounts for possible combinations. During imaging, if two or three atoms occupy the same tweezer, $2 \rightarrow 1$ (green) or $2 \rightarrow 0$ (pink) loss may occur. A small amount of $1 \rightarrow 0$ imaging loss is also accounted for (not shown). The outputs of the simulation P_0, P_1, P_2 and P_3 are compared against the experimentally measured survival probabilities for signs of collisional loss. Three-body loss is expected to map onto a suppression in P_3 due to transfer into other channels in step (b).

Our ability to post-select the experimental data on the number of atoms initially prepared is critical to this approach. By post-selecting for loading of one or two atoms, which occurs in ~ 50 % of experimental shots, we are able to constrain the parameters of the three-atom Monte Carlo simulation, allowing comparison to the three-atom data. Fig. 5.12 shows such a measurement, illustrating post-selection on loading of one, two or three atoms in subfigures (a-b), (c) and (d-e) respectively. We stress that the data presented in Fig. 5.12 are all post-selected from a *simultaneous* measurement.

By post-selecting on shots where one atom was loaded, we directly measure the splitting probability P_{split} into each imaging tweezer A (squares), B (triangles) and C (circles), as shown in Fig. 5.12(a). The splitting probability is input to the two- and three-body simulations on a point-by-point basis. This is necessary because the splitting probability exhibits a dependence on the hold time, which we attribute to cooling of the AOD which changes the diffraction efficiency. By post-selecting on the atom survival in any imaging tweezer, we extract the single-atom survival probability $P_1(t)$ at discrete hold times, as shown in Fig. 5.12(b). Here, the solid lines are the results of the Monte Carlo simulation run 2000 times and the shaded regions show the uncertainty on the simulation, which is computed using a functional approach[12] [281]. We also measure a small amount of $1 \rightarrow 0$ imaging loss $P_{1\rightarrow 0} < 0.01$. The measured splitting probabilities and single-atom survival probability are used to constrain the Monte Carlo simulation for two- and three- body collisions as we now discuss.

[12]The Monte Carlo simulation is a function of variables $f(\alpha, \beta, ...)$. In the functional approach, the errors are computed by evaluating the simulation for $f(\alpha + \xi_\alpha, \beta + \xi_\beta, ...)$

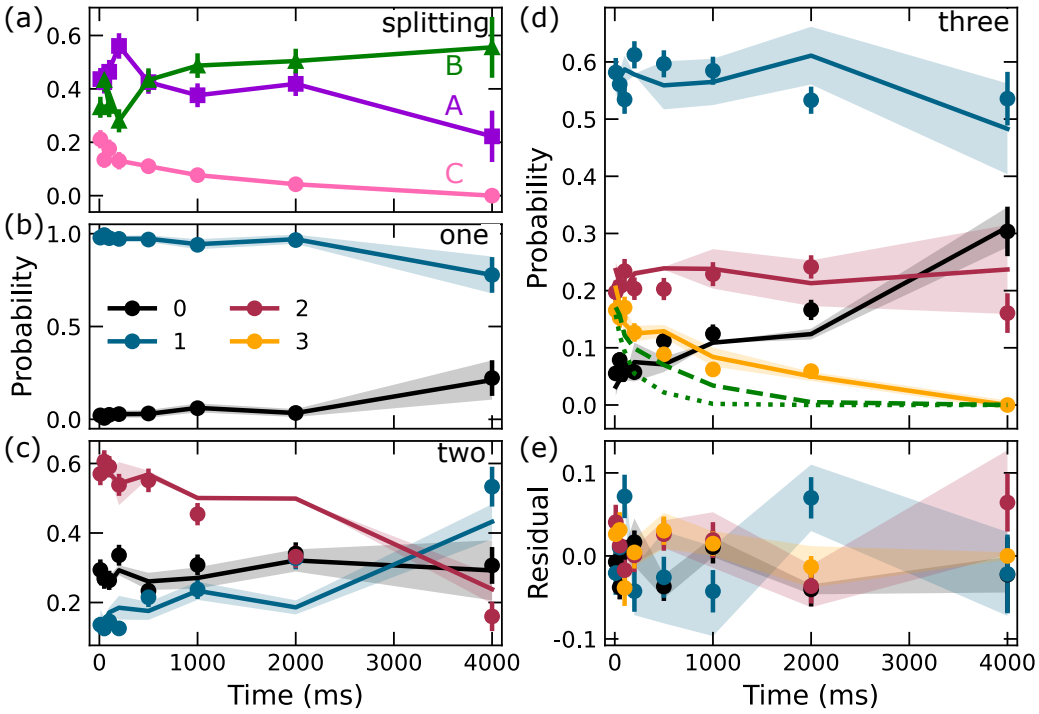

Figure 5.12: Preparation and post-selection of three atoms. The data points show measured survival probabilities and the solid lines are a Monte Carlo simulation with 2000 iterations. The shaded regions indicate the error in the simulation, computed functionally. The data is post-selected on the number of atoms initially loaded in the 3 starting tweezers. (a) One atom loaded initially. The data is post-selected on the final tweezer occupied after splitting, A (squares), B (triangles) or C (circles). (b) Post selection of shots where one atom was loaded initially. (c) Post selection of shots where two atoms were loaded initially. (d) Post-selection of shots where three atoms were loaded initially. The dashed (dotted) lines are simulations for $\tau_3 =$ 1000 ms ($\tau_3 = 300$ ms). (e) Residual of the data and Monte Carlo simulation in (d).

In Fig. 5.12(c), the data is post-selected on shots where two atoms were loaded. We expect $\Gamma_2 = \bar{n}_2 k_2 \sim 0$, since inelastic collisions are precluded in the $(3,3)$ ground state. At short hold times, the zero offset of the two-atom survival probability (red) is therefore attributed to light-assisted collisions when two atoms occupying the same optical tweezer are fluorescence imaged. The probability of $2 \to 1$ loss during imaging is determined from the one-atom survival data at 10 ms to be $P_{2\to1} = 0.32(1)$. The solid lines are a Monte Carlo simulation performed for two atoms, using the measured P_{split},

where ξ_i are the errors on the simulation parameters.

P_1 and $P_{2\to1}$, and setting $\Gamma_2 = 0$. Aside from an outlier at 2000 ms, the zero- (black), one- (blue) and two-atom (red) simulations are in agreement with the measured survival probabilities, indicating negligible two-body loss as expected. We note that the two-body survival P_2 decays exponentially with a $1/e$ time $\tau_2 \approx \tau_1/2$, since the probability for *neither* atom to be lost falls as $P_2 \propto (\exp -t/\tau_1)^2$. The two atom survival falls faster than $\tau_1/2$ because of the uneven P_{split} at longer hold times, which is accounted for in the simulation.

Finally, using the P_{split}, P_1 and P_2 measured individually each hold time, and the measured probabilities of imaging loss $P_{1\to0}$ and $P_{2\to1}$, we are able to compare the measurement post-selected on loading of three atoms to the Monte Carlo simulation. The three-atom survival is shown in Fig. 5.12(d) (yellow) and the residual with the simulation is shown in Fig. 5.12(e). The solid yellow line shows the simulation with the three-body loss rate Γ_3 constrained to zero. The three-atom survival at short hold time $P_3 \sim 0.20$ is consistent with the expected $\sim 6/27$ probability to split all three atoms into separate imaging tweezers. The exponential decay of P_3 is due to the $1/e$ three-atom lifetime of $\tau_3 \approx \tau_1/3$, which is calculated from the one-atom data presented in Fig. 5.12(b). As for P_2, P_3 decays faster than the expectation based on τ_1 because the splitting probabilities become uneven at longer hold times. The simulation of P_3 with $\Gamma_3 = 0$ is qualitatively in line with the measured data, indicating that any recombination occurs on a timescale slower than τ_3. The residual shown in (e) does not exhibit obvious structure indicating loss. For comparison, the dotted and dashed green lines in Fig. 5.12(d) show simulated decays for $\tau_3 = 300$ ms and $\tau_3 = 1000$ ms respectively.

There are several reasons which may explain why three-body loss was not detected. The main limitation was the short timescale available to measure three-body loss, since τ_3 was reduced by the uneven splitting probabilities. However, in the previous sections, we were able to perform Feshbach spectroscopy for hold times of ~ 50 ms. It is therefore possible that other effects limited Γ_3.

Recombination heating could occur if the released energy is insufficient to cause trap loss, so that the collision products remain in the trap with increased kinetic energy [254]. However, the binding energy of the deeply-

bound state formed is expected to be ~ 100 MHz [240] which is $200 \times U/h$, so we expect any collision to guarantee three-body loss. We probed recombination heating by briefly extinguishing the tweezer (see section 3.5.2) to map heating onto loss, however we observed no heating.

The measured three-body loss rate is given by the product $\Gamma_3 = \langle n^2 \rangle k_3$, where $\langle n^2 \rangle$ is the mean-squared density and k_3 is the three-body loss rate coefficient [282]. The low Γ_3 in the experiment is therefore likely due to the combination of a low atomic density, or unfavourably low k_3. We derive an expression for $\langle n^2 \rangle$ in Appendix E. For the trap frequencies and temperatures in the 30 μK collision tweezer, we estimate $\langle n^2 \rangle \sim 1 \times 10^{23}$ cm^{-6}. At 14.5 G, the scattering length is ~ -150 a_0, which allows us to estimate a (rather low) value of $k_3 \sim 1 \times 10^{-28}$ cm^6 s^{-1} from data presented in ref. [253]. The implied loss rate is $\Gamma_3 \sim 10^{-5}$ s^{-1}, so the non-appearance of loss in the current parameter regime is unsurprising.

Several improvements could be implemented in order to observe a three-body loss signal in the collision tweezer. Firstly, since $\langle n^2 \rangle \propto T^{-3}$, a reduction in the atom energy would significantly increase the collision rate. Similarly, enhancement could be gained using a deeper tweezer since $\langle n^2 \rangle \propto \bar{\omega}^6$. We estimate that in a tweezer of depth $U/k_\mathrm{B} = 10$ mK, where the energy of the $n = 0$ motional state is $E_0 \approx 0.3$ μK, that $\Gamma_3 > 1$ s^{-1}, which may be resolvable. We note that such improvements would be more comparable to the parameter regime used in the experiments of ref. [213], in which three-body loss was observed. Furthermore, an obvious improvement would be to perform the measurement at larger scattering length, where we could expect at least a 10-fold enhancement in k_3 [253].

5.3 Collisions of Rb + Cs Atom Pairs

Using the merging sequence established for the 814 nm and 938 nm tweezers in section 4.3.1, we now investigate interspecies atomic collisions using our system. This section is based on work published in ref. [173].

5.3.1 Interspecies Pair Density

We determine the pair overlap density for Rb and Cs in the 938 nm tweezer after merging using the following expression [283, 284], which we derive in Appendix E:

$$\bar{n}_2 = \left(\frac{1}{2\pi k_\mathrm{B}} \frac{m_\mathrm{Rb} \bar{\omega}_\mathrm{Rb}^2}{(T_\mathrm{Cs}/\beta^2 + T_\mathrm{Rb})} \right)^{\frac{3}{2}}. \tag{5.14}$$

Here, $m_\mathrm{Cs}\omega_\mathrm{Cs}^2 = \beta^2 m_\mathrm{Rb}\omega_\mathrm{Rb}^2$. We independently measure temperatures of $T_\mathrm{Cs} = 10(3)$ μK and $T_\mathrm{Rb} = 15(5)$ μK in the 938 nm tweezer after optimised merging. These are within error of the initial values indicating little heating from the merging process. We also measure the trap frequencies for each atom in the merged tweezer by parametric heating. The Cs trap frequencies are $\{\nu_x, \nu_y, \nu_z\} = \{54(5), 80(5), 12(1)\}$ kHz and the Rb trap frequencies are $\{\nu_x, \nu_y, \nu_z\} = \{40(4), 59(3), 9(2)\}$ kHz. For these parameters, we calculate a pair density of $n_\mathrm{Rb,Cs} = 5(2) \times 10^{12}$ cm^{-3}. From independent measurements, we estimate that the heating rate in the 938 nm optical tweezer following merging is 3 μK s^{-1} for Rb and 8 μK s^{-1} for Cs. For a hold time of 500 ms, the heating causes a 20 % reduction in $n_\mathrm{Rb,Cs}$ to $\sim 4 \times 10^{12}$ cm^{-3}, which is within error of the initial value.

5.3.2 Hyperfine State-dependent Rb + Cs collisions

In contrast to the ground-state Cs+Cs collision measurements already discussed, here we investigate two-body loss resulting from hyperfine-changing collisions between Cs and Rb in the 938 nm tweezer. The hyperfine energy splittings in the ground state of ^{87}Rb and Cs are $h \times 6.8$ GHz and $h \times 9.2$ GHz, respectively. If at least one atom is in the upper hyperfine state, then hyperfine-changing collisions can convert this energy (equivalent to > 100 mK, far in excess of the typical ~ 1 mK trap depths) into kinetic

energy shared between the two atoms [285], leading to loss of both atoms from the tweezer.

We probe the rate of hyperfine-changing collisions by varying the time t_{hold} for which the atoms are held together in the 938 nm tweezer before they are separated. There are four possible scenarios when the experiment is initialised: either zero atoms are loaded, one Rb is loaded, one Cs is loaded, or one Rb *and* one Cs atom are loaded, occurring with probabilities $P = 0.229(5),\ 0.224(5),\ 0.263(6),\ 0.284(6)$ respectively, measured over 6000 runs of the experiment. We post-select experimental runs where one Rb and one Cs atom were present in the first fluorescence image. Fig 5.13(a) shows the pair loss for a Cs and Rb pair prepared in a mixture of hyperfine and Zeeman states. Stray external magnetic fields are cancelled to < 0.1 G and no bias field is applied, in order to measure a collision rate averaged over m_f states. Loss due to m_f-changing collisions can be neglected since the energy splitting of Zeeman substates is much smaller than the trap depth. The pair survival probability decreases exponentially, with a commensurate increase in the probability of observing no atoms after the tweezers are separated. The non-zero probability of losing a single Cs atom is due to an artefact of the Cs fluorescence imaging, as discussed in section 3.4.1. The red (blue) dashed line indicates the expected probabilities of observing a single Rb (Cs) atom due to the loss of Cs (Rb) during imaging.

We now examine the loss rates for optically pumped atom pairs. Hyperfine-state optical pumping is achieved using the MOT beams to apply a 7 ms pulse of either cooling or repump light to each atom before the tweezers are merged. This allows the Cs atom to be prepared in either $6^2\mathrm{S}_{1/2}$ $f_{\text{Cs}} = 3$ or $f_{\text{Cs}} = 4$, and the Rb atom to be prepared in either $5^2\mathrm{S}_{1/2}$ $f_{\text{Rb}} = 1$ or $f_{\text{Rb}} = 2$. For optical pumping to both upper and lower hyperfine states, we measure fidelities greater than 99% at short experimental hold times for both Rb and Cs.

Optical pumping of both species gives rise to one of four possible hyperfine combinations for the atom pair: $\{(f_{\text{Rb}},\ f_{\text{Cs}})\} = \{(2,4);\ (2,3);\ (1,4);\ (1,3)\}$. We find that, for the hold times used in the experiment, spontaneous Raman scattering [175, 204] due to the intense 938 nm tweezer light leads to redistribution between the hyperfine states. We therefore analyse the loss of

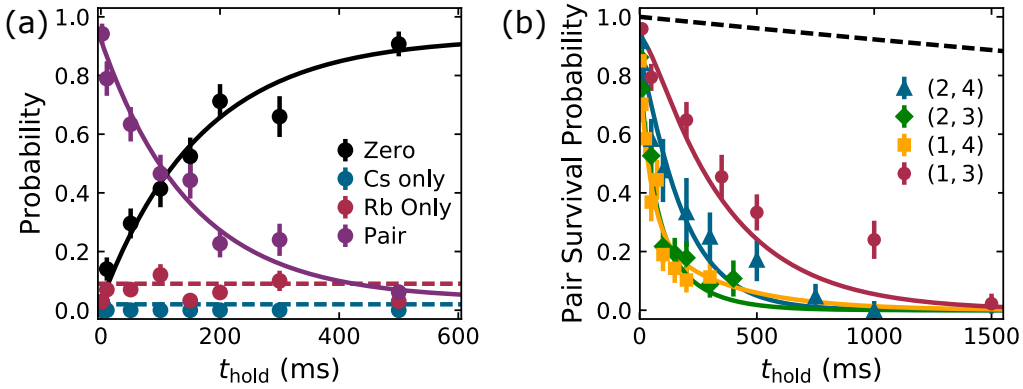

Figure 5.13: Rb and Cs collisions in an optical tweezer. (a) Rb and Cs atoms are merged into a single tweezer, without optical pumping, for a variable time t_{hold}. The pair survival probability (purple) is post-selected for events when a Rb and Cs atom are both loaded. The probability of measuring no atoms after t_{hold} is shown in black. The probability of observing just Rb or Cs is shown in red and blue respectively. The red (blue) dashed line is the expected single-atom Rb (Cs) signal expected due to loss of Cs (Rb) during imaging, extracted from experimental shots where only Cs (Rb) was loaded. (b) Pair survival probability of optically pumped Rb and Cs atoms, post-selected for pair loading events. Before the tweezers are merged, the atoms are first optically pumped to the hyperfine combinations $(f_{\text{Rb}}, f_{\text{Cs}}) = (2, 4)$ (blue triangles), $(2, 3)$ (green diamonds), $(1, 4)$ (yellow squares) and $(1, 3)$ (red circles). The solid lines are fitted to a coupled rate model as described in the text. The black dashed line is the expected pair survival for loss due only to background gas collisions.

atom pairs using a coupled rate model,

$$\frac{d}{dt}\begin{pmatrix} P_{24} \\ P_{23} \\ P_{14} \\ P_{13} \end{pmatrix} = \begin{pmatrix} -\Gamma_{24} - r_{\text{Cs}} - r_{\text{Rb}} & r_{\text{Cs}} & r_{\text{Rb}} & 0 \\ r_{\text{Cs}} & -\Gamma_{23} - r_{\text{Cs}} - r_{\text{Rb}} & 0 & r_{\text{Rb}} \\ r_{\text{Rb}} & 0 & -\Gamma_{14} - r_{\text{Cs}} - r_{\text{Rb}} & r_{\text{Cs}} \\ 0 & r_{\text{Rb}} & r_{\text{Cs}} & -r_{\text{Cs}} - r_{\text{Rb}} \end{pmatrix} \begin{pmatrix} P_{24} \\ P_{23} \\ P_{14} \\ P_{13} \end{pmatrix}, \tag{5.15}$$

where for example $P_{24}(t)$ is the survival probability of the $(2, 4)$ atom pair after a time t, and Γ_{24} is the pair loss rate. The loss rate Γ_{13} does not appear because there are no hyperfine-changing collisions when both atoms are in the lower ground-state manifold.

We include the fraction of spontaneous Raman scattering events which cause a change of f_{Rb} or f_{Cs} in our model by the addition of the rates r_{Rb} and r_{Cs}. We have independently measured these rates for Rb and Cs in the 938 nm

Table 5.3: Two body loss rates for Rb and Cs collisions in a merged optical tweezer. The experimental values are extracted from a rate equation fit to measured data, from which k_2 values are calculated using the effective pair density. The theory values are obtained from coupled-channel calculations as described in ref. [173].

$(f_{\mathrm{Rb}},\ f_{\mathrm{Cs}})$	$\Gamma/2\pi$ (s^{-1})	k_2(expt) $(\mathrm{cm}^3\ \mathrm{s}^{-1})$	k_2(theory) $(\mathrm{cm}^3\ \mathrm{s}^{-1})$
(2, 4)	4(1)	$9(4) \times 10^{-13}$	1.419×10^{-12}
(2, 3)	12(1)	$3(1) \times 10^{-12}$	1.118×10^{-12}
(1, 4)	14(1)	$3(1) \times 10^{-12}$	2.347×10^{-12}

tweezer. At the trap power used we find $r_{\mathrm{Cs}} = 3.9(7)$ Hz and use this to constrain the rate model. The spontaneous Raman scattering rate for Rb is very low due to the greater detuning of the tweezer wavelength from the atomic transitions. Our measurement of r_{Rb} is limited by the single-atom lifetime, indicating an upper limit of $r_{\mathrm{Rb}} < 0.02$ Hz. The true scattering rate is expected to be negligible, so we set $r_{\mathrm{Rb}} = 0$ in Eq. (5.15). We note that calculations using the method of ref. [204] indicate that r_{Cs} could be reduced by a factor of 100 if a (less species-selective) 1064 nm tweezer were used instead.

The measured pair survival probability after a variable hold time in the 938 nm tweezer following merging is shown in Fig. 5.13(b) for each hyperfine-pair combination. We fit Γ_{24}, Γ_{23} and Γ_{14} simultaneously to Eq. (5.15), obtaining the solid lines in Fig. 5.13(b). The extracted loss rates are summarised in table 5.3 for each hyperfine combination. The corresponding two-body loss rate constants, given by $k_2 = \Gamma/n_{\mathrm{Rb,Cs}}$, are also given. Our measured k_2 values are of a similar order of magnitude to those estimated from other (non-tweezer based) experiments on Rb + Cs collisions [286, 287]. The black dashed line shows the pair survival probability expected for loss due only to background gas collisions, using the experimental shots post-selected for loading of a single Rb or Cs atom. The measured $1/e$ lifetimes in this experiment are 26(5) s for Rb and 24(3) s for Cs. As noted above, collisional loss of pairs prepared in $(1, 3)$ is energetically forbidden. However population can leak from this pair state by spontaneous Raman scattering

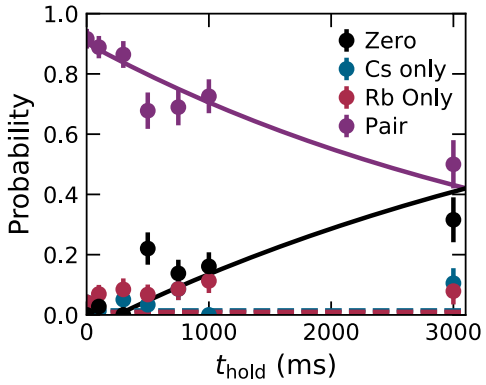

Figure 5.14: Collisions of a Rb+Cs atom pair in a 1064 nm tweezer, prepared in their internal ground states $(f_{\text{Rb}} = 1, m_{f,\text{Rb}} = 1)$ and $(f_{\text{Cs}} = 3, m_{f,\text{Cs}} = 3)$ respectively.

to other pair combinations where hyperfine-changing collisions are allowed, resulting in the slower observed pair loss rate from $(1, 3)$. We independently fit the $(1, 3)$ combination, yielding a $1/e$ time of 0.5(1) s.

The final column in table 5.3 lists theory values of k_2 determined by Jeremy Hutson using coupled-channel scattering calculations as detailed in ref. [173]. The values listed are degeneracy-averaged rate coefficients for a collision energy $E/k_{\text{B}} = 20$ μK. The calculations are approximately within the experimental error bars for $(f_{\text{Rb}}, f_{\text{Cs}}) = (2, 4)$ and (1,4), but rather outside them for (2,3). This can probably be attributed to factors such as uncertainties in the distribution of the initial population among $m_{f,\text{Rb}}$ and $m_{f,\text{Cs}}$.

5.3.3 Maximal-m_f Collisions in a 1064 nm Tweezer

We later repeated the above experiments after transferring the Rb and Cs pair to a 1064 nm collision tweezer (similarly to the Cs+Cs measurements), to reduce spontaneous Raman scattering. Furthermore, the Rb and Cs atoms were prepared in their maximal-m_f states $(f_{\text{Rb}} = 1, m_{f,\text{Rb}} = 1)$ and $(f_{\text{Cs}} = 3, m_{f,\text{Cs}} = 3)$ respectively, rather than a distribution of m_f states.

The result of the collision measurement is plotted in Fig. 5.14. The pair survival $1/e$ time (purple) is 4.1(9) s, which is a factor of 8 longer than the m_f-averaged case. Nevertheless, the presence of loss is surprising because there are no loss channels in the maximal-m_f configuration. This indicates

the presence of further m_f-changing processes, in spite of the greater tweezer detuning: likely this is due to a scattering of light from other sources that we were unable to eliminate.

We expect to perform magnetoassociation to form RbCs molecules from atoms in $(f_{\mathrm{Rb}} = 1, m_{f,\mathrm{Rb}} = 1)$ and $(f_{\mathrm{Cs}} = 3, m_{f,\mathrm{Cs}} = 3)$ in less than 10 ms. Since the $1/e$ pair decay time is a factor of ~ 400 longer, we do not expect spin relaxation to pose an obstacle to molecule formation.

Chapter 6

Conclusion and Outlook

In this thesis I have reported the preparation, control and collisions of ^{87}Rb and Cs atoms, using optical tweezers to prepare and detect the exact number of particles. The experiments described here constitute necessary steps towards the preparation of a single ground-state ^{87}Rb^{133}Cs molecule in an optical tweezer. The rich physics of interacting arrays of single molecules will be accessed by building upon the results of this work.

6.1 Conclusion

The experiments reported were performed in apparatus built from scratch. We described the design considerations and construction of the vacuum apparatus, electrodes and magnetic field coils. The laser systems for laser cooling and optical dipole trapping were presented and characterised. The need for a high-numerical aperture lens was motivated and *ex-situ* characterisation measurements were performed.

The apparatus was used to produce dual magneto-optical traps of Rb and Cs in a science cell, which served as a reservoir of $\approx 1 \times 10^6$ cold (15 μK) atoms. Atoms were loaded from the MOTs into optical tweezers of wavelengths 814 nm and 938 nm. We detailed constraints on the choice of tweezer wavelengths and demonstrated their species-selectivity. We presented characterisation measurements of the atom temperature, trap frequency, light shift and tweezer waists. We reduced the tweezer waists by optimally aligning the

objective and correcting for astigmatism.

Control and detection of the atomic hyperfine and Zeeman sublevels (f, m_f) was presented. We presented an optical pumping scheme for preparing a Cs atom in the maximal-m_f state ($f = 3, m_f = 3$) with a fidelity of 0.99(1) and demonstrated microwave transfer on the spin-stretched transition. We discussed limitations due to spontaneous Raman scattering, finding excellent agreement between experiment and theory which motivated use of a far-off resonant 1064 nm tweezer.

We demonstrated positional control of Cs in a 938 nm tweezer using an acousto-optic deflector. We characterised the AOD and detailed the resolution of technical issues, such as the variable diffraction efficiency and frequency beatnotes. We used this control to produce a 1D array of tweezers which were simultaneously characterised and equalised to < 0.5 %. Implementing array rearrangement, 2 Cs atoms were prepared with 0.84(2) probability and 3 atoms with 0.56(2) probability. Minimum-jerk sweeps of the tweezer were characterised and used to merge tweezers with no resolvable heating, preparing exactly one Rb and one Cs atom in the same optical tweezer.

We measured collisions of Rb and Cs atoms in single optical tweezer. We extracted hyperfine-state-dependent loss rate coefficients and compared them to theoretical results from coupled-channel calculations. Our results demonstrate that the precise control inherent in optical tweezer experiments holds great promise for the study of ultracold collisions of atoms and molecules.

Feshbach spectroscopy of Cs pairs prepared in $(f = 3, m_f = -3)$ was performed at fields up to 125 G, enabling observation of five Feshbach resonances and a zero in the scattering length. The extracted resonance positions and centres were comparable to earlier experiments in bulk gases [263, 264]. Using radiative loss spectroscopy, we observed four Feshbach resonances for Cs pairs prepared in $m_f = 3$. This technique allowed the observation of resonances using pairs of atoms in the lowest-energy channel, which are normally detected via three-body loss in bulk gases.

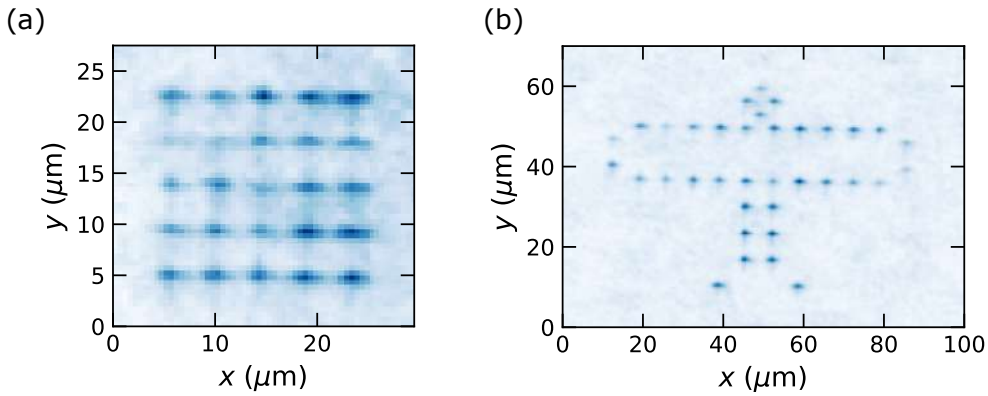

Figure 6.1: 2D arrays of wavelength 1064 nm produced using a SLM. Each image is an average of 500 fluorescence images of Cs atoms trapped in the array. (a) Demonstration of 25 tweezers in a 5×5 array. (b) Truly arbitrary geometries are possible: the Angel of the North is a local source of pride located 1.637×10^{10} μm from the tweezer array.

6.2 Outlook

I leave the project at an exciting time. Building on the work of this thesis, the experiment continues to expand and progress in new directions. Here we discuss some ongoing research goals and give a flavour of what is to come.

6.2.1 2D Arrays of Rb and Cs

Production of arrays of molecules will require extension of the array techniques described in Chapter 4 to Rb, and to two orthogonal axes.

The SLM installed in the 1064 nm tweezer path can be used to create arbitrary arrays of tweezers with low off-resonant scattering rates. Fig. 6.1(a) shows a 5×5 array of 1064 nm tweezers containing Cs, with trap depths ≈ 0.4 mK. As shown in Fig. 6.1(b), truly arbitrary arrays may also be realised. The SLM may also be used to correct for optical aberrations and modify the tweezer axial profile to increase the axial trapping frequency [215].

At the time of writing, a 2D crossed-AOD[1] driven by a second AWG is being characterised. This will be installed in the 814 nm tweezer path to realise 2D arrays of Rb atoms. Rearrangement of 1D Rb arrays will be straightforwardly

[1] AA Opto-Electronics AA.DTS.XY-400

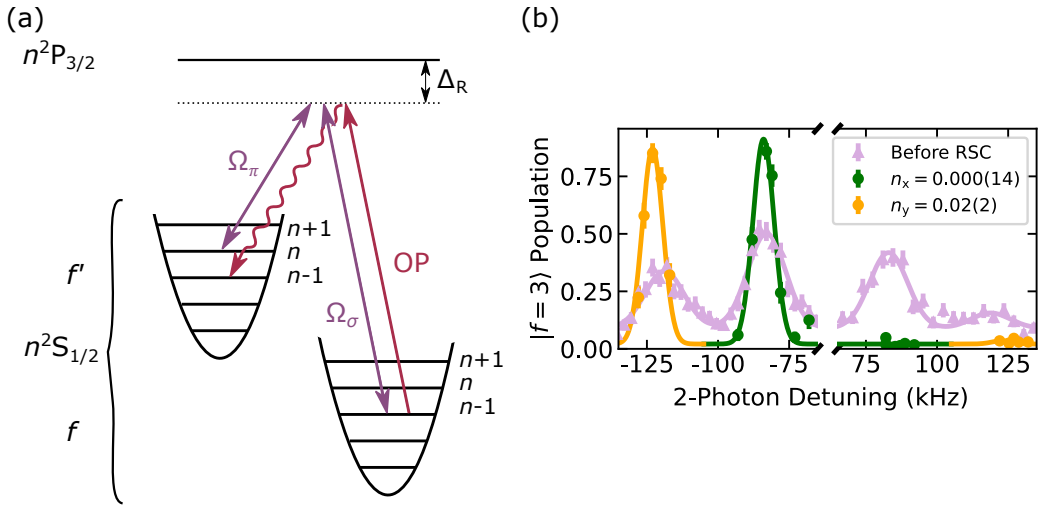

Figure 6.2: Raman sideband cooling. (a) Diagram of the RSC scheme for Rb and Cs. (b) Raman sideband spectroscopy of Cs in the radial x and y directions before (circles) and after (pink triangles) Raman sideband cooling. The suppressed peaks after RSC reveal that the ensemble has successfully been cooled to the motional ground state.

achieved by extending the scheme demonstrated in Chapter 4 so that very soon, arrays of both Rb and Cs atoms will be prepared with rearrangement-enhanced loading probabilities [216]. Improved rearrangement of 938 nm arrays and reduction of noise could easily be achieved by swapping the laser source for a higher-power alternative. SLM and AOD techniques could be combined to facilitate 2D rearrangement of an SLM array [103].

6.2.2 Dual-Species Raman Sideband Cooling

Raman sideband cooling (RSC) is a technique which can be applied to transfer the Rb and Cs ensembles, initially distributed thermally across the motional states of the tweezer, to a single quantum state (with 3D motional occupancy $n = 0$) [125–127, 198, 288, 289]. RSC is essential to the production of a single ^{87}RbCs molecule in optical tweezers, since the probability of magnetoassociation depends on the overlap density of the atoms [79]. Furthermore, the motional level of the molecule formed is inherited from that of the initial atoms [110]. This allows the preparation of a molecule in a single quantum state, making it an excellent candidate for quantum computation schemes [6, 116, 117, 120].

The principle of Raman sideband cooling is illustrated in Fig. 6.2(a). Two Raman beams (purple arrows), detuned $\Delta_R > 40$ GHz from the excited state and offset by the hyperfine ground state splitting address the spin-stretched transition. The Raman beams are used to drive a two-photon Raman transition, which reduces the motional level by $n \to n-1$. An optical pumping pulse (red arrow) returns the atom to the initial hyperfine manifold. Through many repetitions of this sequence using multiple Raman beam pairs addressing both radial and axial trap axes, the atom motional level is incrementally stepped to $n = 0$.

Raman sideband cooling of Rb and Cs has been developed in parallel to the work of this thesis [229]. Fig. 6.2(b) shows Raman sideband spectroscopy of a Cs ensemble before (circles) and after (pink triangles) Raman sideband cooling. After sideband cooling, the right peaks corresponding to $n \to n-1$ transitions are greatly suppressed compared to the left peaks, which correspond to driving $n \to n+1$ transitions. The probability to occupy the ground state can be extracted from the ratio of the sideband amplitudes $P_{n=0} = (1 - A_{\mathrm{RSB}}/A_{\mathrm{BSB}})$ [290]. Following RSC, Rb and Cs have been prepared in the motional ground state with final $P_{n=0}^{\mathrm{Rb}} = 0.85(4)$ and $P_{n=0}^{\mathrm{Cs}} = 0.94(2)$. Furthermore, they have been transferred to the same tweezer using the methods described in Chapter 4 with a final joint motional ground-state occupancy of 0.81(3).

6.2.3 Magnetoassociation

With Rb and Cs atoms prepared in a single optical tweezer [173] (4.3.1) and cooled the ground state [229], magnetoassociation across a Feshbach resonance (section 5.1.2) may proceed [71, 79]. Magnetoassociation will be performed using the established scheme for ^{87}RbCs molecules demonstrated for a bulk gas here in Durham [193, 291] and in Innsbruck [89], which uses Rb and Cs atoms pumped to their absolute ground states $(f = 1, m_f = 1)$ and $(f = 3, m_f = 3)$ respectively (section 4.1.3).

Magnetoassociation is performed by ramping a magnetic field through an avoided crossing at B_0, as shown in Fig. 6.3. The avoided crossing occurs near a Feshbach resonance as the energies of the free and bound states are tuned

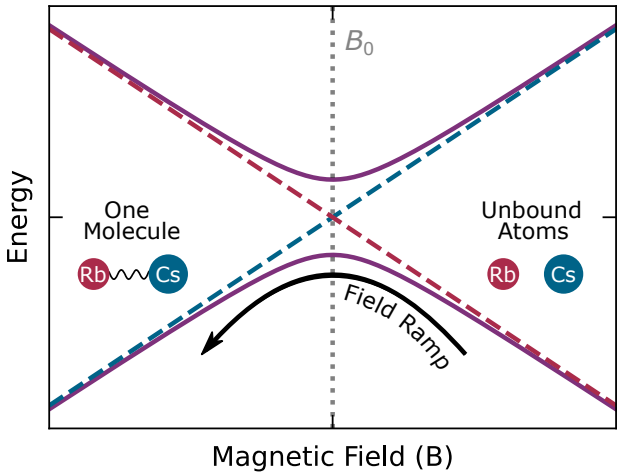

Figure 6.3: Magneto-association of Rb and Cs to form a weakly-bound Feshbach molecule using a Feshbach resonance at B_0 (dotted line). The dashed lines show the free (red) and bound (blue) states in the absence of coupling. The external magnetic field is adiabatically ramped downwards through an avoided crossing (purple lines) at the Feshbach resonance, converting the free atoms to a weakly-bound pair.

into resonance. By ramping the field adiabatically through the resonance, the atoms are made to follow the avoided crossing and are coupled into the bound state. Magnetoassociation to form ^{87}RbCs will be performed by sweeping across the interspecies Feshbach resonance at 197 G, producing molecules in a near-threshold state with a binding energy of $\sim$ 150 kHz [193]. The molecules can be transferred to a more deeply bound state with a binding energy of several MHz, by ramping the field further over a second resonance at 181 G [292].

After optimisation, the reported conversion efficiency into RbCs molecules in the bulk gas experiment in Durham is 2.5 %, yielding around 5000 optically trapped molecules [193]. The conversion efficiency in bulk gases is normally limited by the phase-space density [293] and is reduced by inelastic collisions with the residual atomic population. Magnetoassociation in an optical tweezer is expected to be far more efficient, circumventing these limitations due to the tight confinement and number-control respectively. Magnetoassociation of a NaCs molecule in an optical tweezer has been reported [110]. The reported conversion efficiency from thermal atoms to Feshbach molecules was limited by the RSC fidelity to 47(1) %; the magnetoassociation sweep

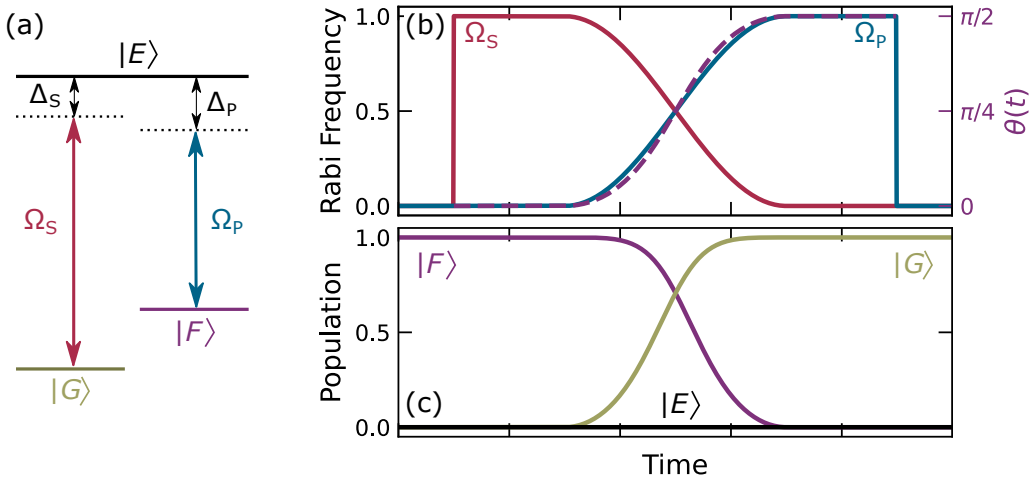

Figure 6.4: Feshbach molecules are transferred to the rovibrational ground state using STIRAP. (a) Lambda-type system established for STIRAP. (b) Time evolution of the pump and Stokes beams' Rabi frequencies. The dashed line shows the resulting variation in mixing angle θ. (c) Fractional population distribution. Ideally the molecules are transferred from $|F\rangle$ to $|G\rangle$ without populating $|E\rangle$.

was $>$ 99 % efficient. Given our current RSC fidelity, we may therefore expect a conversion efficiency of $\sim$ 80 % from thermal atoms to Feshbach molecules.

6.2.4 STIRAP: Transfer to the Ground State

Finally, the weakly-bound ^{87}RbCs Feshbach molecule must be transferred to the rotational and vibrational (rovibrational) ground state. This will be achieved using the technique of STImulated Raman Adiabatic Passage (STIRAP) [294, 295], which too is well-established for bulk ^{87}RbCs samples [81, 90, 296].

The principle of STIRAP is to coherently transfer molecules in the Feshbach state $|F\rangle$ to the rovibrational ground state $|G\rangle$ via an intermediate excited state $|E\rangle$, forming the three-level lambda-type system shown in Fig. 6.4(a). The three states are optically coupled: a "pump" beam couples $|F\rangle$ and $|E\rangle$ with Rabi frequency Ω_P and a "Stokes" beam couples $|E\rangle$ and $|G\rangle$ with Rabi frequency Ω_S. The beams are detuned from $|E\rangle$ by Δ_P and Δ_S respectively.

The three-level system has the Hamiltonian [294]:

$$\hat{H}(t) = \frac{\hbar}{2}\begin{bmatrix} 0 & \Omega_{\mathrm{P}}(t) & 0 \\ \Omega_{\mathrm{P}}(t) & 2\Delta_{\mathrm{P}} & \Omega_{\mathrm{S}}(t) \\ 0 & \Omega_{\mathrm{S}}(t) & 2(\Delta_{\mathrm{P}} - \Delta_{\mathrm{S}}) \end{bmatrix}. \tag{6.1}$$

The eigenstates of $\hat{H}(t)$ for the case of two-photon resonance, $\Delta_{\mathrm{P}} = \Delta_{\mathrm{S}} = 0$, are given by the following linear combinations of $|F\rangle$, $|E\rangle$ and $|G\rangle$:

$$|a^{+}\rangle = \sin\theta \sin\phi\,|F\rangle + \cos\phi\,|E\rangle + \cos\theta \sin\phi\,|G\rangle\,, \tag{6.2a}$$

$$|a^{0}\rangle = \cos\theta\,|F\rangle - \sin\theta\,|G\rangle\,, \tag{6.2b}$$

$$|a^{-}\rangle = \sin\theta \cos\phi\,|F\rangle - \sin\phi\,|E\rangle + \cos\theta \cos\phi\,|G\rangle\,. \tag{6.2c}$$

θ and ϕ are time-varying mixing angles, defined:

$$\tan\theta = \frac{\Omega_{\mathrm{P}}}{\Omega_{\mathrm{S}}}, \tag{6.3}$$

$$\tan 2\phi = \frac{\sqrt{\Omega_{\mathrm{P}}^2 + \Omega_{\mathrm{S}}^2}}{\Delta_{\mathrm{P}}}. \tag{6.4}$$

Transfer of population to $|E\rangle$ is to be avoided, since subsequent spontaneous emission would leak population to optically unaddressed states. The eigenstate of interest is therefore $|a^0\rangle$ which is a dark state with no $|E\rangle$ component. Since the population is prepared in $|F\rangle$ after magnetoassociation, if the mixing angle θ could be swept from 0 to $\pi/2$, it would be possible to transfer the molecular population from $|F\rangle$ to $|G\rangle$ with no accumulation in $|E\rangle$. The temporal profile of the Rabi frequencies $\Omega_{\mathrm{S}}(t)$ and $\Omega_{\mathrm{P}}(t)$ which produce this behaviour are shown in Fig. 6.4(b). Ω_{S} is ramped on first so that all population is initialised in the dark state, since $|a^0\rangle$ will be the only eigenstate with a non-zero $|F\rangle$ component. The Stokes beam is ramped off as the pump beam is ramped on, yielding the correct evolution of θ, shown by the dashed line. The idealised transfer of population which results is plotted in Fig. 6.4(c).

Using this technique, a one-way transfer efficiency for a bulk RbCs sample of 92 % [81] has been reported in Durham. The efficiency is limited by the adiabaticity of the dark state evolution as θ is tuned. Experimentally, decoherence of the pump and Stokes beams and the finite transfer time result in some population coupling to $|E\rangle$, where it is lost by spontaneous decay [295].

We expect STIRAP to be readily applicable to a single ^{87}RbCs Feshbach molecule in an optical tweezer. Transfer to the ground state using STIRAP has already been demonstrated for ^{40}KRb molecules confined to an optical lattice [297]. More recently, an array of NaCs molecules in an optical tweezer array was transferred to the ground state with 82 % efficiency, via Raman transfer instead of STIRAP [112, 113]. We estimate, using our RSC efficiency and expected magnetoassociation and STIRAP efficiencies, that the total conversion efficiency from thermal atoms to ground-state molecules will be around 70 %. Extension of magnetoassociation and STIRAP to an array of tweezers is expected to be relatively straightforward, requiring a power-equalised array like the one realised in section 4.2.3.

6.2.5 New Horizons: a Hybrid Quantum System

An exciting new research direction for the project will be to interface ground-state polar molecules with rubidium Rydberg atoms [109] also confined in optical tweezers. The hybrid system will be take advantage of the long rotational coherence times of ultracold molecules and the large interaction energies of Rydberg atoms. Such a scheme could be used for non-destructive readout of the molecular state [122, 123]. Alternatively, a Rydberg atom could be used to mediate fast quantum gates operations between molecules [298]. Research will also focus on the production of Giant Polyatomic Rydberg Molecules (GPRyM), which are triatomic bound states formed by a Rydberg atom and an ultracold polar molecule interacting via the charge-dipole interaction [299, 300].

6.3 Concluding Remarks

The techniques demonstrated in this thesis have enabled the control and study of collisions of individual Rb and Cs atoms. Production of single ^{87}RbCs atoms will soon be realised using trusted methods, opening up a myriad of applications in quantum science. It truly is an exciting time for atomic and molecular physics: the full and exquisite control of microscopic quantum systems of atoms *and* molecules is now within our grasp.

Appendix A

Magnetic Field Coil Data

Here we present more detailed information on the characterisation of the magnetic field coils discussed in section 2.4.

A magnetic field coil of radius R with N turns carrying current I may be treated as a single coil carrying current NI by assuming the differing positions of each coil turn can be ignored:

$$B(z) = \frac{\mu_0 N I R^2}{2\Big(R^2 + z^2\Big)^{3/2}}, \tag{A.1}$$

where μ_0 is the permeability of free space and z is the axial coordinate. The field produced by multiple coils is additive. If two coils of identical radius and current are separated by a distance S, the axial field is:

$$B(z) = \frac{\mu_0 N I R^2}{2}\left(\frac{1}{\Big(R^2 + \Big(z + \frac{S}{2}\Big)^2\Big)^{3/2}} \pm \frac{1}{\Big(R^2 + \Big(z - \frac{S}{2}\Big)^2\Big)^{3/2}}\right). \tag{A.2}$$

If the current in each coil is driven in the same-sense, the plus is taken since the fields add. In the opposite-sense configuration, the minus is taken since the fields cancel each other. The field gradient is obtained by taking the

derivative of Eq. (A.2):

$$\frac{\partial B(z)}{\partial z} = \frac{-3\mu_0 N I R^2}{2}\left(\frac{z+\frac{S}{2}}{\left(R^2+\left(z+\frac{S}{2}\right)^2\right)^{5/2}} \pm \frac{z-\frac{S}{2}}{\left(R^2+\left(z-\frac{S}{2}\right)^2\right)^{5/2}}\right). \quad \text{(A.3)}$$

Again, the plus sign is taken if the coil currents are same-sense, in which case the magnetic field gradient at the centre of the coils is zero. The field curvature $\partial^2 B/\partial z^2$ at this position can be non-zero however. The curvature can be minimised to zero in the Helmholtz configuration, which occurs for $S = R$.

Alternatively the coil currents can be driven in an opposite-sense configuration to produce a magnetic field gradient. In this case, the minus sign is taken and the field gradient Eq. (A.3) is non-zero. The configuration resulting in the most uniform field gradient is called the anti-Helmholtz configuration. Here, the second derivative of the gradient (i.e. the third derivative of Eq. (A.2)) is set to zero and evaluated. One finds that the anti-Helmholtz configuration occurs when $S = \sqrt{3}R$ [301].

The six coil pairs used in the experiment were discussed in Chapter 2. Five of the pairs are same-sense: shim coil pairs, the jump coils and the bias coils. Additionally, the jump and bias coils are arranged in the Helmholtz configuration. The quadrupole field coils are run opposite sense and are arranged in the anti-Helmholtz configuration. The shim coils are labelled either with respect to the lab, or with respect to the more convenient tweezer coordinate system, with the mappings N/S$\leftrightarrow x$, E/W$\leftrightarrow y$ and U/D$\leftrightarrow z$

The coils were characterised using an axial Hall probe (Hirst Magnetics GM08 Gaussmeter), which was used to measure the axial magnetic field along the central axis of the coils. By least-squares fitting the measured field profile, it is possible to extract the Gauss per Amp and Gauss per Amp per centimetre values of the coil pairs. This is more simply accomplished by working in terms of 'equivalent coils', which treats each coil as having infinitesimal thickness and a single turn, $N = 1$ in Eq. (A.2) [302]. Fitting with S and R as free parameters yields the radius and separation of the equivalent coils R_{eq} and S_{eq} respectively.

All the coils are made from insulated copper wire. The MOT, Feshbach and

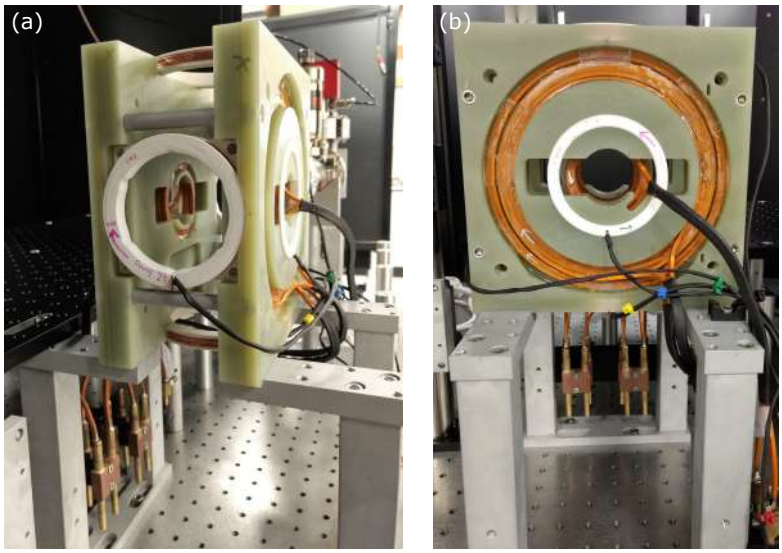

Figure A.1: Photographs of the coil assembly before installation in the final position. (a) Photograph from the front corner of magnetic field coil assembly. (b) Side view of the coil assembly.

jump coils are made from square 3.5 × 3.5 mm wire with a hole through the core of diameter 2 mm for water-cooling. The MOT, Feshbach and jump coils are all water-cooled due to the power dissipated through them. The shim coil wire is circular with 1 mm diameter and is not water-cooled.

For each coil we now list useful values and present measurements of their field profiles through their axis of symmetry, from which equivalent coil values are determined.

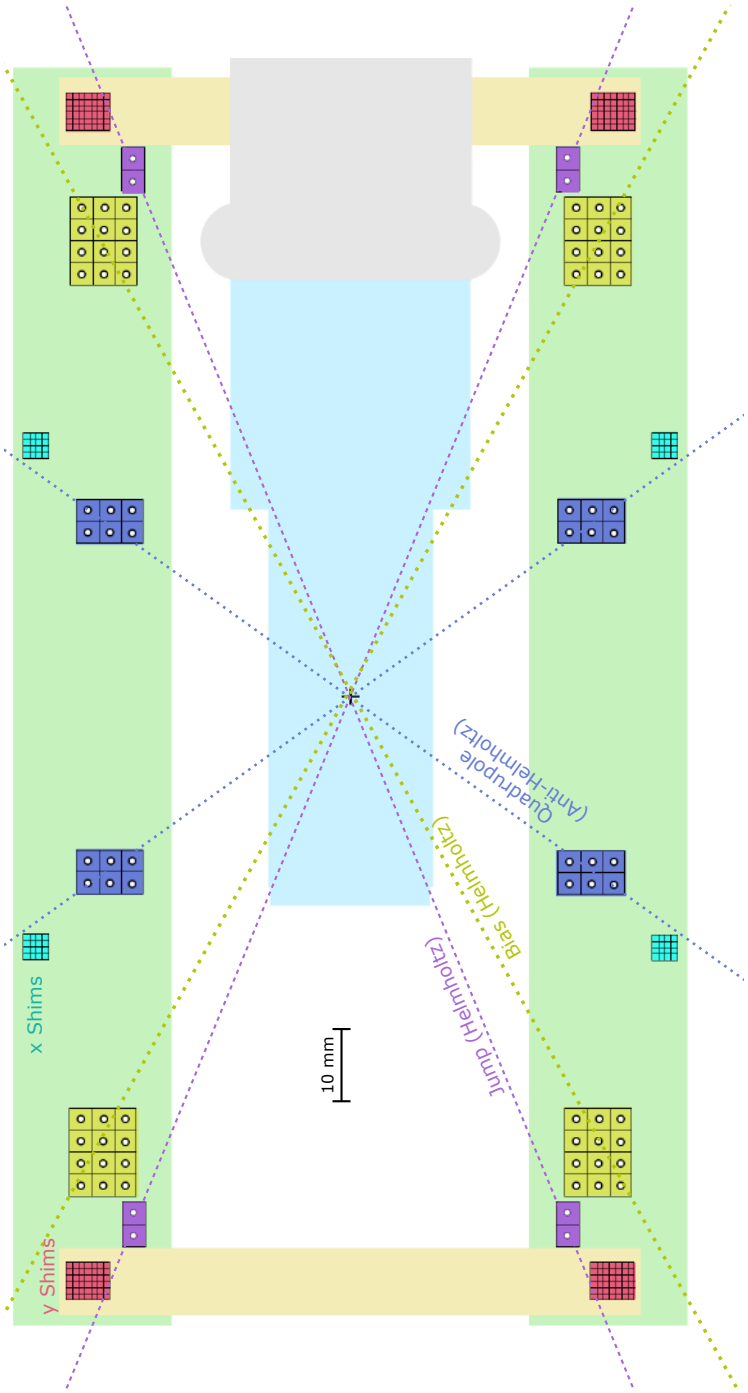

Figure A.2: Cross-section through the horizontal plane of the science cell and magnetic field coils. The z shim coils (U/D) are into the plane of the page and are not shown. The dashed lines indicate the Helmholtz and anti-Helmholtz conditions for the jump, bias and quadrupole coils. The science cell, 3D-printed and G10 mounting are shown for reference.

A.1 Quadrupole (MOT) coils

The MOT coils are used to generate the quadrupole field required for magneto-optical trapping of rubidium and caesium vapours, which is the first stage of the experiment.

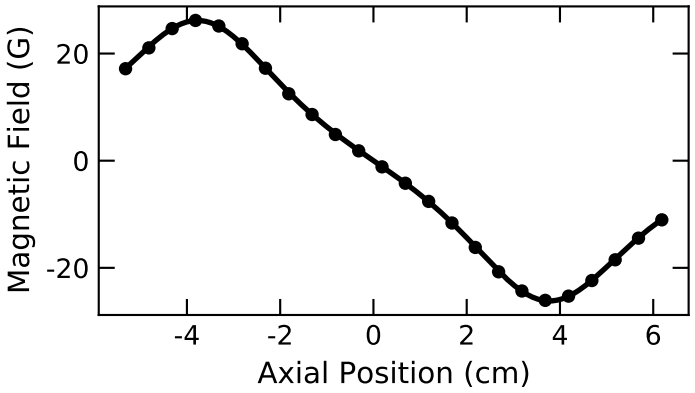

Figure A.3: Axial field of the MOT coils at a current of 20.00(1) A. The solid line is an equivalent coil fit to the data. Errorbars estimated due to noise are ± 0.15 G and too small to be seen.

Equivalent coil value	Value	Error (±)
R_{eq} (cm)	2.77	0.01
S_{eq} (cm)	7.47	0.01
Field (G A^{-1})	0.000	0.001
Gradient (G A^{-1} cm^{-1})	0.2992	0.0006
Wire gauge (mm)	3.5×3.5	-
Resistance per coil pair (mΩ)	3.76	0.05
N_{turns}	3×2	-

Table A.1: Equivalent coil parameters and associated errors obtained from fitting the measured data with Eq. (A.3).

A.2 Bias Coils

The Bias coils are used to generate a magnetic bias field of ~ 200 G, which is sufficient for magnetoassociation of ^{87}Rb and ^{133}Cs into a weakly-bound Feshbach molecule.

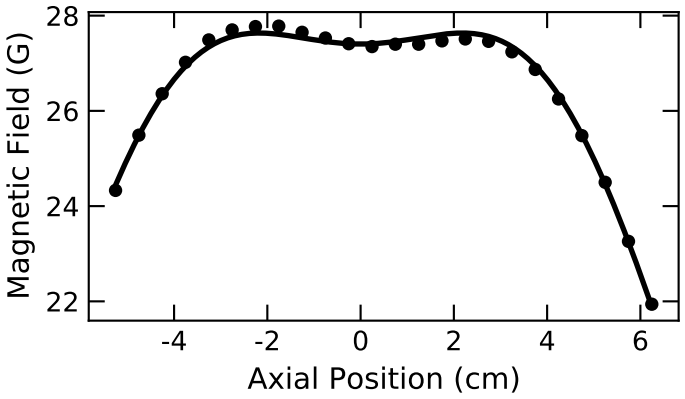

Figure A.4: Axial field of the Feshbach coils at a current of 20.00(1) A. The solid line is an equivalent coil fit to the data. Errorbars estimated due to noise are $\pm$ 0.15 G and too small to be seen. We note the asymmetry not captured by the fit, which is due to differences in the winding of each coil and is particularly noticeable due to the low winding number.

Equivalent coil value	Value	Error ($\pm$)
R_{eq} (cm)	7.29	0.09
S_{eq} (cm)	8.07	0.04
Field (G A^{-1})	1.3702	0.0004
Curvature (G A^{-1} cm^{-2})	0.059	0.007
Wire gauge (mm)	3.5×3.5	-
Resistance per coil pair (mΩ)	20.16	0.05
N_{turns}	3×4	-

Table A.2: Equivalent coil parameters and associated errors obtained from fitting measured data with Eq. (A.2).

A.3 Jump Coils

The jump coils are allow for for rapid changes in the bias field due to their fewer turns compared to the bias coils.

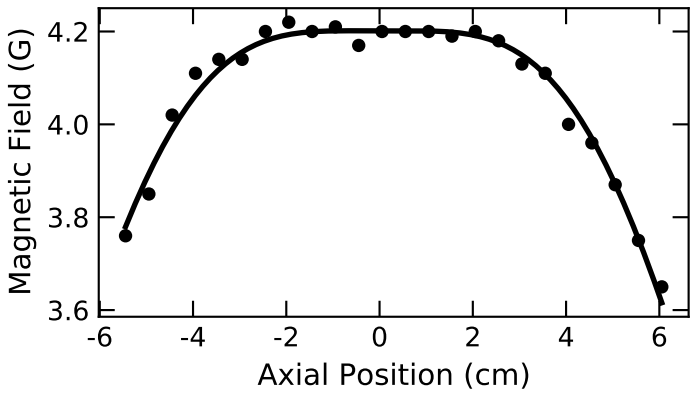

Figure A.5: Axial field of the jump coils at a current of 20.00(1) A. The solid line is an equivalent coil fit to the data. Errorbars estimated due to noise are ± 0.15 G and too small to be seen.

Equivalent coil value	Value	Error (±)
R_{eq} (cm)	8.9	0.3
S_{eq} (cm)	9.0	0.1
Field (G A^{-1})	0.2101	0.0001
Curvature (G A^{-1} cm^{-2})	0.0063	0.0009
Wire gauge (mm)	3.5×3.5	-
Resistance per coil pair(mΩ)	3.89	0.05
N_{turns}	1×2	-

Table A.3: Equivalent coil parameters and associated errors obtained from fitting measured data with Eq. A.2.

A.4 U/D (z) Shim Coils

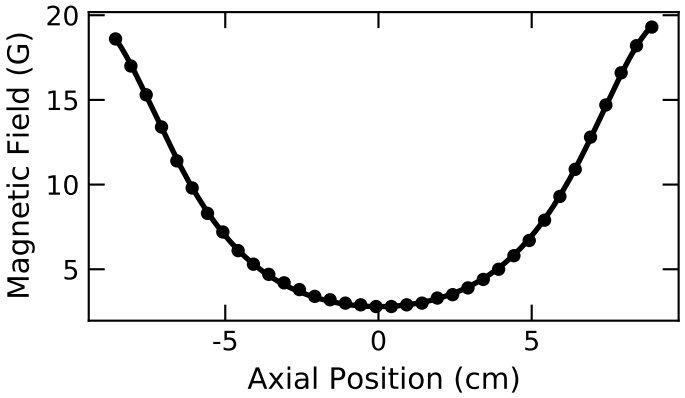

Figure A.6: Axial field of the U/D-shim coils at a current of (3.011(1)) A. The solid line is an equivalent coil fit to the data. Errorbars estimated due to noise are ± 0.15 G and too small to be seen.

Equivalent coil value	Value	Error (±)
R_{eq} (cm)	4.33	0.01
S_{eq} (cm)	19.03	0.05
Field (G A^{-1})	0.927	0.004
Curvature (G A^{-1} cm^{-2})	0.025	0.003
Wire gauge (mm)	1×1	-
Resistance per coil pair(mΩ)	471.12	0.05
N_{turns}	7×6	-

Table A.4: Equivalent coil parameters and associated errors obtained from fitting measured data with Eq. A.2.

A.5 E/W (y) Shim Coils

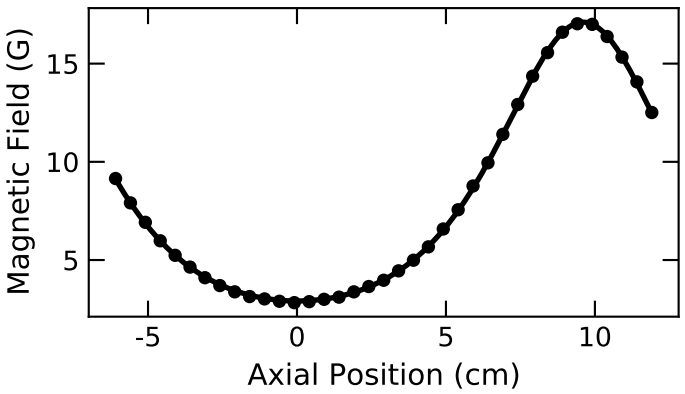

Figure A.7: Axial field of the E/W-shim coils at a current of 3.103(1) A. The solid line is an equivalent coil fit to the data. Errorbars estimated due to noise are ± 0.15 G and too small to be seen.

Equivalent coil value	Value	Error (±)
R_{eq} (cm)	4.74	0.01
S_{eq} (cm)	19.24	0.02
Field (G A^{-1})	0.939	0.003
Curvature (G A^{-1} cm^{-2})	0.0	0.4
Wire gauge (mm)	1×1	-
Resistance per coil pair (mΩ)	541.90	0.05
N_{turns}	7×6	-

Table A.5: Equivalent coil parameters and associated errors obtained from fitting measured data with Eq. (A.2).

A.6 N/S (x) Shim Coils

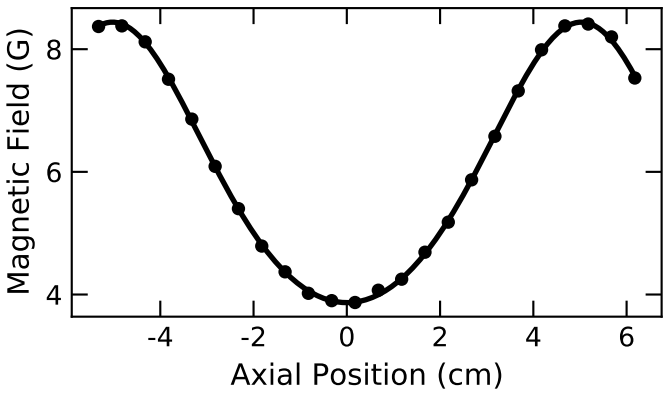

Figure A.8: Axial field of the N/S-shim coils at a current of 3.103(1) A. The solid line is an equivalent coil fit to the data. Errorbars estimated due to noise are ± 0.15 G and too small to be seen.

Equivalent coil value	Value	Error (±)
R_{eq} (cm)	4.05	0.01
S_{eq} (cm)	10.20	0.02
Field (G A^{-1})	1.246	0.004
Curvature (G A^{-1} cm^{-2})	0.09	0.02
Wire gauge (mm)	1×1	-
Resistance per coil pair (mΩ)	172.03	0.05
N_{turns}	4×4	-

Table A.6: Equivalent coil parameters and associated errors obtained from fitting measured data with Eq. (A.2).

Appendix B

Absorption Imaging

In the early stages of the experiment, the Cs MOT was characterised using absorption imaging. In this technique, a weak near-resonant probe beam is shone through the atom cloud onto a camera. Absorption of laser light by the atoms reduces the intensity incident on the camera, so that the 'shadow' cast by the cloud is imaged. The extent of the shadow can be used to infer the cloud $1/e$ width σ, and the amount of absorption can be used to infer the atom number. Experimentally, the absorption imaging probe beam was aligned along the $+x$ axis (outcoupled from the OP fibre, see Fig. 2.19), so that information on the y and z directions was inferred.

Three camera exposures of identical length are taken to generate each absorption image. The first exposure proceeds as described above, with the probe beam shining through the atoms. The second image is taken with the probe beam on after the atoms have dispersed, and serves as a reference image. The final image is a dark image with no illumination and is used in background subtraction. The three images I_{atoms}, I_{ref} and I_{dark} are combined using the following expression to calculate the optical depth (OD) for a given camera pixel [303]:

$$\text{OD} = \ln\left(\frac{I_{\text{ref}} - I_{\text{dark}}}{I_{\text{atoms}} - I_{\text{dark}}}\right). \tag{B.1}$$

Using the effectiv epixel size, one can infer the cloud extent from the image. By summing over pixels in the image, the optical depth can be used calculate

the atom number with the expression [303]:

$$N = \frac{A}{\zeta} \sum_{\mathrm{y,z}} \mathrm{OD}(y, z), \tag{B.2}$$

where A is the effective pixel size and ζ is the atomic absorption cross section.

Appendix C

Quantum Harmonic Oscillator Relations

An atom confined near the lowest-energy motional state of an optical tweezer is a quantum harmonic oscillator (QHO). The motional levels n are equally spaced by an energy corresponding to the trap frequency, $\hbar\omega$. The energy of motional level n is:

$$E_n = \hbar\omega\left(n + \frac{1}{2}\right). \tag{C.1}$$

We would like to know: given an ensemble temperature T, what is the probability to occupy the n^{th} motional level, and what is the mean motional occupancy $\bar{n}$? The answer may be derived using statistical mechanics. We follow the derivations presented in refs. [304, 305].

From the Boltzmann distribution, the probability to occupy any motional level P_n is proportional[1] to the Boltzmann factor for level n, which is energy-dependent:

$$P_n \propto e^{-E_n/k_\mathrm{B}T} = e^{-\beta E_n}, \tag{C.2}$$

where k_B is the Boltzmann constant and $\beta \doteq \frac{1}{k_\mathrm{B}T}$. The probability to be in state n is then given by:

$$P_n = \frac{e^{-\beta E_n}}{\sum\limits_n e^{-\beta E_n}} = \frac{1}{Z}e^{-\beta E_n}, \tag{C.3}$$

[1]The density of states may be neglected because a motional level n has no sublevels.

where the partition function Z has been defined as the sum of all Boltzmann factors, assuming there are many motional states ($\to \infty$) and which serves to as a normalisation factor to give P_n. Substituting Eq. (C.1):

$$\begin{aligned} P_n &= \frac{e^{-\hbar\omega\beta(n+\frac{1}{2})}}{\sum\limits_n e^{-\hbar\omega\beta(n+\frac{1}{2})}} \\ &= \frac{e^{-\hbar\omega\beta(n+\frac{1}{2})}}{e^{-\hbar\omega\beta/2}\sum\limits_n \left(e^{-\hbar\omega\beta}\right)^n} \\ &= e^{-\hbar\omega\beta n}(1-e^{-\beta\hbar\omega}), \end{aligned} \tag{C.4}$$

where in the third line, the known result for the geometric series $\sum\limits_{n=0}^{\infty}(e^{-x})^n = 1/(1-e^{-})$ has been used.

The mean value of n is given by $\bar{n} = \sum np(n)$, which we compute as follows. Setting $x \doteq e^{-\beta\hbar\omega}$, we have:

$$\begin{aligned} \bar{n} &= (1-x)\sum_{n=0}^{\infty} nx^n \\ &= \frac{x}{(1-x)}, \end{aligned} \tag{C.5}$$

where the known result for the power series $\sum\limits_{n=0}^{\infty} nx^n = x/(1-x)^2$ was used in the second line. Finally, we recover the mean motional level presented in Eq. (3.9):

$$\bar{n} = \frac{e^{-\beta\hbar\omega}}{1-e^{-\beta\hbar\omega}} = \frac{1}{e^{\hbar\omega/k_{\mathrm{B}}T}-1}. \tag{3.9 revisited}$$

Using this definition, P_n can be rewritten in terms of $\bar{n}$ to recover Eq. (3.10):

$$P_n(\bar{n}) = \frac{\bar{n}^n}{(1+\bar{n})^{n+1}}, \tag{3.10 revisited}$$

by rearranging $x^n(1-x)$ to the form $(\frac{x}{1-x})^n(1-x)^{n+1}$.

Appendix D

Ray Transfer Matrices

The ray transfer (or ABCD) matrices are a powerful tool for estimating the propagation of laser through an optical system [306]. The effect of optical elements on the waist and divergence of a Gaussian beam can be estimated, as well as changes to the beam pointing in a ray picture. The ABCD matrices were used in this thesis for calculating the cylindircal lens required to correct for astigmatism (Chapter 3) and for calculating the conversion from the AOD deflection angle to a tweezer displacement (Chapter 4).

A Gaussian beam of wavelength λ may be defined by the complex beam parameter q, which encapsulates the radius of curvature R and waist w_0 of the beam:

$$\frac{1}{q} = -i\frac{\lambda}{\pi w_0^2} + \frac{1}{R}. \tag{D.1}$$

The net effect of a linear optical system on the beam is given by the ABCD matrix of the system [307]:

$$M = \begin{pmatrix} A & B \\ C & D \end{pmatrix} = M_n M_{n-1} ... M_2 M_1, \tag{D.2}$$

where the total optical system M is the matrix product of each optical element M_i. Successive optical elements modify R and w_0, so that the final complex beam parameter is related to the initial q by:

$$q' = \frac{Aq + B}{Cq + D}. \tag{D.3}$$

Optical elements may be represented by a 2×2 matrix. q' may therefore be calculated by determining the parameters A, B, C and D through matrix multiplication. Eq. (D.3) can then be rearranged to yield R' and w_0'.

A thin lens is described by the matrix:

$$M_{\text{thin}} = \begin{pmatrix} 1 & 0 \\ -1/f & 1 \end{pmatrix}, \tag{D.4}$$

where f is the focal length. Propagation in free space over a distance d is represented by the matrix:

$$M_{\text{d}} = \begin{pmatrix} 1 & d \\ 0 & 1 \end{pmatrix}. \tag{D.5}$$

As a simple example, focussing of a Gaussian beam by the objective to form an optical tweezer would be given by the following ABCD matrix:

$$M = \begin{pmatrix} A & B \\ C & D \end{pmatrix} = \begin{pmatrix} 1 & f_{\text{obj}} \\ 0 & 1 \end{pmatrix} \begin{pmatrix} 1 & 0 \\ -1/f_{\text{obj}} & 1 \end{pmatrix}. \tag{D.6}$$

M can instead be applied to a ray vector $\underline{v}$ which is described by the position r and the angle θ of the ray with respect to the propagation axis, to yield the final ray vector $\underline{v}'$ of the beam:

$$\underline{v}' = M\underline{v} = M \begin{pmatrix} r \\ \theta \end{pmatrix}. \tag{D.7}$$

The results of the ABCD matrices assume Gaussian optics and do not describe diffraction-limited beams. It is good practice to verify ABCD calculations using a more sophisticated ray-tracing software package such as Zemax.

Appendix E

Atom Density in a Tweezer

The collision measurements performed in this thesis depend on the density of atom pairs prepared in a single optical tweezer. The atom densities are a function of the tweezer trap frequencies and the atom energy. The expressions for the pair density derived here are suitable for homo- and hetero-nuclear atom pairs where each atom may possess a different energy.

E.1 One-Atom Density

In a harmonic potential, the density profile of a single atom follows a Gaussian distribution in each of the trap axes. The 3D density profile is given by the product of the distribution in the separate axes [97]:

$$n_1(x,y,z) = n_0 \prod_{i=x,y,z} \exp\left(-\frac{mi^2\omega_i^2}{2k_\mathrm{B}T}\right), \tag{E.1}$$

where n_0 is the peak density at the centre of the tweezer and $\omega/2\pi$ is the trap frequency along an axis of the trap $i = x, y, z$. n_0 can be calculated by integrating Eq. (E.1) across all space and setting equal to the number of atoms in the tweezer N:

$$n_0 \int_{\text{all space}} \prod_{i=x,y,z} \exp\left(-\frac{mi^2\omega_i^2}{2k_\mathrm{B}T}\right) di = N. \tag{E.2}$$

This expression can be evaluated using the known result of the Gaussian integral, $\int \exp(-ax^2)dx = \sqrt{\pi/a}$, yielding:

$$n_0 = N\left(\frac{m\bar{\omega}^2}{2\pi k_\mathrm{B}T}\right)^{\frac{3}{2}}, \tag{E.3}$$

where the geometric mean trap frequency $\bar{\omega} = \sqrt[3]{\omega_x\omega_y\omega_z}$ has been introduced. For a single atom in a tweezer, $N = 1$. In the following two-atom density derivation, n_0 will be used as a normalisation factor.

E.2 Two-Atom Density

The relevant parameter for the case of two atoms in a single tweezer is the mean *overlap* density n_2, which quantifies the probability to find two atoms in the same space [192]. It is *not* equivalent to setting $N = 2$ in Eq. (E.3). The pair loss rate for homonuclear atoms Γ_2 is related to the k_2 loss coefficient by [282]:

$$\dot{N} = -k_2 \int_{-\infty}^{\infty} n_1^2(r)dr^3 = -k_2\bar{n}_2. \tag{E.4}$$

The overlap is given more generally for a heteronuclear atom pair with masses m_1 and m_2, trap frequencies $\omega_{i,1}$ and $\omega_{i,2}$ and temperatures T_1 and T_2 by the integral:

$$\bar{n}_2 = \int n_1(r)n_2(r)dr^3 = n_{0,1}n_{0,2}\int \prod_{i=x,y,z} \exp\left(-\frac{m_1 i^2\omega_{i,1}^2}{2k_\mathrm{B}T_1}\right)\exp\left(-\frac{m_2 i^2\omega_{i,2}^2}{2k_\mathrm{B}T_2}\right)dr^3. \tag{E.5}$$

Here, the normalisation constants for each atom $n_{0,1}$ and $n_{0,2}$ are given by Eq. (E.3). Defining $m_2\omega_2^2 = \beta^2 m_1\omega_1^2$ [283] and again using the Gaussian integral to evaluate, the following expression for the overlap density is obtained [283, 284]:

$$\bar{n}_2 = \left(\frac{1}{2\pi k_\mathrm{B}}\frac{m_1\bar{\omega}_1^2}{(T_2/\beta^2 + T_1)}\right)^{\frac{3}{2}}. \tag{5.14 revisited}$$

For a homonuclear pair as in the Feshbach resonance study of Chapter 5,

this expression simplifies to:

$$\bar{n}_2 = \left(\frac{m\bar{\omega}^2}{4\pi k_\mathrm{B} T} \right)^{\frac{3}{2}}, \qquad \text{(5.12 revisited)}$$

where T is the mean temperature of the atom pair. From this equation it can be seen that the pair density scales with the tweezer power as $\bar{n}_2 \propto P^{3/4}$, since $\bar{\omega}$ and T are both proportional to $\sqrt{P}$.

E.3 Three-Atom Density

The three body loss rate for collisions in an optical tweezer, assuming all collision participants are lost, is given by the product $\Gamma_3 = \langle n^2 \rangle k_3$ [282], where k_3 is the three-body loss rate coefficient with unit $\mathrm{cm}^6\ \mathrm{s}^{-1}$. The mean-squared density $\langle n^2 \rangle$ can be calculated using [282]:

$$\langle n^2 \rangle = \int n_1(r) n_2(r) n_3(r) dr^3. \tag{E.6}$$

For a homonuclear triplet of the same temperature, we find that:

$$\langle n^2 \rangle = \left(\frac{m^2 \bar{\omega}^4}{12\pi^2 k_\mathrm{B}^2 T^2} \right)^{\frac{3}{2}}. \tag{E.7}$$

Dimensional analysis shows the units of this expression are inverse length to the sixth power, in line with expectation.

Bibliography

[1] L. D. Carr, D. DeMille, R. V. Krems, and J. Ye, *Cold and Ultracold Molecules: Science, Technology and Applications*, N. J. Phys. **11**, 055049 (2009). See page: 1.

[2] S. A. Moses, J. P. Covey, M. T. Miecnikowski, D. S. Jin, and J. Ye, *New Frontiers for Quantum Gases of Polar Molecules*, Nat. Phys. **13**, 13 (2017). See page: 1.

[3] J. A. Blackmore *et al.*, *Ultracold Molecules for Quantum Simulation: Rotational Coherences in CaF and RbCs*, Quantum Sci. Technol. **4**, 014010 (2018). See pages: 1, 6, and 119.

[4] D. DeMille, J. M. Doyle, and A. O. Sushkov, *Probing the Frontiers of Particle Physics with Tabletop-Scale Experiments*, Science **357**, 990 (2017). See pages: 1 and 2.

[5] R. V. Krems, *Cold Controlled Chemistry*, Phys. Chem. Chem. Phys. **10**, 4079 (2008). See page: 1.

[6] D. DeMille, *Quantum Computation with Trapped Polar Molecules*, Phys. Rev. Lett. **88**, 067901 (2002). See pages: 1, 3, and 180.

[7] W. S. Bakr, J. I. Gillen, A. Peng, S. Fölling, and M. Greiner, *A Quantum Gas Microscope for Detecting Single Atoms in a Hubbard-Regime Optical Lattice*, Nature **462**, 74 (2009). See pages: 1 and 7.

[8] N. Schlosser, G. Reymond, I. Protsenko, and P. Grangier, *Sub-Poissonian Loading of Single Atoms in a Microscopic Dipole Trap*, Nature **411**, 1024 (2001). See pages: 1, 7, and 60.

[9] A. M. Kaufman and K.-K. Ni, *Quantum science with optical tweezer arrays of ultracold atoms and molecules*, Nat. Phys. **17**, 1324 (2021). See pages: 1, 60, 116, and 132.

[10] R. P. Feynman, *Simulating physics with computers*, Int. J. Theor. Phys. **21**, 467 (1982). See page: 1.

[11] R. Barnett, D. Petrov, M. Lukin, and E. Demler, *Quantum Magnetism with Multicomponent Dipolar Molecules in an Optical Lattice*, Phys. Rev. Lett. **96**, 190401 (2006). See page: 1.

[12] M. Aymar and O. Dulieu, *Calculation of Accurate Permanent Dipole Moments of the Lowest $\Sigma^{+1,3}$ States of Heteronuclear Alkali Dimers Using Extended Basis Sets*, J. Chem. Phys. **122**, 204302 (2005). See page: 1.

[13] B. Yan *et al.*, *Observation of Dipolar Spin-Exchange Interactions with Lattice-Confined Polar Molecules*, Nature **501**, 521 (2013). See pages: 2 and 8.

[14] S. Malinovskaya, I. Novikova, M. L. Wall, K. R. A. Hazzard, and A. M. Rey, *Quantum Magnetism with Ultracold Molecules* (World Scientific, 2015), chap. 1, pp. 3–37. See pages: 2 and 20.

[15] A. V. Gorshkov, K. R. Hazzard, and A. M. Rey, *Kitaev Honeycomb and Other Exotic Spin Models with Polar Molecules*, Mol. Phys. **111**, 1908 (2013). See page: 2.

[16] W. Lechner and P. Zoller, *From Classical to Quantum Glasses with Ultracold Polar Molecules*, Phys. Rev. Lett. **111**, 185306 (2013). See page: 2.

[17] A. Micheli, G. K. Brennen, and P. Zoller, *A Toolbox for Lattice-Spin Models with Polar Molecules*, Nat. Phys. **2**, 341 (2006). See page: 2.

[18] M. A. Baranov, M. Dalmonte, G. Pupillo, and P. Zoller, *Condensed Matter Theory of Dipolar Quantum Gases*, Chem. Rev. **112**, 5012 (2012). See page: 2.

[19] J. Stuhler *et al.*, *Observation of Dipole-Dipole Interaction in a Degenerate Quantum Gas*, Phys. Rev. Lett. **95**, 150406 (2005). See page: 2.

[20] J. J. McClelland and J. L. Hanssen, *Laser Cooling without Repumping: A Magneto-Optical Trap for Erbium Atoms*, Phys. Rev. Lett. **96**, 143005 (2006). See page: 2.

[21] K. Aikawa *et al.*, *Bose-Einstein Condensation of Erbium*, Phys. Rev. Lett. **108**, 210401 (2012). See page: 2.

[22] M. Lu, S. H. Youn, and B. L. Lev, *Trapping Ultracold Dysprosium: A Highly Magnetic Gas for Dipolar Physics*, Phys. Rev. Lett. **104**, 063001 (2010). See page: 2.

[23] J. T. Wilson *et al.*, *Trapping Alkaline Earth Rydberg Atoms Optical Tweezer Arrays*, Phys. Rev. Lett. **128**, 033201 (2022). See page: 2.

[24] C. S. Adams, J. D. Pritchard, and J. P. Shaffer, *Rydberg Atom Quantum Technologies*, J. Phys. B: At. Mol. Opt. Phys **53**, 012002 (2019). See page: 2.

[25] A. Browaeys and T. Lahaye, *Many-Body Physics with Individually Controlled Rydberg Atoms*, Nat. Phys. **16**, 132 (2020). See page: 2.

[26] M. S. Safronova *et al.*, *Search for New Physics with Atoms and Molecules*, Rev. Mod. Phys. **90**, 025008 (2018). See page: 2.

[27] J. J. Hudson *et al.*, *Improved Measurement of the Shape of the Electron*, Nature **473**, 493 (2011). See page: 2.

[28] J. Baron *et al.*, *Order of Magnitude Smaller Limit on the Electric Dipole Moment of the Electron*, Science **343**, 269 (2014). See page: 2.

[29] V. Andreev *et al.*, *Improved Limit on the Electric Dipole Moment of the Electron*, Nature **562**, 355 (2018). See page: 2.

[30] C. Chin, V. V. Flambaum, and M. G. Kozlov, *Ultracold Molecules: New Probes on the Variation of Fundamental Constants*, N. J. Phys. **11**, 055048 (2009). See page: 2.

[31] V. V. Flambaum and M. G. Kozlov, *Enhanced Sensitivity to the Time Variation of the Fine-Structure Constant and m_p/m_e in Diatomic Molecules*, Phys. Rev. Lett. **99**, 150801 (2007). See page: 2.

[32] D. DeMille *et al.*, *Enhanced Sensitivity to Variation of m_e/m_p in Molecular Spectra*, Phys. Rev. Lett. **100**, 043202 (2008).

[33] T. Zelevinsky, S. Kotochigova, and J. Ye, *Precision Test of Mass-Ratio Variations with Lattice-Confined Ultracold Molecules*, Phys. Rev. Lett. **100**, 043201 (2008). See page: 2.

[34] S. Ospelkaus *et al.*, *Quantum-State Controlled Chemical Reactions of Ultracold Potassium-Rubidium Molecules*, Science **327**, 853 (2010). See page: 3.

[35] P. S. Żuchowski and J. M. Hutson, *Reactions of Ultracold Alkali-Metal Dimers*, Phys. Rev. A **81**, 060703 (2010). See page: 3.

[36] M. H. G. de Miranda *et al.*, *Controlling the Quantum Stereodynamics of Ultracold Bimolecular Reactions*, Nat. Phys. **7**, 502 (2011). See page: 3.

[37] X. Ye, M. Guo, M. L. González-Martínez, G. Quéméner, and D. Wang, *Collisions of Ultracold $^{23}Na^{87}Rb$ Molecules with Controlled Chemical Reactivities*, **4** (2018). See page: 3.

[38] M. Mayle, B. P. Ruzic, and J. L. Bohn, *Statistical Aspects of Ultracold Resonant Scattering*, Phys. Rev. A **85**, 062712 (2012). See page: 3.

[39] M. Mayle, G. Quéméner, B. P. Ruzic, and J. L. Bohn, *Scattering of Ultracold Molecules in the Highly Resonant Regime*, Phys. Rev. A **87**, 012709 (2013). See page: 3.

[40] A. Christianen, M. W. Zwierlein, G. C. Groenenboom, and T. Karman, *Photoinduced Two-Body Loss of Ultracold Molecules*, Phys. Rev. Lett. **123**, 123402 (2019). See page: 3.

[41] P. D. Gregory, J. A. Blackmore, S. L. Bromley, and S. L. Cornish, *Loss of Ultracold ^{87}Rb^{133}Cs Molecules via Optical Excitation of Long-Lived*

Two-Body Collision Complexes, Phys. Rev. Lett. **124**, 163402 (2020). See page: 3.

[42] Y. Liu *et al.*, *Photo-excitation of long-lived transient intermediates in ultracold reactions*, Nature Physics **16**, 1132 (2020). See page: 3.

[43] T. Karman and J. M. Hutson, *Microwave Shielding of Ultracold Polar Molecules*, Phys. Rev. Lett. **121**, 163401 (2018). See page: 3.

[44] P. W. Shor, *Algorithms for Quantum Computation: Discrete Logarithms and Factoring*, in *Proceedings 35th Annual Symposium on Foundations of Computer Science*, pp. 124–134, 1994. See page: 3.

[45] A. Barenco, D. Deutsch, A. Ekert, and R. Jozsa, *Conditional Quantum Dynamics and Logic Gates*, Phys. Rev. Lett. **74**, 4083 (1995). See page: 3.

[46] S. F. Yelin, K. Kirby, and R. Côté, *Schemes for Robust Quantum Computation with Polar Molecules*, Phys. Rev. A **74**, 050301 (2006). See pages: 3 and 21.

[47] J. Zhu, S. Kais, Q. Wei, D. Herschbach, and B. Friedrich, *Implementation of Quantum Logic Gates using Polar Molecules in Pendular States*, J. Chem. Phys. **138**, 024104 (2013).

[48] F. Herrera, Y. Cao, S. Kais, and K. B. Whaley, *Infrared-Dressed Entanglement of Cold Open-Shell Polar Molecules for Universal Matchgate Quantum Computing*, N. J. Phys. **16**, 075001 (2014).

[49] M. Karra, K. Sharma, B. Friedrich, S. Kais, and D. Herschbach, *Prospects for Quantum Computing with an Array of Ultracold Polar Paramagnetic Molecules*, J. Chem. Phys **144**, 094301 (2016). See page: 3.

[50] L. R. Liu *et al.*, *Building One Molecule from a Reservoir of Two Atoms*, Science **360**, 900 (2018). See pages: 4 and 7.

[51] L. Anderegg *et al.*, *An Optical Tweezer Array of Ultracold Molecules*, Science **365**, 1156 (2019). See pages: 4, 8, 116, and 153.

[52] C. J. Foot, *Atomic Physics* (Oxford University Press, 2004). See pages: 4, 31, and 33.

[53] M. R. Tarbutt, *Laser Cooling of Molecules*, Contemp. Phys. **59**, 356 (2018). See page: 4.

[54] B. K. Stuhl, B. C. Sawyer, D. Wang, and J. Ye, *Magneto-optical Trap for Polar Molecules*, Phys. Rev. Lett. **101**, 243002 (2008). See page: 4.

[55] E. B. Norrgard, D. J. McCarron, M. H. Steinecker, M. R. Tarbutt, and D. DeMille, *Submillikelvin Dipolar Molecules in a Radio-Frequency Magneto-Optical Trap*, Phys. Rev. Lett. **116**, 063004 (2016). See page: 4.

[56] H. J. Williams *et al.*, *Characteristics of a Magneto-Optical Trap of Molecules*, N. J. Phys. **19**, 113035 (2017). See page: 4.

[57] L. Anderegg *et al.*, *Radio Frequency Magneto-Optical Trapping of CaF with High Density*, Phys. Rev. Lett. **119**, 103201 (2017). See pages: 4 and 5.

[58] N. E. Bulleid *et al.*, *Characterization of a Cryogenic Beam Source for Atoms and Molecules*, Phys. Chem. Chem. Phys. **15**, 12299 (2013). See page: 5.

[59] V. Zhelyazkova *et al.*, *Laser Cooling and Slowing of CaF Molecules*, Phys. Rev. A **89**, 053416 (2014). See page: 5.

[60] X. Wu *et al.*, *A Cryofuge for Cold-Collision Experiments with Slow Polar Molecules*, Science **358**, 645 (2017). See page: 5.

[61] H. L. Bethlem, G. Berden, and G. Meijer, *Decelerating Neutral Dipolar Molecules*, Phys. Rev. Lett. **83**, 1558 (1999). See page: 5.

[62] E. Narevicius *et al.*, *Stopping Supersonic Oxygen with a Series of Pulsed Electromagnetic Coils: A Molecular Coilgun*, Phys. Rev. A **77**, 051401 (2008). See page: 5.

[63] N. J. Fitch and M. R. Tarbutt, *Principles and Design of a Zeeman-Sisyphus Decelerator for Molecular Beams*, ChemPhysChem **17**, 3609. See page: 5.

[64] J. F. Barry, D. J. McCarron, E. B. Norrgard, M. H. Steinecker, and D. DeMille, *Magneto-Optical Trapping of a Diatomic Molecule*, Nature **512**, 286 (2014). See page: 5.

[65] M. T. Hummon *et al.*, *2D Magneto-Optical Trapping of Diatomic Molecules*, Phys. Rev. Lett. **110**, 143001 (2013). See page: 5.

[66] A. L. Collopy *et al.*, *3D Magneto-Optical Trap of Yttrium Monoxide*, Phys. Rev. Lett. **121**, 213201 (2018). See page: 5.

[67] S. Truppe *et al.*, *Molecules Cooled Below the Doppler limit*, Nat. Phys. **13**, 1173 (2017). See page: 5.

[68] I. Kozyryev *et al.*, *Sisyphus Laser Cooling of a Polyatomic Molecule*, Phys. Rev. Lett. **118**, 173201 (2017). See page: 5.

[69] J. Lim *et al.*, *Laser Cooled YbF Molecules for Measuring the Electron's Electric Dipole Moment*, Phys. Rev. Lett. **120**, 123201 (2018). See page: 5.

[70] K. M. Jones, E. Tiesinga, P. D. Lett, and P. S. Julienne, *Ultracold Photoassociation Spectroscopy: Long-Range Molecules and Atomic Scattering*, Rev. Mod. Phys. **78**, 483 (2006). See pages: 5, 143, 162, and 163.

[71] T. Köhler, K. Góral, and P. S. Julienne, *Production of cold molecules via magnetically tunable Feshbach resonances*, Rev. Mod. Phys. **78**, 1311 (2006). See pages: 5, 83, 148, and 181.

[72] A. Guttridge, M. D. Frye, B. C. Yang, J. M. Hutson, and S. L. Cornish, *Two-Photon Photoassociation Spectroscopy of CsYb: Ground-State Interaction Potential and Interspecies Scattering Lengths*, Phys. Rev. A **98**, 022707 (2018). See page: 5.

[73] S. L. Cornish, N. R. Claussen, J. L. Roberts, E. A. Cornell, and C. E. Wieman, *Stable* ^{85}Rb *Bose-Einstein Condensates with Widely Tunable Interactions*, Phys. Rev. Lett. **85**, 1795 (2000). See pages: 5 and 148.

[74] T. Weber, J. Herbig, M. Mark, H.-C. Nägerl, and R. Grimm, *Bose-Einstein Condensation of Cesium*, Science **299**, 232 (2003). See pages: 5, 148, and 149.

[75] G. Roati *et al.*, ^{39}K *Bose-Einstein Condensate with Tunable Interactions*, Phys. Rev. Lett. **99**, 010403 (2007). See pages: 5 and 148.

[76] F. K. Fatemi, K. M. Jones, and P. D. Lett, *Observation of Optically Induced Feshbach Resonances in Collisions of Cold Atoms*, Phys. Rev. Lett. **85**, 4462 (2000). See page: 5.

[77] J. M. Sage, S. Sainis, T. Bergeman, and D. DeMille, *Optical Production of Ultracold Polar Molecules*, Phys. Rev. Lett. **94**, 203001 (2005). See page: 5.

[78] J. Deiglmayr *et al.*, *Formation of Ultracold Polar Molecules in the Rovibrational Ground State*, Phys. Rev. Lett. **101**, 133004 (2008). See page: 5.

[79] C. Chin, R. Grimm, P. Julienne, and E. Tiesinga, *Feshbach Resonances in Ultracold Gases*, Rev. Mod. Phys. **82**, 1225 (2010). See pages: 5, 148, 161, 164, 180, and 181.

[80] P. S. Julienne, E. Tiesinga, and T. Köhler, *Making Cold Molecules by Time-Dependent Feshbach Resonances*, J. Mod. Opt. **51**, 1787 (2004). See page: 6.

[81] P. K. Molony *et al.*, *Production of Ultracold* $^{87}Rb^{133}Cs$ *in the Absolute Ground State: Complete Characterisation of the Stimulated Raman Adiabatic Passage Transfer*, ChemPhysChem **17**, 3811. See pages: 6, 183, and 184.

[82] K.-K. Ni *et al.*, *A High Phase-Space-Density Gas of Polar Molecules*, Science **322**, 231 (2008). See pages: 6 and 148.

[83] M.-G. Hu *et al.*, *Direct observation of bimolecular reactions of ultracold KRb molecules*, Science **366**, 1111 (2019). See pages: 6 and 148.

[84] J. W. Park, S. A. Will, and M. W. Zwierlein, *Ultracold Dipolar Gas of Fermionic* ^{23}Na^{40}K *Molecules in Their Absolute Ground State*, Phys. Rev. Lett. **114**, 205302 (2015). See pages: 6 and 148.

[85] H. Yang *et al.*, *Observation of magnetically tunable Feshbach resonances in ultracold* $^{23}Na^{40}K + {}^{40}K$ *collisions*, Science **363**, 261 (2019). See pages: 6 and 148.

[86] T. M. Rvachov *et al.*, *Long-Lived Ultracold Molecules with Electric and Magnetic Dipole Moments*, Phys. Rev. Lett. **119**, 143001 (2017). See pages: 6 and 148.

[87] J. G. Danzl *et al.*, *Quantum Gas of Deeply Bound Ground State Molecules*, Science **321**, 1062 (2008). See pages: 6 and 148.

[88] F. Lang, K. Winkler, C. Strauss, R. Grimm, and J. H. Denschlag, *Ultracold Triplet Molecules in the Rovibrational Ground State*, Phys. Rev. Lett. **101**, 133005 (2008). See pages: 6 and 148.

[89] T. Takekoshi *et al.*, *Towards the Production of Ultracold Ground-State RbCs Molecules: Feshbach Resonances, Weakly Bound States, and the Coupled-Channel Model*, Phys. Rev. A **85**, 032506 (2012). See pages: 6, 100, 148, and 181.

[90] P. K. Molony *et al.*, *Creation of Ultracold* $^{87}Rb^{133}Cs$ *Molecules in the Rovibrational Ground State*, Phys. Rev. Lett. **113**, 255301 (2014). See pages: 6, 21, 22, 148, and 183.

[91] M. Guo *et al.*, *Creation of an Ultracold Gas of Ground-State Dipolar* $^{23}Na^{87}Rb$ *Molecules*, Phys. Rev. Lett. **116**, 205303 (2016). See pages: 6 and 148.

[92] P. D. Gregory, J. Aldegunde, J. M. Hutson, and S. L. Cornish, *Controlling the Rotational and Hyperfine State of Ultracold* $^{87}Rb^{133}Cs$ *Molecules*, Phys. Rev. A **94**, 041403 (2016). See pages: 6 and 22.

[93] S. A. Will, J. W. Park, Z. Z. Yan, H. Loh, and M. W. Zwierlein, *Coherent Microwave Control of Ultracold* $^{23}Na^{40}K$ *Molecules*, Phys. Rev. Lett. **116**, 225306 (2016). See page: 6.

[94] M. Greiner, O. Mandel, T. Esslinger, T. W. Hänsch, and I. Bloch, *Quantum Phase Transition from a Superfluid to a Mott Insulator in a Gas of Ultracold Atoms*, Nature **415**, 39 (2002). See page: 7.

[95] W. S. Bakr *et al.*, *Probing the Superfluid–to–Mott Insulator Transition at the Single-Atom Level*, Science **329**, 547 (2010). See page: 7.

[96] C. Weitenberg *et al.*, *Single-Spin Addressing in an Atomic Mott Insulator*, Nature **471**, 319 (2011). See page: 7.

[97] R. Grimm, M. Weidemüller, and Y. B. Ovchinnikov, *Optical Dipole Traps for Neutral Atoms*, Adv. Atom. Mol. Opt. Phys. **42**, 95 (2000). See pages: 7, 66, 68, 90, 111, and 202.

[98] N. Schlosser, G. Reymond, and P. Grangier, *Collisional Blockade in Microscopic Optical Dipole Traps*, Phys. Rev. Lett. **89**, 023005 (2002). See pages: 7 and 73.

[99] J. R. Moffitt, Y. R. Chemla, S. B. Smith, and C. Bustamante, *Recent Advances in Optical Tweezers*, Annu. Rev. Biochem. **77**, 205 (2008). See page: 7.

[100] D. Gao *et al.*, *Optical Manipulation from the Microscale to the Nanoscale: Fundamentals, Advances and Prospects*, Light Sci. Appl. **6**, e17039 (2017). See page: 7.

[101] W. Lee, H. Kim, and J. Ahn, *Three-Dimensional Rearrangement of Single Atoms Using Actively Controlled Optical Microtraps*, Opt. Express **24**, 9816 (2016). See page: 7.

[102] M. Endres *et al.*, *Atom-by-Atom Assembly of Defect-Free One-Dimensional Cold Atom Arrays*, Science **354**, 1024 (2016). See pages: 116, 119, 122, and 127.

[103] D. Barredo, S. de Léséleuc, V. Lienhard, T. Lahaye, and A. Browaeys, *An Atom-by-Atom Assembler of Defect-Free Arbitrary Two-Dimensional Atomic Arrays*, Science **354**, 1021 (2016). See pages: 116, 117, 122, and 180.

[104] D. Barredo, V. Lienhard, S. de Léséleuc, T. Lahaye, and A. Browaeys, *Synthetic Three-Dimensional Atomic Structures Assembled Atom by Atom*, Nature **561**, 79 (2018). See pages: 7 and 116.

[105] J. P. Covey, I. S. Madjarov, A. Cooper, and M. Endres, *2000-Times Repeated Imaging of Strontium Atoms in Clock-Magic Tweezer Arrays*, Phys. Rev. Lett. **122**, 173201 (2019). See page: 7.

[106] A. W. Young *et al.*, *Half-minute-scale atomic coherence and high relative stability in a tweezer clock*, Nature **588**, 408 (2020). See page: 7.

[107] H. Bernien *et al.*, *Probing Many-Body Dynamics on a 51-atom Quantum Simulator*, Nature **551**, 579 (2017). See pages: 7 and 116.

[108] H. Labuhn *et al.*, *Tunable Two-Dimensional Arrays of Single Rydberg Atoms for Realizing Quantum Ising Models*, Nature **534**, 667 (2016). See page: 7.

[109] M. Saffman, T. G. Walker, and K. Mølmer, *Quantum Information with Rydberg Atoms*, Rev. Mod. Phys. **82**, 2313 (2010). See pages: 7 and 185.

[110] J. T. Zhang *et al.*, *Forming a Single Molecule by Magnetoassociation in an Optical Tweezer*, Phys. Rev. Lett. **124**, 253401 (2020). See pages: 8, 149, 180, and 182.

[111] J. D. Hood *et al.*, *Multichannel interactions of two atoms in an optical tweezer*, Phys. Rev. Res. **2**, 023108 (2020). See pages: 8 and 149.

[112] J. T. Zhang *et al.*, *An optical tweezer array of ground-state polar molecules*, https://arxiv.org/abs/2112.00991v1, 2021. See pages: 8, 116, 127, and 185.

[113] W. B. Cairncross *et al.*, *Assembly of a Rovibrational Ground State Molecule in an Optical Tweezer*, Phys. Rev. Lett. **126**, 123402 (2021). See pages: 8 and 185.

[114] L. W. Cheuk *et al.*, *Observation of Collisions between Two Ultracold Ground-State CaF Molecules*, Phys. Rev. Lett. **125**, 043401 (2020). See pages: 8, 116, and 153.

[115] L. Caldwell and M. R. Tarbutt, *Sideband Cooling of Molecules in Optical Traps*, Phys. Rev. Research **2**, 013251 (2020). See page: 8.

[116] K.-K. Ni, T. Rosenband, and D. D. Grimes, *Dipolar Exchange Quantum Logic Gate with Polar Molecules*, Chem. Sci. **9**, 6830 (2018). See pages: 8 and 180.

[117] R. Sawant *et al.*, *Ultracold Polar Molecules as Qudits*, N. J. Phys. **22**, 013027 (2020). See pages: 8 and 180.

[118] D. P. DiVincenzo, *The Physical Implementation of Quantum Computation*, Fortschritte der Phys. **48**, 771. See page: 8.

[119] F. Arute *et al.*, *Quantum supremacy using a programmable superconducting processor*, Nature **574**, 505 (2019). See page: 8.

[120] M. Hughes *et al.*, *Robust entangling gate for polar molecules using magnetic and microwave fields*, Phys. Rev. A **101**, 062308 (2020). See pages: 9 and 180.

[121] D. Luo *et al.*, *Framework for simulating gauge theories with dipolar spin systems*, Phys. Rev. A **102**, 032617 (2020). See page: 9.

[122] E. Kuznetsova, S. T. Rittenhouse, H. R. Sadeghpour, and S. F. Yelin, *Rydberg-atom-mediated nondestructive readout of collective rotational states in polar-molecule arrays*, Phys. Rev. A **94**, 032325 (2016). See pages: 9 and 185.

[123] M. Zeppenfeld, *Nondestructive detection of polar molecules via Rydberg atoms*, Europhys. Lett. **118**, 13002 (2017). See page: 185.

[124] K. Wang, C. P. Williams, L. R. B. Picard, Y. N. Y., and K.-K. Ni, *Enriching the quantum toolbox of ultracold molecules with Rydberg atoms*, https://arxiv.org/abs/2204.05293, 2022. See page: 9.

[125] A. M. Kaufman, B. J. Lester, and C. A. Regal, *Cooling a Single Atom in an Optical Tweezer to Its Quantum Ground State*, Phys. Rev. X **2**, 041014 (2012). See pages: 9, 131, and 180.

[126] J. D. Thompson, T. G. Tiecke, A. S. Zibrov, V. Vuletić, and M. D. Lukin, *Coherence and Raman Sideband Cooling of a Single Atom in an Optical Tweezer*, Phys. Rev. Lett. **110**, 133001 (2013). See page: 67.

[127] K. Wang *et al.*, *Preparation of a Heteronuclear Two-Atom System in the Three-Dimensional Ground State in an Optical Tweezer*, Phys. Rev. A **100**, 063429 (2019). See pages: 9 and 180.

[128] L. R. Liu *et al.*, *Molecular Assembly of Ground-State Cooled Single Atoms*, Phys. Rev. X **9**, 021039 (2019). See pages: 9, 129, and 131.

[129] P. D. Gregory, *Coherent Control of Ultracold Polar Molecules*, PhD thesis, Durham University, 2017. See pages: 18 and 21.

[130] H. P. Büchler *et al.*, *Strongly Correlated 2D Quantum Phases with Cold Polar Molecules: Controlling the Shape of the Interaction Potential*, Phys. Rev. Lett. **98**, 060404 (2007). See page: 20.

[131] J. L. Bohn, *Electric Dipoles at Ultralow Temperatures*, in *Cold Molecules: Theory, Experiment, Applications*, edited by R. V. Krems, W. C. Stwalley, and F. B., chap. 6, CRC Press, 2009. See page: 20.

[132] G. Quéméner and P. S. Julienne, *Ultracold Molecules Under Control!*, Chem. Rev. **112**, 4949 (2012). See page: 20.

[133] K. K. Ni, *A Quantum Gas of Polar Molecules*, PhD thesis, University of Colorado, 2003. See pages: 20 and 21.

[134] C. Fellows, R. Gutterres, A. Campos, J. Vergès, and C. Amiot, *The RbCs $X1\Sigma^+$ Ground Electronic State: New Spectroscopic Study*, J. Mol. Spectrosc. **197**, 19 (1999). See page: 20.

[135] M. W. Gempel *et al.*, *Versatile Electric Fields for the Manipulation of Ultracold NaK Molecules*, N. J. Phys. **18**, 045017 (2016). See page: 21.

[136] P. K. Molony, *Creation of Ultracold Polar Ground-State RbCs Molecules*, PhD thesis, Durham University, 2017. See page: 22.

[137] H. Miller, *Surface flashover of insulators*, IEEE Trans. on Electr. Insul. **24**, 765 (1989). See page: 25.

[138] N. M. Jordan, Y. Y. Lau, D. M. French, R. M. Gilgenbach, and P. Pengvanich, *Electric Field and Electron Orbits Near a Triple Point*, J. Appl. Phys. **102**, 033301 (2007). See page: 25.

[139] J. P. Covey, *Enhanced Optical and Electric Manipulation of a Quantum Gas of KRb Molecules*, PhD thesis, University of Colorado, 2017. See page: 25.

[140] E. Hudson, *Experiments on Cold Molecules Produced via Stark Deceleration*, PhD thesis, University of Colorado, 2006. See page: 26.

[141] M. H. Anderson, J. R. Ensher, M. R. Matthews, C. E. Wieman, and E. A. Cornell, *Observation of Bose-Einstein Condensation in a Dilute Atomic Vapor*, Science **269**, 198 (1995). See page: 30.

[142] N. F. Ramsey, *History of Atomic Clocks*, J Res Natl Bur Stand (1977) **88**, 301 (1983). See page: 30.

[143] B. H. Bransden and C. J. Joachain, *Physics of Atoms and Molecules* (Longman Group Limited, 1983). See page: 31.

[144] D. A. Smith and I. G. Hughes, *The Role of Hyperfine Pumping in Multilevel Systems Exhibiting Saturated Absorption*, Am. J. Phys. **72**, 631 (2004). See page: 33.

[145] B. E. Sherlock and I. G. Hughes, *How weak is a weak probe in laser spectroscopy?*, Am. J. Phys. **77**, 111 (2009). See page: 33.

[146] D. J. McCarron, S. A. King, and S. L. Cornish, *Modulation Transfer Spectroscopy in Atomic Rubidium*, Meas. Sci. Technol. **19**, 105601 (2008). See page: 34.

[147] D. J. McCarron, *A Quantum Degenerate Mixture of* ^{87}*Rb and* ^{133}*Cs*, PhD thesis, Durham University, 2011. See page: 35.

[148] M. A. Zentile *et al.*, *ElecSus: A program to calculate the electric susceptibility of an atomic ensemble*, Comput. Phys. Commun. **189**, 162 (2015). See page: 36.

[149] P. Siddons, C. S. Adams, C. Ge, and I. G. Hughes, *Absolute absorption on rubidium D lines: comparison between theory and experiment*, J. Phys. B: At. Mol. Opt. Phys **41**, 155004 (2008). See page: 36.

[150] L. Weller, R. J. Bettles, P. Siddons, C. S. Adams, and I. G. Hughes, *Absolute absorption on the rubidium D1line including resonant dipole–dipole interactions*, J. Phys. B: At. Mol. Opt. Phys **44**, 195006 (2011). See page: 36.

[151] G. H. Zhang, B. Braverman, A. Kawasaki, and V. Vuletić, *Note: Fast compact laser shutter using a direct current motor and three-dimensional printing*, Rev. Sci. Instrum. **86**, 126105 (2015). See page: 38.

[152] C. S. Adams and I. G. Hughes, *Optics f2f* (Oxford University Press, 2019). See pages: 43, 64, and 116.

[153] J. M. Geary, *Introduction to Lens Design: With Practical Zemax Examples* (Willman-Bell, 2002). See pages: 43 and 45.

[154] C. Robens *et al.*, *High numerical aperture (NA=0.92) for imaging and addressing of cold atoms*, Opt. Lett. **42**, 1043 (2017). See page: 43.

[155] F. Kleißner, *Assembly and Characterization of a High Numerical Aperture Microscope for Single Atoms*, Master's thesis, Univserity of Bonn, 2014. See pages: 44 and 45.

[156] R. Oldenbourg and S. Inouyé, *Microscopes*, in *Handbook of Optics Vol II*, edited by M. Bass, chap. 17, McGraw-Hill, 1995. See page: 45.

[157] C. J. R. Sheppard, *Depth of Field in Optical Microscopy*, Journal of Microscopy **149** (1988). See page: 47.

[158] T. Wiles, *Dynamics of Bright Solitary Matter Waves*, PhD thesis, Durham University, 2013. See page: 56.

[159] A. Ashkin, *Acceleration and Trapping of Particles by Radiation Pressure*, Phys. Rev. Lett. **24**, 156 (1970). See page: 60.

[160] A. Fuhrmanek, R. Bourgain, Y. R. P. Sortais, and A. Browaeys, *Light-assisted collisions between a few cold atoms in a microscopic dipole trap*, Phys. Rev. A **85**, 062708 (2012). See pages: 60 and 73.

[161] E. L. Raab, M. Prentiss, A. Cable, S. Chu, and D. E. Pritchard, *Trapping of Neutral Sodium Atoms with Radiation Pressure*, Phys. Rev. Lett. **59**, 2631 (1987). See page: 62.

[162] A. M. Steane, M. Chowdhury, and C. J. Foot, *Radiation force in the magneto-optical trap*, J. Opt. Soc. Am. B **9**, 2142 (1992).

[163] I. G. Hughes and C. S. Adams, *Laser cooling and trapping*, in *Handbook of Laser Technology and Applications*, edited by C. Webb and J. Jones, chap. 6, CRC Press, 2003. See page: 65.

[164] K. N. Jarvis, J. A. Devlin, T. E. Wall, B. E. Sauer, and M. R. Tarbutt, *Blue-Detuned Magneto-Optical Trap*, Phys. Rev. Lett. **120**, 083201 (2018). See page: 62.

[165] M. Harris, *Realisation of a cold mixture of rubidium and caesium*, PhD thesis, Durham University, 2008. See page: 65.

[166] A. Marchant, *Formation of bright solitary matter-waves*, PhD thesis, Durham University, 2012. See page: 65.

[167] P. D. Lett *et al.*, *Observation of Atoms Laser Cooled below the Doppler Limit*, Phys. Rev. Lett. **61**, 169 (1988). See page: 65.

[168] J. Mitroy, M. S. Safronova, and C. W. Clark, *Theory and applications of atomic and ionic polarizabilities*, J. Phys. B: At. Mol. Opt. Phys **43**, 202001 (2010). See page: 67.

[169] A. Ratkata *et al.*, *Measurement of the tune-out wavelength for* ^{133}Cs *at 880 nm*, Phys. Rev. A **104**, 052813 (2021). See page: 67.

[170] B. Arora, M. S. Safronova, and C. W. Clark, *Magic wavelengths for the np−ns transitions in alkali-metal atoms*, Phys. Rev. A **76**, 052509 (2007). See pages: 67 and 127.

[171] M. S. Safronova, W. R. Johnson, and A. Derevianko, *Relativistic many-body calculations of energy levels, hyperfine constants, electric-dipole matrix elements, and static polarizabilities for alkali-metal atoms*, Phys. Rev. A **60**, 4476 (1999). See page: 68.

[172] M. S. Safronova and C. W. Clark, *Inconsistencies between lifetime and polarizability measurements in Cs*, Phys. Rev. A **69**, 040501 (2004). See page: 68.

[173] R V Brooks *et al.*, *Preparation of one 87Rb and one 133Cs atom in a single optical tweezer*, N. J. Phys. **23**, 065002 (2021). See pages: 68, 116, 171, 174, 175, and 181.

[174] H. J. Metcalf and P. van der Straten, *Laser Cooling and Trapping* (Springer, 1999). See pages: 69 and 107.

[175] R. A. Cline, J. D. Miller, M. R. Matthews, and D. J. Heinzen, *Spin relaxation of optically trapped atoms by light scattering*, Opt. Lett. **19**, 207 (1994). See pages: 69, 112, 114, and 172.

[176] K. Jooya, N. Musterer, K. W. Madison, and J. L. Booth, *Photon-scattering-rate measurement of atoms in a magneto-optical trap*, Phys. Rev. A **88**, 063401 (2013). See page: 69.

[177] N. R. Hutzler, L. R. Liu, Y. Yu, and K.-K. Ni, *Eliminating light shifts for single atom trapping*, N. J. Phys. **19**, 023007 (2017). See pages: 69 and 87.

[178] Y. H. Fung and M. F. Andersen, *Efficient collisional blockade loading of a single atom into a tight microtrap*, N. J. Phys. **17**, 073011 (2015). See page: 73.

[179] A. Gallagher and D. E. Pritchard, *Exoergic collisions of cold Na*-Na*, Phys. Rev. Lett. **63**, 957 (1989). See page: 73.

[180] A. J. Hilliard, Y. H. Fung, P. Sompet, A. V. Carpentier, and M. F. Andersen, *In-trap fluorescence detection of atoms in a microscopic dipole trap*, Phys. Rev. A **91**, 053414 (2015). See page: 77.

[181] M. O. Brown, T. Thiele, C. Kiehl, T.-W. Hsu, and C. A. Regal, *Gray-Molasses Optical-Tweezer Loading: Controlling Collisions for Scaling Atom-Array Assembly*, Phys. Rev. X **9**, 011057 (2019). See pages: 83 and 135.

[182] L. D. Brown, T. T. Cai, and A. DasGupta, *Interval Estimation for a Binomial Proportion*, Stat. Sci. **16**, 101 (2001). See page: 83.

[183] S. J. Blundell and K. M. . Blundell, *Concepts in Thermal Physics* (Oxford University Press, 2009). See page: 83.

[184] C. Tuchendler, A. M. Lance, A. Browaeys, Y. R. P. Sortais, and P. Grangier, *Energy distribution and cooling of a single atom in an optical tweezer*, Phys. Rev. A **78**, 033425 (2008). See page: 85.

[185] J. Dalibard and C. Cohen-Tannoudji, *Dressed-atom approach to atomic motion in laser light: the dipole force revisited*, J. Opt. Soc. Am. B **2**, 1707 (1985). See page: 87.

[186] Y. R. P. Sortais *et al.*, *Diffraction-limited optics for single-atom manipulation*, Phys. Rev. A **75**, 013406 (2007). See page: 90.

[187] R. K. Hanley, *Creation of a strontium microtrap: Towards a spin-squeezed atomic clock*, PhD thesis, Durham University, 2018. See page: 91.

[188] C. Tuchendler, *Nouvelle génération de dispositif à microscope de grande ouverture pour le piégeage d'atomes individuels*, PhD thesis, Institut d'Optique, 2014. See page: 91.

[189] J. Joykutty, V. Mathur, V. Venkataraman, and V. Natarajan, *Direct Measurement of the Oscillation Frequency in an Optical-Tweezers Trap by Parametric Excitation*, Phys. Rev. Lett. **95**, 193902 (2005). See page: 92.

[190] T. A. Savard, K. M. O'Hara, and J. E. Thomas, *Laser-noise-induced heating in far-off resonance optical traps*, Phys. Rev. A **56**, R1095 (1997). See pages: 93 and 128.

[191] D. Steck, *White Paper: Practical Flatness*, available at https://www.semrock.com, 2018. See page: 95.

[192] L. R. Liu, *Building Single Molecules - Reactions, Collisions, and Spectroscopy of Two Atoms*, PhD thesis, 2019. See pages: 96 and 203.

[193] M. P. Köppinger *et al.*, *Production of Optically Trapped* ^{87}RbCs *Feshbach Molecules*, Phys. Rev. A **89**, 033604 (2014). See pages: 100, 181, and 182.

[194] G. Breit and I. I. Rabi, *Measurement of Nuclear Spin*, Phys. Rev. **38**, 2082 (1931). See page: 100.

[195] D. Steck, *Quantum and Atom Optics*, available at http://steck.us/teaching, 2007. See pages: 100 and 107.

[196] E. Arimondo, M. Inguscio, and P. Violino, *Experimental determinations of the hyperfine structure in the alkali atoms*, Rev. Mod. Phys. **49**, 31 (1977). See page: 100.

[197] S. Kuhr *et al.*, *Analysis of dephasing mechanisms in a standing-wave dipole trap*, Phys. Rev. A **72**, 023406 (2005). See pages: 102, 104, and 111.

[198] P. Sompet *et al.*, *Zeeman-insensitive cooling of a single atom to its two-dimensional motional ground state in tightly focused optical tweezers*, Phys. Rev. A **95**, 031403 (2017). See pages: 104, 107, and 180.

[199] S. Silver, editor, *Microwave Antenna Theory and Design* (McGraw-Hill, 1984). See page: 108.

[200] R. Bloom, *Few-Body Collisions in a Quantum Gas Mixture of* ^{40}K *and* ^{87}Rb *Atoms*, PhD thesis, University of Colorado, 2014. See page: 109.

[201] O. Wales, *Splitting and recombination of bright-solitary-matter waves*, PhD thesis, Durham University, 2019. See page: 109.

[202] T. Nakamura and S. Yokokawa, *Loop antenna with a branch wire for circular polarization*, Electron. Commun. Jpn. **70**, 110 (1987). See page: 109.

[203] Y. Murakami, A. Yoshida, K. Ieda, and T. Nakamura, *Rectangular loop antenna for circular polarization*, Electron. Commun. Jpn. **79**, 42 (1996). See page: 109.

[204] R. Ozeri *et al.*, *Hyperfine Coherence in the Presence of Spontaneous Photon Scattering*, Phys. Rev. Lett. **95**, 030403 (2005). See pages: 111, 112, 172, and 174.

[205] R. Louden, *The Quantum Theory of Light* (Oxford University Press, 1983). See page: 112.

[206] P. Xu *et al.*, *Interaction-induced decay of a heteronuclear two-atom system*, Nat. Commun. **6**, 7803 (2015). See page: 113.

[207] I. S. Madjarov *et al.*, *An Atomic-Array Optical Clock with Single-Atom Readout*, Phys. Rev. X **9**, 041052 (2019). See page: 116.

[208] B. J. Lester, N. Luick, A. M. Kaufman, C. M. Reynolds, and C. A. Regal, *Rapid Production of Uniformly Filled Arrays of Neutral Atoms*, Phys. Rev. Lett. **115**, 073003 (2015). See page: 116.

[209] S. Saskin, J. T. Wilson, B. Grinkemeyer, and J. D. Thompson, *Narrow-Line Cooling and Imaging of Ytterbium Atoms in an Optical Tweezer Array*, Phys. Rev. Lett. **122**, 143002 (2019).

[210] C. Sheng *et al.*, *Defect-free arbitrary-geometry assembly of mixed-species atom arrays*, https://arxiv.org/abs/2106.06144v1, 2021. See page: 116.

[211] M. A. Norcia, A. W. Young, and A. M. Kaufman, *Microscopic Control and Detection of Ultracold Strontium in Optical-Tweezer Arrays*, Phys. Rev. X **8**, 041054 (2018). See page: 116.

[212] J. Beugnon *et al.*, *Two-Dimensional Transport and Transfer of a Single Atomic Qubit in Optical Tweezers*, Nat. Phys. **3**, 696 (2007). See page: 116.

[213] L. A. Reynolds *et al.*, *Direct Measurements of Collisional Dynamics in Cold Atom Triads*, Phys. Rev. Lett. **124**, 073401 (2020). See pages: 116, 149, 151, 164, and 170.

[214] H. Kim *et al.*, *In situ single-atom array synthesis using dynamic holographic optical tweezers*, Nat. Commun. **7**, 13317 (2016). See page: 116.

[215] J.-B. Béguin *et al.*, *Reduced volume and reflection for bright optical tweezers with radial Laguerre–Gauss beams*, Proc. Natl. Acad. Sci. U.S.A **117**, 26109 (2020). See pages: 116 and 179.

[216] K. Singh, S. Anand, A. Pocklington, J. T. Kemp, and H. Bernien, *A dual-element, two-dimensional atom array with continuous-mode operation*, https://arxiv.org/abs/2110.05515v1, 2021. See pages: 117 and 180.

[217] D. Stuart and A. Kuhn, *Single-atom trapping and transport in DMD-controlled optical tweezers*, N. J. Phys. **20**, 023013 (2018). See page: 117.

[218] D. Ohl de Mello *et al.*, *Defect-Free Assembly of 2D Clusters of More Than 100 Single-Atom Quantum Systems*, Phys. Rev. Lett. **122**, 203601 (2019). See page: 117.

[219] A. Goutzoulis, D. Pape, and S. Kulakov, *Design and Fabrication of Acousto-Optic Devices* (CRC Press, 1994). See page: 117.

[220] C. V. Raman and N. S. Nagendra Nathe, *The diffraction of light by high frequency sound waves: Part I.*, Proc. Indian Acad. Sci. **2**, 406 (1935). See page: 117.

[221] Lekavich, J., *White Paper: Basics of Acousto-Optical Devices*. See pages: 117 and 121.

[222] C. Shannon, *Communication in the Presence of Noise*, Proc. IRE **37**, 10 (1949). See page: 122.

[223] M. Schroeder, *Synthesis of low-peak-factor signals and binary sequences with low autocorrelation (Corresp.)*, IEEE Trans. Inf. Theory **16**, 85 (1970). See page: 126.

[224] J. Ojarand and M. Min, *Recent Advances in Crest Factor Minimization of Multisine*, Elektron. ir Elektrotech. **23**, 59 (2017). See page: 126.

[225] S. K. Schnelle, E. D. van Ooijen, M. J. Davis, N. R. Heckenberg, and H. Rubinsztein-Dunlop, *Versatile two-dimensional potentials for ultra-cold atoms*, Opt. Express **16**, 1405 (2008). See page: 128.

[226] K. Henderson, C. Ryu, C. MacCormick, and M. G. Boshier, *Experimental demonstration of painting arbitrary and dynamic potentials for Bose–Einstein condensates*, N. J. Phys. **11**, 043030 (2009).

[227] R. V. Brooks, *Creating Arbitrary Trapping Potentials for Ultracold Atoms*, Master's thesis, 2017. See page: 128.

[228] T. Flash and N. Hogan, *The coordination of arm movements: an experimentally confirmed mathematical model*, J. Neurosci. **5**, 1688 (1985). See page: 129.

[229] S. Spence, R. V. Brooks, D. K. Ruttley, A. Guttridge, and S. L. Cornish, *Preparation of one ^{87}Rb and one ^{133}Cs atom in the motional ground state of a single optical tweezer*, https://arxiv.org/abs/2205.09457, 2022. See pages: 131 and 181.

[230] T. Grünzweig, A. Hilliard, M. McGovern, and M. F. Andersen, *Near-deterministic preparation of a single atom in an optical microtrap*, Nat. Phys. **6**, 951 (2010). See pages: 135 and 162.

[231] J. Weiner, V. S. Bagnato, S. Zilio, and P. S. Julienne, *Experiments and theory in cold and ultracold collisions*, Rev. Mod. Phys. **71**, 1 (1999). See page: 141.

[232] L. S. Butcher, D. N. Stacey, C. J. Foot, and K. Burnett, *Ultracold collisions for Bose Einstein condensation*, Phil. Trans. R. Soc. Lond. A **357**, 1421 (1999). See pages: 145 and 147.

[233] B. Bransden and C. Joachain, *Quantum Mechanics 2nd Ed.* (Pearson, 2000). See pages: 142 and 145.

[234] J. Dalibard, *Collisional dynamics of ultracold atomic gases*, in *Proc. Intl. Sch. Phys.*, 2002. See pages: 143 and 145.

[235] J. M. Hutson, *Feshbach resonances in ultracold atomic and molecular collisions: threshold behaviour and suppression of poles in scattering lengths*, New J. Phys **9**, 152 (2007). See page: 157.

[236] C. J. Pethick and H. Smith, *Bose–Einstein Condensation in Dilute Gases*, 2nd ed. (Cambridge University Press, 2008). See pages: 141, 145, and 147.

[237] P. S. Julienne and F. H. Mies, *Collisions of ultracold trapped atoms*, J. Opt. Soc. Am. B **6**, 2257 (1989). See pages: 143 and 144.

[238] H. Boesten, C. Tsai, D. Heinzen, A. Moonen, and B. Verhaar, *Time-independent and time-dependent photoassociation of spin-polarized rubidium*, J. Phys. B: At. Mol. Opt. Phys **32**, 287 (1999). See page: 143.

[239] H. M. J. M. Boesten, C. C. Tsai, B. J. Verhaar, and D. J. Heinzen, *Observation of a Shape Resonance in Cold-Atom Scattering by Pulsed Photoassociation*, Phys. Rev. Lett. **77**, 5194 (1996). See page: 143.

[240] M. Berninger *et al.*, *Feshbach resonances, weakly bound molecular states, and coupled-channel potentials for cesium at high magnetic fields*, Phys. Rev. A **87**, 032517 (2013). See pages: 144, 147, 149, 156, 164, 165, and 170.

[241] M. D. Frye, B. C. Yang, and J. M. Hutson, *Ultracold Collisions of Cs Atoms in Excited Zeeman and Hyperfine States*, Phys. Rev. A **100**, 022702 (2019). See pages: 144, 149, 156, 157, and 163.

[242] A. J. Moerdijk, B. J. Verhaar, and A. Axelsson, *Resonances in ultracold collisions of* ^{6}Li, ^{7}Li, *and* ^{23}Na, Phys. Rev. A **51**, 4852 (1995). See page: 147.

[243] R. V. Brooks *et al.*, *Feshbach Spectroscopy of Cs Atom Pairs in Optical Tweezers*, https://arxiv.org/abs/2204.08877, 2022. See pages: 148, 158, 160, and 161.

[244] E. Tiesinga, B. J. Verhaar, and H. T. C. Stoof, *Threshold and resonance phenomena in ultracold ground-state collisions*, Phys. Rev. A **47**, 4114 (1993). See page: 148.

[245] S. Inouye *et al.*, *Observation of Feshbach resonances in a Bose–Einstein condensate*, Nature **392**, 151 (1998). See page: 148.

[246] E. Tiesinga, A. J. Moerdijk, B. J. Verhaar, and H. T. C. Stoof, *Conditions for Bose-Einstein condensation in magnetically trapped atomic cesium*, Phys. Rev. A **46**, R1167 (1992). See page: 148.

[247] M. Greiner, C. A. Regal, and D. S. Jin, *Emergence of a Molecular Bose–Einstein Condensate from a Fermi Gas*, Nature **426**, 537 (2003). See page: 148.

[248] M. Bartenstein *et al.*, *Crossover from a Molecular Bose-Einstein Condensate to a Degenerate Fermi Gas*, Phys. Rev. Lett. **92**, 120401 (2004).

[249] T. Bourdel *et al.*, *Experimental Study of the BEC-BCS Crossover Region in Lithium 6*, Phys. Rev. Lett. **93**, 050401 (2004). See page: 148.

[250] K. E. Strecker, G. B. Partridge, A. G. Truscott, and R. G. Hulet, *Formation and propagation of matter-wave soliton trains*, Nature **417**, 150 (2002). See page: 148.

[251] L. Khaykovich *et al.*, *Formation of a Matter-Wave Bright Soliton*, Science **296**, 1290 (2002). See page: 148.

[252] E. A. Donley *et al.*, *Dynamics of Collapsing and Exploding Bose-Einstein Condensates*, Nature **412**, 295 (2001). See page: 148.

[253] T. Kraemer *et al.*, *Evidence for Efimov Quantum States in an Ultracold Gas of Caesium Atoms*, Nature **440**, 315 (2006). See pages: 148, 149, 164, and 170.

[254] T. Weber, J. Herbig, M. Mark, H.-C. Nägerl, and R. Grimm, *Three-Body Recombination at Large Scattering Lengths in an Ultracold Atomic Gas*, Phys. Rev. Lett. **91**, 123201 (2003). See pages: 148, 149, and 169.

[255] K. Xu *et al.*, *Formation of Quantum-Degenerate Sodium Molecules*, Phys. Rev. Lett. **91**, 210402 (2003). See page: 148.

[256] C. Chin, V. Vuletić, A. J. Kerman, and S. Chu, *High Resolution Feshbach Spectroscopy of Cesium*, Phys. Rev. Lett. **85**, 2717 (2000). See page: 149.

[257] S. Sala *et al.*, *Coherent Molecule Formation in Anharmonic Potentials Near Confinement-Induced Resonances*, Phys. Rev. Lett. **110**, 203202 (2013). See page: 149.

[258] K. Jachymski, *Precise Feshbach resonance spectroscopy using tight anharmonic traps*, J. Phys. B: At. Mol. Opt. Phys **53**, 065302 (2020). See page: 149.

[259] M. Arndt, M. Ben Dahan, D. Guéry-Odelin, M. W. Reynolds, and J. Dalibard, *Observation of a Zero-Energy Resonance in Cs-Cs Collisions*, Phys. Rev. Lett. **79**, 625 (1997). See page: 149.

[260] J. Söding, D. Guéry-Odelin, P. Desbiolles, G. Ferrari, and J. Dalibard, *Giant Spin Relaxation of an Ultracold Cesium Gas*, Phys. Rev. Lett. **80**, 1869 (1998).

[261] D. Guéry-Odelin, J. Söding, P. Desbiolles, and J. Dalibard, *Strong evaporative cooling of a trapped cesium gas*, Opt. Express **2**, 323 (1998).

[262] S. A. Hopkins *et al.*, *Measurement of elastic cross section for cold cesium collisions*, Phys. Rev. A **61**, 032707 (2000).

[263] P. J. Leo, C. J. Williams, and P. S. Julienne, *Collision Properties of Ultracold ^{133}Cs Atoms*, Phys. Rev. Lett. **85**, 2721 (2000). See pages: 149, 160, and 178.

[264] C. Chin *et al.*, *Precision Feshbach spectroscopy of ultracold* Cs_2, Phys. Rev. A **70**, 032701 (2004). See pages: 149, 150, 156, 163, 164, and 178.

[265] V. Vuletić, C. Chin, A. J. Kerman, and S. Chu, *Suppression of Atomic Radiative Collisions by Tuning the Ground State Scattering Length*, Phys. Rev. Lett. **83**, 943 (1999). See pages: 150, 161, and 163.

[266] M. McGovern, A. J. Hilliard, T. Grünzweig, and M. F. Andersen, *Counting atoms in a deep optical microtrap*, Opt. Lett. **36**, 1041 (2011). See page: 153.

[267] N. C. Jackson *et al.*, *Number-resolved imaging of ^{88}Sr atoms in a long working distance optical tweezer*, SciPost Phys. **8**, 38 (2020). See page: 153.

[268] J. Hutson and M. Frye, Private Communication (2022). See page: 164.

[269] V. Vuletić, A. J. Kerman, C. Chin, and S. Chu, *Observation of Low-Field Feshbach Resonances in Collisions of Cesium Atoms*, Phys. Rev. Lett. **82**, 1406 (1999). See page: 161.

[270] C. Chin, A. J. Kerman, V. Vuletić, and S. Chu, *Sensitive Detection of Cold Cesium Molecules Formed on Feshbach Resonances*, Phys. Rev. Lett. **90**, 033201 (2003). See page: 161.

[271] K. Burnett, P. S. Julienne, and K.-A. Suominen, *Laser-Driven Collisions between Atoms in a Bose-Einstein Condensed Gas*, Phys. Rev. Lett. **77**, 1416 (1996). See page: 162.

[272] Fioretti, A. *et al.*, *Photoassociative spectroscopy of the Cs_2 0g- long-range state*, Eur. Phys. J. D **5**, 389 (1999). See page: 162.

[273] D. J. Thompson and R. E. Scholten, *Narrow linewidth tunable external cavity diode laser using wide bandwidth filter*, Rev. Sci. Instrum. **83**, 023107 (2012). See page: 163.

[274] M. J. Mark, F. Meinert, K. Lauber, and H.-C. Nägerl, *Mott-Insulator-Aided Detection of Ultra-Narrow Feshbach Resonances*, SciPost Phys. **5**, 55 (2018). See page: 163.

[275] S. Kotochigova, E. Tiesinga, and P. S. Julienne, *Relativistic ab initio treatment of the second-order spin-orbit splitting of the $a^3\Sigma_u^+$ potential of rubidium and cesium dimers*, Phys. Rev. A **63**, 012517 (2000). See page: 163.

[276] M. Berninger *et al.*, *Universality of the Three-Body Parameter for Efimov States in Ultracold Cesium*, Phys. Rev. Lett. **107**, 120401 (2011). See page: 164.

[277] R. Grimm, *Efimov States in an Ultracold Gas: How it Happened in the Laboratory*, Few-Body Syst. **60**, 23 (2019). See page: 164.

[278] P. O. Fedichev, M. W. Reynolds, and G. V. Shlyapnikov, *Three-Body Recombination of Ultracold Atoms to a Weakly Bound s Level*, Phys. Rev. Lett. **77**, 2921 (1996). See page: 165.

[279] P. F. Bedaque, E. Braaten, and H.-W. Hammer, *Three-body Recombination in Bose Gases with Large Scattering Length*, Phys. Rev. Lett. **85**, 908 (2000). See page: 165.

[280] J. P. D'Incao, *Few-body physics in resonantly interacting ultracold quantum gases*, J. Phys. B: At. Mol. Opt. Phys **51**, 043001 (2018). See page: 165.

[281] I. G. Hughes and T. P. A. Hase, *Measurements and their Uncertainties* (Oxford, 2010). See page: 167.

[282] J. L. Roberts, N. R. Claussen, S. L. Cornish, and C. E. Wieman, *Magnetic Field Dependence of Ultracold Inelastic Collisions near a Feshbach Resonance*, Phys. Rev. Lett. **85**, 728 (2000). See pages: 170, 203, and 204.

[283] M. Anderlini *et al.*, *Model for collisions in ultracold-atom mixtures*, Phys. Rev. A **72**, 033408 (2005). See pages: 171 and 203.

[284] A. Guttridge *et al.*, *Interspecies thermalization in an ultracold mixture of Cs and Yb in an optical trap*, Phys. Rev. A **96**, 012704 (2017). See pages: 171 and 203.

[285] B. Ueberholz, S. Kuhr, D. Frese, V. Gomer, and D. Meschede, *Cold collisions in a high-gradient magneto-optical trap*, J. Phys. B: At. Mol. Opt. Phys **35**, 4899 (2002). See page: 172.

[286] H. M. Gibbs and R. J. Hull, *Spin-Exchange Cross Sections for* Rb^{87}-Rb^{87} *and* Rb^{87}-Cs^{133} *Collisions*, Phys. Rev. **153**, 132 (1967). See page: 174.

[287] M. Anderlini *et al.*, *Sympathetic cooling and collisional properties of a Rb-Cs mixture*, Phys. Rev. A **71**, 061401 (2005). See page: 174.

[288] Y. Yu *et al.*, *Motional-ground-state cooling outside the Lamb-Dicke regime*, Phys. Rev. A **97**, 063423 (2018). See page: 180.

[289] N. Lorenz, L. Festa, L.-M. Steinert, and C. Gross, *Raman Sideband Cooling in Optical Tweezer Arrays for Rydberg Dressing*, SciPost Phys. **10**, 52 (2021). See page: 180.

[290] F. Diedrich, J. C. Bergquist, W. M. Itano, and D. J. Wineland, *Laser Cooling to the Zero-Point Energy of Motion*, Phys. Rev. Lett. **62**, 403 (1989). See page: 181.

[291] H.-W. Cho *et al.*, *Feshbach spectroscopy of an ultracold mixture of* ^{85}*Rb and* ^{133}*Cs*, Phys. Rev. A **87**, 010703 (2013). See page: 181.

[292] P. D. Gregory *et al.*, *A simple, versatile laser system for the creation of ultracold ground state molecules*, N. J. Phys. **17**, 055006 (2015). See page: 182.

[293] E. Hodby *et al.*, *Production Efficiency of Ultracold Feshbach Molecules in Bosonic and Fermionic Systems*, Phys. Rev. Lett. **94**, 120402 (2005). See page: 182.

[294] K. Bergmann, H. Theuer, and B. W. Shore, *Coherent population transfer among quantum states of atoms and molecules*, Rev. Mod. Phys. **70**, 1003 (1998). See pages: 183 and 184.

[295] N. V. Vitanov, A. A. Rangelov, B. W. Shore, and K. Bergmann, *Stimulated Raman adiabatic passage in physics, chemistry, and beyond*, Rev. Mod. Phys. **89**, 015006 (2017). See pages: 183 and 184.

[296] T. Takekoshi *et al.*, *Ultracold Dense Samples of Dipolar RbCs Molecules in the Rovibrational and Hyperfine Ground State*, Phys. Rev. Lett. **113**, 205301 (2014). See page: 183.

[297] S. A. Moses *et al.*, *Creation of a low-entropy quantum gas of polar molecules in an optical lattice*, Science **350**, 659 (2015). See page: 185.

[298] E. Kuznetsova, S. T. Rittenhouse, H. R. Sadeghpour, and S. F. Yelin, *Rydberg atom mediated polar molecule interactions: a tool for molecular-state conditional quantum gates and individual addressability*, Phys. Chem. Chem. Phys. **13**, 17115 (2011). See page: 185.

[299] S. T. Rittenhouse and H. R. Sadeghpour, *Ultracold Giant Polyatomic Rydberg Molecules: Coherent Control of Molecular Orientation*, Phys. Rev. Lett. **104**, 243002 (2010). See page: 185.

[300] R. González-Férez, S. T. Rittenhouse, P. Schmelcher, and H. R. Sadeghpour, *A protocol to realize triatomic ultralong range Rydberg molecules in an ultracold KRb gas*, J. Phys. B: At. Mol. Opt. Phys **53**, 074002 (2020). See page: 185.

[301] P. Tierney, *Magnetic trapping of an ultracold ^{87}Rb-^{133}Cs atomic mixture*, PhD thesis, Durham University, 2009. See page: 187.

[302] S. Händel, *Experiments on ultracold quantum gases of ^{85}Rb and ^{87}Rb*, PhD thesis, Durham University, 2011. See page: 187.

[303] A. Rakonjac, *A Versatile Collider For Ultracold Atoms*, PhD thesis, University of Otago, 2012. See pages: 196 and 197.

[304] R. Baierlein, *Thermal Physics* (Cambridge University Press, 1999). See page: 198.

[305] J. McGreevy, *Lecture Notes: Statistical Mechanics at Fixed Temperature (Canonical Ensemble)*, https://mcgreevy.physics.ucsd.edu/, 2012, Accessed 3 February 2022. See page: 198.

[306] H. Kogelnik and T. Li, *Laser Beams and Resonators*, Appl. Opt. **5**, 1550 (1966). See page: 200.

[307] P. A. Bélanger, *Beam propagation and the ABCD ray matrices*, Opt. Lett. **16**, 196 (1991). See page: 200.